DENSELY INTEGRATED MICRORING-RESONATOR BASED COMPONENTS FOR FIBER-TO-THE-HOME APPLICATIONS

Edwin Jan Klein

Promotiecommissie:

Promotor:	Prof. Dr. A. Driessen	Universiteit Twente
Leden:	Prof. Dr. M. Pollnau	Universiteit Twente
	Prof. Dr. Ir. R. Baets	Universiteit Gent
	Prof. Dr. Ir. W.C. Van Etten	Universiteit Twente
	Dr. A. Melloni	Politecnico di Milano
	Dr. Ir. R.G. Heideman	LioniX B.V.
	Dr. Ir. H. De Waardt	Technische Universiteit Eindhoven.

The research carried out in this thesis was carried out at the Integrated Optical Microsystems (IOMS) Group of the MESA Research Institute and the Faculty of Electrical Engineering, Mathematics and Computer Science (EEMCS), University of Twente, PO. Box 217, 7500 AE Enschede, The Netherlands.

The work was financially supported by the EC funded IST-Project NAIS, Next-Generation Active Integrated-Optic Subsystems, (IST-2000-28018), and by the Dutch Freeband Communication Project “Broadband Photonics”.

Cover design:

The illustration on the cover shows a “Hyper resonator”, so named for its complex resonant nature. This circuit, given to me by Ronald Dekker as a brainteaser, sat idle on a post-it for nearly three years after it was first drawn. Since then it has become a taunting symbol of the complexity of seemingly simple circuits until, at the very end of four years of research, a simulation tool was finally created that could simulate this and many other circuits.
However, not only this software was created but also several micro-resonator based devices of such complexity that they required packaging and the development of control electronics before being able to operate. As such the three inner circles in the “Hyper resonator” have also come to symbolize the three pillars that form the basis of this thesis is: simulation software, fabricated optical devices and their controlling hardware. Without the development of any one of these this thesis might have looked quite different…

ISBN 978-90-365-2495-7

DENSELY INTEGRATED MICRORING-RESONATOR BASED COMPONENTS FOR FIBER-TO-THE-HOME APPLICATIONS

PROEFSCHRIFT

Ter verkrijging van
de graad van doctor aan de Universiteit Twente,
op gezag van de rector magnificus,
prof. dr. W.H.M. Zijm,
volgens besluit van het College voor Promoties
in het openbaar te verdedigen
op 11 April 2007 om 15.00 uur

door

Edwin Jan Klein
geboren op 20 januari 1976
te Zwolle

Dit proefschrift is goedgekeurd door:
Prof. Dr. Alfred Driessen

To my parents…

Abstract

This thesis describes the design, realization and characterization of densely integrated optical components based on thermally tunable microring resonators fabricated in Si_3N_4/SiO_2.

Chapter 1 "Introduction"
In this chapter a brief introduction and overview are given of current broadband communication networks to provide a background for the work presented in this thesis. Current copper based networks are unable to meet future bandwidth demands and will therefore be slowly replaced with optical networks. A promising technology for these networks is WDM-PON. Currently, however, this technology is too expensive. The Broadband Photonics and NAIS projects within which the presented work was carried out both seek to lower the cost of WDM-PON implementations through dense integration of reconfigurable optical components based on optical microring resonators.

Chapter 2 "The micro-resonator"
In the second chapter the operating principle of a microring resonator is explained and the basic parameters that govern its operation are introduced. The filter frequency-domain responses for single as well as serial higher order systems based on two resonators are derived. Solutions for typical problems that occur when designing resonators such as a Free Spectral Range (FSR) that is too small or a filter shape that does not meet the desired specifications are also given.

Chapter 3 "Design"
In the third chapter the design of microring resonator based devices is discussed in general terms. Several performance parameters are introduced that can be used to translate the requirements of a certain application into specific values of the basic microring resonator parameters.
For microring resonators with a radius of 50 μm (FSR≈4.2 nm) , which is the case for most of the devices presented in this thesis, it is shown that for telecom applications a good target for the field coupling coefficients is between 0.4 and 0.6 when reasonable losses of 2 dB/cm are assumed for the resonator. The methodologies for creating an actual resonator design from these basic parameters are also given. In addition design aspects on a device level (the whole device layout) are discussed. Here it is shown that for these resonators the miniaturization of devices that incorporate these

resonators is limited by the spacing of the fibers in the fiber array used for pigtailing rather than the size of the individual resonators.

Chapter 4 "Simulation and analysis"

In Chapter 4 some of the tools that were created to aid in the design and characterization of microring resonator based devices are presented. In particular the analytical and numerical methods used to fit measured resonator responses are examined in detail. Another tool that is discussed is Aurora, a tool that was created to perform simulations on complex optical circuits containing resonators. The simulations performed by Aurora are time-domain based. Although the simulation principle, based on the delayed forwarding of signals between optical components, is fairly simple, it is nonetheless very powerful and allows for a very fast simulation of highly complex optical circuits.

Chapter 5 "Fabrication"

In Chapter 5 three distinct fabrication processes are described. Each process was designed for a specific resonator type. The simplest process was designed for laterally coupled resonators. This process does not suffer from resonator misalignment but is critical where the resolution of the lithography is concerned. A more complex process was designed for vertically coupled resonators. The lithographic requirements of this process are less important although the process is highly susceptible to resonator misalignment. The most elaborate fabrication process is based on stepper lithography. This allows for very small feature sizes as well as a high alignment accuracy which is very important from a device yield perspective. The only downside is that the maximum size of devices is limited to 22 by 22 mm. However, devices made in a materials system with a high index contrast such as Si_3N_4/SiO_2 will often be smaller than this. The stepper process also included chemical mechanical polishing of the separation layer between the ring resonator and the port waveguides in order to reduce the losses in the resonator caused by an abrupt "lifting" of the resonator on top of the port waveguides.

Chapter 6 "Microring-resonator building blocks"

In Chapter 6 the design of a basic resonator building block is given. This building block is based on a 2.0 x 0.14 μm port waveguide from where the light is coupled into a ring resonator that has waveguide dimensions of 2.5 x 0.18 μm and a radius of 50 μm. On top of the resonator a heater is placed to be able to shift its resonance wavelength. Depending on the resonator radius (25 or 50 μm) and the thickness of the cladding layer on top of the resonator (3 or 4 μm) resonance shifts between 7 pm/mW and 21 pm/mW have been observed. By using an overshoot in the electrical signal that drives the heater, thermal modulation frequencies up to 10 KHz could be observed. Also demonstrated in this chapter is a wavelength selective optical switch based on two cascaded resonators. The switch measures only 200 μm x 200 μm. The "on/off" attenuation of the switch is 12 dB. When the switch is "on" the crosstalk with the adjacent channels is ≈-20 dB (channel spacing of 0.8 nm). The on chip insertion loss of the switch is around 5 dB. A Vernier resonator based on two resonators with a radius of 46 μm and 55 μm is also demonstrated. The combined FSR is ≈28 μm.

Chapter 7 "Densely integrated devices for WDM-PON"
In Chapter 7 the design and characterization of two different types of OADM, for use at 1310 nm or at 1550 nm, and a Router are discussed. The 1550 nm OADM could be fully tuned and could be configured to drop one or more channels. In addition system level measurements were performed in this OADM. A 40 Gbit/s could be dropped to a single channel without a significant penalty in BER. In addition multicasting was demonstrated. The same reconfigurability was also shown for the 1300 nm OADM. Finally the 1300 nm router is discussed and basic functionality of the router, dropping one, two or three channels to a single output is demonstrated.

Chapter 8 "Polarization independent devices"
A major problem of microring resonator based devices is that it is often very difficult to make them polarization independent. Although this can by solved by introducing polarization diversity in the devices this also doubles the number of resonators and creates a number of new problems. In Chapter 8 a method is described where a single microring resonator is used bi-directionally so that a single resonator effectively operates as if two resonators are present. The number of resonators that is required to implement polarization diversity in a device is therefore more or less the same (there is a minor overhead) as the number of resonators in an implementation that uses polarization independent resonators.

Chapter 9 "Discussion and conclusions"
Finally, in Chapter 9, conclusions are drawn based on the results presented in this thesis.

Samenvatting

Dit proefschrift beschrijft het ontwerp, de realisatie en de karakterisatie van hoog geïntegreerde optische componenten gebaseerd op thermisch verstembare microring resonatoren in het Si_3N_4/SiO_2 materiall system.

Hoofdstuk 1 "Introductie"
In dit hoofdstuk worden een korte introductie en overzicht gegeven van huidige breedband communicatie netwerken om een achtergrond te geven van het onderzoek dat gepresenteerd wordt in dit proefschrift. Huidige netwerken gebaseerd op koper zijn niet in staat om tegemoet te komen aan de toekomstige vraag om bandbreedte van de consument. Daardoor worden deze geleidelijk aan vervangen door optische netwerken. Een veelbelovende techniek hiervoor is WDM-PON. Op dit moment echter, is deze technologie nog te duur voor gebruik. urrently, however, this technology is too expensive. De Broadband Photonics en NAIS projecten waarbinnen het werk dat gepresenteerd wordt in deze thesis is uitgevoerd hadden beide als belangrijke doelstelling om de kosten van een WDM-PON network te reduceren. Dit door zeer hoog geïntegreerde en reconfigureerbare optische componenten te ontwikkelen op basis van microring resonatoren.

Hoofdstuk 2 "De micro-resonator"
In het tweede hoofdstuk wordt de werking van de microring resonator uitgelegd en worden de basis parameters die de werking van de resonator bepalen geïntroduceerd. De frequentie domein filter responses van enkele alsook van twee seriëel gekoppelde resonatoren worden afgeleid. Oplossingen voor typische problemen die voor kunnen komen bij het ontwerp van micro resonatoren zoals een Free Spectral Range (FSR) die te klein is of een filter vorm die niet voldoet aan de specificaties worden ook aangedragen.

Hoofdstuk 3 "Ontwerp"
In het derde hoofdstuk wordt het ontwerp van microring resonatoren besproken in algemene termen. Een aantal performance parameters worden geïntroduceerd die gebruikt kunnen worden om gewenste specificaties van een applicatie te vertalen in specifieke waarden van de basis parameters.
Voor microring resonatoren met een radius van 50 µm (FSR≈4.2 nm) , zoals geldt voor de meeste resonatoren die gepresenteerd worden in dit proefschrift, wordt aangetoond dat een goed doelgebied voor de veld koppelings coëfficienten ligt tussen 0.4 en 0.6 als redelijke bochtverliezen van 2 dB/cm worden aangenomenn voor de resonator. De methodieken voor het ontwerpen van een resonator aan de hand van deze basis parameters worden ook gegeven. Voorts wordt er ingegaan op de ontwerp

aspecten op component niveau (betreffende de gehele device layout). Een conclusie die hier getrokken wordt, is dat de gegeven resonatoren niet de limiterende factor voor verdere miniaturisatie zijn. Echter, de afstand van 250 μm van de fibers in een fiber array zorgt ervoor dat de componenten niet verder verkleind kunnen worden.

Hoofdstuk 4 "Simulatie en analyse"
In hoofdstuk 4 worden een aantal van de programma's die gemaakt zijn om te helpen bij het ontwerp en de analyse van op microring resonator gebaseerde componenten gepresenteerd. In het bijzonder worden de analytische en numerieke algoritmes besproken die gebruikt worden voor het fitten van gemeten microring resonator responses. Een ander programma dat besproken wordt, is Aurora, een simulatieprogramma dat special gebouwd werd om simulaties te kunnen doen aan complexe optische schakelingen die microring resonatoren bevatten.

Hoofdstuk 5 "Fabricage"
In hoofdstuk 5 worden drie specifieke fabricage processen beschreven. Elk proces is bedoeld om gebruikt te worden om een specifiek soort resonator te fabriceren. Het meest eenvoudige proces is bedoeld voor het fabriceren van lateral gekoppelde resonatoren. Dit proces is ongevoelig voor resonator plaatsing ten opzichte van de poort golfgeleiders maar is kritisch wat betreft de resolutie van de lithografie. Een enigszins ingewikkelder proces werd gebruikt voor de fabricage van vertikaal gekoppelde resonatoren. De lithografische resolutie is van minder belang in dit proces. Dit process is echter zeer gevoelig voor de uitlijning van de resonator op de poort golfgeleiders. Het meest uitvoerige proces werd gebruikt voor de fabricage van resonatoren met behulp van stepper lithografie. Met stepper lithografie kan een hoge lithografische resolutie behaald worden alsook een goede uitlijning wat zeer belangrijk is met het oog op het reduceren van uitval van gefabriceerde componenten. The most elaborate fabrication process is based on stepper lithography. Het enige minpunt is dat de maximum grootte van de componenten is gelimiteerd tot ongeveer 22 bij 22 mm. Echter, componenten die gemaakt worden in een hoog contrast material system zoals Si_3N_4/SiO_2 zullen niet snel deze grootte bereiken. In het fabricage proces gebruikt in combinatie met de stepper, werd ook chemisch mechanisch polijsten toegepast op de laag tussen de poort golfgeleiders en the ring resonator. Dit om de verliezen te reduceren die optraden bij het plotselinge "oplichten" van de resonator golfgeleider op de locatie van de poort golfgeleiders.

Hoofdstuk 6 "Microring-resonator bouw blokken"
In hoofdstuk 6 wordt het ontwerp van een microring resonator bouw blok gegeven. Dit bouw blok is gebaseerd op een 2.0 x 0.14 μm poort golfgeleider vanwaar licht ingekoppeld in een ring resonator met een kanaal afmeting van 2.5 x 0.18 μm en een radius van 50 μm. Bovenop deze resonator is een verwarmingselement geplaatst waarmee de resonantie golflengte verstemd kan worden. Afhankelijk van de radius van de ring resonator (25 of 50 μm) en de dikte van de buffer lag bovenop de resonator (3 of 4 μm) warden resonantie verschuivingen van 7 pm/mW tot 21 pm/mW waargenomen. Door gebruikmaking van pulsvorming in het electrisch aansturingssignaal van het verwarmingselement konden thermische modulatie frequenties gehaald worden tot 10 KHz. In dit hoofdstuk word took een golflengte afhankelijke optische schakelaar besproken welke is gebaseerd op twee in serie geschakelde microring resonatoren. De oppervlakte van de schakelaar is slechts 200 μm x 200 μm. De "aan/uit" signal onderdrukking van de schakelaar 12 dB. Als de

schakelaar “aan” is, dan is de overspraak met de naastgelegen kanalen ≈-20 dB (bij een kanaal afstand van 0.8 nm). De op-chip signal verlizen zijn rond de 5 dB. Een Vernier resonator gebaseerd op twee ringen met een radius van 46 μm en 55 μm wordt ook gepresenteerd. De gecombineerde FSR van deze resonator is ≈28 μm.

Hoofdstuk 7 “Hoog geïntegreerde optische componenten voor WDM-PON”
In hoofdstuk 7 worden het ontwerp en de karakterisatie van twee types OADM, werkend bij 1310 nm en 1550 nm, en een Router besproken. De 1550 nm OADM kon volledig worden geconfigureerd om een enkel of meerdere kanalen te droppen. Systeem niveau metingen uitgevoerd aan de OADM lieten zien dat een 40 Gbit/s gedropped kon worden naar een enkele drop poort zonder een significante penalty in de BER. Tevens is er multicasting gedemonstreerd. De 1300 nm OADM kon op gelijke wijze worden geconfigureerd. Basis functionaliteit van de 1300 nm router kon ook worden aangetoond door het droppen van een, twee of drie kanalen naar een enkele drop poort.

Hoofdstuk 8 “Polarisatie onafhankelijke componenten”
Een groot probleem bij op microring resonator gebaseerde componenten is dat het vaak moeilijk is om deze polarisatie onafhankelijk te maken. Hoewel dit opgelost kan worden door het gebruik van polarisatie diversiteit in de componenten, verdubbeld dit ook het aantal benodigde microring resonatoren en creëert tevens een aantal nieuwe problemen. In hoofdstuk 8 wordt een methode gepresenteerd waarbij een enkele microring resonator bidirectioneel wordt gebruikt zodat deze effectief werkt als twee resonatoren. Het aantal resonatoren wat nodig is voor het implementeren van polarisatie diversiteit kan daardoor vrijwel gelijk blijven (er is een kleine toename) aan het aantal resonatoren in een component gebaseerd op polarisatie onafhankelijke resonatoren.

Hoofdstuk 9 “Discussie and conclusie”
Ten slotte, in hoofdstuk 9, worden er conclusies getrokken gebaseerd op de resultaten die gepresenteerd zijn in dit proefschrift.

Contents

ABSTRACT ..... **I**

SAMENVATTING ..... **IV**

CHAPTER 1 INTRODUCTION **1**

1.1 PREFACE 2
1.2 BROADBAND TO THE HOME 3
1.3 BRINGING FIBER TO THE HOME 5
1.3.1 Passive optical networks *5*
1.3.2 Ethernet Point to Point networks *5*
1.3.3 Wavelength Division Multiplexed PON *6*
1.4 PROJECTS 6
1.4.1 NAIS *6*
1.4.2 Broadband Photonics *7*
1.5 OUTLINE 8

CHAPTER 2 THE MICRO-RESONATOR **11**

2.1 INTRODUCTION 12
2.2 OPERATIONAL DESCRIPTION 12
2.2.1 Four port filter operation *13*
2.1.2 Transient resonator behavior *14*
2.3 MICRORING RESONATOR MODEL 15
2.3.1 Directional coupler model *15*
2.3.2 Ring waveguide model *17*
2.3.3 Combined model *18*
2.4 SPECTRAL RESPONSE OF A SINGLE RESONATOR 18
2.4.1 The drop response *19*
2.4.2 The through response *21*
2.5 MR FILTER BANDWIDTH VERSUS REJECTION RATIO 22
2.6 MULTIPLE-RESONATOR FILTERS 24
2.7 VERNIER OPERATION 29
2.8 RESONATOR TUNING 31
2.8.1 Wavelength tuning methods *31*
2.8.2 Wavelength tuning range *34*
2.8.3 Filter shape tuning *36*
2.8.3.1 Changing the field coupling coefficients 36
2.8.3.2 Changing the resonator attenuation 37

CHAPTER 3 DESIGN **39**

3.1 INTRODUCTION 40
3.2 THE MICRO-RESONATOR USED IN TELECOM APPLICATIONS 41
3.2.1 Drop port on-resonance insertion loss *42*
3.2.2 Filter rejection ratio *43*
3.2.3 Filter bandwidth *44*
3.2.4 Channel Crosstalk *45*
3.2.5 Through port insertion loss *46*
3.2.6 Through port on-resonance residual power *47*
3.2.7 Design parameter summary *49*
3.3 GEOMETRICAL DESIGN CHOICES 50
3.3.1 Micro-resonator geometry *50*
3.3.2 Vertical or lateral coupling *51*
3.4 MATERIAL SYSTEM 53
3.5 VERTICAL RESONATOR DESIGN 55
3.5.1 Resonator design *55*
3.5.2 Resonator propagation losses *56*
3.5.3 Determination of the coupling coefficients *57*
3.6 LATERAL RESONATOR DESIGN 59
3.6.1 Port waveguide and resonator design *60*

3.6.2 Overlap loss reduction *61*
3.6.3 Setting the lateral field coupling coefficient *63*
3.7 COMPONENT DESIGN CONSIDERATIONS 64
3.7.1 Creating a design layout for pigtailing purposes *65*
3.7.2 Tapers *66*
3.7.3 Optimal port waveguide bend radius *67*

CHAPTER 4 **SIMULATION AND ANALYSIS** **69**

4.1 INTRODUCTION 70
4.2 MICRO-RESONATOR INVESTIGATOR 71
4.2.1 Transient response *72*
4.2.2 Increasing the computational efficiency *74*
4.3 RFIT 75
4.4 DROPZONE 77
4.5 AURORA 81
4.5.1 Architecture *82*
4.5.2 Simulation method *84*
4.5.2.1 Primitives 84
4.5.2.2 The execution engine 88
4.5.3 Validation of the simulation method *91*
4.5.4 Strengths and weaknesses of the simulation method *96*
4.5.4.1 Simulation strengths 96
4.5.4.2 Simulation weakness 99
4.5.5 Simulations on complex structures *102*
4.5.5.1 The hyper-resonator 102
4.5.5.2 Simulation of a waveguide grating 104

CHAPTER 5 FABRICATION **109**

5.1 INTRODUCTION 110
5.2. FABRICATION AND MASK DESIGN OF LATERALLY COUPLED RESONATORS 111
5.2.1 Fabrication *111*
5.2.2 Mask layout *113*
5.3. FABRICATION AND MASK DESIGN OF VERTICALLY COUPLED RESONATORS DEFINED USING CONTACT LITHOGRAPHY 115
5.3.1 Fabrication *115*
5.3.2 Packaging *116*
5.3.3 Mask layout *118*
5.4. FABRICATION AND MASK DESIGN OF VERTICALLY COUPLED RESONATORS DEFINED USING STEPPER LITHOGRAPHY 120
5.4.1 Stepper lithography and mask design *120*
5.4.2 Fabrication *124*

CHAPTER 6 MICRORING-RESONATOR BUILDING BLOCKS **129**

6.1 INTRODUCTION 130
6.2 A VERTICALLY COUPLED MICRORING RESONATOR BASED BUILDING BLOCK 131
6.2.1 Dimensions of the oxide layers *133*
6.2.2 Dimensions of the resonator and port waveguides *134*
6.2.3 Chromium heater design *138*
6.2.4 Heater characterization *141*
6.3 CHARACTERIZATION OF SINGLE, VERTICALLY COUPLED MICRORING RESONATORS 144
6.3.1 Measurement setup *144*
6.3.2 The importance of phase-matching and the fitting of resonator responses *147*
6.3.3 Microring resonator thermal tuning and modulation frequency *151*
6.4 A WAVELENGTH SELECTIVE OPTICAL SWITCH BASED ON MICRORING RESONATORS 154
6.4.1 Switch design *154*
6.4.2 Characterization *155*
6.4.3 Vernier switch *156*

CHAPTER 7 DENSELY INTEGRATED DEVICES FOR WDM-PON **159**

7.1 INTRODUCTION 160
7.2. A RECONFIGURABLE ADD-DROP MULTIPLEXER BASED ON MICRORING RESONATORS 163

7.2.1 Design and fabrication ... *163*
7.2.1 Spectral measurements ... *165*
7.2.2 Spectral measurements ... *167*
7.3 FLEXIBLE Λ-MULTICASTING ROUTER FOR USE IN ACCESS NETWORKS ... 169
7.3.1 Router implementation using micro-resonators ... *169*
7.3.2 Router design ... *171*
7.3.3 Improved OADM design ... *174*
7.3.4 Characterization ... *175*
7.3.4.1 Characterization of the OADM ... 176
7.3.4.2 Characterization of the Router ... 179
CHAPTER 8 POLARIZATION INDEPENDENT DEVICES ... 183
8.1 INTRODUCTION ... 184
8.2 POLARIZATION DIVERSITY ... 185
8.3 POLARIZATION INDEPENDENCE THROUGH BI-DIRECTIONAL USE OF THE MICRO-RESONATOR ... 186
8.4 POLARIZATION DIVERSE ROUTER ... 189
CHAPTER 9 DISCUSSION AND CONCLUSIONS ... 193
APPENDIX A. MASON'S RULE ... 195
APPENDIX B. CROSSTALK DERIVATION ... 197
LIST OF ACRONYMS ... 199
LIST OF SYMBOLS ... 201
BIBLIOGRAPHY ... 203
PUBLICATION LIST ... 215
DANKWOORD/ACKNOWLEDGEMENTS ... 221

Chapter 1

Introduction

The devices discussed in this thesis all have an intended application in a WDM-PON access network. This type of network is seen as a possible successor to current network solutions such as PON and ADSL in order to satisfy the ever increasing bandwidth demands from consumers. The reasons for this are explained in this chapter by providing a short history and overview on the rise of fiber optic networks and competing broadband technologies. In addition a description is given of the two projects within which the work presented in this thesis was carried out.

1.1 Preface

In the late 80's and 90's of the past century an unprecedented overhaul of world Telecommunications took place. By 1999 [1] almost half of the 189 members of the International Telecommunication Union had at least partially privatized their telecom operators. The privatization of traditional telecom operators caused a surge in cross border acquisitions and mergers and eventually gave rise to transnational systems that superseded national carriers in scope and function.
In every economic sector corporate networks invested billions in hardware and software needed to enlarge and modernize their proprietary systems. Fueled by proclamations of business and academic commentators of an information revolution and promises that the internet backbone requirements would double every 3.7 months [2] financial markets were only too happy to answer calls from existing and would-be network suppliers and technology-startups. In the last two years of the telecom boom alone $35 billion was spent by companies worldwide, laying 160 million kilometers of optical fiber for broadband networks.
Then, in late 2000, the bubble burst. As Figure 1.1 shows, capital expenditures hugely outpaced revenues and by 2001 only 5% of the 160 million km of fiber laid out worldwide had been "lit"[3].

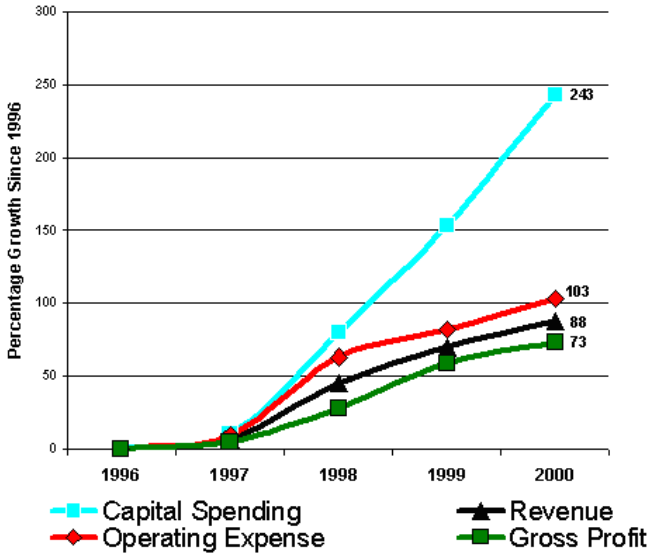

Figure 1.1. Capital expenditures and profit growth in the late 1990's.
(Source: Optical Oracle, *Light Reading*)

Within a year large companies such as Lucent and Nortel saw their revenues fall by 42% and 39% percent respectively [4] whilst the entire industry lost nearly 500.000 jobs and $2 trillion in market value [2]. The industry was down but not out however. Whilst investments virtually froze to a standstill the bandwidth demands of consumers never ceased to increase. This eventually sparked renewed interest from the industry in recent years with major business activities started in 2003 and 2004 to bring fiber with higher bandwidth capabilities of up to 100 Mbps to the consumer [5]. Currently though the consumer market is still dominated by competing broadband technologies such as Digital Subscriber Line (DSL) and Cable.

1.2 Broadband to the home

DSL and Cable technologies will be the dominant medium to bring broadband to the consumer for many years to come, as the forecast in Figure 1.2 shows, with an expected number of subscribers surpassing 370 million in 2010. These technologies have been natural candidates for broadband access because they can use the often installed base of copper wire for telephony and coaxial cable for television but allow significant gains in bandwidth compared with dial-up modems. The overall cost for broadband access for both the consumer and network provider can thus be significantly lower than competing solutions such as fiber and wireless.

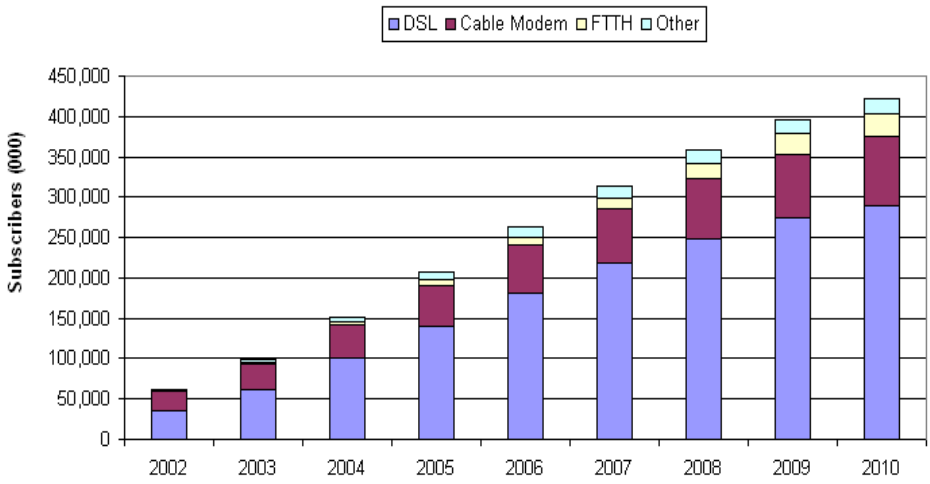

Figure 1.2. Global broadband subscriber forecast until 2010.
(Source: Broadbandtrends.com)

In using these technologies, however, there is always a compromise. While cable typically offers about double the bandwidth of DSL it is a shared bandwidth solution where the bandwidth per user scales down with the number of subscribers. Likewise DSL is hampered by the fact that there is always a compromise between bandwidth and distance to the subscriber due to its electrical nature. This is also illustrated in Figure 1.3 that shows the maximum bit rate versus distance for a number of DSL implementations [6,7,8]. Currently most countries have deployed Asymmetric Digital Subscriber Line (ADSL), with bit rates up to 8 Mbps, but the faster standards such as ADSL2 and ADSL2+ are rapidly introduced. The ADSL2+ standard can support bit rates of up to 25 Mbps for distances less than 900 meters.

At these distances ADSL2+ is a significant competitor to Fiber-to-the-Home (FTTH) in locations where the average distance to the subscriber is low. This is evidenced in Europe where, due to its high population density, the dominating focus is on xDSL in contrast to the less densely populated United States where, in part due to recent investments by Verizon, fiber is gaining momentum.

Population density is not the only factor, however; government regulation can also play an important role. In a densely populated country as Japan for instance, xDSL would be the favorable solution in terms of cost. Instead FTTH is the preferred option. FTTH in Japan has undergone rapid deployment with commercial activities started in 2001 [5]. This is largely due to Japanese government policy and the Nippon

Telegraph and Telephone Corporation (NTT) that have already focused on optical fiber for over 20 years.

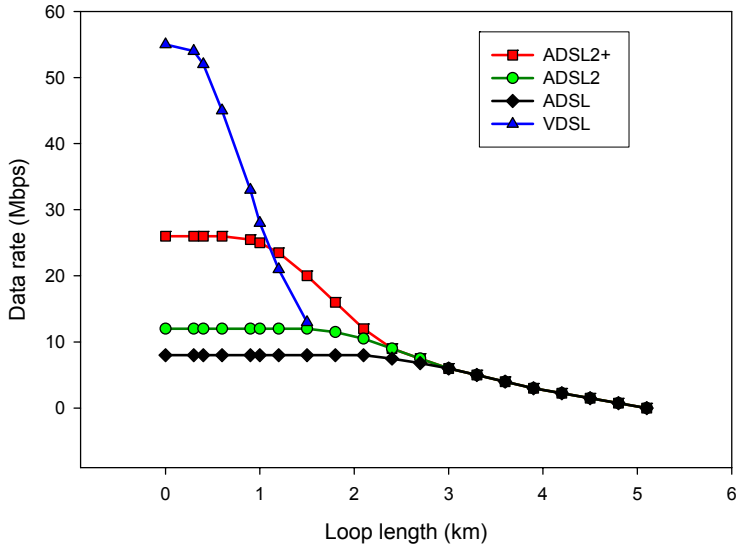

Figure 1.3. DSL Loop length versus data rate.

As a result the country already has a Fiber-to-the-Curb (FTTC) infrastructure which helps to reduce the cost of FTTH deployment. In addition aerial fiber is allowed which speeds up deployment and reduces cost.

Interestingly, xDSL can also be seen as a driving force behind FTTH rather than a major competitor. Currently subscriber demand for triple play services, which combine internet, telephony and high definition television (HDTV), is on the rise. In addition a bandwidth race is developing due to increased competition between operators with broadband sold on a speed/price formula. Here dropping prices and clever marketing will lead subscribers to want bandwidth far beyond what they actually require. Network operators have to respond to this with ever faster xDSL offerings. In this respect Japan offers a glimpse of the future.
Japanese fiber networks are often of the Fiber-to-the-Building (FTTB) type where fiber can terminate optically for individual homes. They can, however, also be completed by a Very high bit-rate Digital Subscriber Line (VDSL) network in an apartment building. For short distances less than 300m the VDSL and the faster VDSL2 (up to 100 Mbps) solutions can deliver fast broadband using conventional copper lines. By combining FTTC or FTTB with VDSL network operators can therefore provide more economic high bandwidth connections since not every subscriber requires a costly direct fiber connection [9].
Since VDSL is not fundamentally different from the current ADSL implementations - all use the same Discrete Multi-Tone (DMT) line-coding method - it shows a migratory path to be taken by network operators in Europe. These can slowly and economically upgrade current ADSL and ADSL2 networks to VDSL supported by fiber, all driven by consumer demand. The demand for faster DSL thus brings the fiber networks that support the DSL ever closer to the subscriber until finally fully fledged FTTH networks are created.

1.3 Bringing Fiber to the Home

The last link between the subscriber and the first point of connection to a network infrastructure is the so-called Access Network (AN). The previously mentioned xDSL and FTTH as well as other technologies such as Cable and Wireless (WIFI) are possible implementations of this network. Within the access network FTTH may be implemented in several topologies. The two main competing topologies are Ethernet Point to Point (P2P) and the Passive Optical Network (PON) in the form of Ethernet PON (EPON) or the newer Gigabit PON (GPON).

1.3.1 Passive optical networks

Passive optical networks were first introduced in the 1980's. Since prices for fiber optic cable and optical transceivers were very high at the time a topology was devised that could share these resources. To this end PON networks use a Point to Multi-Point (P2MP) topology as shown in Figure 1.4a.

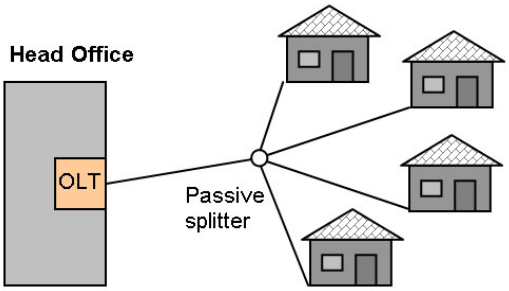

Figure 1.4a. Passive optical network.

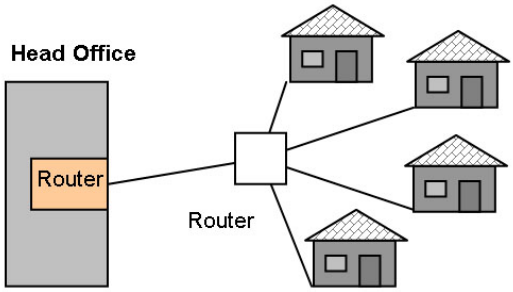

Figure 1.4b. Ethernet based Point to point network.

In this topology an Optical Line Terminal (OLT) at the head office is connected to a single strand of fiber that goes out to a passive optical splitter near the customers' premises. Here the signal is typically divided into 32 different lines using a passive splitter. Each of these lines is connected to an Optical Network Unit (ONU) on a customers' premise. Downstream data is therefore transmitted to all users with each ONU having to determine which packets are for that customer. The PON uses one wavelength for downstream traffic and another for upstream traffic. The latest specifications call for downstream traffic from the OLT to the ONU to be transmitted at a wavelength 1490 nm while upstream traffic is transmitted from the ONU at 1310 nm [10].

1.3.2 Ethernet Point to Point networks

In an Ethernet point to point network each customers' ONU has a direct fiber connection to a central router at the Head Office (HO) or an aggregation router in the street cabinet, as shown in Figure 1.4b. Like the PON the point to point network uses one wavelength for downstream traffic and another for upstream traffic. In the past the cost of optical fiber and transceivers, as well as the maintenance cost of the active components in the field, has been prohibitive in the deployment of P2P networks.

Today, however, the cost of optical fiber and transceivers is a fraction of they used to be and P2P is beginning to show several advantages over PON.
By nature, the OLT in a PON is an expensive component because it needs to be able to send a broadband optical signal up to 20 or 30 km with enough power to light up 32 or more ONUs. Therefore an OLT doesn't start to become economical until a large percentage of the total supported ONUs is served [11]. In addition, because many users share the same fiber, the bandwidth for each user will decrease when new users are added. Furthermore, the fact that many users share the same fiber also means any upgrade to a higher aggregate bandwidth always affects multiple users (all users will have to upgrade simultaneously), thus becoming a costly exercise.
In contrast the P2P network can be upgraded on a per-user basis and can achieve much higher bit rates at longer distances because no synchronization is required and no bandwidth is shared between users.

1.3.3 Wavelength Division Multiplexed PON

Combining many of the benefits of P2P and traditional passive optical networks Wavelength Division Multiplexed (WDM)-PON is seen as a possible successor [12]. WDM-PON uses the same passive network topology as PON but the addition of many wavelengths implicates that many different services can be run side by side. Customers, for instance, that require higher bit rates can then do so by transferring to a different wavelength with this service. Changes are then only required at the head office and the customers' premises, keeping the PON system out in the field unchanged.
For now, however, the biggest problem for WDM-PON is cost. For true WDM narrowband tunable or wavelength specific lasers are required in the ONUs on the customer side. Such ONUs, however, will be prohibitively expensive in an industry that looks for €100 to €250 solutions.

1.4 Projects

The work presented in this thesis was carried out within the final two years of the three year NAIS project and the first two years of the ongoing Broadband Photonics project. An important goal in both these projects was to create cost-effective devices for use in WDM-PON networks.

1.4.1 NAIS

The EC funded NAIS (Next generation Active Integrated optic Sub-systems) project [13] aimed to exploit recent insights in electro-optical materials and technological advances in optical Microring Resonators to create a densely integrated optic subsystem (ONU) with an application in WDM-PON. The technological scope of the subsystem, shown in Figure 1.5, sees functions such as optical switching, modulation, multiplexing and filtering integrated on a single optical chip. Only a high-speed detector and a broadband light source, which through the use of integrated optical filters can be implemented using a low-cost LED, are kept off-chip.

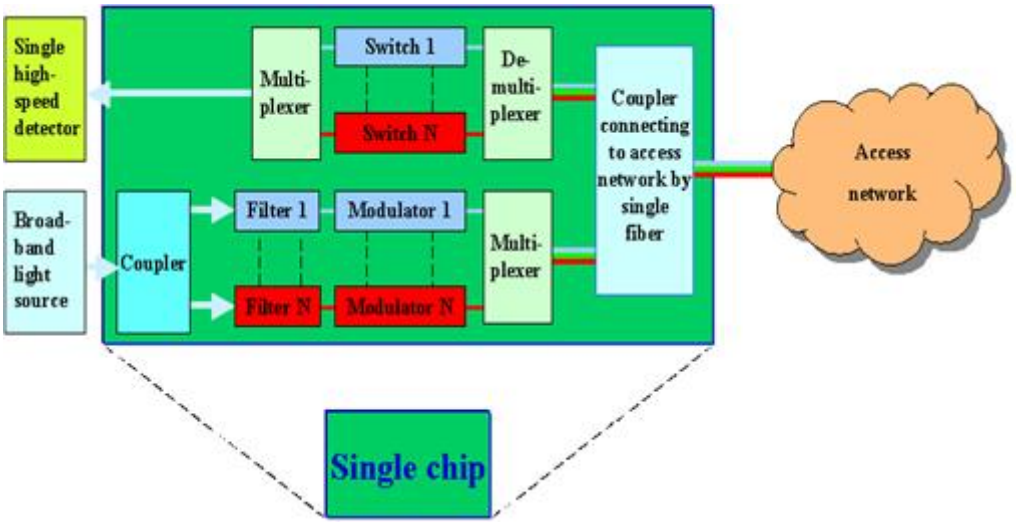

Figure 1.5. The technological scope of the NAIS project.

All functions on chip are implemented in a scalable manner so that additional optical channels can easily be integrated, eventually allowing hundreds of channels per chip.
The high levels of integration required for such devices can be obtained through the use of microring resonators which are able to perform a wide range of optical functions at typical dimensions less than 100 μm. Through the combination of microring resonators with novel polymers that exhibit large electro-optic effects, active components, such as high speed modulators, can be created.
A new generation integrated optic subsystem is thus developed that, through dense integration and novel materials, allows large-scale manufacturability and can potentially lead to low-cost WDM-ONUs.
Within the NAIS project research groups and companies are joined together to perform a chain of activities that include the study and development of novel electro-optic and high index passive materials, the development and application of design tools, and the design and technological realization of micro-resonator based devices.
The NAIS related work presented in this thesis focuses on this last activity with the design, implementation and characterization of tunable microring resonator based filters and switches.

1.4.2 Broadband Photonics

The Broadband Photonics Project [14] develops reconfigurable access networks for providing the user with congestion-free access and abundant exchange of abundant amounts of information.
By enabling the network operator to easily and remotely reconfigure his access network, the capacity distribution across the users can timely be adapted to his varying service demands. Optical fiber carrying multiple wavelength channels (WDM) is chosen for the broadband flexible network infrastructure. The project puts emphasis on low cost, which is a crucial factor for success in the access market. Therefore reconfigurable access network architectures and access network modules are being investigated. Compact low-power photonic integrated circuits and intelligent network reconfiguration mechanisms are key research items in the project. A concept of the network is shown in Figure 1.6.

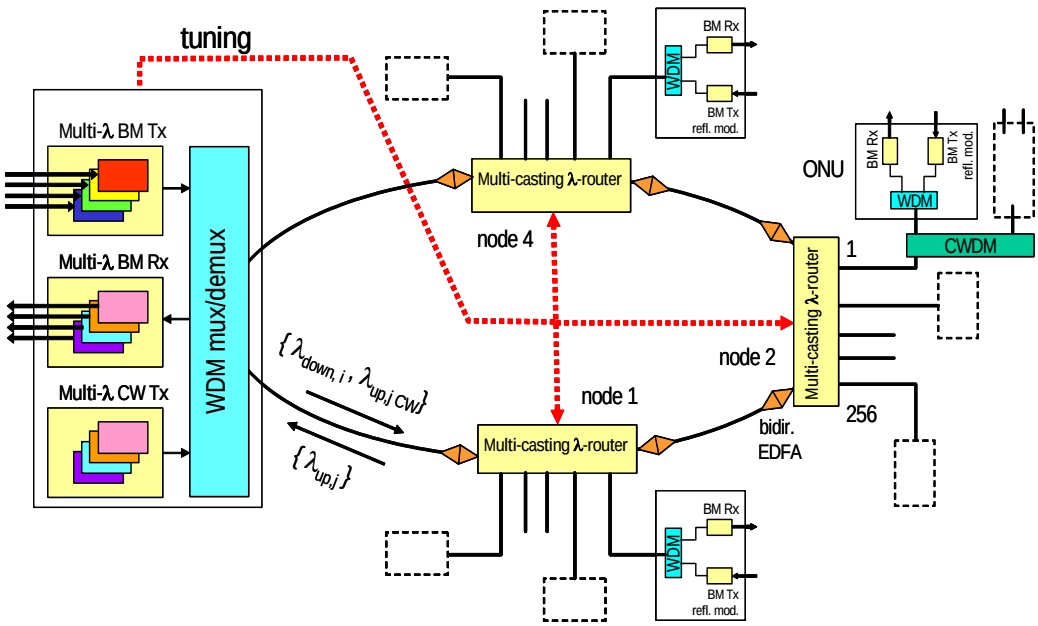

Figure 1.6. The Broadband Photonics network concept.

The concept aims for up to 1024 users that can be connected to a single network topology. This topology consists of up to 4 routers (3 shown) each connecting up to 256 users to a ring network, which is used for redundancy. The ring network is connected to a head-end node through which signals are communicated across the network and from which the various routers can be controlled to implement load balancing and schemes such as multicasting.
Key components to be developed within the Broadband photonics project are a reflective ONU and a multicasting router based on microring resonators. The multicasting router and a related component, a reconfigurable optical add drop multiplexer (ROADM), both based on microring resonators are, amongst other devices, presented in this thesis.

1.5 Outline

This thesis is structured as follows:

- In Chapter 2, the principle of operation of the microring resonator, which is used in all of the optical components presented in this thesis, will be discussed. Also, the basic parameters that govern its operation are introduced and using these parameters the frequency-domain responses of single and second order microring resonator based filters will be derived. This chapter will also discuss some of the limitations that designs based on single (first order) resonators may face and offers several solutions based on the use of multiple resonators. In the final section of this chapter the various methods that can be used to tune various aspects of the resonator such as its resonance frequency, which is crucial in devices such as the OADM and the Router, or its filter shape are discussed.
- In Chapter 3 the design of microring resonator based devices is discussed in general terms. Several performance parameters are introduced that can be used to translate the requirements of a certain application into specific values of the basic microring resonator parameters. The methodologies for transforming

these basic parameters into actual resonator designs are given for a laterally and a vertically coupled resonator. Apart from the design of the resonators some important issues related to overall device design, up to the prototype level, are also be discussed.

- In Chapter 4 some of the tools that were created to aid in the design and characterization of microring resonator based devices are presented. In particular the analytical and numerical methods used to fit measured resonator responses are examined in detail. Aurora, a tool created to perform simulations on complex optical circuits containing resonators, is also discussed in this chapter.
- In Chapter 5 the fabrication processes used to fabricate the various devices presented in this thesis are described in detail. Also the implications that a certain process has on the design of the masks used in that process are discussed.
- In Chapter 6 a specific design for a basic resonator building block is given. This building block consists of a single thermally tunable resonator and was used as the fundamental unit (i.e. the same resonator design was used many times) in the OADM and Router discussed in Chapter 7. Some important aspects in the design of a resonator building block are illustrated using the wavelength response and thermal tuning measurements on a number of (steadily improving) resonator designs. Also presented are the wavelength selective switch and a Vernier filter based on two resonators.
- In Chapter 7 the design and characterization of two different types of OADM, for use at 1310 nm or at 1550 nm, and a Router are discussed. For 1550 nm OADM system level measurements performed at 40 Gbit/s are also presented.
- A major problem of microring resonator based devices is that it is often very difficult to make them polarization independent. Although this can by solved by introducing polarization diversity in the devices this doubles the number of resonators in the devices and creates a number of new problems. In Chapter 8 a method is described for creating a polarization diverse device that does not double the number of resonators and that also has several other advantages.
- Finally, in Chapter 9, general conclusions based on the work presented in this thesis will be drawn.

Chapter 2

The Micro-Resonator

In this chapter the basic principle behind the operation of the micro-resonator will be given and the basic equations that describe its operation will be derived. In addition it will be shown that the resonator has certain limitations concerning its Free Spectral Range and filter response. For this several solutions such as, for instance, the use of higher order filters are offered. In the final section of this chapter several methods of active tuning will be discussed because it is this tuning that gives the micro-resonator its attractive functionality as will be shown in several other chapters.

2.1 Introduction

Integrated optic microring resonators were first proposed by Marcatili in 1969 [15]. These resonators find their origin in the field of fiber optic ring resonators [16, 17] and micrometer sized resonant spheres and droplets [18-20]. These resonators are, like the Fabry-Perot resonator (FP), a class of resonant filters that, due to internal optical feedback, achieve high frequency selectivity.
Functionally these resonators behave similar to the Fabry-Perot resonator and share its Lorentzian-like frequency response. The integrated optic microring-resonator, however, has the linear cavity of the FP replaced by a loop waveguide and the cavity mirrors replaced by a directional coupler or, occasionally, a Multi Mode Interferometer (MMI). In an integrated optics FP the cavity the mirrors are commonly created using cleaved facets or reflective gratings, both of which are difficult to integrate when produced on a large scale. However, the use of directional couplers in a microring resonator allows, depending on the index contrast, ring radii as small as a few micrometers [21, 22]. The microring-resonator is therefore a highly attractive component for Large Scale Integrated Optics (LSIO) [23-26]. In addition, by careful design of the resonator geometry and choice of the materials system it can be made to perform a wide range of functions. Aside from its use as a highly selective passive filter the microring resonator has seen application as an optical delay line element, a dispersion compensator and even as a highly sensitive sensor [27-30]. Using electro-optic polymers or materials such as silicon-on-insulator (SOI), Gallium-Arsenide (GaAs) and Indium-Phosphide (InP) high speed modulators can be created [31-36] and also microring-resonator lasers [37-42] have been demonstrated.

2.2 Operational description

Most integrated optics microring resonators operate as either a two or a four port device. In a two-port resonator the resonant cavity is coupled to a single port waveguide and therefore has only a single in and output, as shown in Figure 2.1a. This type of resonator is ideally suited as a dispersive or attenuating element and has been used in dispersion compensation [43, 44] and true-time-delay [45] applications. The two port configuration can also be used for making lasers [37, 41] and sensors [27-29]. It is, however, less useful as a wavelength filtering element in the applications described in this thesis and is therefore not further covered.

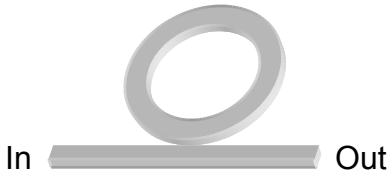

Figure 2.1a. Two port ring resonator.

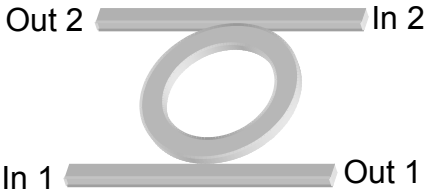

Figure 2.1b. Four port ring resonator.

Conversely, the four port configuration is ideal for this task. Used throughout this thesis the four port configuration, shown in Figure 2.1b, is created by adding an additional port waveguide to the two-port resonator. This effectively transforms the micro-resonator into a wavelength selective filter that allows signals of certain wavelengths to be transferred from one port waveguide to the other.

2.2.1 Four port filter operation

The transfer of power between the two port waveguides of a four port micro-resonator is only possible at discrete wavelength regions at which the optical path length of the light in the resonator is an integer multiple of its effective wavelength. The process by which power is transferred through the resonator is characterized by three distinct phases: the initial, transient and the equilibrium phase.

In the initial phase, shown in Figure 2.2a, incoming light I_{in} of a certain wavelength propagates along one of the port waveguides of the micro-resonator. When the light reaches the first coupler a small power fraction $\kappa_1^2 \cdot I_{in}$ is evanescently coupled into the resonator. Most of the light, however, will continue its path along the port waveguide as $I_{through}$ The light I_{cav1} that is now in the resonator will propagate along the resonator until it reaches the other port waveguide and the second coupler. Here a small fraction $\kappa_2^2 \cdot I_{cav1}$ of the light is coupled out of the resonator as I_{drop} while the larger fraction I_{cav2} continues its roundtrip towards the first coupler.

In the transient phase the dominant factor that determines the buildup of power the resonator is the modal phase of the light I_{cav2} as it interferes with the light in the port waveguide at the first coupler. If the resonance condition:

$$\varphi_r = m \cdot 2\pi \,,\ m \in \mathrm{N} \tag{2.1}$$

is satisfied for the roundtrip phase of I_{cav2}, constructive interference will occur at the resonator side of the first coupler, resulting in a net increase of power within the resonator. At the same time destructive interference at the port waveguide side results in a decrease of the power $I_{through}$, as shown in Figure 2.2b.

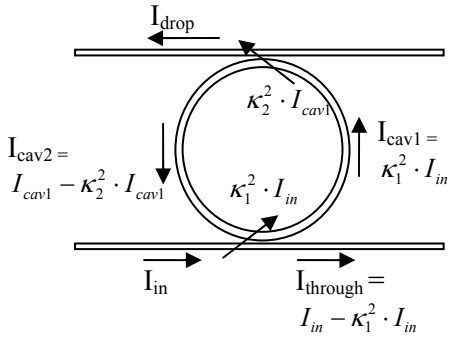

Figure 2.2a. Light coupling into the micro-resonator in the initial phase.

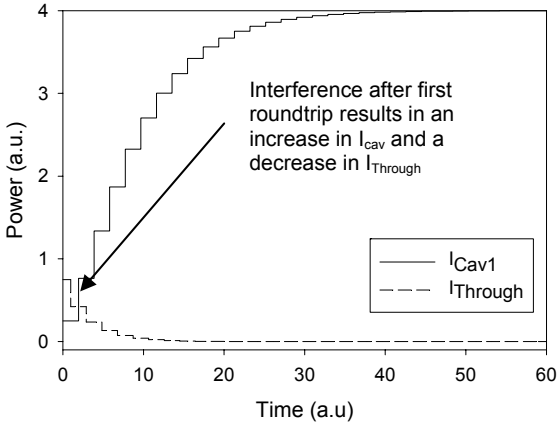

Figure 2.2b. Constructive interference at the first coupler results in a build-up of power in the resonator while reducing the power $I_{Through}$.

The process of power enhancement within the cavity while transferring more power from I_{in} will repeat itself many times as I_{cav2} continues to interfere with the light in the port waveguide on every roundtrip. In tandem the dropped power I_{drop} will also increase according to $I_{drop} = \kappa_2^2 \cdot I_{cav1}$. The intra-cavity power cannot rise indefinitely, however, and at a certain power level a state of equilibrium is reached between the

light I_{cav2} in the cavity and the light in the port waveguide I_{in}. At this point no additional power can be transferred from I_{in} and the resonator is operating in a steady state condition. The power in the through port $I_{through}$ is now at its lowest level while the power in the drop port I_{drop} is at its highest level. The resonator has thus effectively transferred power from the input to the drop port.

2.1.2 Transient resonator behavior

As described in the previous section all the power that is transferred from the (first) input waveguide into the resonator is dropped to the second port waveguide (for a loss-less the resonator). The transient drop response of a micro-resonator in full resonance, which can be found from the intra-cavity power using $I_{drop} = \kappa_2^2 \cdot I_{cav1}$, is shown in Figure 2.3a. In this Figure the transient buildup of power and the stable equilibrium phase where the dropped power no longer fluctuates can be identified.
Figure 2.3b shows the transient step response of a resonator that is near full resonance. In this case the roundtrip phase of the light in the cavity is not exactly $2 \cdot m\pi$, but constructive interference within the resonator cavity, and thus power buildup, can still occur. However, the maximum attainable intra-cavity power is reduced and as a result the maximum dropped power level is lower compared to that of a resonator in full resonance.

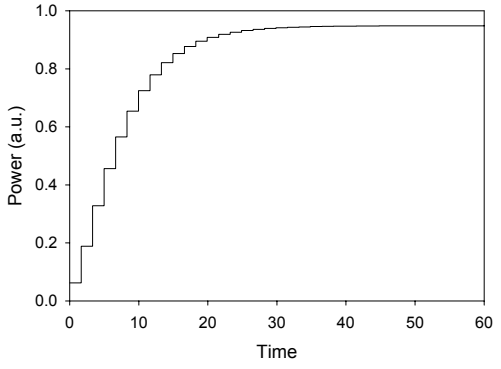

Figure 2.3a. Transient drop response at full resonance.

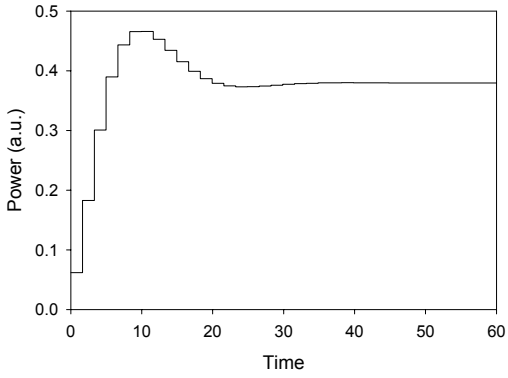

Figure 2.3b. Transient drop response near full resonance.

In a resonator that is completely off resonance the roundtrip phase of the light in the resonator cavity is equal to $(2.m+1).\pi$. It will therefore interfere destructively with the light that enters the cavity. This has the effect that the power of the light that enters the cavity is reduced below its initial value of $\kappa_1^2 \cdot I_{in}$, thereby blocking the transfer of power from the input to the drop port. This is also visible in Figure 2.3c where, after an initial peak in power, the drop power converges to a significantly lower value.

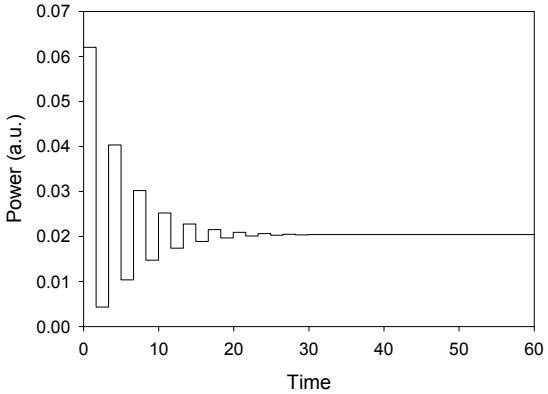

Figure 2.3c. Transient drop response at off-resonance.

2.3 Microring resonator model

The qualitative description of the previous paragraph can also be translated into a quantitative mathematical model. This model can be used to find the spectral behavior of the microring resonator and serves as the basis from which many important performance parameters can be derived.
The parameters that are used to define the mathematical model of the microring-resonator are summed up in Figure 2.4. These parameters are either related to the two coupling regions between the ring and port waveguides or the ring resonator itself. These parts are therefore discussed individually before proceeding to the overall model.

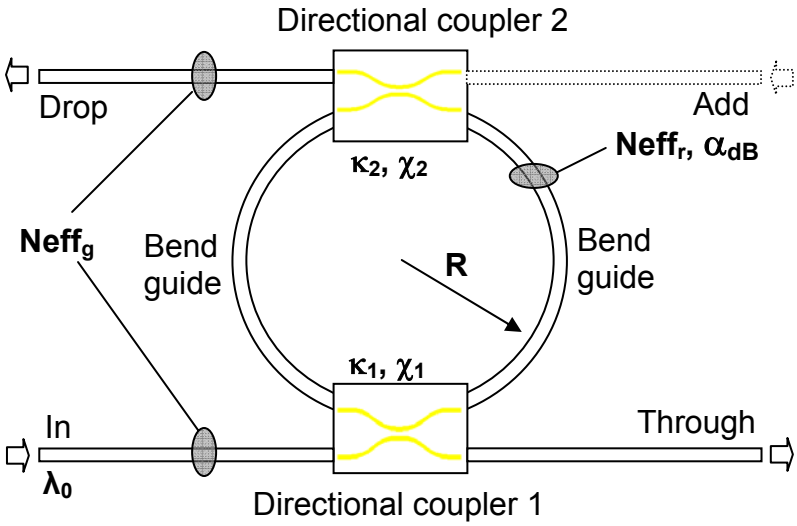

Figure 2.4. Micro-resonator model components and parameters (κ_1 and κ_2 are field coupling coefficients).

2.3.1 Directional coupler model

The coupling region between the port waveguide and the ring resonator can be modeled as a 2x2 directional coupler. The transmission characteristics of this coupler can be expressed by its transfer matrix as [46]:

$$M_A = \sqrt{1-\chi_c^{\,2}}\begin{bmatrix} \cos(\Delta.L_{eff}) - jA\cdot\sin(\Delta.L_{eff}) & -jB\cdot\sin(\Delta.L_{eff}) \\ -jB\cdot\sin(\Delta.L_{eff}) & \cos(\phi) + j\cdot A\sin(\Delta.L_{eff}) \end{bmatrix} \tag{2.2}$$

where χ_c is fraction of the power that is lost in the coupler and L_{eff} is the effective coupling length between the resonator and port waveguides. The parameters Δ, A and B are related to the coupler asymmetry and are defined as:

$$A = \left(\beta_r - \beta_g\right)/2\Delta \tag{2.3}$$

$$B = \kappa_c / \Delta \tag{2.4}$$

$$\Delta = \sqrt{\left(\frac{\beta_r - \beta_g}{2}\right)^2 - \kappa_c^2} \tag{2.5}$$

where κ_c is the coupling constant of the port and resonator waveguides and β_r and β_g are the propagation constants. The propagation constants are related to the effective refractive index $Neff_r$ of the ring resonator and that of the port waveguide $Neff_g$ via:

$$\beta_i = 2\pi \cdot Neff_i / \lambda_0 \tag{2.6}$$

Examination of Equations (2.2-2.6) shows that the effective refractive indices $Neff_r$ and $Neff_g$ are very important parameters in the overall operation of the microring-resonator. The difference between $Neff_r$ and $Neff_g$, called the phase mismatch, determines the maximum of the field coupling between the port and ring waveguides. In the case that strong coupling is required the mismatch should therefore be carefully controlled as it may otherwise limit the coupling to a range lower than what is required for a certain device implementation.

If the effective refractive indices are equal then the coupling regions of the resonator can be described using the simplified transfer matrix for symmetric couplers:

$$M_S = \sqrt{1-\chi_c^2}\begin{bmatrix} \cos(\kappa_c.L_{eff}) & -j\sin(\kappa_c.L_{eff}) \\ -j\sin(\kappa_c.L_{eff}) & \cos(\kappa_c.L_{eff}) \end{bmatrix} \tag{2.7}$$

which is found by setting $Neff_r = Neff_g$, in Equations (2.2-2.6). In this case complete coupling between the waveguides is possible.

Equations (2.2) and (2.7) can also be written as:

$$M = \sqrt{1-\chi_c^2}\begin{bmatrix} \mu & -j\kappa \\ -j\kappa & \mu \end{bmatrix} \tag{2.8}$$

In this equation the field coupling coefficient κ ($0<\kappa<1$) is the fraction of the light that is coupled between the ring and port waveguides. The fraction of the light that remains in the port waveguide is μ and is related to κ via $\mu = \sqrt{1-\kappa^2}$. Also, if (2.8) is used to describe a symmetric coupler, $\kappa = \sin(\kappa_c.L_c)$ and $\mu = \cos(\kappa_c.L_c)$.

Describing the coupler transfer matrix using the field coupling coefficient is more useful than using either Equation (2.2) or (2.7). This is because the values of κ_c and L_{eff} can be hard to determine when dealing with resonators. Determining the coupling constant of a standard directional coupler that consists of two parallel waveguides is fairly straightforward as it can be found by calculating the modes in a cross-section of the coupler using a 2D modesolver. In the case of the couplers used in the microring resonator, however, determining the coupling constant (and even L_{eff}) can be a very challenging task. In the vertically coupled resonator discussed in Chapter 6, for instance, the coupling region consists of a bend and a straight waveguide. In addition, these waveguides that may also have a phase mismatch, are offset in the vertical

plane. A 2D simulation of the cross-section is therefore not sufficient to calculate the field coupling coefficient. It is then easier not to calculate κ_c and L_{eff}, but to calculate the field coupling coefficient κ directly via a 3D simulation of the entire coupler using for instance Coupled Mode Theory (CMT) [47-49] or the Beam Propagation Method (BPM) [50].

While the transfer matrix in Equation (2.8) includes the coupler loss χ_c, this loss term is not included in the equations that describe the micro-resonator from here on. It should be noted, however, that while the omission of the loss term may be largely valid for the microring-resonators presented in this thesis it is not correct to do so in general. For micro-resonators with a small radius of several microns for instance, it has been shown that significant losses can occur due to abrupt modal changes in the coupling region [51].

2.3.2 Ring waveguide model

The ring resonator consists of a single circular waveguide. In the model of the resonator, however, this waveguide is split in two halves that are connected to each other via the two couplers. The two halves of the resonator can be described by the field propagation term S_R of the light in these waveguides:

$$S_R = e^{-j\frac{\varphi_r}{2}} \cdot \sqrt{\chi_r} \tag{2.9}$$

In this equation φ_r is the roundtrip phase and χ_r is the roundtrip loss factor of the light in the resonator. The roundtrip phase is defined as:

$$\varphi_r = \frac{(2.\pi)^2}{\lambda_0} \cdot R \cdot n_g \tag{2.10}$$

where R is the radius of the ring resonator. The parameter n_g is the group index of the mode in the waveguide defined [52] as:

$$n_g = Neff_r(\lambda_0) - \lambda_0 \left.\frac{\partial Neff_r}{\partial \lambda}\right|_{\lambda_0} \tag{2.11}$$

The roundtrip loss factor χ_r is defined as:

$$\chi_r = 10^{\frac{-\alpha_r}{20}}, \ \alpha_r = 2\pi \cdot R \cdot \alpha_{dB} \tag{2.12}$$

where α_r is the roundtrip loss of the resonator in dB and α_{dB} (α_{dB} >0) is the loss of the mode in the ring waveguide in dB/m.

2.3.3 Combined model

The descriptions of the couplers and bend waveguides that make up the micro-resonator can be combined into a full model of a resonator. This model, which is shown in Figure 2.5, is based on a notation derived from control engineering where feed forward or feedback paths are clearly visible. This notation aids in the creation of the analytical description of the resonator through Mason's rule (See Appendix A) as will be shown in the next paragraph. The model shown here assumes a unidirectional resonator. In essence, a resonator is a bi-directional component where light can propagate in opposing directions within the resonator. Light propagation in two directions in the resonator may be intentional, as illustrated in Chapter 8**,** but is most often an undesired by-product of back scattering in the ring resonator or, in the case of a ring-resonator laser, an inherent property of omnidirectional emission. In all these instances, however, light propagating in one direction has negligible interaction with the counter propagating light so that in the case of bi-directional behavior the resonator can be described by treating this resonator as two separate unidirectional resonators.

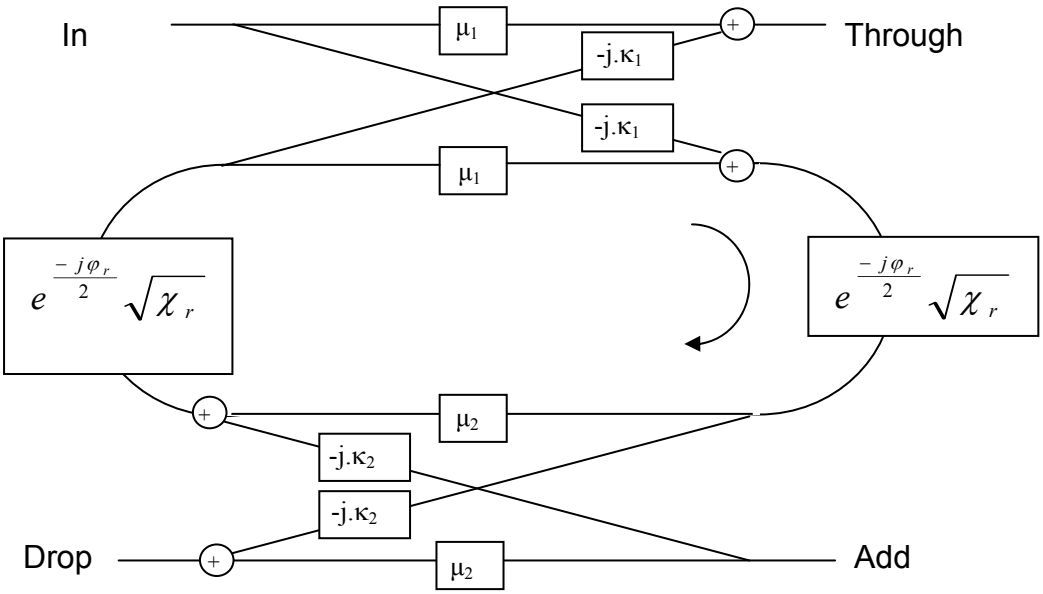

Figure 2.5. Control engineering representation of a unidirectional four port micro-resonator.

2.4 Spectral response of a single resonator

The spectral responses of a resonator are commonly referred to as the through and the drop response. The drop response signifies the power fraction of the light that is transferred by the resonator from the **In** port to the **Drop** port as a function of the wavelength of this light. Similarly the through response signifies the power fraction of the light that is extracted by the resonator from the **In** port to the **Through** port. The drop and through responses can be found by identifying in Figure 2.5 all the paths the light in the resonator may follow from respectively the input to the drop port and from the input to the trough port and then applying Mason's rule to find a mathematical expression from the paths.

2.4.1 The drop response

In the model of Figure 2.5 only two paths can be identified between the in and the drop port. This leads to the simplified model of Figure 2.6 in which the direct path from the in to the drop port as well as the feedback loop caused by the resonator can be discerned.

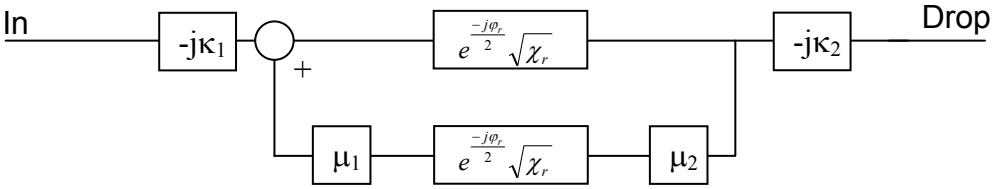

Figure 2.6. Simplified resonator model used to obtain the drop response.

By applying Mason's rule to this simplified model transfer function (2.13) is obtained.

$$\frac{E_{Drop}}{E_{In}} = \frac{-\kappa_1\kappa_2 \cdot e^{\frac{-j\varphi_r}{2}}\sqrt{\chi_r}}{1-\mu_1\mu_2 \cdot e^{-j\varphi_r}\chi_r} \tag{2.13}$$

In order to find the power dropped by the ring resonator the equation is squared and rearranged as:

$$\frac{P_{Drop}}{P_{In}} = \frac{\left|-\kappa_1\kappa_2 \cdot e^{\frac{-j\varphi_r}{2}}\sqrt{\chi_r}\right|^2}{\left|1-\mu_1\mu_2 \cdot e^{-j\varphi_r}\chi_r\right|^2} = \frac{k_1^2\kappa_2^2 \cdot \chi_r}{(1-\mu_1\mu_2 \cdot \chi_r)^2 + 4\mu_1\mu_2 \cdot e^{-\alpha_r}\sin^2(\varphi_r/2)} \tag{2.14}$$

This can be simplified further and is most often written as:

$$\frac{P_{Drop}}{P_{In}} = \frac{H}{1+F_C\sin^2(\varphi_r/2)} \tag{2.15}$$

where H is given by:

$$H = \frac{\kappa_1^2\kappa_2^2 \cdot \chi_r}{(1-\mu_1\mu_2 \cdot \chi_r)^2} \tag{2.16}$$

Also, H is also the maximum power available in the drop port for a resonator in resonance:

$$P_{Drop\_Max} = H = \frac{H}{1+F_C\sin^2((\varphi_{r=2\pi})/2)} \tag{2.17}$$

Fc is the so-called finesse factor defined as:

$$F_C = \frac{4\mu_1\mu_2 \cdot \chi_r}{(1-\mu_1\mu_2 \cdot \chi_r)^2} \tag{2.18}$$

The Finesse F of the resonator can be determined from the finesse factor following:

$$F = \frac{\pi}{2\arcsin(1/\sqrt{F_C})} \approx \frac{\pi\sqrt{\mu_1\mu_2 \cdot \chi_r}}{1-\mu_1\mu_2 \cdot \chi_r} \tag{2.19}$$

The finesse is a measure of the quality of the microresonator and can be related to the storage capacity or quality factor Q of the resonator through:

$$Q = \frac{F\lambda_0}{FSR} \tag{2.20}$$

where FSR is the Free Spectral range of the resonator, defined as the distance between two consecutive fringes or resonance peaks. The free spectral range is determined by:

$$FSR = \frac{\lambda_0^2}{2\pi \cdot n_g \cdot R} \tag{2.21}$$

From the free spectral range and the finesse the bandwidth of the resonator can be calculated. The bandwidth $\Delta\lambda_{FWHM}$ is defined as the Full Width at Half Maximum of the drop response and relates to the Finesse and the FSR as:

$$\Delta\lambda_{FWHM} = \frac{FSR}{F} \tag{2.22}$$

The free spectral range and full width half maximum are also illustrated in Figure 2.7. Here three fringes of the drop response of a microring-resonator are drawn, obtained for R=50 μm, $\kappa_1 = \kappa_2$=0.5, α_{dB}=1 dB/cm and n_g=1.5.

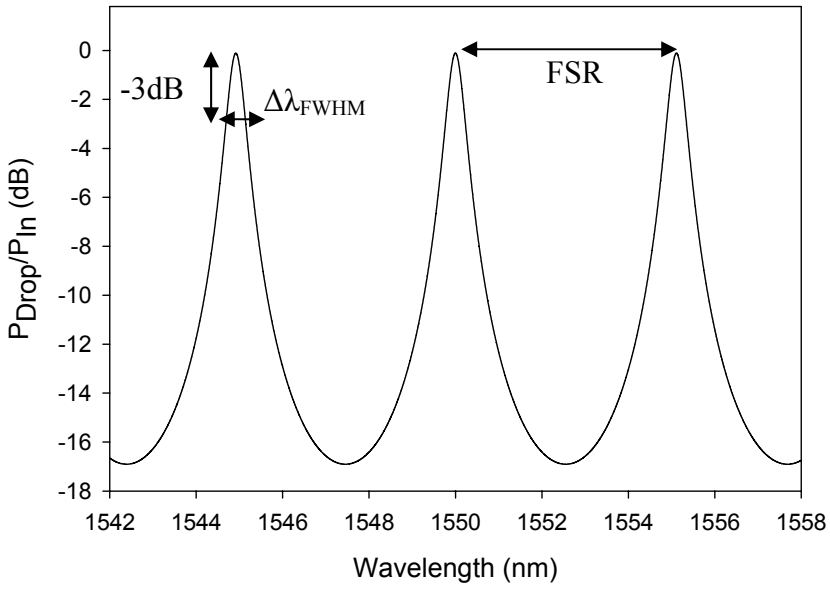

Figure 2.7. Microring resonator drop response.

2.4.2 The through response

The through response of a micro-resonator can be derived from Figure 2.5 in a way similar to that of the drop response by identifying all the paths the light may follow from the **In** port to the **Through** port. This leads to the simplified model of Figure 2.8. in which the feedback loop caused by the resonator and a feed-forward path through the first coupler can be discerned.

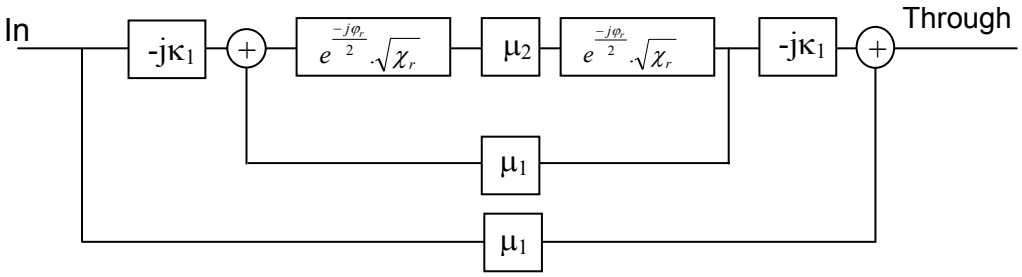

Figure 2.8. Simplified resonator model used to obtain the through response.

The application of Mason's rule then leads to the field transfer function of (2.23):

$$\frac{E_{Through}}{E_{In}} = \frac{\mu_1 - \mu_2 \cdot e^{-j\varphi_r}\chi_r}{1 - \mu_1\mu_2 \cdot e^{-j\varphi_r}\chi_r} \tag{2.23}$$

The power in the through port is then given by:

$$\frac{P_{Through}}{P_{In}} = \frac{\mu_1^2 - 2\chi_r \cdot \mu_1\mu_2 \cdot \cos(\varphi) + \chi_r^2 \cdot \mu_2^2}{1 - 2\chi_r \cdot \mu_1\mu_2 \cdot \cos(\varphi) + \mu_1^2\mu_2^2 \cdot \chi_r^2} \tag{2.24}$$

By substitution of the cosine in the denominator and rearranging expression (2.24), the through response can be written in a way analogous the drop response of (2.15):

$$\frac{P_{Through}}{P_{In}} = \frac{G}{1 + F_C \sin^2(\varphi/2)} \tag{2.25}$$

where G is given by:

$$G = \frac{\mu_1^2 - 2\chi_r \cdot \mu_1\mu_2 \cdot \cos(\varphi) + \chi_r^2 \cdot \mu_2^2}{(1 - \mu_1\mu_2 \cdot \chi_r)^2} \tag{2.26}$$

The trough response of (2.24) is shown in Figure 2.9 where three fringes are drawn for R=50 μm, $\kappa_1 = \kappa_2$=0.5, α_{dB}=1 dB/cm and n_g=1.5.

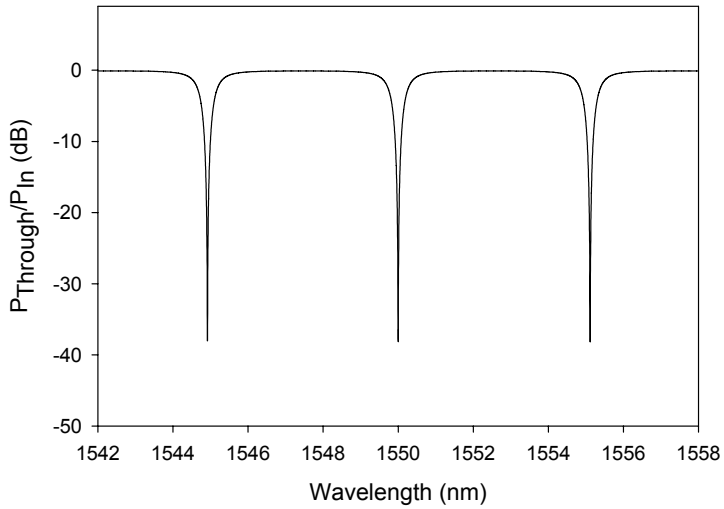

Figure 2.9. Microring resonator through response.

2.5 MR Filter bandwidth versus rejection ratio

Two important parameters in filter design are the filter bandwidth and its ability to reject unwanted signals. For a micro-resonator the definition of the bandwidth $\Delta\lambda_{FWHM}$ and the filter rejection ratio S_{RR} is illustrated in Figure 2.10.

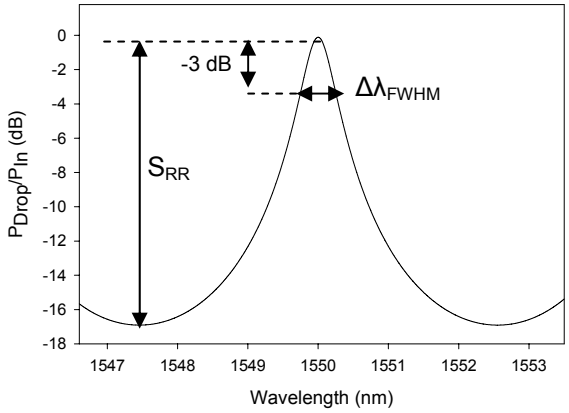

Figure 2.10. Definition of the filter rejection ratio S_{RR} and bandwidth $\Delta\lambda_{FWHM}$ in the response of a micro-resonator.

The bandwidth of a micro-resonator was previously defined in (2.22) as the spectral width in which the micro-resonator still drops half of its maximum power.
The filter rejection ratio S_{RR} of a micro-resonator can be defined as the ratio of the power that is transferred on resonance ($\varphi_r=2\pi$) and the power that is transferred by the resonator when it is completely off resonance ($\varphi_r=\pi$). The S_{RR} can be found by using Equation (2.15) and dividing the power dropped by a resonator in resonance by the power dropped off resonance as in (2.27):

$$S_{RR} = 10 \cdot \log\left(\frac{P_{On\,Res}}{P_{Off\,Res}}\right) = 10 \cdot \log\left(\frac{\dfrac{H}{1 + F_C \cdot \sin^2(\pi)}}{\dfrac{H}{1 + F_C \cdot \sin^2(\pi/2)}}\right) = 10 \cdot \log(1 + F_C) \qquad (2.27)$$

Substitution with (2.18) then gives:

$$S_{RR} = 10.\log\left(\frac{(1+\mu_1\mu_2\cdot\chi_r)^2}{(1-\mu_1\mu_2\cdot\chi_r)^2}\right) \tag{2.28}$$

where S_{RR} is expressed in dB.
The S_{RR} is proportional to the finesse of the resonator. The exact relationship between the finesse and the S_{RR} can be found by rewriting (2.28) as a function of S_{RR}:

$$\mu_1\mu_2\cdot\chi_r = \frac{\sqrt{10^{\frac{S_{RR}}{10}}}-1}{\sqrt{10^{\frac{S_{RR}}{10}}}+1} \tag{2.29}$$

Substitution of (2.29) in (2.19) then leads to:

$$F \approx \frac{\pi\sqrt{\mu_1\mu_2\cdot\chi_r}}{1-\mu_1\mu_2\cdot\chi_r} = \frac{\pi\sqrt{10^{\frac{S_{RR}}{10}}-1}}{2} \tag{2.30}$$

In general filter design there is always a tradeoff to be made between the bandwidth of a filter and the filter rejection ratio. That a micro-resonator based filter is no exception to this rule is apparent by substituting (2.30) in (2.22):

$$\Delta\lambda_{FWHM} = \frac{2.FSR}{\pi\sqrt{10^{\frac{S_{RR}}{10}}-1}} = \frac{\lambda_0^2}{n_g\cdot R\cdot\pi^2\sqrt{10^{\frac{S_{RR}}{10}}-1}} \tag{2.31}$$

This equation can be used to plot the bandwidth $\Delta\lambda_{FWHM}$ of the resonator as a function of the rejection ration for a number of effective resonator radii (R_{Eff}=$R.n_g$) as is done in Figure 2.11.

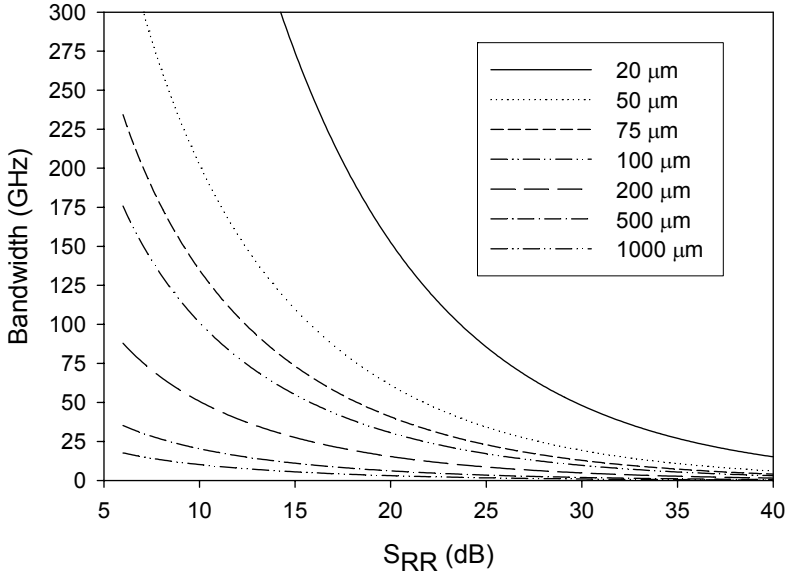

Figure 2.11. Maximum achievable bandwidth as a function of S_{RR} for a number of different effective radii (simulated for λ_0=1550nm)

The figure shows that it can be very difficult if not impossible to create a single ring resonator that achieves a high rejection ratio as well as a large bandwidth. Assuming for instance that a resonator with an effective radius of ≈87 μm, similar to that of the basic resonator building block presented in later chapters, is used in a device with bandwidth requirements of 40 GHz then an S_{RR} of at most 20 dB can be achieved. While this may be sufficient in some cases, typical telecom applications often require rejection ratios at least an order of magnitude higher.
Decreasing the radius of a resonator can be a possible solution to this problem. In most cases, however, the minimum radius of the resonator is limited by the choice of materials and the fabrication technology. An attractive alternative is then offered by higher order filters, which will be discussed in the next paragraph.

2.6 Multiple-resonator filters

Similar to the higher order filters well known from the field of electronic engineering multiple resonators can also be combined to form more complex filters. Although the higher number of resonators requires more space on-chip or, in some cases, is more technologically demanding, the resulting filter characteristics can often be very rewarding. Figure 2.12 shows two of the most common filter implementations. These are the first order resonator cascade and second order serial filter in Figures 2.12a and 2.12b respectively.

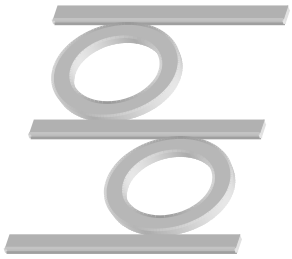

Figure 2.12a. First order MR cascade.

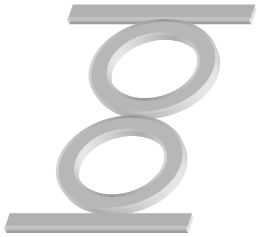

Figure 2.12b. Second order serial MR.

The first order cascade filter in Figure 2.12a already has significant advantages over a single micro-resonator. It is created by using multiple resonators of equal geometry where each resonator has its own set of port waveguides that guide light from one resonator to the next. Because this type of filter is based on multiple copies of the basic single resonator geometry it is relatively straightforward to calculate the response. The filter function is given by:

$$\frac{P_{Drop}{}^{n}}{P_{In}} = \left(\frac{H}{1 + F_C \cdot \sin^2(\varphi_r / 2)} \right)^n \tag{2.32}$$

where n is the number of resonators in the cascade.

In a higher order serial filter [53-58], of which the second order variant is shown in Figure 2.12b the intermediate waveguide between the micro-resonators is omitted and light is coupled directly between the resonators. This causes the light not only to resonate in the individual resonators but also between the resonators. This can also be seen in Figure 2.13b that shows the drop port model of the second order resonator in Figure 2.13a. In this model the feedback loops that account for the resonance in the individual resonators (short dash boxes) are supplemented by an additional feedback loop (long dash) that creates an additional resonance.

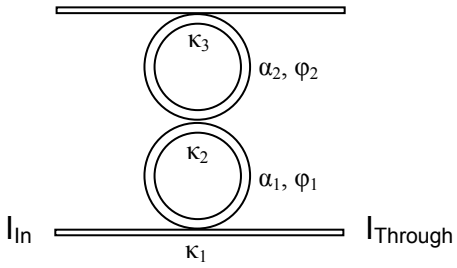

Figure 2.13a. Model parameters for a second order serial MR filter.

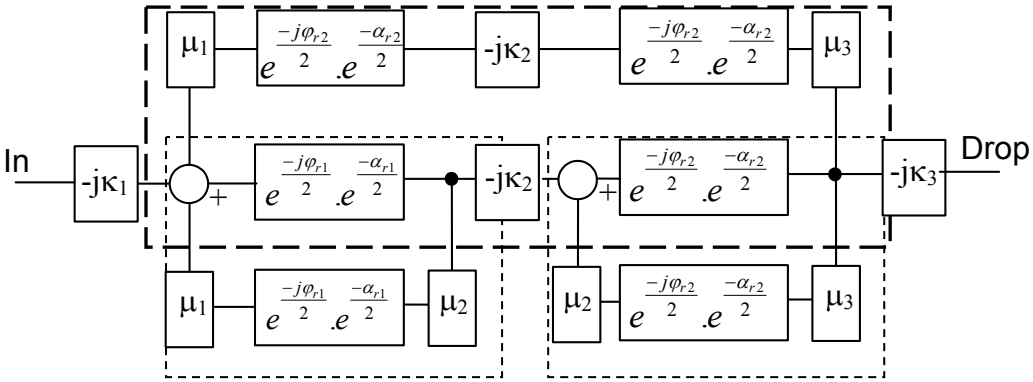

Figure 2.13b. Simplified drop-port model of a second order serial MR filter.

It is this additional feedback loop that gives the response of this filter some interesting properties when compared with the cascade filter. The drop response of this filter can be derived from Figure 2.13b and is given by:

$$\frac{P_{Drop}}{P_{In}} = \left| \frac{j\kappa_1\kappa_2\kappa_3 \cdot e^{\frac{-j(\varphi_1+\varphi_2)}{2}} \sqrt{\chi_{r1}\chi_{r2}}}{1-\mu_1\mu_2 \cdot e^{-j\varphi_1}\chi_{r1} - \mu_2\mu_3 \cdot e^{-j\varphi_2}\chi_{r2} + \mu_1\mu_3 \cdot e^{-j(\varphi_1+\varphi_2)}\chi_{r1}\cdot\chi_{r2}} \right|^2 \tag{2.33}$$

where α_n and φ_n are the loss and phase terms of the respective resonators.

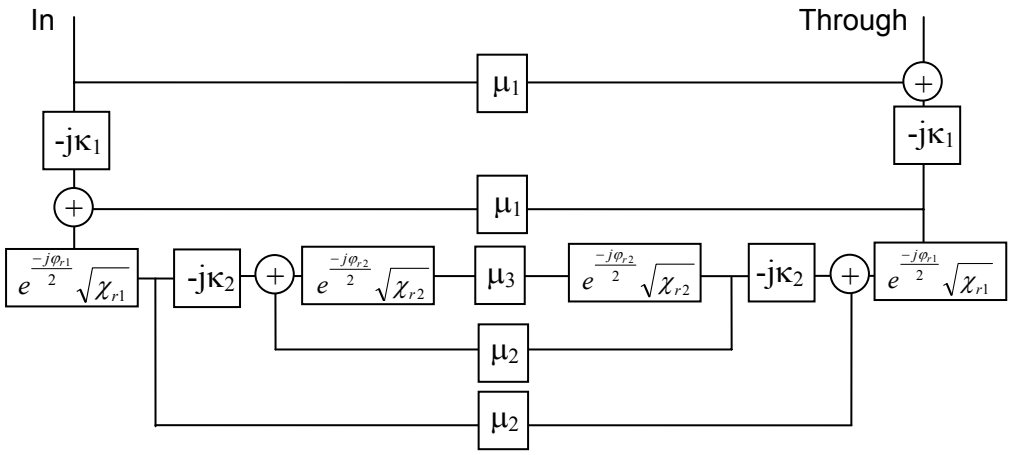

Figure 2.14. Simplified through-port model of a second order serial MR filter.

Similarly the through port response of the filter can be derived from Figure 2.14:

$$\frac{P_{Through}}{P_{In}} = \left| \mu_1 - \frac{\kappa_1^2 \cdot \left(\mu_2 \cdot e^{-j\varphi_2} \chi_{r2} - \mu_3 \cdot e^{-j(\varphi_1+\varphi_2)} \chi_{r1}\chi_{r2} \right)}{1 - \mu_1\mu_2 \cdot e^{-j\varphi_1} \chi_{r1} - \mu_2\mu_3 \cdot e^{-j\varphi_2} \chi_{r2} + \mu_1\mu_3 \cdot e^{-j(\varphi_1+\varphi_2)} \chi_{r1}\chi_{r2}} \right|^2 \tag{2.34}$$

A very important parameter in the operation of the second order filter is the coupling strength between the two resonators, κ_2. When κ_2 is too low in relation to the field coupling coefficients κ_1 and κ_3 then insufficient power will be dropped by the second order resonator. In this regime the resonators are under-coupled. Conversely, when κ_2 is too high the individual resonators are over-coupled, resulting in an undesirable filter shape.
The value of κ_2 for which the maximum power is dropped without distorting de filter shape is obtained at the so-called critical coupling κ_c. The value for which critical coupling is achieved in a symmetrically coupled second order resonator (when $\kappa_1 = \kappa_3$) is given [59] by:

$$\kappa_c \approx \frac{\kappa_1^2}{2 - \kappa_1^2} \tag{2.35}$$

Figure 2.15 shows the filter responses of an under-, critically- and over-coupled second order resonator filter for $\kappa_1=\kappa_3=0.5$. For these values critical coupling is achieved at $\kappa_2 \approx 0.14$.

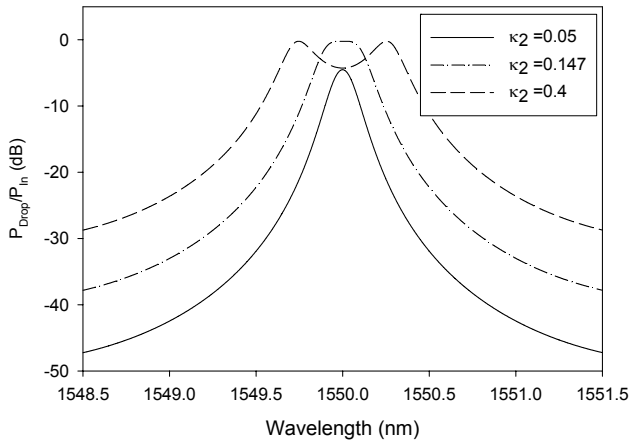

Figure 2.15. Second order response for an under, critically and over coupled κ_2.

In Figure 2.16 a comparison is made between the filter responses of a single resonator, two resonators in series, and a second order resonator.

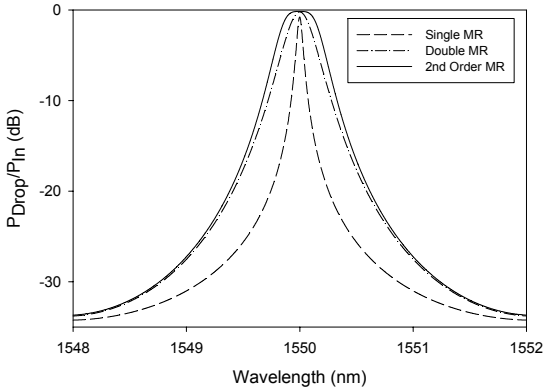

Figure 2.16a. Comparison between filter responses for α_{dB}=1 dB/cm.

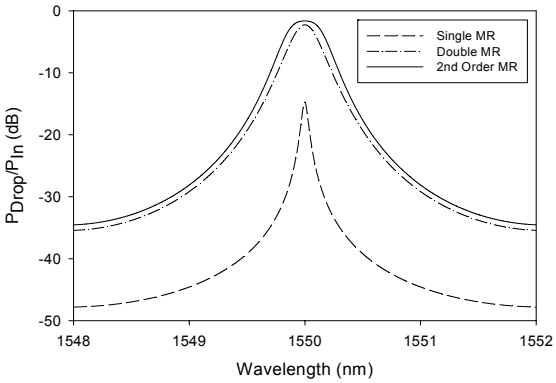

Figure 2.16b. Comparison between filter responses for α_{dB}=10 dB/cm.

As a basis for the comparison the S_{RR} was used. Although other important filter properties such as the channel crosstalk (discussed in Chapter 3.2.4) could also have been used for this comparison, the S_{RR} has been chosen in particular because of its relevance to the "on/off" performance of the MR based switch presented in Chapter 6 and the router discussed in Chapter 7. In order to make the comparison the field coupling coefficients of all filters were set such that a rejection ratio of ≈33 dB was achieved in all filters. For comparatively low cavity waveguide losses of 1 dB/cm this S_{RR} was achieved for the parameter values given in to Table 2.1. The corresponding filter responses are shown in Figure 2.16a. Here, both the cascaded MR and the second order MR show a clear advantage over the single order MR. While the $\Delta\lambda_{FWHM}$ of the single MR response is only 0.054 nm (≈6.8 GHz) the cascaded and second order MR offer respectively 0.25 nm and 0.38 nm (≈31 and 48 GHz), thereby greatly increasing the available bandwidth at the same S_{RR}. Overall the second order filter shows the best performance. Compared with the cascaded MR the second order filter has a flattened top, which can also be seen more clearly in Figure 2.15, and a steeper roll-off. This is in fact a typical characteristic of the serial higher order filter where the addition of more resonators causes the filter response to look increasingly box-shaped [54].

Table 2.1. MR Filter parameters required for S_{RR}≈33 dB at α_{dB}=1 dB/cm.

	Single MR	**Cascaded MR**	**Second order MR**
κ_1	0.195	0.5	0.58
κ_2	0.195	0.5	0.58
κ_{21}		0.5	
κ_{22}		0.5	
κ_3			0.2
Radius MR1 (μm)	50	50	50
Radius MR2 (μm)		50	50
n_g	1.84	1.84	1.84

In Figure 2.16b the same responses are shown but now at higher losses of 10 dB/cm. The parameters of these responses are given in Table 2.2. At these higher losses the

differences between the filters become even more pronounced. The dropped power of the single order MR is more than 12 dB below that of the cascaded MR. This large difference is due to the very small coupling coefficients required for the single order MR to achieve the 33 dB S_{RR}. Combined with the high losses this only allows a small power fraction to be dropped. Again the best filter of choice is the second order filter with 1 dB more power dropped than the cascaded filter. Although this may seem to implicate that, when a single order resonator is no longer sufficient for a specific task, second order MR or even higher order filters are preferred over cascaded filters this is largely dependent on the available technology. This is because the resonators in the serially coupled higher order filters couple directly with each other. Due to the circular geometry in the coupling region, however, the gap size between the resonators may have to be quite small in order to achieve the required coupling between the resonators. The choice between the filter types may therefore ultimately be made based on the available lithography.

Table 2.2. MR Filter parameters required for S_{RR}≈33 dB at α_{dB}=10 dB/cm.

	Single MR	**Cascaded MR**	**Second order MR**
κ_1	0.09	0.48	0.57
κ_2	0.09	0.48	0.57
κ_{21}		0.48	
κ_{22}		0.48	
κ_3			0.19
Radius MR1 (µm)	50	50	50
Radius MR2 (µm)		50	50
n_g	1.84	1.84	1.84

Instead of cascading the MRs in series they can also be placed in parallel [60-66] as shown in Figure 2.17. This offers certain (fabrication) advantages over a series coupled filter. In a series coupled filter the resonance wavelengths of all MRs have to be identical for optimal performance. However, in a parallel MR filter the optical signal goes through all MRs simultaneously which relaxes this strict requirement. Also, because the resonators are all coupled directly to the port waveguides in stead of each other, the lithographical requirements are more relaxed because no (typically small) coupling gaps are present between the resonators. The disadvantage, however, is that the distance L_c between the resonators is a highly important parameter in the performance of these filters and should typically be as close to a small odd multiple of a quarter wavelength [60] for optimum filter performance.

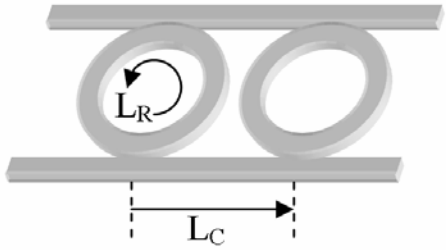

Figure 2.17. Second order serial MR.

In practical designs this may, however, be difficult to achieve. In addition this filter is highly susceptible to variations in the thickness and width of the port waveguides as these will result in a different effective path length between the resonators. In contrast, variations in port waveguide thickness will not greatly affect the performance of serial coupled resonators (only the coupling changes slightly). Although small variations in L_c can be compensated using, for instance, thermal tuning, this is also possible for variations in resonance in a series coupled MR filter. Provided that the lithography is available to define the small gaps between the resonators the series coupled MR filter is therefore preferred over the parallel MR filter.

2.7 Vernier operation

The roundtrip losses that can be allowed in a resonator are greatly dependent on the type of application in which it will be used. High finesse (e.g. F>500) applications may for instance require roundtrip losses lower than 0.01 dB if the power dropped by the resonator is not to be sacrificed too severely. In telecom applications, that have a high bandwidth requirement, however, a finesse of 10-20 may already be sufficient and higher losses of around 0.1 dB per 360° roundtrip can be allowed. The allowable roundtrip losses in turn set, dependent on the effective index contrast, a lower limit for the bend radius of the micro-resonator and thus its free spectral range.

A problem arises when the maximum obtainable effective refractive index in a certain technology does not allow for a resonator to be built with a sufficiently large FSR. A resonator created in stoichiometric Si_3N_4/SiO_2 for instance has a minimum bend radius of 20 μm, allowing for a FSR of ≈10 nm. If this resonator is used in a telecom application in the C-band of the ITU grid, which spans roughly 40 nm, it will still drop at least four channels which is often undesirable.

A similar problem arises when, from a design perspective, a certain radius is favored while, from a device perspective, a much smaller radius is required. Most of the Si_3N_4/SiO_2 resonators discussed in the following chapters for instance, have a radius of 50 μm because of phase matching and resonator "tuning" related requirements.
The tuning in particular can limit the FSR. Certain tuning methods that operate by changing the effective refractive index of the resonator for instance, may only do this by a very small amount. Reducing the FSR is then one option to enlarge the tuning since the tuning range itself is independent of the FSR as will be shown in Chapter 2.8. It is therefore possible to tune across a relatively larger part of the FSR, which in turn allows for greater possible changes in for instance the power dropped by the resonator.

In most cases these problems can be solved through the use of the so called Vernier-effect [64-67]. The Vernier-effect in micro-resonators is based on the principle that, for resonators of unequal radius placed in series, maximum power throughput is only possible when the positions of the maxima of the individual responses coincide. It therefore allows a large free spectral range to be created out of two or more resonators with a substantially larger radius. The benefits or technological necessity of a small FSR can therefore be combined with large FSR device requirements. For a Vernier filter comprised of two resonators the maxima coincide when:

$$M \cdot FSR_1 = N \cdot FSR_2 = FSR_{Tot} \tag{2.36}$$

where M and N are integers and have no common divisor. Using (2.36) it can be shown that if, for instance, one ring has a FSR of 4.5 nm and the other has a FSR of 4 nm, their combined FSR is 36 nm, nearly the width of the ITU C-band. The through and drop responses of this particular arrangement are shown in Figure 2.18a for a Vernier filter comprised of two resonators placed in serial cascade as depicted in Figure 2.18b. The responses were obtained for R_1=45 μm, R_2=50 μm, $\kappa_{1,2,3,4}$=0.4 and α_{dB}=1 dB/cm.

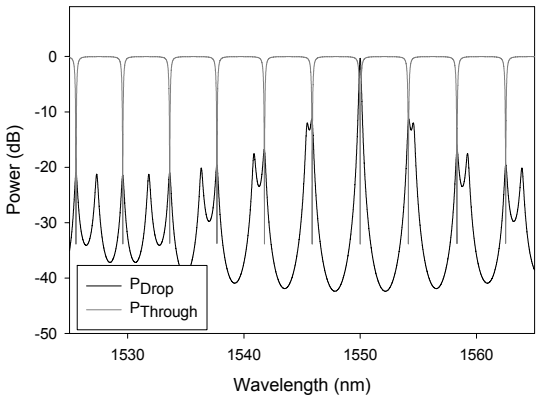

Figure 2.18a. Through and drop response of a Vernier serial cascade resonator.

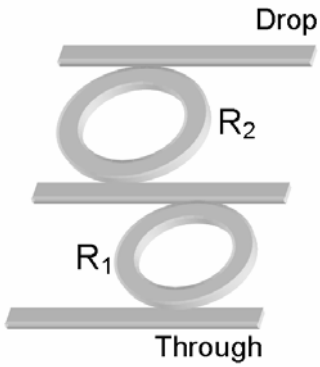

Figure 2.18b. Vernier serial cascade resonator.

The drop response clearly shows that the maximum dropped power through the filter occurs only once in the 40 nm range shown, at λ=1550 nm. A potentially negative side effect of the Vernier filter, the "side lobes", occurs in the response at those frequencies where there is still some overlap between the responses of the individual resonators. In the shown drop response the power dropped by highest side lobe is still -11 dB, enough to cause interference in most applications. By carefully choosing the radius and finesse of the comprising resonators, however, these effects may be limited. In addition cleanup filters can be added to improve the spectrum [68, 69].
Another potential problem of the Vernier cascade resonator can be seen in the through response. Because the two resonators in the filter are essentially separated from each other the first resonator will simply drop all frequencies for which it is in resonance. This poses a problem in devices where many (Vernier) filters are placed along the same waveguide because power that is dropped but not used by filters on this waveguide is essentially lost for successive filters.
A second (or higher) order Vernier filter, as shown in Figure 2.19b can then offer a solution. In the responses of this filter, obtained for R_1=45 μm, R_2=50 μm, $\kappa_{1,3}$=0.4, κ_2=0.086 and α_{dB}=1 dB/cm, the through response now only shows a clear dip at λ=1550 nm whereas only minor notches are seen at other wavelengths.

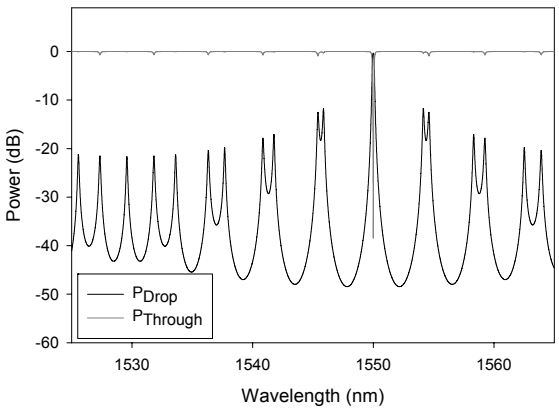

Figure 2.19a. Through and drop response of a second order Vernier resonator.

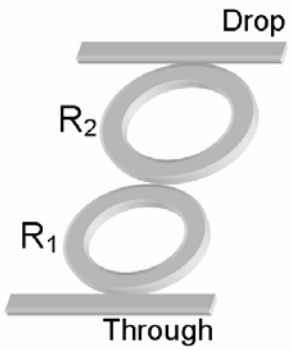

Figure 2.19b. Second order Vernier resonator.

2.8 Resonator tuning

In addition to the use of optical resonators in a passive filters such as those described in the previous paragraphs it is also possible to actively vary some of the parameters of the micro-resonator, thereby altering its response. This process of "tuning" can be used to compensate for errors in fabrication but is more commonly used to add some form of active functionality.
In the case of the micro-resonator two main types of tuning can be distinguished. The first type alters the resonator in such a way that its resonant wavelength is shifted but does not alter the shape of its response. The second type does not shift the response of the resonator but rather changes the shape of the filter response.

2.8.1 Wavelength tuning methods

The resonant wavelength of a resonator can be shifted (tuned) by changing the optical roundtrip path length of the resonator. The most straightforward way to change the optical path length is to change the index in one or all of the materials of the resonator waveguide. This will change the effective index which, in turn, will alter the roundtrip phase of the light in the resonator and therefore the wavelength for which it achieves maximum resonance. A few of the effects that can change the optical index of a waveguide are:

Thermo-optic:
The thermo-optic effect uses heat to change the refractive index of the waveguide materials [70-76]. The thermo-optic effect in materials is relatively large when compared to other effects. Certain materials, such for instance polymers or silicon, can have a very high thermo-optic coefficient (TOC) in the order of 10^{-4} °C^{-1} ($\Delta n/\Delta T$). Other materials such Si_3N_4 and SiO_2, used to fabricate many of the devices in the following chapters, have a lower TOC in the order of 10^{-5} °C^{-1}.
Generally the thermo-optic effect is easy to use because it only requires the addition of a heating element to an already existing device. Since this element is commonly implemented using a thin-film metal resistor [73] it has to be placed at some distance from the waveguide in order to avoid optical losses. When the heater is switched on

the heat will therefore first have to travel some distance before it reaches the waveguide. Likewise, when the heater is switched off, the heat will have to be conducted away to a heatsink. This limits both the speed and the power efficiency of this approach. In Si_3N_4/SiO_2 based resonators modulation frequencies of up to 10 kHz have been observed [75]. Other approaches, using for instance the waveguide itself as a heater allow for substantially higher frequencies because the heat capacity of the waveguide, instead of that of the surrounding layers is now the dominating factor. For waveguides made in silicon where this heating method is used modulation frequencies up to 700 KHz [76] have been reported. The relatively low maximum modulation frequencies make the thermo-optic effect impractical for use in modulators or applications where very high switching frequencies are required. However, in applications where a large tuning range is required or where millisecond switching times suffice, such as for instance in routing applications the thermo-optic effect can be the least complex if not the best solution.

Electro-optic:
The electro-optic effect is based on a change that occurs in the index of certain materials when these are subjected to an electric field. This change is created through such physical phenomena as the linear Pockels or the quadratic or DC-Kerr [77] effect. The Pockels effect is a linear electro-optic effect for which the index is proportional to an externally applied field. The effect only occurs in non-centrosymmetric crystal materials such as for instance lithium niobate ($LiNbO_3$), DAST (4-dimethylamino-N-methyl-4-stilbazolium tosylate) [78] or in poled polymers [79]. The DC-Kerr-effect occurs in transparent isotropic materials and has its origin in a nonlinear polarization generated in the material under the influence of a relatively slowly varying external electric field. The change in refractive index due to the Kerr effect is expressed as:

$$\Delta n = \lambda_0 . K . E^2 \tag{2.37}$$

Where K (m/V^2) is the Kerr constant, λ_0 is the wavelength in vacuum and E is the amplitude of the applied field. Both the Kerr and the Pockels effect allow for very high modulation frequencies in the gigahertz range [80-84]. In addition power is only dissipated when the strength of the applied field is altered. In a steady-state (not at high frequencies) condition this is a considerable advantage when compared to, for instance, the thermo-optic effect where power is continuously dissipated in order to maintain a certain temperature. The disadvantage of the electro-optic effect, however, is that its magnitude is generally very small, often several orders of magnitude below that of the thermo-optic effect. This makes it difficult to use this effect for anything other than modulating when used in micro-resonators. A possible compromise may be found, however, in the use of liquid crystals (LC) as the active material [85]. The electro-optic effect in these crystals manifests itself as a change in the birefringence caused by rotating molecules. This physical rotation of the molecules makes the actual process of tuning rather slow, in the order of several milliseconds in nematic liquid crystals [86]. However, the rotation of the molecules does create very large changes in refractive index, with values larger than 0.3 reported [87]. Devices based on liquid crystals would therefore allow for tuning ranges and modulation frequencies comparable to or larger than those typically found in thermally tuned devices. The power dissipation in these devices will be considerably lower, however.

Plasma-dispersion:
The plasma dispersion effect [88-92] uses excess free carriers to introduce a change in index. It can be used in semi-conducting materials such as for instance silicon or gallium-arsenide. In waveguides made from these materials free carriers can be introduced by external current injection, for instance through the use of a p-i-n diode configuration [89] or through optical excitation using two-photon absorption (TPA) [91, 92].
The free carriers that cause the change in index have a certain lifetime in the waveguide material. The speed with which changes in index can be made is therefore ultimately limited by the lifetime of the free carriers. This can be a problem in for instance a material such as silicon for which carrier lifetime is relatively high. The maximum modulation frequencies in silicon devices that use this effect are therefore often limited to a few gigahertz.

Opto-optic:
In non-linear optical (NLO) materials light can be used to change the index of a material [93]. This effect is obtained at high intensities through the optical Kerr effect. The optical Kerr effect is related to the DC effect. However, in this case the electric field that creates the change in index is supplied by the light propagating in the material. The change in index is therefore dependent on the intensity of the light I:

$$n = n_0 + n_2 I \tag{2.38}$$

where n_2 is the second-order nonlinear refractive index. In fused silica n_2 is relatively low, around 3 10^{-16} cm^2/W. In semiconductors, however, it can be much higher and, when combined with the field enhancement capabilities of a micro-resonator, can be high enough for practical use. Also sub-pico second switching has been demonstrated in SOI waveguides [94] based on high-power femtosecond pulses.

Micro-mechanic optical:
The refractive index of a waveguide can also be changed through the use of a mechanical actuator in a Micro-Electro-Mechanical System (MEMS). This is for instance demonstrated in [29] where a cantilever beam is brought in close proximity to the resonator waveguide, thereby changing its refractive index.

Chemo-optical:
The chemo-optical effect is based on the change in index of refraction that occurs when a material is altered in chemical composition. This might for instance occur when a chemically active layer forms chemical bonds with ions and molecules in its environment. The added species cause a minute change in the refractive index or absorption of the active layer which can be detected [95]
Another possibility is to have a solvent, such as for instance water, as the active layer in which other molecules can be dissolved. The refractive index or absorption in this layer then changes as a function of the concentration of the molecules in the solution. This has for instance been used in micro-resonator based sensors [27, 28, 30, 96].

Laser-trimming: Laser trimming is a process that permanently alters the index of a waveguide. In the process a high power laser is focused on the waveguide. The intense heat will locally alter [97] the structure of the waveguide and thereby its

index. Although this can be a time consuming process when many resonators need to be trimmed it can be a valuable tool in the "fine tuning" process of a resonator. This can be especially important in passive micro-resonators that have no other means of tuning or in very small resonators where even small variations in the index can cause a large deviation of the resonance frequencies as will be shown later in Equation (2.44).

2.8.2 Wavelength tuning range

All of the effects mentioned in the previous paragraph create a change in the index in one or all of the materials that make up a waveguide. Together, these changes constitute a change in the effective refractive index *Neff* of the waveguide by $\Delta Neff$. Using Equation (2.11) this can be translated to a change in group index Δn_g. An expression that determines the shift in resonance wavelength $\Delta\lambda_s$ as a function of this parameter can be found by first combining the resonance condition (2.1) and the expression of the roundtrip phase (2.10) into:

$$\varphi_r = m \cdot 2\pi = \frac{(2\pi)^2}{\lambda_0} \cdot R \cdot n_g \;\Leftrightarrow\; m = \frac{2\pi}{\lambda_0} \cdot R \cdot n_g \;,\; m \in \mathrm{N} \tag{2.39}$$

This equation can then be rearranged to provide the shift in the resonance wavelength $\Delta\lambda_s$ as a function of the change in the group index Δn_g for a certain fringe order m:

$$\frac{2\pi \cdot R \cdot (n_g + \Delta n_g)}{m} = \lambda_0 + \Delta\lambda_s \tag{2.40}$$

Substituting (2.39) for a given m back into in Equation (2.40) then gives:

$$\Delta\lambda_s = \frac{\lambda_0 . \Delta n_g}{n_g} \tag{2.41}$$

This equation shows that the resonance shift is only proportional to the change in group index of the resonator waveguide and is independent of its radius. It is therefore not possible to change the radius of the resonator in order to get a larger tuning range of the resonant wavelength. A larger radius will at most enlarge the relative tuning range $\Delta\lambda_{max}$/FSR. Ultimately the maximum tuning range is limited by the maximum of Δn_g which will be different depending on what tuning method is used.

This is not a problem in most thermo-optically tuned devices where, depending on the materials and geometry used, the tuning range might be as large as 40 nm at a wavelength of 1550 nm. In fact, thermally tuned resonators with a heater on top of the resonators can actually benefit from a smaller radius as the power consumption in the proportionally smaller heater drops.

In electro-optically or opto-optically tuned devices, however, the effects are generally very small. The tuning range is therefore generally limited to values well below 1 nm. Although this excludes these devices from applications where large tuning ranges of several nm are required, such as for instance add-drop multiplexers and routers the range may still be large enough for use in resonator based modulators.

Whether or not the tuning range is large enough can be determined by looking at the modulation depth that is possible for a given maximum Δn_g. The modulation depth ΔMod (in dB) is the difference between the power dropped by a resonator that is in full resonance at a certain wavelength λ_0 and the power dropped at that same wavelength when the resonator is tuned by Δn_g, as illustrated in Figure 2.20.

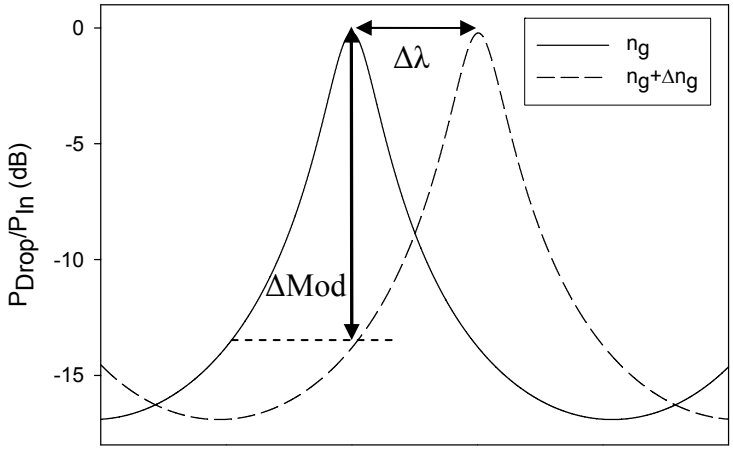

Figure 2.20. Modulation depth and resonance shift.

The modulation depth is given by:

$$\Delta Mod = 10\log\left(\frac{P_{\lambda_0}}{P_{\lambda_0,\Delta n_g}}\right) = 10\log\left(1 + F_C \sin^2\left(\frac{2\pi}{\lambda_0}\pi \cdot R \cdot \Delta n_g\right)\right) \tag{2.42}$$

Where $P_{\lambda 0}$ is the maximum power at resonance wavelength λ_0 and $P_{\lambda 0,\Delta ng}$ is the power at that wavelength when n_g changes by Δn_g. This equation can be rewritten to give the change in group index that is required to achieve a certain modulation depth:

$$\Delta n_g = \lambda_0 \cdot \arcsin\left(\sqrt{\left(10^{\frac{\Delta Mod}{10}} - 1\right)/F_C}\right)/2\pi^2 \cdot R \quad (\Delta Mod < S_{RR}) \tag{2.43}$$

The same method that was used in the derivation of Equation (2.41) can also be used to find the effect of an increase in ring radius on the resonance shift:

$$\Delta\lambda_s \approx \frac{\Delta R \cdot \lambda_0}{R} \tag{2.44}$$

This equation describes a passive way of tuning a MR through a change in radius. This can be used in for instance the design of an array of switches that all need to switch a different channel and therefore require slightly different resonance frequencies. It also shows that the fabrication of micro-resonators is a highly critical process: for a resonator with a radius of 50 μm a change in radius of only 10 nm can already cause a shift in resonance wavelength of 0.31 nm (almost 40 GHz) at λ_0=1550 nm. In smaller resonators this problem increases even further. Typical silicon

resonators for instance have a radius around 10 μm. In these resonators a small 1 nm change would already cause a shift of 0.15 nm (almost 20 GHz), which is already considered as non acceptable much in many telecom applications.

2.8.3 Filter shape tuning

In addition to shifting the resonant wavelength of the micro-resonator by tuning its refractive index, it is also possible to tune the field coupling coefficients and the losses of the resonator. Altering either of these will result in an actual change in the shape of the filter response rather than just a shift across the spectrum.

2.8.3.1 Changing the field coupling coefficients

The most straightforward way of tuning the coupling coefficients of a resonator is by placing a heater on top of the coupling region between the resonator and its port waveguides as shown in Figure 2.21. The heating of the coupler will change the effective coupling length L_C and therefore the field coupling coefficient. The magnitude of this change is proportional to the length of the coupling region. It is therefore important to have a sufficiently long coupling region in order to have a large tuning range of the coupling coefficient. The use of this type of tuning is therefore mainly limited to resonators with a large radius or racetrack resonators that typically have a long coupling region.

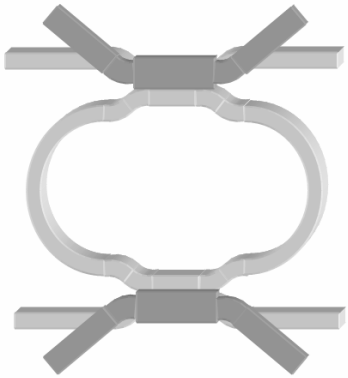

Figure 2.21. Adjustment of the coupling coefficient by direct Coupler tuning.

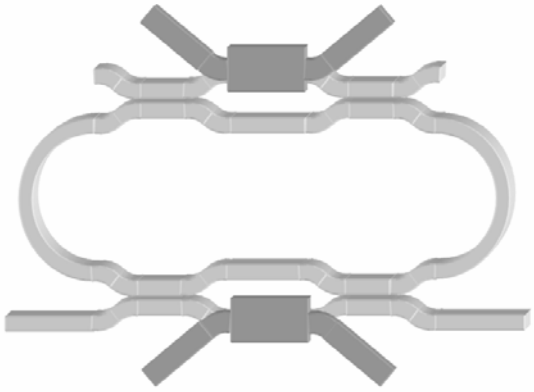

Figure 2.22. Indirect adjustment of the coupling coefficient via MZI tuning.

A problem that occurs when the coupling region of the resonator is tuned directly is that it can be difficult to create a tunable coupler that can address the entire range (from zero to one) of amplitude coupling. This will often require a very long coupler which is not practical in most cases. A better way of controlling the coupling is then to use a Mach-Zehnder interferometer to tune the coupling between the resonator and port waveguide. This MZI is inserted in the coupling region as shown in Figure 2.22 and generally consists of two -3dB couplers and a tunable branch. This allows for tuning across the entire range while keeping the length of the individual couplers small.

By tuning the coupling coefficients of the micro-resonator, a number of parameters associated with its filter response can be adjusted. Amongst the most useful of these parameters are the power dropped by the resonator and its finesse.

Figure 2.24 shows the effect of the coupling coefficients on the dropped power for a number of cavity roundtrip losses. Clearly, very large differences in dropped power

can be achieved by tuning the coupling coefficients from normal (i.e. κ=0.4-0.7) to very low values. The tuning of the coupling is therefore ideal for use in wavelength selective micro-resonator based switches. In fact, this approach allows for far greater attenuation than the switch based on resonance frequency tuning presented in a later chapter. This is because the latter approach is fundamentally limited by the fixed depth of the resonance frequency response whereas the tuning of the coupling coefficients can actually change this response in its entirety. Regardless of this fact, this approach is often not practical for use in telecom applications due to the large resonator radius (and therefore small FRS) required to implement coupler tuning. In an attempt to circumvent this problem an interesting approach based on MEMS has, however, been taken by M.M.Lee et al.[98]. This approach uses a micro-electro-mechanical actuator to physically vary the distance between the port waveguides and the resonator. This offers a large tuning range of the coupling coefficient and can be used on micro-resonator of virtually any size.

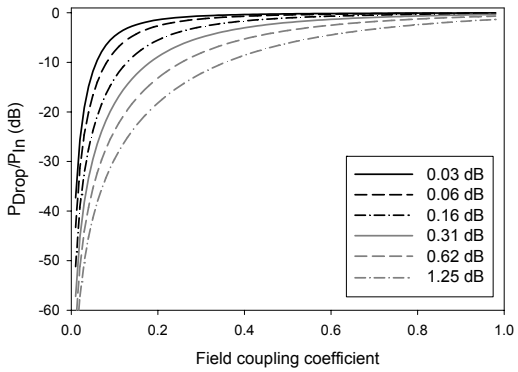

Figure 2.24. Dropped power as a function of the field coupling coefficient with the roundtrip loss α_r as a parameter.

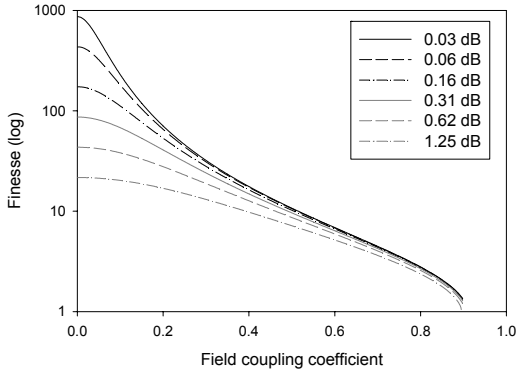

Figure 2.25. Finesse as a function of the field coupling coefficient with the roundtrip loss α_r as a parameter.

An application where a small resonator radius is of less importance is described in [45] where micro-resonators are used to create a time delay in signals sent to a phased array antenna. The delay time in the individual resonators is dependent on their finesse. The tuning of the coupling coefficients is therefore an ideal way to change this delay time across a wide range because they can greatly affect the finesse 2.25.

2.8.3.2 Changing the resonator attenuation

The effect that a change in the losses inside the micro-resonator has on its filter response is largely similar to the effects seen for changes in its coupling coefficients. Like the tuning of the coupling coefficients, the tuning of the attenuation changes the finesse and the on-resonance dropped power of the resonator. This is for instance shown in Figure 2.26a where the drop response of a resonator with $\kappa_1=\kappa_2=0.5$ and R=50 μm is given for several values of the waveguide attenuation. However, there are also some fundamental differences between these two tuning methods.

The first important difference lies in the complexity of the tuning method. As described in the previous paragraph the tuning of the couplers either requires a large coupling length, resulting in a comparatively large resonator radius, or, alternatively,

a rather complex MEMS based solution. In addition to this neither method is very fast when compared to some of the other tuning methods described in Chapter 2.6.1. Of course, instead of thermal tuning a faster method such as electro-optic tuning can be used. However, due to the significantly smaller effects involved, this would require even longer couplers. Adjusting the cavity losses on the other hand is possible using very fast methods such as for instance plasma dispersion [99] or optical pumping of the resonator waveguide doped with rare earths like erbium or neodymium [100]. Also a loss tuning implementation based on MEMS [101] has been demonstrated. This device, although comparable in tuning speed to the MEMS coupling tuning solution, is easier to implement because it requires only one actuator placed on top of the resonator. In devices that require high speed modulation (tuning) loss tuning is therefore preferable to the tuning of the coupling constants.

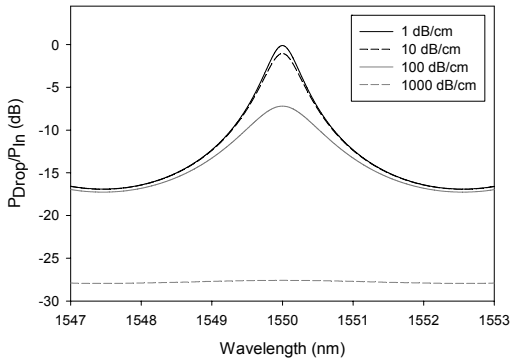

Figure 2.26a. Resonator Drop-port spectrum for different cavity waveguide losses.

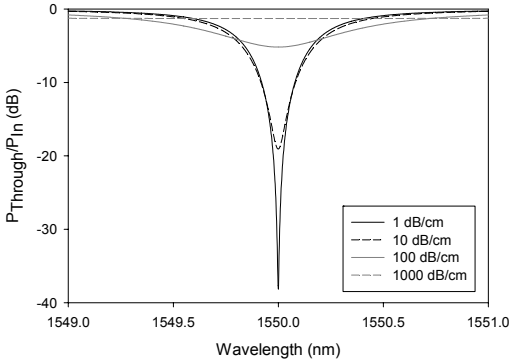

Figure 2.26b. Resonator Through-port spectrum for different cavity waveguide losses.

The second important difference lies in the fact that when the losses in a micro-resonator are tuned to a very high value, thereby effectively switching the resonator off, there will always be a penalty on the signal that passes the resonator. When the coupling coefficients are tuned to zero the resonator essentially becomes invisible to this signal. When tuning the losses, however, the coupling values are fixed to a certain value κ_t. If it is assumed that all power is lost within the resonator at maximum resonator attenuation a fraction of the power input signal $P_{In}.\kappa_t^2$ will therefore be lost inside the resonator. This can also be seen in Figure 2.26b where, for a resonator with $\kappa_1 = \kappa_2 = 0.5$ and $R = 50\mu m$, around 1.3 dB is lost in the through port for the high losses of 1000 dB/cm. This may not be a problem when a single or only a few resonators are used in a device. It can, however, quickly become a bottleneck in telecom devices in which many resonators are present on the same bus. Although the losses could in theory be reduced by lowering κ_t this is often not possible due to dropped power and bandwidth requirements of these devices. The use of the loss tuning method should therefore be carefully weighed against other options in such devices.

Chapter 3

Design

In the previous chapter the basic principles that underlie the operation of a micro-resonator have been explained using a bottom up approach. If the resonator is to be used in a real-life application, however, it is best to start by looking at the various requirements of that application. These requirements, expressed in specifications of the performance parameters, can then be used to decide the target values of the basic parameters, such as for instance the coupling coefficients of the micro-resonator design. This chapter will begin by discussing a number of performance parameters with an emphasis on the use of the micro-resonator in telecom devices. This is followed by some guidelines for choosing the right resonator geometry. The design methodologies for both the lateral as well as the vertically coupled resonators are then given. Finally some important issues related to device design, up to the prototype level, will be discussed without going into actual device implementations.

3.1 Introduction

The most important question that needs to be addressed when designing a micro-resonator or a component comprised of multiple micro-resonators is: “For what will the resonators be used ?”. Micro-resonators are often considered as the basic building blocks for optical circuitries of the future and, like their electronic counterpart, the transistor, have to be designed specifically for a certain task where its suitability for that task often makes it less suitable for another.

An interesting example of this can be found in the field of all optical switching. The basic concept of all optical switching is that one optical signal can switch another optical signal because it brings about a change in the material (e.g. in index or losses) in which both signals propagate. In general this requires the switching signal to be of a very high intensity. One solution to achieving these high intensities is through the use of a micro-resonator where the intra-cavity intensities can be many orders of magnitude above the input intensities.
The intra-cavity power of a micro-resonator at full resonance can be found by setting $\varphi_r=2\pi$ in Equation (2.14) and dividing the result by κ_2^2 :

$$\frac{P_{Cav\_Max}}{P_{In}} = \frac{\kappa_1^2 \chi_r}{(1-\mu_1\mu_2\chi_r)^2} \tag{3.1}$$

In Figure 3.1 the intra cavity power of a micro-resonator has been plotted as a function of the field coupling coefficient with the intra-cavity losses as a parameter.

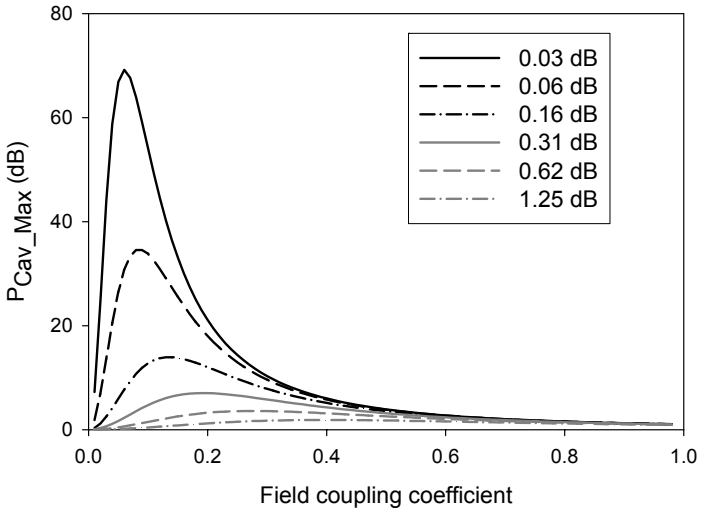

Figure 3.1. Intra-cavity power as a function of the field coupling coefficient for several resonator roundtrip losses.

The Figure shows that in a resonator the highest power enhancement is only possible for very low field coupling coefficients and low cavity losses. For instance, for resonator roundtrip losses of 0.03 dB (equivalent to a resonator with a radius of 50 μm and waveguide losses of 1 dB/cm) a maximum enhancement of ≈70 dB is achieved at $\kappa_1=\kappa_2=0.06$. The same resonator, however, will achieve only 20 dB enhancement for the moderately higher value of $\kappa_1=\kappa_2=0.2$. From the perspective of all optical switching it therefore makes sense to optimize the micro-resonator for very low losses and very small coupling coefficients. In literature such optimized

resonators, based on reflown silica toroid resonators have been reported to achieve a Q>1 10^8 [102]. Although claims are sometimes made that such devices could be used in fast switching routers or modulators this can be, by the very nature of the resonator, a contradiction in terms. Resonators with a high finesse can reach very high intra-cavity intensities due to the many roundtrips of the light within the cavity. The same high number of roundtrips, however, also makes that the buildup to the equilibrium state in the resonator takes much longer, thereby reducing its bandwidth. This is readily shown by calculating the bandwidth and power dropped by a particular resonator in resonance from Equations (2.22) and (2.17). For the resonator in the example with $\kappa_1=\kappa_2=0.06$ these are respectively 1.5 GHz and 25% (-6 dB), both of which are wholly inadequate for state-of-the-art telecom applications.

3.2 The micro-resonator used in telecom applications

Telecom applications, such as for instance those presented in later chapters, are generally driven by the (increasing) demand for high bandwidth and low losses. When applying these demands to the filter characteristics of a micro-resonator, parameters such as finesse and intra-cavity power are quickly relegated to the background and other parameters become highly important. These parameters are:

- Drop port Insertion Loss (IL_{Drop})
- Filter rejection ratio (S_{RR})
- Channel Cross-Talk (CT)
- Filter bandwidth ($\Delta\lambda_{FWHM}$)
- Through port insertion loss ($IL_{Through}$)
- Through port on-resonance port residual power (P_{TRes})

All these parameters (except the CT) and their relation to the through and drop responses of the micro-resonator have been marked in Figures 3.2a and 3.2b and will be discussed in the following paragraphs. For the value of these parameters a resonator with a radius of 50 μm is assumed because this specific radius, or a radius close to it, is used in most of the devices presented in later chapters.

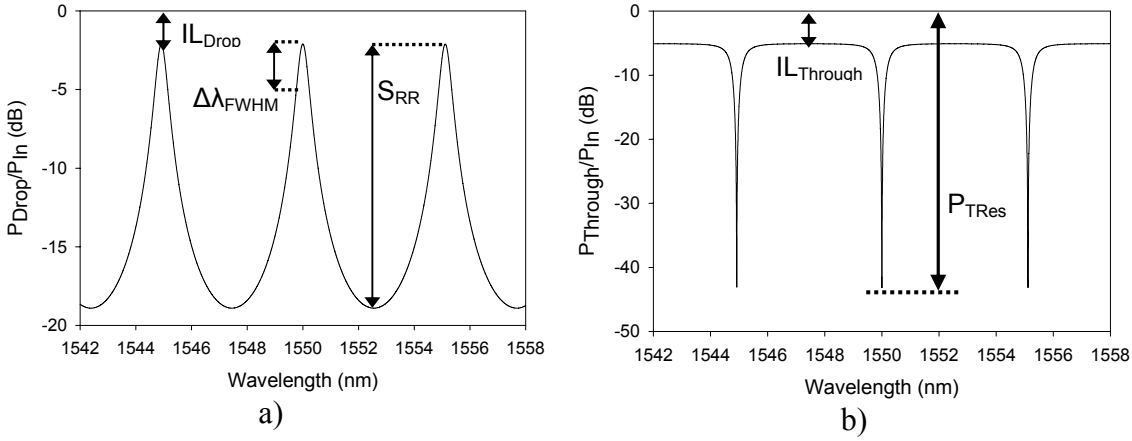

Figure 3.2. Parameters related to the drop a) and through port b) filter response of a micro-resonator.

3.2.1 Drop port on-resonance insertion loss

The insertion loss IL_{Drop} is a measure of the efficiency with which light of a certain frequency can be transferred by a micro-resonator from the in to the drop port. This parameter is especially important for micro-resonator based devices because of their resonant nature. Depending on the field coupling coefficient even moderate cavity losses quickly lower the power that can be dropped. Since many micro-resonator based devices can incorporate a number of MRs in cascade configuration, such as shown in Figure 3.3, the IL_{Drop} can easily become the dominant factor in overall device losses.

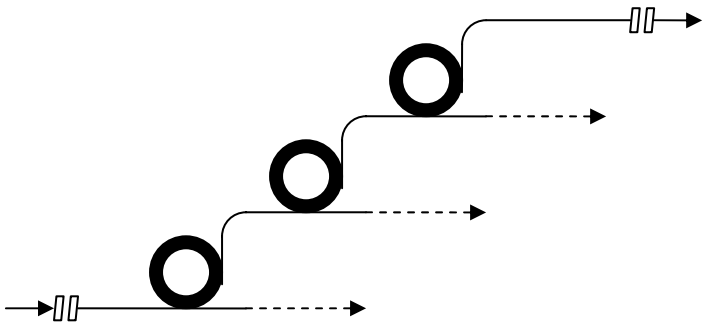

Figure 3.3. Drop port insertion losses can quickly add up and may largely dictate overall device IL performance.

The insertion losses can be found by taking Equation (2.14) for a resonator on resonance where $\varphi_r=2\pi$.

$$IL_{Drop} = -10 \cdot \log\left(\frac{H}{1 + F_C \cdot \sin^2(\pi)}\right) = -10 \cdot \log H = -10 \cdot \log\left(\frac{\kappa_1^2 \kappa_2^2 \chi_r}{(1 - \mu_1 \mu_2 \chi_r)^2}\right) \quad (3.2)$$

Ideally IL_{Drop} has a value as close to zero as possible. Due to resonator losses, however, not all power is extracted from the in-port in addition to the power lost within the cavity.

Figure 3.4 shows the insertion loss as a function of the field coupling coefficient κ ($\kappa_1=\kappa_2$) and the roundtrip losses $\alpha_r=2.\pi.R.\alpha_{dB}$ in the resonator. As is evident from the figure, IL_{Drop} rises sharply for small coupling coefficients. In theory, the higher insertion losses can be reduced by lowering the roundtrip losses. In practice, however, although reduction of scattering induced losses may be possible, the bend and intrinsic material losses pose a hard lower limit.

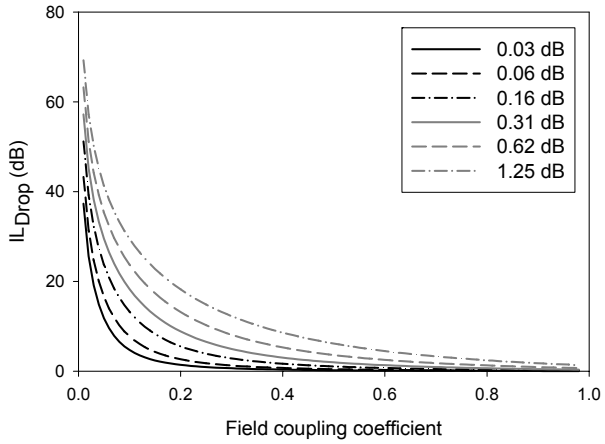

Figure 3.4. Drop insertion loss as a function of the field coupling coefficient for several resonator roundtrip losses.

3.2.2 Filter rejection ratio

In Chapter 2.4 the filter rejection ratio was first introduced. The filter rejection ratio, which was previously shown to be:

$$S_{RR} = 10.\log\left(\frac{(1+\mu_1\mu_2\chi_r)^2}{(1-\mu_1\mu_2\chi_r)^2}\right) \tag{3.3}$$

is plotted in Figure 3.5 as a function of the coupling coefficient and the roundtrip losses with values identical to those of Figure 3.4.

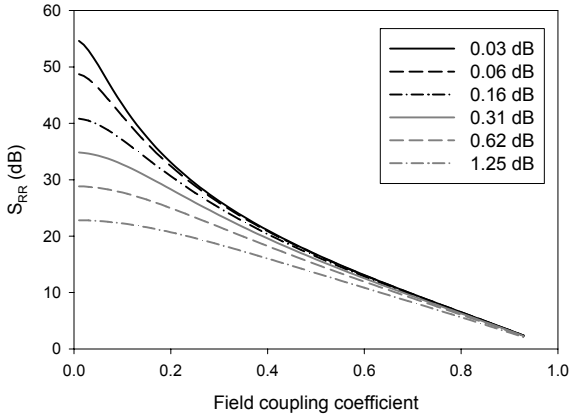

Figure 3.5. Drop selectivity as a function of the field coupling coefficient for several resonator roundtrip losses.

From Figure 3.4 it could already be concluded that the coupling coefficient should not be chosen too small because of the rise in insertion losses. However, from Figure 3.5 it can be concluded that the coupling coefficient should not be chosen too high either since it will adversely affect the filter rejection ratio. Both the high insertion losses at small coupling coefficients and the low selectivity at high coupling therefore limit the useful range of the coupling coefficient in resonator based designs. This is especially true for telecom applications where both low insertion losses and a high rejection ratio are required.

3.2.3 Filter bandwidth

In Chapter 2.5 it was already shown that there is a direct tradeoff between the resonator filter rejection ratio and its bandwidth. In Equation (2.31) the bandwidth was already expressed in terms of the free spectral range and S_{RR} but it does not provide a clear relation to the cavity losses and coupling coefficients required. This is therefore done in Equation (3.4) which can be found by combining (2.22) and (2.30):

$$\Delta\lambda_{FWHM} \approx \frac{FSR(1-\mu_1\mu_2\chi_r)}{\pi\sqrt{\mu_1\mu_2\chi_r}} = \frac{\lambda_0^2(1-\mu_1\mu_2\chi_r)}{2n_g.R.\pi^2\sqrt{\mu_1\mu_2\chi_r}} \tag{3.4}$$

Figure 3.6 shows the filter bandwidth of a resonator with n_g=1.5 at λ_0=1550 nm for a number of cavity losses.

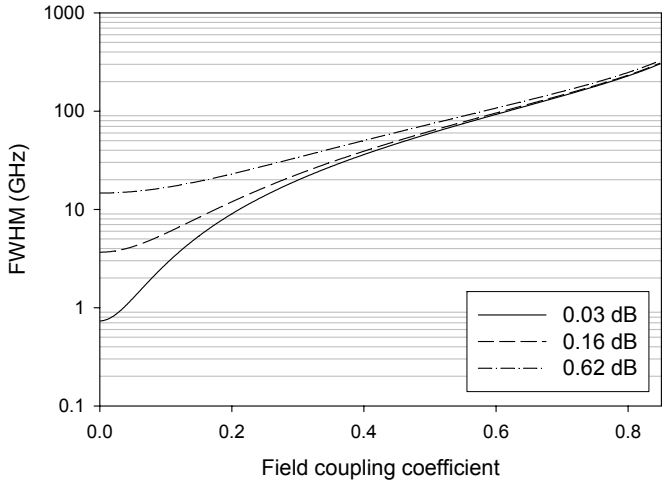

Figure 3.6. Filter bandwidth vs. coupling coefficient for three different roundtrip losses.

For low coupling coefficients the cavity roundtrip loss is clearly an important parameter to be considered as it affects the filter bandwidth quite significantly. The increase of bandwidth for an increase in losses is, however, due to an overall reduction of resonator performance, including the finesse and the dropped power. For moderate to large coupling (>0.4) the effect of the cavity losses is relatively minor and the bandwidth is mainly determined by the coupling coefficients. In 3.1.1 and 3.1.2 it was already stated that for practical uses in telecom the coupling coefficients should not be chosen too high or too low. By choosing a particular filter bandwidth this range can be narrowed down even further. A bandwidth of 10 GHz (≈0.08 nm) will for instance require the field coupling κ to be >0.2. For a bandwidth of 40 GHz the coupling needs to be increased even further to >0.4 (at a roundtrip loss of 0.03 dB). Another way to increase the filter bandwidth, as follows from Equation (3.4), is to decrease the radius of the resonator. The added benefit of this is that it will keep some of the other resonator parameters, such as for instance the S_{RR}, more or less unchanged whereas these would be greatly affected by a change of the coupling. In many instances, however, a reduction in radius will not be possible as was explained in Chapter 2.6.

3.2.4 Channel Crosstalk

An ideal optical telecom system provides a large bandwidth as well as a high filter rejection ratio. The high rejection ratio is required in order to keep the channel crosstalk as low as possible. The adjacent channel crosstalk (CT) is the measure by which an optical signal in one channel can interfere with a signal in an adjacent channel. This is illustrated in Figure 3.7. In which the vertical lines show the locations of different channels on, in this instance, the ITU grid [103].

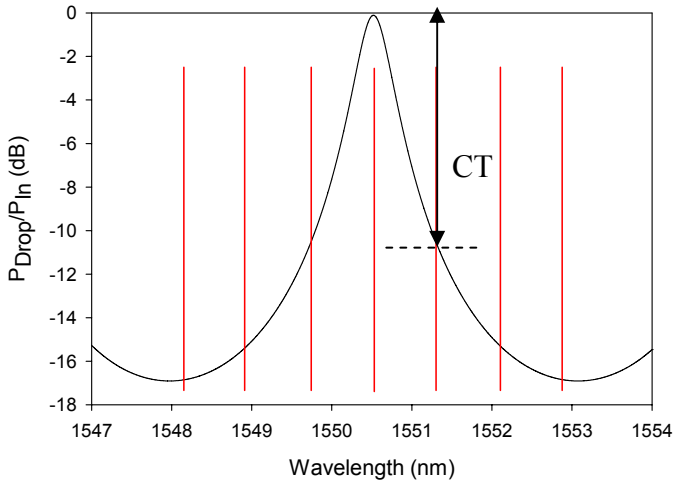

Figure 3.7. Definition of the adjacent channel crosstalk.

The adjacent channel crosstalk is here defined as the relative power fraction of a signal that is present on a channel adjacent to the channel λ_c on which this signal is transmitted. Following the derivation given in Appendix B the crosstalk can be expressed in terms of the channel separation $\Delta\lambda_{cs}$, the Finesse and the Free Spectral Range:

$$CT \equiv 10.\log\left(\frac{P_{drop}(\lambda=\lambda_c+\Delta\lambda_{cs})}{P_{drop}(\lambda=\lambda_c)}\right) = -10\log\left(1+\frac{\sin^2(\pi.\Delta\lambda/FSR)}{\sin^2(\pi/2F)}\right) \qquad (3.5)$$

Figures 3.8a and 3.8b respectively show the crosstalk of a single resonator at an ITU channel spacing of 50 GHz and 100 GHz ($\Delta\lambda_{cs}\approx$0.8 nm) for a resonator with R=50 µm and n_g=1.5 at λ_0=1550 nm.
These figures show that the crosstalk can potentially be a major problem when a micro-resonator is used as a filter in applications that use these channel spacings.
Although very low crosstalk values of <40 dB are possible this is only true for very low values of the coupling coefficient. By imposing a bandwidth requirement of 10 GHz for instance the values of the crosstalk become -20 dB and -26 dB for 50 and 100 GHz respectively. While the value of -26 dB at 100 GHz spacing is still respectable both values degrade to a respective -9 dB and -14 dB for a bandwidth requirement of 40 GHz.
One way of lowering the crosstalk is to reduce the radius of the resonator if this is technologically feasible. However, the resulting reduction is minimal. By halving the radius of the resonator to 25 µm for instance, the crosstalk of a resonator is only reduced by 5 dB. Therefore the only real option is to resort to higher order filters such as those described in Chapter 2.5. Not only do these allow for broader filter shapes

(resulting in a higher bandwidth) but also offer a steeper filter "roll-off" that reduces the channel crosstalk.

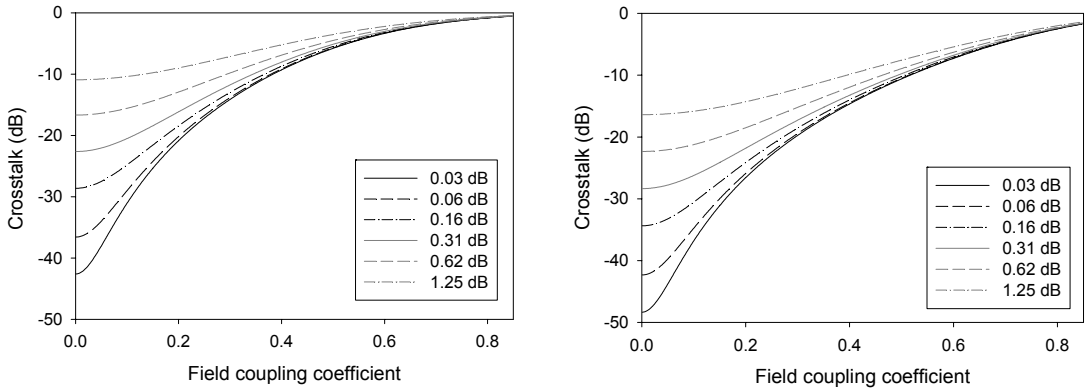

Figure 3.8a. Channel crosstalk of a single resonator filter for $\Delta\lambda_{cs}$=50 GHz a) and $\Delta\lambda_{cs}$=100 GHz b) and for several resonator roundtrip losses.

3.2.5 Through port insertion loss

In some applications, such as for instance the router described in Chapter 7, many resonators are present on the same bus waveguide as shown in Figure 3.9.

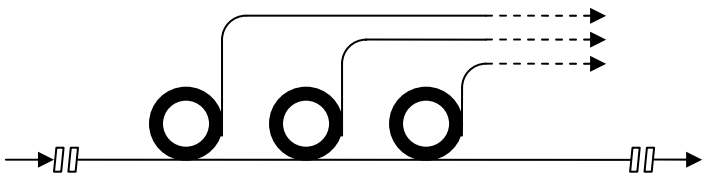

Figure 3.9. When many resonators are present on the same bus it will reduce the power of the signals on that bus.

Since each of these resonators extracts some of the power from the bus waveguide, even at frequencies for which they are not in resonance, the power of the signals in the bus waveguide will be reduced with every passing of a resonator. If there is only one channel on the bus waveguides then all resonators that do not drop this signal can be tuned maximally off resonance with respect to this signal ($\varphi_r=(2.m+1).\pi$. In this case the reduction in power (insertion loss, $IL_{Through}$) on the signal on the bus for each resonator that is passed is given by:

$$IL_{Through} = -10\log\left(\frac{(\mu_1+\mu_2\chi_r)^2}{(1+\mu_1\mu_2\chi_r)^2}\right) \tag{3.6}$$

In Figure 3.10a the through port insertion loss for this situation is shown as a function of the field coupling coefficient for a number of roundtrip losses. As can be seen the insertion loss is relatively insensitive to the roundtrip losses. At a coupling of 0.5 the $IL_{Through}$ is only 0.04 dB so that, up to twenty five micro-resonators can easily be allowed to be on the same bus if a total signal loss of 1 dB is acceptable. For coupling coefficients higher than 0.7, however, the insertion loss becomes quite considerable and these should therefore be avoided in most applications.

In most cases, rather than a single channel there will be multiple channels on the bus so that the resonators cannot be tuned to be maximally off for all channels. In these cases the power that is extracted from a channel on the bus can be calculated using:

$$IL_{Through\_\Delta\lambda} = -10\log\left(\frac{\mu_1^2 - 2\chi_r \cdot \mu_1\mu_2 \cdot \cos(2\pi \cdot \Delta\lambda_{cr} / FSR) + \chi_r^2 \cdot \mu_2^2}{1 - 2\chi_r \cdot \mu_1\mu_2 \cdot \cos(2\pi \cdot \Delta\lambda_{cr} / FSR) + \mu_1^2\mu_2^2 \cdot \chi_r^2}\right) \qquad (3.7)$$

where $\Delta\lambda_{cr}$ is the difference between the center wavelength of a channel on the bus and the resonance wavelength of the resonator. In a practical application a single free channel (i.e. a channel that is not present on the bus) might be chosen to "park" all resonators that should not drop a signal. If the spacing between the channels is defined as $\Delta\lambda_{cs}$ then $\Delta\lambda_{cr}=\Delta\lambda_{cs}$.
Figure 3.10b shows the through port insertion loss for this situation calculated for this case where $\Delta\lambda_{cr}$=0.8 nm (≈100 GHz @ λ=1550 nm) for a resonator with R=50 μm and n_g=1.5 at λ_0=1550 nm. As can be expected the losses are considerably higher in this case. For a field coupling of 0.5 the $IL_{Through}$ has now risen to 0.4 dB (for α_r=0.03 dB). That this can have a significant effect in the behavior of a device is for instance shown in the drop response measurements of the 1300 nm OADM presented in Chapter 7. Here the power dropped power by the fourth resonator on the bus is ≈ 2dB lower than that of the first resonator on the bus.

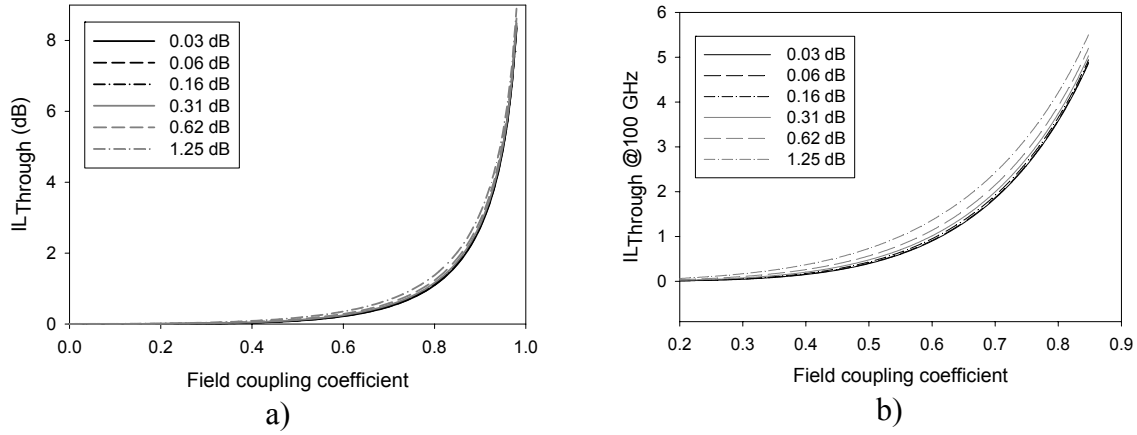

Figure 3.10. Through port insertion loss as a function of the field coupling coefficient for several resonator roundtrip losses. In a) the resonator is tuned to be maximally off-resonance for a channel on the bus while in b) the resonance wavelength of the resonator differs by 0.8 nm from the channel center wavelength.

3.2.6 Through port on-resonance residual power

In many applications the small power fraction that is still present in the in the through port of a resonator at resonance is not an issue. However, in some applications, this residual power can create some undesirable results.
In the add-drop multiplexer shown in Figure 3.11 for instance the residual power in the through port of the first resonator can interfere with the signal that is added by the second resonator. This may result in detection errors in the added signal when its power is in the same order of magnitude as the power of the through port signal.

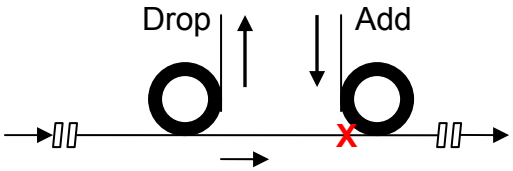

Figure 3.11. Residual channel power may interfere with other operations in a device.

In the case of the polarization independent router described in Chapter 8 the residual through port signal will even show up as a reflection in the input signal which is highly undesirable for telecom applications. It is therefore important to design the resonators in these applications in such a way that the through port residual power is as low as possible. For a resonator in resonance this power P_{TRes} is given by:

$$\frac{P_{T\,\mathrm{Re}\,s}}{P_{In}} = 10\log\left(\frac{(\mu_1 - \mu_2\chi_r)^2}{(1-\mu_1\mu_2\chi_r)^2}\right) \tag{3.8}$$

As can be seen in Figure 3.12 the residual through port power is quite sensitive to the resonator roundtrip losses. These should therefore be as low as possible. Also, from the perspective of the residual power, the coupling between the resonator and the port waveguides should be is high as possible.

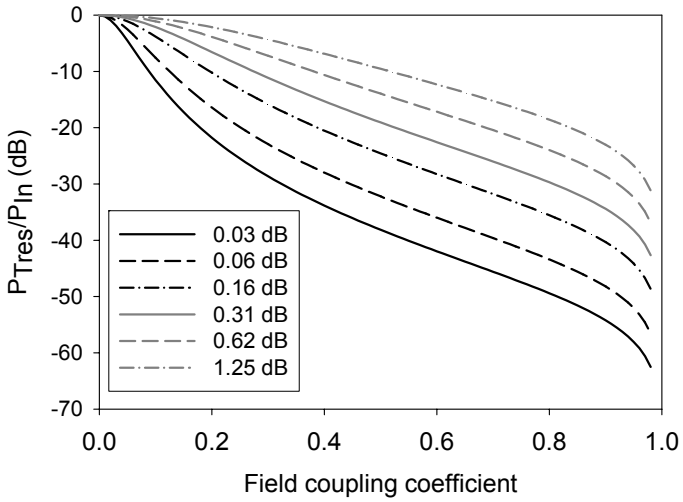

Figure 3.12. Through port residual power as a function of the field coupling coefficient for a number of resonator roundtrip losses.

3.2.7 Design parameter summary

In Table 3.1 the parameters discussed in the previous paragraphs and the requirements they place on the roundtrip losses α_r and coupling κ have been summarized.

Table 3.1. Parameter design rules for a micro-resonator used in telecom applications.

Parameter	α_r	κ
IL_{Drop}	low	medium to high
P_{TRes}	low	medium to high
$\Delta\lambda_{FWHM}$	not so important	κ high enough to obtain desired bandwidth
CT	low to medium	low
$IL_{Through}$	not important	low
S_{RR}	low	low to medium

In practice a balance will have to be found between the requirements of the three upper and the three lower parameters in this table. In most applications the lower limit of κ will be set by the bandwidth requirement while the upper limit is set by the S_{RR} or the CT. For the micro-resonators used in the following chapters this range is often between 0.4 and 0.6. A good maximum target for the roundtrip losses in this range is then ≈0.06 dB (about 2 dB/cm for a resonator with a 50 μm radius).

3.3 Geometrical design choices

After the most suitable values for the micro-resonator parameters, such as the roundtrip losses and the coupling coefficients, have been found through careful examination of the system parameters, the actual micro-resonator can be designed. However, before the resonator can be designed, the decision has to be made on what kind of resonator to use. Up to this point the micro-resonators used in the analytical discussion and the various figures assumed a micro-resonator geometry where the resonant cavity is formed by a ring. This is not the only useful geometry, however. Depending on the application in which the micro-resonator is used other cavity geometries are also possible and may actually be superior to that of the ring resonator.

3.3.1 Micro-resonator geometry

The three most commonly used resonator types are shown in Figure 3.13. These are the previously introduced ring resonator, the disc and the racetrack resonator.

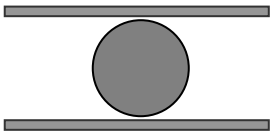

Figure 3.13a. Disc resonator.

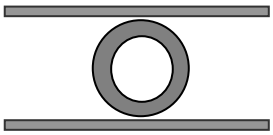

Figure 3.13b. Ring resonator.

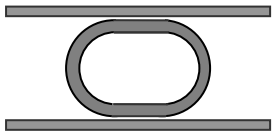

Figure 3.13c. Racetrack resonator.

Disc resonators, due to their single edge geometry, have inherently low losses compared to the other geometries. Disc resonators are therefore attractive for use in sensing systems [27] that, in order to achieve a high sensitivity, require many roundtrips of the light within the resonator. A downside to the disc resonator compared to the other geometries is that it is more susceptible to higher order modes which make it a less attractive option in telecom applications.

In a ring-resonator these higher order modes can be suppressed by choosing the width of the ring in such a way that, while the fundamental mode is still propagating as a whispering gallery mode, higher order modes are suppressed by losses incurred through lower waveguide confinement and edge scattering.
A problem that occurs for both the disc and ring geometries is that for small radii the coupling length between the resonator and port waveguides becomes very short, resulting in often undesirable low resonator coupling. Although this problem can in part be solved by reducing the coupling gap between the resonator and its port waveguides it is eventually limited by lithographical resolution and losses within the coupling section due to modal overlap losses [51].

A racetrack shaped resonator is created by elongating the coupling region of a ring resonator through the addition of a straight waveguide. This makes the racetrack resonator more effective than a ring resonator at small ring radii due its comparatively higher coupling with the port waveguides. In addition the coupling strength of a racetrack resonator is easier to adjust since it requires a change in the length of the

straight waveguide instead of a lithographically more challenging change in coupling gap width.
A downside to using a racetrack resonator is that it can have substantially higher losses compared to disc or ring resonators. This is caused by transition losses that occur at the interfaces between the straight and ring waveguides where the propagating modes have to adapt to the changing geometry. These transition losses are of most concern at low contrasts where achieving a good modal overlap between straight and ring modes can be challenging. In high index materials such as silicon nitride and silicon, however, creating a low loss transition is less problematic because of better modal confinement.

3.3.2 Vertical or lateral coupling

Besides deciding on the general geometry of the resonator a choice has to be made on how the resonator will be coupled to its port waveguides. The two options that can be considered for this are vertical and lateral coupling where each option has its own advantages and disadvantages.

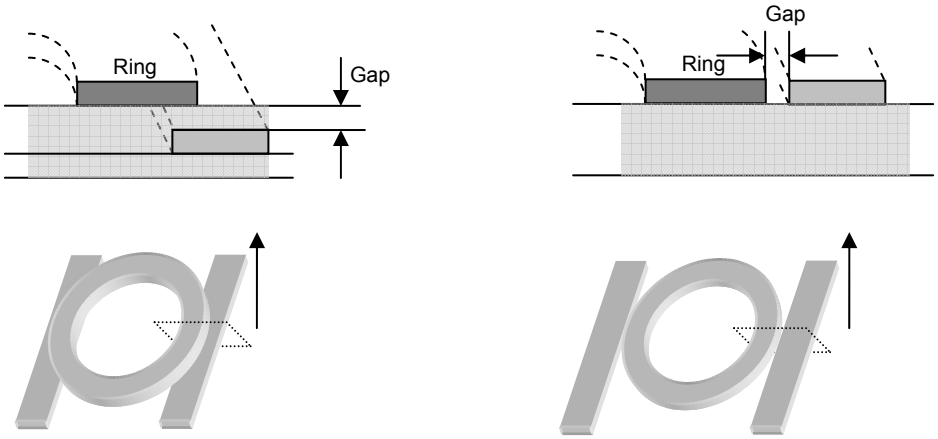

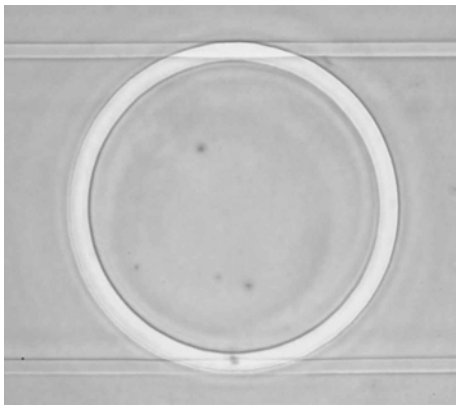

Figure 3.14. Cross-section, top-view and fabricated example of a vertically coupled resonator.

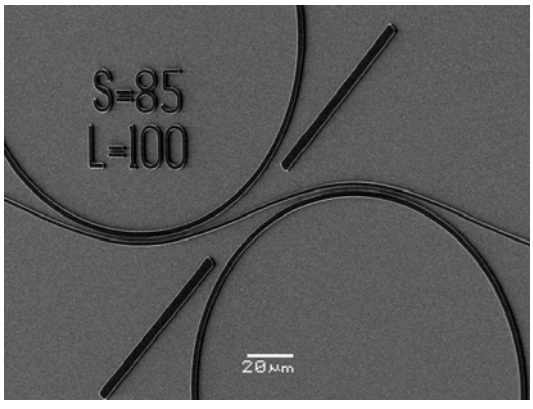

Figure 3.15. Cross-section, top-view and fabricated example of a laterally coupled resonator.

For vertical coupling the resonator and the port waveguides are placed in different layers as is shown for a ring resonator in Figure 3.14. For lateral coupling the

resonator and the port waveguide are placed next to each other in the same layer as is shown in Figure 3.15. The main discerning factor between these configurations lies in how the gap between the resonator and port waveguides is defined. Since the gap between the port and resonator waveguides largely defines the coupling κ and thus the behavior of the resonator this gap needs to be accurately set.

For vertical coupling the gap can be accurately controlled by the thickness of the layer deposited on top of the port waveguide (separation layer). The gap is therefore fabrication process dependent and can usually be controlled down to a few nanometers. An additional benefit lies in the fact that if the coupling turns out to be too small or too large only the thickness of the separation layer needs to be adjusted and no new mask design is required. Due to the fact that the resonator and the port waveguides are in different layers there is an additional degree of freedom in the choice of waveguide materials. It is for instance possible to combine low loss SiON port waveguides with a high index contrast Si_3N_4 ring resonator. However, it also poses some problems. The most notable of these is in the alignment of the resonator to the port waveguides. Misalignment will lead to an asymmetry between the couplers on the input and the drop side, which leads to undesirable resonator behavior or, in the worst case, an inability to couple light in or out of the resonator. Additionally the extra manufacturing steps involved in making the extra waveguide layer are time consuming (and thus expensive) and cause the device to be more susceptible to manufacturing errors.

The problems that a vertical resonator design faces are essentially solved by the lateral design. The alignment between the resonator and the port waveguides is now solely defined by the mask design. Due to the fact that both the resonator and port waveguides are in one layer manufacturing is also faster and less prone to errors. However, there are also some important downsides to lateral coupling. Because the resonator and port waveguides are defined on the same mask, the resolution of the lithography can become a limiting factor in the choice of the gap-width between these waveguides. The gap cannot be too large because no coupling would occur, but also not too small because the gap might not open. Depending on the maturity of the available technology this can be an important factor in the choice between lateral or vertical coupling. Another problem is that design errors related to the coupling coefficients of the resonators require a whole new mask to be designed and fabricated, unless many variations of a design have been made on a mask to preempt these errors

3.4 Material system

Besides the geometrical type of resonator the material system in which the micro-resonator will be fabricated also plays an important role in the resonator design. A waveguide core fabricated in a material such as silicon for instance allows for very small devices to be built due to its very high refractive index. However, as Equation (2.44) showed these devices will also be more sensitive to the fabrication process. In addition silicon is quite sensitive to changes in temperature due to its comparatively high thermo-optical coefficient of 1.84 10^{-4} °C^{-1}. While this can be highly useful for making thermo-optical devices with a wide tuning range [104] it also makes these devices more sensitive to changes in ambient temperature.

In addition to deciding which material will be used for the core, a material for the cladding layer, which will be put on top of the waveguides, also has to be chosen in many instances. This layer might be added to serve as a passivation or protective layer or, in the case of thermally tuned resonators to act as a separation layer to place the metal electrode a safe distance away from the waveguides. Since the cladding is part of the resonator waveguide its index influences the confinement of the resonator mode and thus its losses. Although it might be expected that the lowest modal losses are achieved for the highest index contrast between the ring waveguide and the cladding this is not necessarily the case. This is for example shown in Figure 3.16 where the refractive index and the modal attenuation of the TE_0 mode are given as a function of the upper cladding index (the substrate is SiO_2 with n=1.45). These parameters were calculated for a bend waveguide with a width of 2.5 µm, a height of 300 nm and a radius of 25 µm at a wavelength of 1550 nm.
The figures show that the modal losses of the resonator can be minimized for a cladding index of about 1.4, giving losses of about 0.35 dB/cm. They also show that a cladding with $n_c \approx 1.47$ has about the same pure bending losses as an air cladding with n_c=1. For a cladding with an index >1.48 the losses quickly become unacceptable. The reason for the unexpected decrease of the bending losses for $n_c \approx 1.4$ lies in the fact that at this value the fundamental mode has its highest confinement. At indices higher than 1.4 the reduced contrast between the core and the cladding decreases the confinement. For indices lower than 1.4 the asymmetry of the waveguide reduces the modal confinement [105].

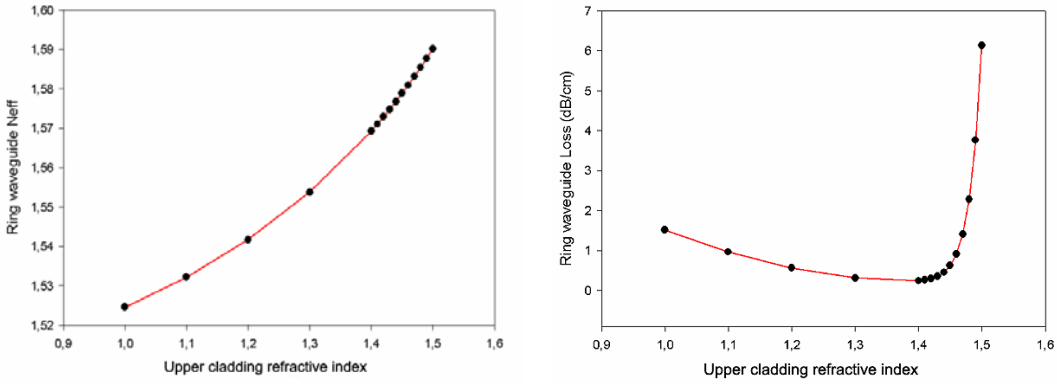

Figure 3.16. Effective refractive index (left) and attenuation (right) of the fundamental mode in a bend waveguide as a function of the upper cladding index.

Another important fact when comparing the losses for n_c=1 and n_c=1.47 is that although the bending losses are equal for these indexes, the total losses for a ring resonator with n_c=1.47 will in fact be lower. This is because the scattering losses in the waveguide due to surface roughness are increased with the difference in refractive index between core and cladding [106, 107] as shown by Equation (3.9).

$$\alpha_{scatter} \approx \frac{(n_{core}^2 - n_c^2)^2}{\lambda^4} \tag{3.9}$$

Using this equation the losses due to scattering for an air cladded MR can be calculated to be approximately 3 and 2.2 times higher than the losses for a ring with a cladding index of 1.47 and 1.4 respectively. Depending on the fabrication process it may therefore often be favorable to add a cladding, even if this is not required by the application.

3.5 Vertical resonator design

The design of a vertically coupled resonator can be described in three phases. These are, in chronological order:

- Decide in which material system the resonator will be fabricated.
- Design the resonator such that the desired radius is reached at acceptable roundtrip losses. Then design a monomodal port waveguide that is sufficiently phase matched to the resonator to achieve the field coupling required by the device in which the resonator will be used.
- Set the field coupling coefficients to their required values. For this the lateral as well as the vertical distance between the resonator and port waveguides can be varied.

3.5.1 Resonator design

The vertically coupled resonator consists of two optical layers. Its design strategy as shown in Figure 3.17 is therefore relatively simple because the port and resonator waveguides can be designed separately.

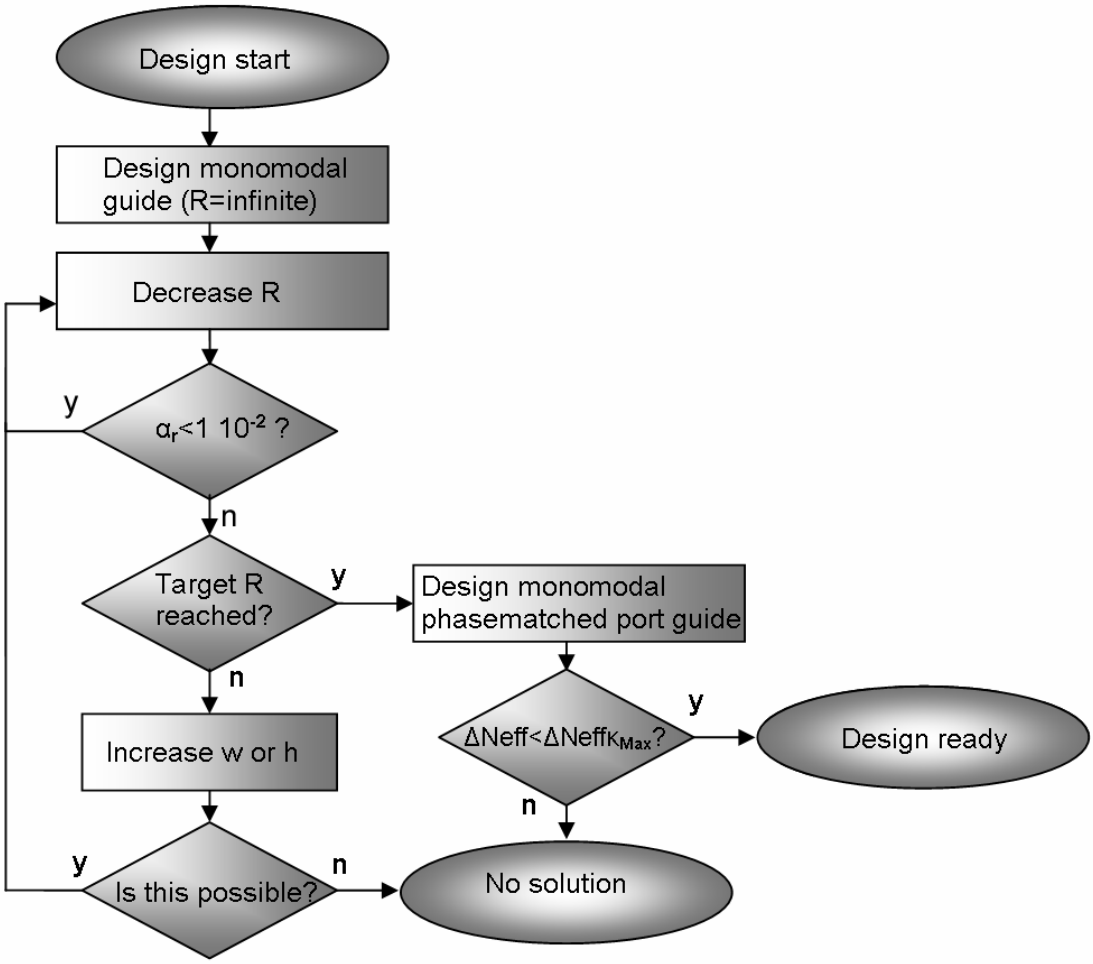

Figure 3.17. Vertical resonator design strategy.

The flowchart of the design can be described as follows:

1. Start by designing a monomodal waveguide geometry.
2. Lower the radius of this waveguide until the bend losses become too high.
3. Reduce these losses by increasing the width and/or height of the bend and continue decreasing the radius. This process repeats itself until the desired radius is reached or no further improvement is possible. This might for instance be the case if the thickness of the waveguide cannot be increased due to technological constraints. The thickness of a Si_3N_4 layer for instance is typically limited to 300 nm due to material stress.
4. If a resonator of the desired radius is found then a waveguide has to be designed with an effective refractive index that is close to that of the resonator. The ideal case is to have full phasematching ($\Delta Neff$=0.0) because it simplifies other design aspects. However, in theory the difference in effective indices only has to be lower than $\Delta Neff\kappa_{Max}$ which is here defined as the maximum difference in refractive index for which certain desired field coupling coefficients are still possible (provided that the effective length of the coupling region is also long enough for the desired field coupling coefficients).

3.5.2 Resonator propagation losses

As was shown in Chapter 3.2 the losses in the resonator can be an important factor contributing to its performance. There are three contributing factors to the losses within the cavity:

- Bending losses, also referred to as “pure” bending losses. These losses are due to the fact that the phase front of a mode needs to remain planar as it traverses a bend as is shown in Figure 3.18. This is only possible if the tangential speed of the wave front increases with increasing radius. However, at the radiation caustic the tangential speed approaches the speed of light (in the material of the waveguide). Beyond this point the tail of the mode has to break off from the guided mode and will radiate outside the waveguide causing propagation losses.

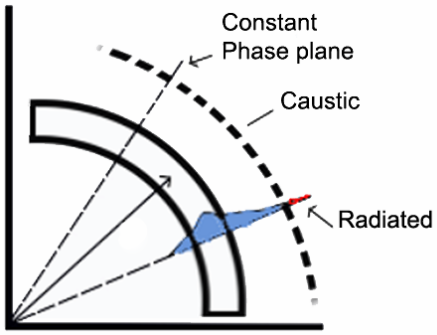

Figure 3.18. Radiation losses within a bend.

- Intrinsic material losses, caused by absorption of power in the materials of which the waveguides are made.

- Other material losses, such as scattering at imperfections within the waveguide or due to surface roughness of the waveguide that are often related to the fabrication process.

The material and fabrication losses are determined by the quality of processing and the choice of materials and are therefore difficult to reduce without considerable effort. The pure bending losses, however, can be controlled by changing the width, height and radius of the resonator. In Section 3.2.7 it was already mentioned that acceptable roundtrip losses are in the order of 0.06 dB and these dimensions should therefore be optimized to achieve this. In many instances it may be rewarding to reduce the losses even further. Caution should then be taken, however, with respect to the first and higher order modes in the resonator. When the fundamental mode losses are reduced this will also reduce the losses of the higher order modes and while propagation losses of 200 dB/cm may seem high, this is still sufficient to create a 3 dB resonance dip in the trough response of a resonator with a radius of 50 μm and $\kappa_1=\kappa_2=0.5$.

3.5.3 Determination of the coupling coefficients

In a vertically coupled resonator a straight waveguide couples to a bend waveguide that has an offset both in the lateral and vertical direction. Due to this complex coupling region geometry the field coupling coefficients can be very hard to determine. Typical approaches might for instance use 3D-FDTD or BPM but these are either very time consuming or, if BPM is used, not very accurate for small resonators. Hence, a faster method [48, 49, 108, 109] based on coupled mode theory (CMT) was used to calculate the coupling for coefficients. This method was developed within the NAIS framework by the AAMP group [110] at the University of Twente and typically takes less than a minute to calculate the coupling coefficient for a given coupler geometry.

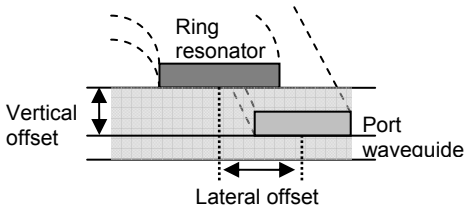

Figure 3.19. Definition of the vertical and lateral offset.

By using this software to calculate the coupling coefficients for a number of vertical and lateral offsets, which are defined as shown in Figure 3.19, the most suitable geometry can be determined for a given coupling coefficient. That the phase matching greatly influences the coupling coefficients can be seen in the calculation results in Figure 3.20a and 3.20b. The first figure shows the coupling coefficients that were calculated for a geometry in which the resonator and the port resonators were well matched ($\Delta Neff$=0.008), allowing for a maximum power coupling of more than 0.9. When the phase matching is less perfect, however, the maximum coupled power can be greatly reduced. The results shown in the second figure were for instance obtained by slightly increasing the resonator thickness of the matched geometry to create a phase mismatch of $\Delta Neff$=0.040.

While the resonator in the phase-mismatched example only has a maximum power coupling of 0.5 this is not necessarily a problem as long as the coupling coefficients required by the design can be met. However, if it is possible, a phase matched resonator is the preferred option due to increased fabrication tolerances. A comparison between the data in Figures 3.20a and 3.20b shows that the phase matched resonator is less sensitive to variations in the lateral offset at a given vertical offset. A phase matched resonator is therefore more tolerant to errors in the lateral alignment which is typically one of the biggest problems in the fabrication of vertically coupled resonators. In addition minor variations in the layer thickness between the port waveguides in the resonator also have less effect.

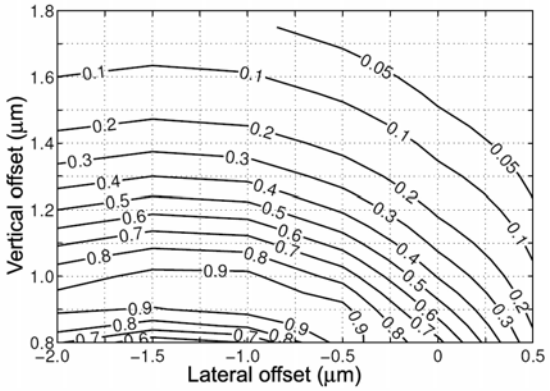

Figure 3.20a. The power coupling coefficient (κ^2) as a function of the lateral and vertical offset for Δ*Neff*=0.008.

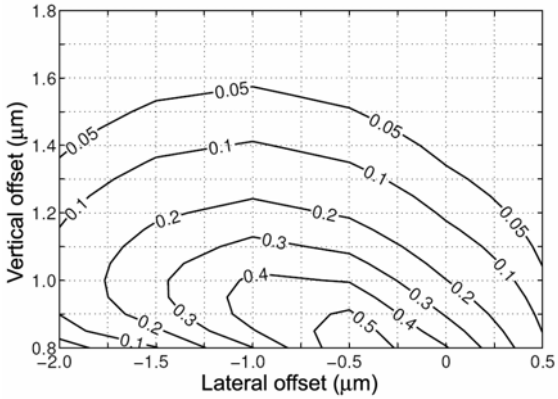

Figure 3.20b. The power coupling coefficient (κ^2) as a function of the lateral and vertical offset for Δ*Neff*=0.04.

3.6 Lateral resonator design

The laterally coupled micro-resonator, although being easier to fabricate than the vertically coupled resonator, is more complicated to design.
The higher complexity is due to the fact that both the resonator and port waveguides are defined in the same optical layer and therefore inherently have the same waveguide thickness. The only variable that therefore makes the difference between a resonator and a port waveguide is their width. For a resonator the width is generally chosen large to reduce its bending losses. The width of the port waveguides on the other hand has to be small enough to ensure mono-modality. Increasing the width of the resonator, however, can only reduce the bending losses by a limited amount. Therefore, if after widening the waveguide the losses are still too high for a certain desired radius, the only option is to increase the layer thickness. This will in turn require a reduction in de width of the port waveguides so that these remain mono-modal. Although this balancing act works to a certain degree it is ultimately limited by the fabrication technology that places a lower limit on the width of the waveguides.

Additional complexity is added to the design process when the laterally coupled micro-resonator is a true ring-resonator. In such a resonator the phase matching between the resonator and port waveguides has to be considered in the design. This complicates the design task because the resonator and port waveguides have the same height and can therefore only be varied in width to keep the difference between their refractive indices as low as possible.

The problem of the phase matching can be avoided altogether by choosing a racetrack instead of a ring resonator. As was previously mentioned in Section 3.3.1 this type of resonator has slightly higher roundtrip losses due to the overlap losses between the bend and straight waveguide sections that make up the resonator. By careful design, however, these losses can remain low and in many devices the additional losses can be compensated for by an increase of the coupling coefficients. In high index devices made in, for instance, silicon this might not even be necessary since the overlap losses are typically very small for these devices.
For this reason all the lateral resonators presented in later chapters are of the racetrack type. An additional reason for doing so was the fact that the lithography at the MESA+ Research institute [111] simply cannot reliably define gaps smaller than 0.7 μm. Midrange coupling coefficients (≈0.5) would therefore simply not be possible for a small-radius ring-resonator.

The design of the laterally coupled racetrack resonator, like that of the vertically coupled resonator, can be described in three phases. These can be summarized as:

- Decide in which material system the resonator will be fabricated.
- Design the resonator and the port waveguides such that the desired radius is reached at acceptable roundtrip losses, the port waveguides are monomodal and the overlap losses are small.
- Set the field coupling coefficients to their required values. For the racetrack resonator this is achieved by choosing an appropriate length of the straight waveguide section of the racetrack.

3.6.1 Port waveguide and resonator design

After the choice of the materials in which the resonator is to be fabricated the resonator and port waveguides can be designed based on the properties of these materials such as their refractive index and fabrication restrictions (e.g. maximum layer thickness). This design process is described in the flowchart in Figure 3.21.

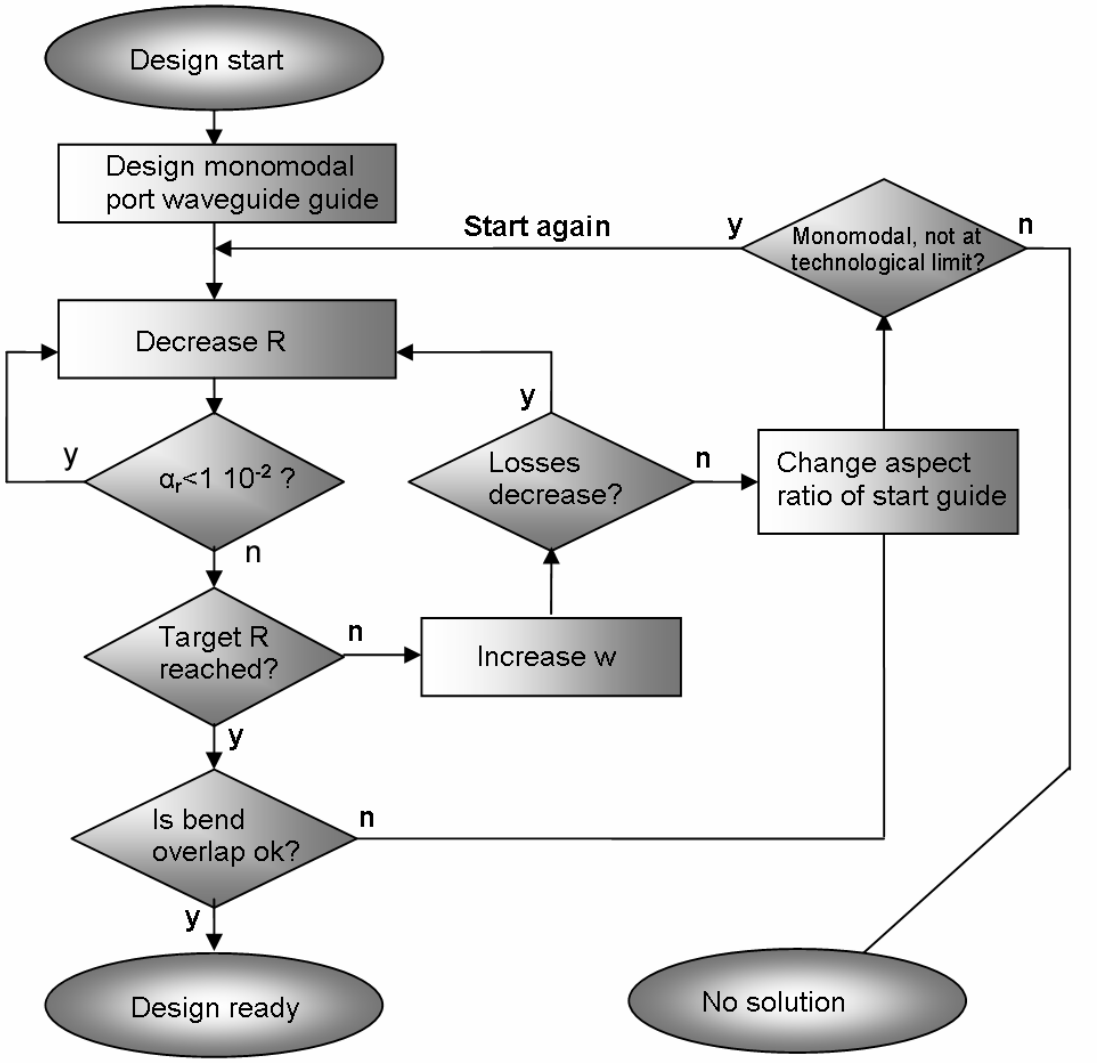

Figure 3.21. Lateral resonator design strategy.

This flowchart can be described as follows:

1. Start by designing a monomodal port waveguide geometry. This will be the geometry of the port waveguides and is used as the starting point from which the bend geometry is derived.
2. Lower the radius of this waveguide until the bend losses become too high.
3. Reduce these losses by increasing the width of the bend and continue decreasing the radius. This process repeats itself until the desired radius is reached or no further improvement is possible.
4. If it is not possible the reach the desired radius then the process has to restart at #1 with a new monomodal port waveguide that has a higher confinement if this is allowed by the chosen technology.

5. When the desired radius is finally reached the overlap losses have to be checked. If the overlap losses between the original port waveguide geometry and the new resonator geometry are acceptable the design is finished.

3.6.2 Overlap loss reduction

The overlap losses in a racetrack resonator are caused by a misalignment between the mode of the bend and the straight sections. As shown in Figure 3.22a the maximum of the modal field in a straight waveguide is located in the center. However, in a bend waveguide the maximum of the modal field is shifted away from the center as shown in Figure 3.22b. Therefore, if these waveguides are placed center to center the overlap is often not ideal and can result in significant losses.

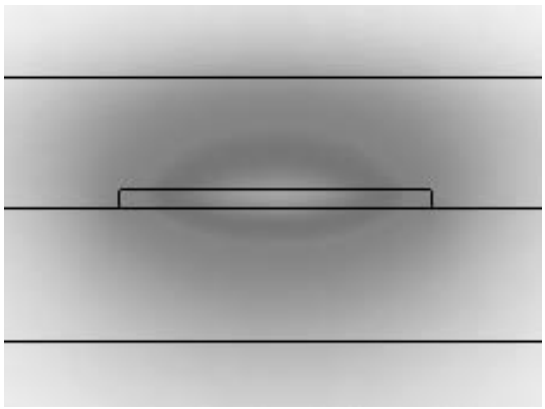

Figure 3.22a. Modal field in a straight waveguide.

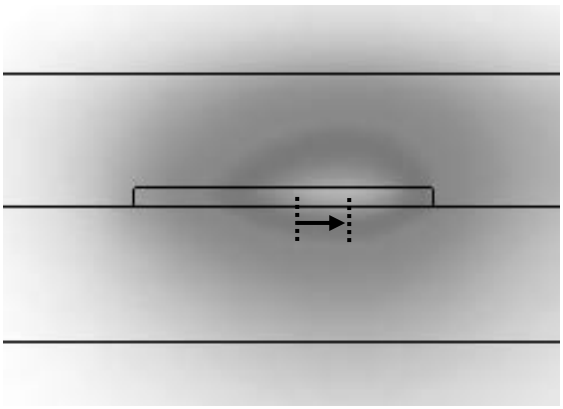

Figure 3.22b. Modal field in a bend waveguide (bend curves to the left).

If the overlap losses are too high then there are three possible options to reduce these losses:

1. Try to change the aspect ratio of the waveguides, and redesign the bend and port waveguides to see if there is an improvement in the overlap losses.
2. Insert a bend with a slowly decreasing radius to taper between the straight and bend sections of the racetrack or replace the bend section altogether. The latter will make the racetrack into a true oval shaped resonator. Because the radius of the bend is slowly decreased the overlap losses can be greatly reduced. The downside of this method is that it requires a substantial length over which the bend radius is reduced. It will therefore increase the overall roundtrip length which will require another resonator design cycle to reduce the resonator roundtrip length back to its original value.
3. Improve the overlap between the bend and the straights in the racetrack by shifting the bend laterally with respect to the straight. [112].

The last method is by far the easiest since it only requires a minor shift of the waveguides. Figure 3.23a shows how this shift is applied to the design of the resonator and Figure 3.23b shows it implemented in a fabricated device. While the offset of the bend cannot remove the overlap losses entirely it can work quite well, especially for waveguides with a high index (e.g. n>1.7). Figures 3.24a and 3.24b [113] for instance show the optimum offsets and associated losses for a racetrack resonators built in Si_3N_4 as a function of the bend radius. At a radius of 110 μm the

overlap losses are only 0.06 dB at an offset of 175 nm. This is an improvement of ≈ 0.2 dB over the same configuration without the bend offset. Considering that the losses of racetrack with a bend radius of R=110 μm and realistic bend losses of 2 dB/cm is only 0.14 dB this is quite substantial.

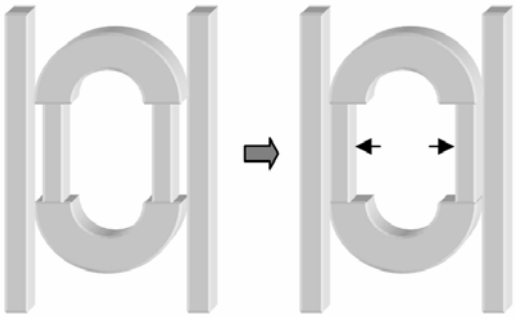

Figure 3.23a. Shifting the bend to reduce the overlap losses (shifted on the right).

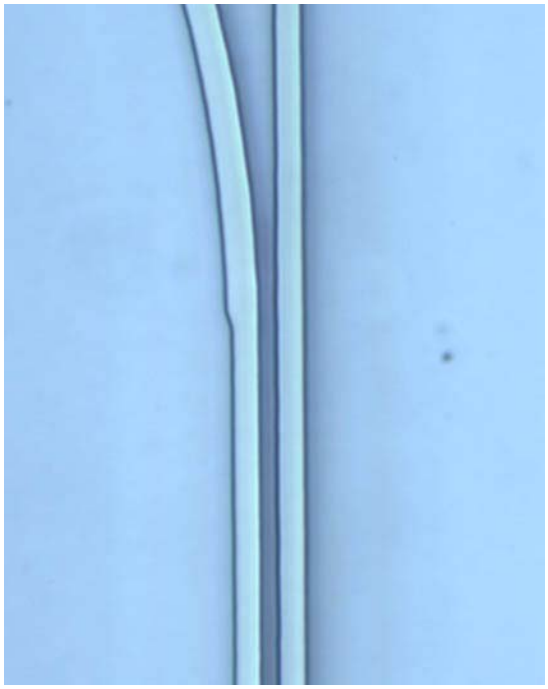

Figure 3.23b. Offset in a fabricated racetrack with some smoothing occurring at the interface between the straight and bend.

In fabricated devices the overlap losses may actually be a bit lower than the calculations predict. This is due to some smoothing of the interface between the bend and the straight that functions as a (very short) taper. The smoothing, which is also visible in Figure 3.23b, is due to the lithography that cannot image the small features at this interface.

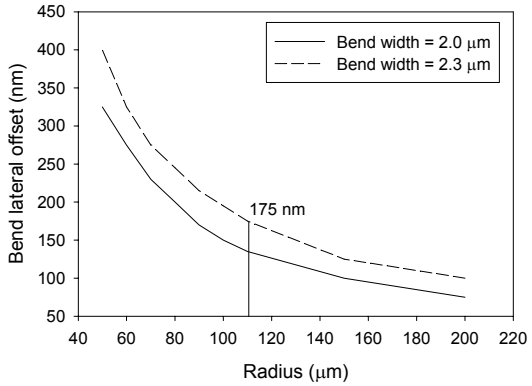

Figure 3.24a. Optimum lateral offset vs. bend radius.

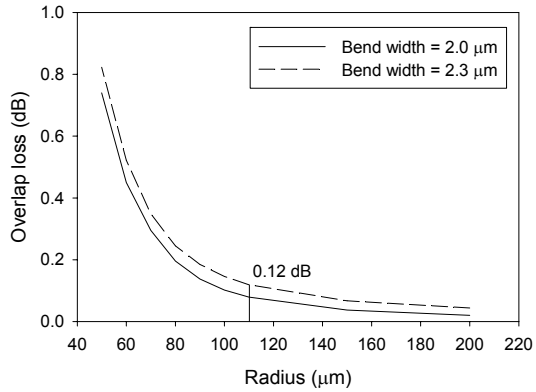

Figure 3.24b. Overlap losses, obtained at the optimum lateral offset, vs. the bend radius.

3.6.3 Setting the lateral field coupling coefficient

When the basic geometries of the port and resonator waveguides are known and the overlap losses have been minimized the resonator design can be finalized by setting the coupling coefficients. For a coupling region geometry as shown in Figure 3.25 the field coupling coefficients can be calculated using

$$\kappa = \sin\left(\frac{\pi}{2}\frac{L + L_{end}}{L_C}\right) \tag{3.10}$$

where

$$L_C = \frac{2\pi}{\kappa_c} = \frac{\lambda_0}{2.\left|Neff_1 - Neff_2\right|} \tag{3.11}$$

is the coupling length required for completely coupling light of wavelength λ_0 from one waveguide to another. The effective refractive index of the coupled modes $Neff_i$ can be readily found using a mode solver. The end length L_{end} is the contribution in the total coupling length of the bend sections and is given by Madsen [52] as

$$L_{end} = \sqrt{2\pi.R.d_0} \tag{3.12}$$

where R is the bend radius and d_0 the gap width between the port waveguides and the straight sections of the racetrack.

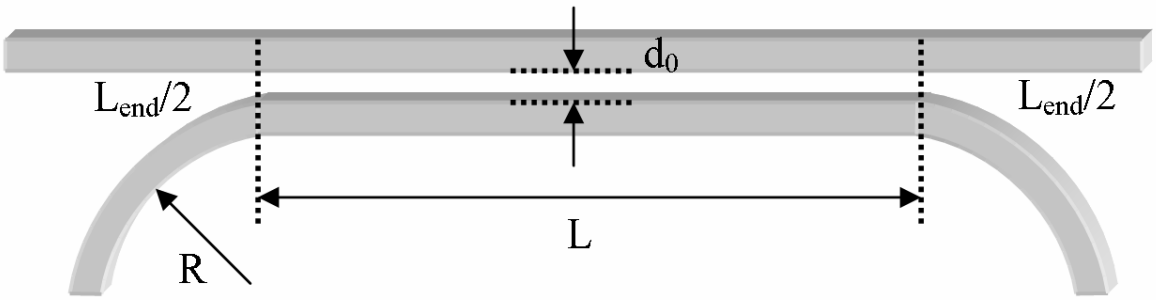

Figure 3.25. Racetrack coupling region geometry.

3.7 Component design considerations

In both the NAIS and Broadband Photonics projects there has been a continuous drive towards more complex and more densely integrated devices.
One reason for the dense integration lies in the reduction of the cost of these devices. The router that will be discussed in a later chapter for instance has a footprint smaller than 10 mm^2 including I/O and electrodes. A four inch wafer can therefore contain approximately 750 devices while a twelve inch wafer can hold more than 7000. Even if one such wafer would cost € 100.000 to fabricate the individual router chips will only be around €15, although this calculation conveniently ignores the often considerable cost of packaging.
Another far more practical reason, at least within these projects, was that the dense integration offered more variations of devices to compensate for alignment errors between the resonators to the port waveguides. As will be explained in Chapter 5 these could be partially reduced by creating devices with a range of built in alignment errors. Although the alignment errors are essentially removed by the change from contact to stepper lithography the latter still requires dense integration due to the comparatively small exposure area of the stepper reticle. This area measures roughly 2 by 2 cm and is copied many times across the wafer. All variations of a certain device therefore have to be built within this area.

In addition to designing devices such as the OADM and the router for dense integration these have also, without exception, been designed for fiber pigtailing. Apart from the fact that pigtailed devices are more robust and easier to demonstrate it was, in the case of these devices, also a necessary requirement for full characterization.
Simple devices, such as the cascaded resonator filter comprised of two resonators and the single resonator shown in Figures 3.26a and 3.13b only feature one input and one or two outputs. These devices are therefore easy to characterize using fibers or lenses. Also, if these devices require thermal tuning at most three electrode pads need to be connected which can easily be done using probe pins.

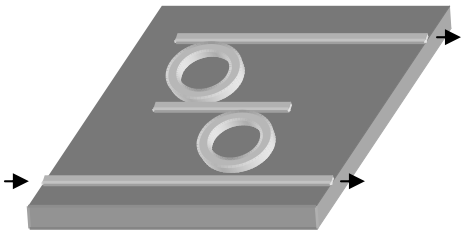

Figure 3.26a. Cascaded MR filter comprised of two resonator

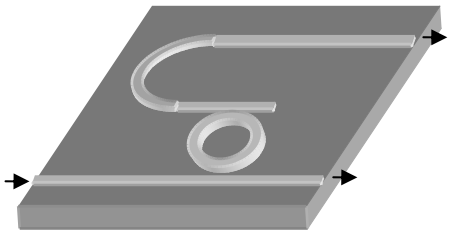

Figure 3.26b. Single MR filter.

A more complex device such as for instance the OADM, however, has five in- and outputs. Several of these may need to be connected simultaneously for full characterization. This is difficult to do with normal fibers or lenses but a fiber array, in which several fibers are spaced at 250 μm intervals, is ideal for this task.

In addition this device has five electrodes that need contacting. It is, however, very difficult to use probe pins for this due to the small size of the device. Although it is possible to create custom probe pins to solve this problem it would require a new set of these for every device type. The alternative is then to bond the electrodes to a standard carrier chip and glue the fiber array(s) to the device, thus creating a stable setup for measuring.

3.7.1 Creating a design layout for pigtailing purposes

Perhaps the most trivial implication of making a micro-resonator based device that can be attached to a fiber array is that a large part of the layout and size of these devices is dominated by the fiber array. This is because devices have to be at least as wide as the distance between the first and the last fiber in the array and therefore always a multiple of 250 µm. Since most of the micro-resonators discussed in this thesis have a diameter of 100 µm they can always be placed within this spacing and are therefore of lesser importance in the layout of the device.

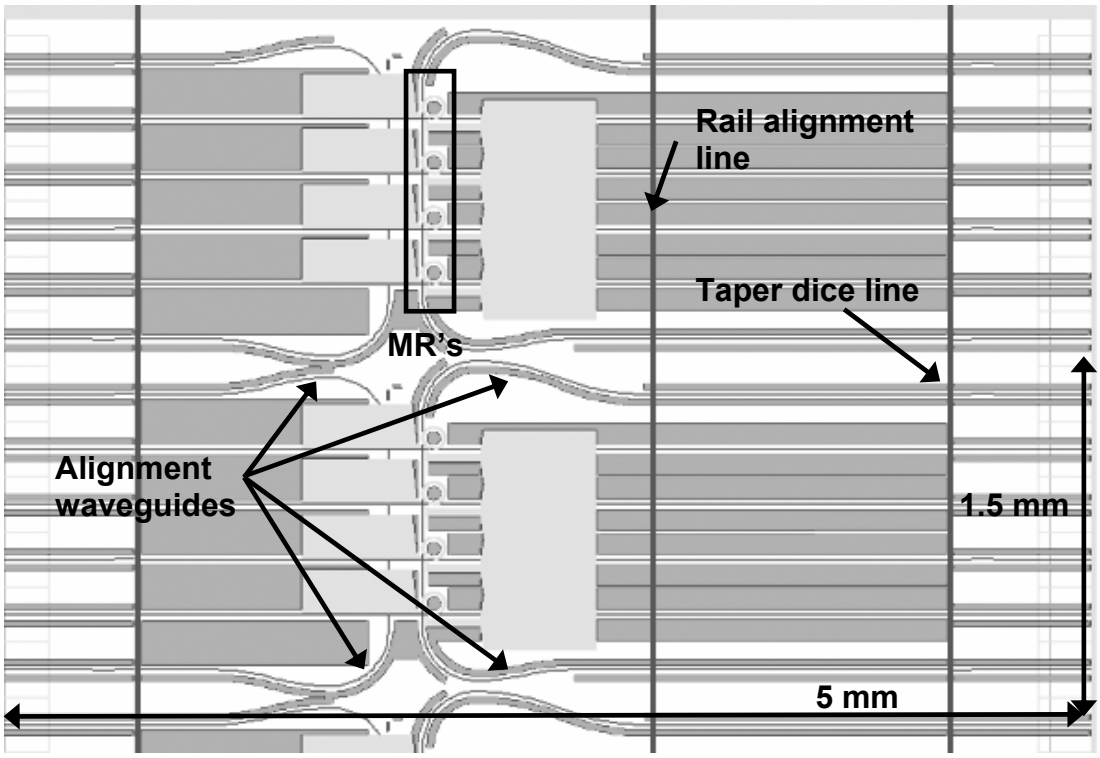

Figure 3.27. Important design features required for fiber array to chip coupling.

In Figure 3.27 a small section of a stepper reticle is shown. In this section two OADMs can be seen side by side, each measuring 5 by 1.5 mm (width x height). The fiber array spacing is clearly the dominant factor in this example. The layout is largely determined by the four add-drop ports that, at a spacing of 250 µm, run across the full width of the device whereas the space taken up by the resonators is negligible in comparison.
The two other important features related to a design that uses fiber arrays can also be seen in this figure. These are the alignment waveguides and the glass rail alignment line. The alignment waveguides form a direct connection between the outer most fibers in the fiber array that can be used to properly align the fiber array to the chip.

By maximizing the power through these outermost connections the best alignment for the connections between them is also automatically found. The alignment waveguide and the right side of the OADMs shown in the example performs a dual function because it is also the input and express output of the device. In many cases, however, such a dual function is not possible so that the alignment waveguide needs to be wrapped around the device to cause the least possible interference with the operation of the device.
The rail alignment line is not part of the actual device but is drawn in one of the metallization layers on top of the device. This line is therefore visible by the naked eye and can be used to accurately glue a glass rail on top of the device. This glass rail is required to increase the cross-sectional area to which the fiber array can be glued. Because the glass rail covers the device up to the rail alignment line it is important that no structures that need to be accessible are placed beyond this line.

3.7.2 Tapers

When standard (e.g. SMF-28) or even high numerical aperture (HNA) fibers or fiber arrays are used to couple light into high contrast waveguides significant losses can occur at the facets. However, these losses can be reduced through the use of a suitable spot-size converter. This converter can be implemented in a number of different ways, using for instance non-periodic waveguide segments [114, 115] or a y-branch [116]. One of the least complicated methods, however, is to use a tapering of the port waveguides to match the spot sizes [117].

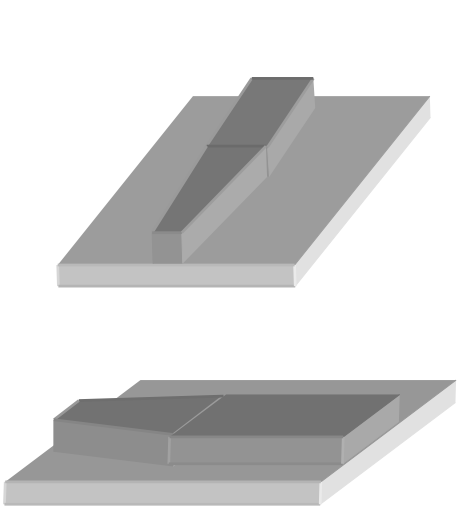

Figure 3.28a. Top and side-view of a horizontal taper.

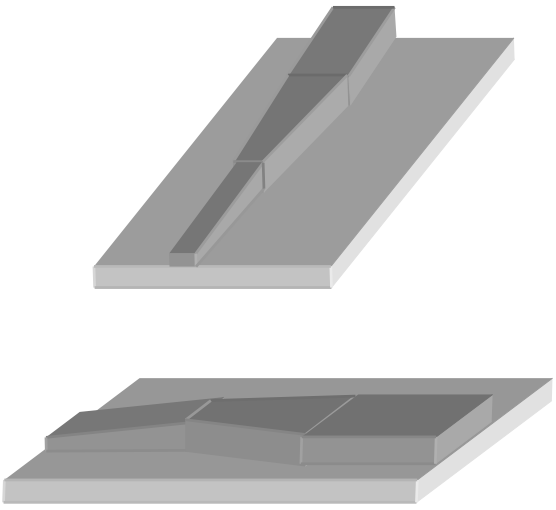

Figure 3.28b. Top and side-view of a tapering in both the horizontal as well as the vertical direction.

The most commonly used taper is the horizontal (lateral) taper, for instance used in the switch and early OADM designs. Since in this taper, as shown in Figure 3.28a, only the width of the waveguide is varied it can be implemented using the same mask that defines the port waveguides. In later OADM designs this taper was combined with a vertical taper section as shown in Figure 3.28b. This can improve the fiber chip coupling losses quite significantly because it allows for a mode expansion in both the lateral as well as the vertical direction. It does, however, require an additional mask

step to define the vertical slope of the waveguide as will be explained in more detail in Chapter 5.

For both taper types it is important that the taper itself does not add to the coupling losses. The tapers therefore have to be designed to be adiabatic. The taper angle θ_t for which this can be achieved [112] is given by

$$\theta_t(s) \leq \frac{\rho(s).(N_{eff} - n_{clad})}{\lambda_c} \tag{3.13}$$

where n_{clad} is the index of the cladding layer, *Neff* the effective index of the waveguide at position s, and ρ the half width of the waveguide at that position. The definition of these parameters is also given in Figure 3.29.

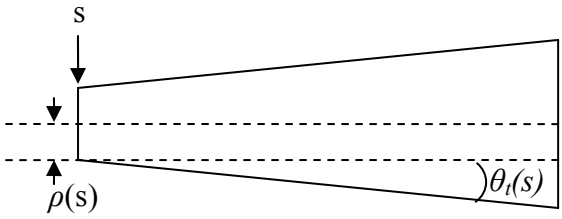

Figure 3.29. Definition of taper parameters.

3.7.3 Optimal port waveguide bend radius

The minimum size of some devices, like the OADM, is largely dictated by the fiber array. In other devices, however, especially those made in low-contrast materials, the minimum size is directly related to the minimum achievable bend radius of the port waveguides. That this radius can affect the design size in quite a significant way is for instance shown in Figure 3.30a. In this layout of a single micro-resonator device nearly two thirds of the device is taken up by the return bend in the drop port of the device. While this particular layout can be improved by inserting an S-bend as shown in Figure 3.30b this might not be possible in many other cases.

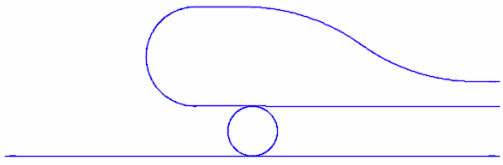

Figure 3.30a. Standard single resonator layout.

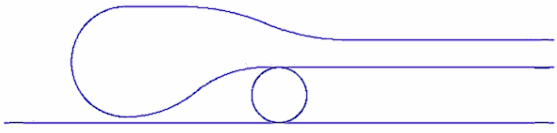

Figure 3.30b. Improved layout with reduced height.

From a design perspective it is therefore critical to know what the minimum bend radius of a port waveguide is to achieve the best possible layout. Not only the minimum radius is of importance, however, but also the maximum radius should be determined. At small bend radii the waveguide losses in a, for instance, 180-degree bend are largely determined by the pure bend losses. For large radii, however, these losses are relatively insignificant while the scatter and material losses become more

important, due to the fact that the light needs to travel a longer distance to cover a 180-degree bend.

$$Loss_{Bend\_total} = \pi.R(\alpha_R + \alpha_{S,M}) \tag{3.14}$$

The total losses (in dB) incurred by a 180-degree bend are given by (3.14) in which α_R (dB/cm) is the pure bending loss found through simulations and $\alpha_{S,M}$ are the scattering and material losses.

As an example Figure 3.31a shows the pure bend losses of a Si_3N_4 waveguide, calculated using the commercially available Selene bend-modesolver [50], as a function of the bend radius. This waveguide, with a width of 2 μm and a height of 0.14 μm is the basic port waveguide used in nearly all of the devices described in this thesis. When the pure bend losses are combined with the material and scatter losses the 180-degree bend losses shown in Figure 3.31b are obtained. In this figure it can be observed, for instance, that a bend with a radius of 100 μm is has the same 180 degree bend loss as a bend with a radius of 500 μm for $\alpha_{S,M}$=2 dB/cm, thereby showing that a large bend radius is not necessarily better than a small bend radius. Rather, the optimal radius of this waveguide is found between 150 μm and 250 μm. All devices that use this type of port waveguide have therefore been designed with reference to these values.

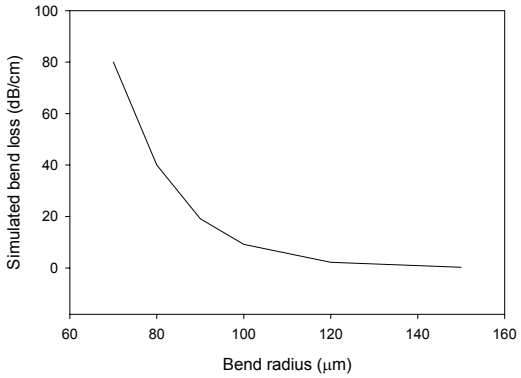

Figure 3.31a. Bend loss versus the bend radius.

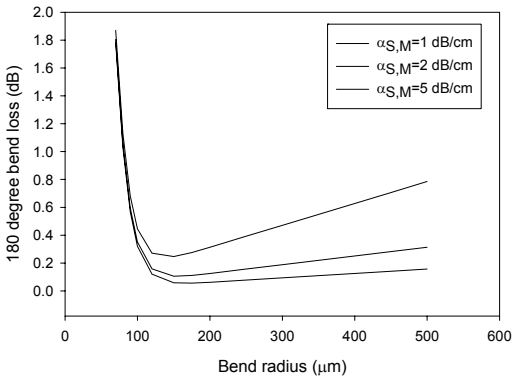

Figure 3.31b. Bend loss in a 180-degree bend versus the bend radius.

Chapter 4

Simulation and analysis

During the course of both the NAIS and broadband project many programs have been created to create a better insight into the operation of micro-resonators or to simply be able to create novel devices. These programs include tools for both simulations as well as data-analysis of which the relevant aspects will be discussed in this chapter.
In addition the Aurora simulation tool is presented. This tool has been specifically designed to simulate highly complex optical devices consisting of many separate or even higher order coupled resonators. Contrary to common methods the calculations of this program use a comparatively simple and possibly novel scheme based in the time domain from which the frequency response can easily be derived.

4.1 Introduction

As was shown in the previous chapter a large number of parameters has to be considered when designing a micro-resonator. For the calculation of these parameters several tools have been used:

- The commercially available modesolver Selene [50], used to calculate the effective refractive indices and waveguide attenuations of straight waveguides and bends.
- The AAMP CMT3D software [108-110] that was developed within the NAIS project to calculate the coupling coefficients of a micro-resonator.
- The Micro-resonator Investigator (MRI) tool that visualizes most of the parameters discussed in the previous chapters and allows for real-time interaction with these parameters.

The MRI tool was created as a visualization wrapper around most of the equations that describe the different aspects of the micro-resonator. Since these equations have already been discussed in depth in the previous chapters the focus of the discussion of this program in Paragraph 4.2 will be on the alterations that were made to Equations (2.17) and (2.25) to make them faster to compute. The algorithm used to obtain the transient resonances of the micro-resonator will also be addressed as this will help to explain the algorithms that will be discussed in Paragraph 4.5 for the high level Aurora simulation tool. In addition to the simulation tool MRI additional programs were written to analyze measurement results. These were:

- The RFit tool, that uses a brute-fore method to fit measured micro-resonator responses.
- DropZone, a tool that provides a fast analytical method for fitting the responses of resonators with symmetric coupling coefficients.

The RFit tool builds upon the computational changes in MRI to speed up the brute-force fitting of the micro-resonator responses and is briefly discussed in Paragraph 4.3. If it is assumed that a resonator is symmetrically coupled to its port waveguides and has negligible coupler losses then it is possible to calculate coupling coefficients as well as the cavity losses directly from the depth of the through and drop responses. The equations used for this have been implemented in the DropZone program and will be given in Paragraph 4.4.

At an early stage during the NAIS project it was realized that, in order to quickly evaluate new designs, a specialized program for high level design would be nearly indispensable because of increasing device complexity. While the numerous basic devices simulated in the MRI tool can still be easily described in equations such as (2.17) and (2.25) this would be impossible to do for something as complex as the router. However, at that time there were no programs were available that could adequately perform these simulations. The decision was therefore made to create an entirely new program that would be specifically designed to deal with devices consisting of many resonators. This program, called Aurora, will be discussed section 4.5.

4.2 Micro-Resonator Investigator

The MRI tool, of which a screenshot is shown in Figure 4.1, offers quick interactive control of microring-resonator parameters such as the radius, loss and coupling coefficients for a number of simple microring resonator configurations. The simulations that can be performed are:

- Transient drop port response of a single resonator.
- Wavelength response for the through- and drop ports of a single resonator.
- Bimodal response of a single resonator. This was used to study the effects of additional modes in the resonator.
- Comparison between a non-tuned and a tuned (by $\Delta Neff$) resonator.
- Cascaded dual resonator response. The two resonators in cascade form the basis of the micro-resonator based switch discussed in a following chapter. The radius of the additional resonator can be set individually to allow exploration of Vernier filters.
- Cascaded triple resonator response. Used to examine the effects of an additional resonator to the switch or Vernier configuration.
- Second order through and drop response. This configuration can be used for improved filter performance over a single MR but also allows improvements when used as a Vernier filter or switch.
- Third order through and drop response.

In addition to this the program allows for the visualization of the parameters discussed in Chapter 3 as a function of the field coupling coefficients and the waveguide attenuation in the micro-resonator.

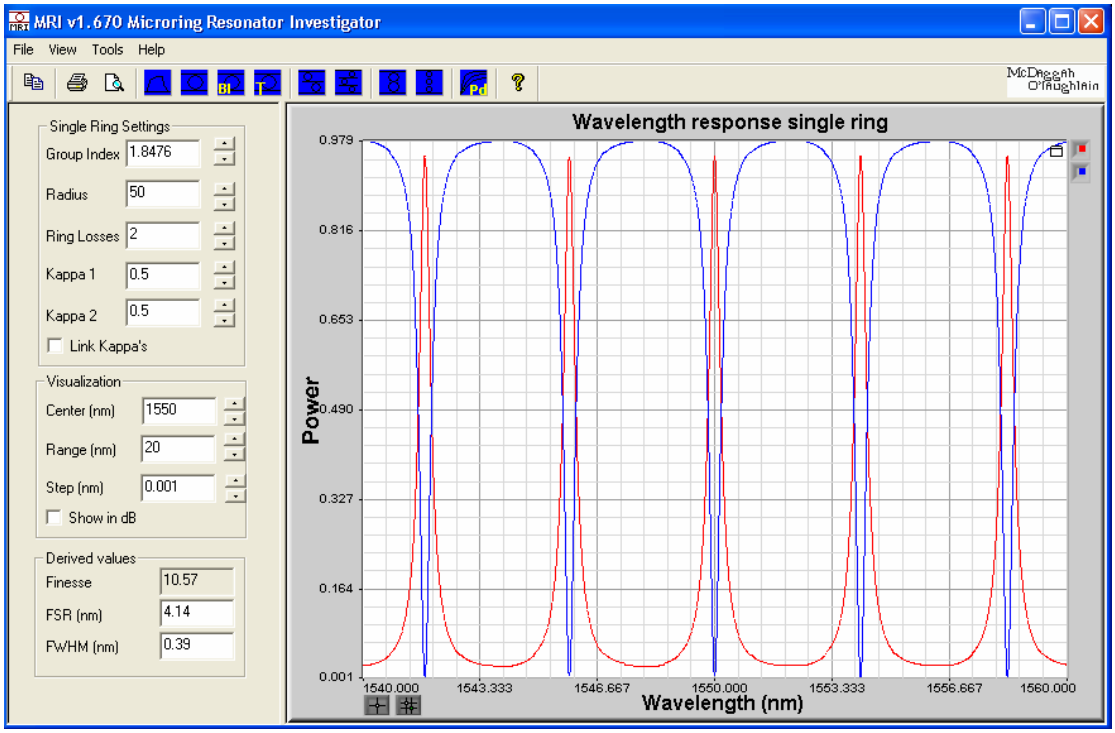

Figure 4.1. MRI Screenshot showing the simulation of a first order resonator.

4.2.1 Transient response

Although the calculation of the transient step response of a micro-resonator is a rather trivial exercise, it represents one of the most basic implementations of the algorithms used in the Aurora tool. The pseudo code of the transient response calculation algorithm is therefore given in Listing 4.1 to explain the origin of the calculation methods used in Aurora.

Listing 4.1. Pseudo code for calculating the transient drop response.

```
//Note: All port values are assumed to be complex and therefore contain both the amplitude
//and the phase
Set all ports to 0;
Set the "In" port to 1;
Calculate the delay time Td of one half of the resonator;

Set the current simulation time T to 0;
Set the maximum simulation time TMax to a suitable value;

    Loop
    {
        Calculate the values at the "Through" and "O1" ports from the "In" and "I1" ports
        using the coupler propagation matrix (eq. 2.8); //Coupler calculation

        Multiply the value at the "O1" port with the waveguide attenuation and the phase
        delay (eq. 2.9) to obtain the value at "I2"; //Waveguide calculation

        T=T+Td; //Time propagation caused by the waveguide

        Calculate the values at the "Drop" and "O2" ports from the "Add" and "I2" ports using
        the coupler propagation matrix; //Coupler calculation

        Save the current value at the "Drop" port for the current time (T);

        Multiply the value at the "O2" port with the waveguide attenuation and the phase
        delay to obtain the value at "I1"; //Waveguide calculation

        T=T+Td; //Time propagation caused by the waveguide
    } while T<TMax;

//The saved values of the "Drop" port can now be plotted against the saved time values T to
//give the transient response
```

The code implements an iterative process that in essence forwards signals between the individual parts, as discussed in Chapter 2.3, that make up the micro-resonator. The connections between these parts are defined as ports. These ports, in this example given the names shown Figure 4.2, hold the intermediate values of the calculations of each part of the micro-resonator.
It is important to note that the parts can be identified as either time propagating, such as the waveguides, or instantaneous, such as the couplers, for which the propagation time is 0. While this is not strictly correct since actual couplers always have a certain length and therefore an associated time delay this simplification generally holds unless very small resonators are used [51]. The simulation time is therefore only increased after the calculation of the waveguides. This concept is one of the

fundamental assumptions used in the creation of the Aurora program as will be explained further in Paragraph 4.5.

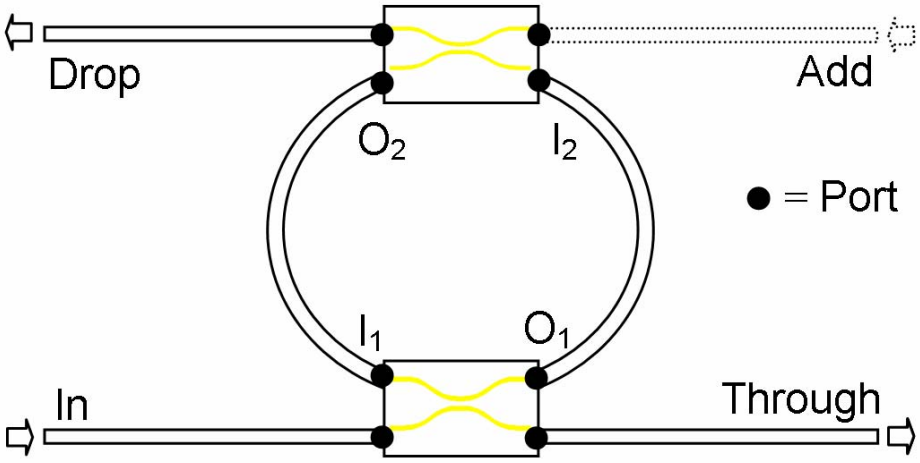

Figure 4.2. Resonator port definition.

The values of the drop port that have been saved at time T for each iteration can be combined to form a transient drop response as shown in Figure 4.3.

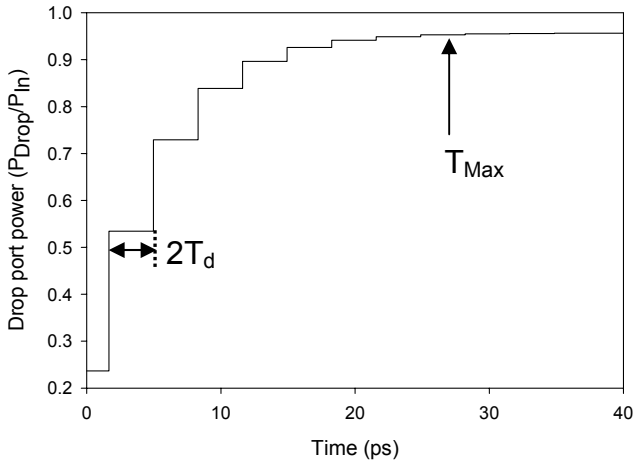

Figure 4.3. Transient drop response at full resonance.

As can be seen in this figure it is important that the time T_{Max} at which the iteration ends is chosen sufficiently high to allow the drop port signal to converge to its maximum value. Simulations in MRI have shown that a good value for T_{Max} is given by $T_{Max} \approx 10.\tau_d$ where τ_d is the cavity ring down-time given by [118, 119]:

$$\tau_d = \frac{F \cdot R \cdot n_g}{c} \tag{4.1}$$

This cavity ring down-time relates to the rate at which the power of the light within a cavity decreases when no further power is supplied to the resonator (i.e. the signal on the input port is changed from 1 to 0):

$$P_{Cav}(t) = P_{Cav,t=0} \cdot e^{-t/\tau_d} \tag{4.2}$$

Under the condition that the power of the light in the drop port has reached its maximum at $T=T_{Max}$ the final value of the transient response calculated at a wavelength λ_i will be equal to the wavelength response calculated at that wavelength:

$$\frac{P_{Drop}(t=T_{Max})\big|_{\lambda_i}}{P_{In}} \approx \frac{H}{1+F_C.\sin^2(\varphi_r/2)}\bigg|_{\lambda_i} \tag{4.3}$$

This makes it possible to combine a number of time domain responses, calculated for a range of wavelengths, into a single frequency domain response. This method is therefore used in the Aurora program.

4.2.2 Increasing the computational efficiency

The main goal of the MRI program was to allow a user to interact with the parameters that describe the micro-resonator in real-time. It was therefore important that, if possible, the equations should be optimized for performance to keep the time lag to a minimum. In this respect the equations that describe the through and drop response are especially important since these are not only used to display the responses in the MRI program but also in the brute force fitting methods employed by RFit.

The through and drop equations in their original for are written as:

$$\frac{P_{Drop}}{P_{In}} = \frac{k_1^2\kappa_2^2\chi_r}{1+\mu_1^2\mu_2^2\chi_r^2-2\mu_1\mu_2\chi_r\cdot\cos(\varphi)} \tag{4.4}$$

$$\frac{P_{Through}}{P_{In}} = \frac{\mu_1^2+\mu_2^2\chi_r^2-2\mu_1\mu_2\chi_r\cdot\cos(\varphi)}{1+\mu_1^2\mu_2^2\chi_r^2-2\mu_1\mu_2\chi_r\cdot\cos(\varphi)} \tag{4.5}$$

These equations are fairly computationally intensive due to the large number of multiplications involved. However, since $\cos(\varphi)$ is the only variable during a wavelength scan, it is also easy to express these equations as a combination of partial terms. These terms are:

$$F_1 = 2\mu_1\mu_2\chi_r \tag{4.6}$$

$$F_2 = 1+0.25F_1^2 \tag{4.7}$$

$$F_3 = \kappa_1^2(\mu_2^2\chi_r^2-1) \tag{4.8}$$

$$F_4 = \kappa_1^2\kappa_2^2\chi_r \tag{4.9}$$

$$F_5 = \frac{1}{F_2-F_1.\cos(\varphi)} \tag{4.10}$$

Using these terms the through and drop responses can now be written as:

$$\frac{P_{Through}}{P_{In}} = 1 + F_5.F_3 \tag{4.11}$$

$$\frac{P_{Drop}}{P_{In}} = F_5.F_4 \tag{4.12}$$

The partial terms F_1 to F_4 can be pre-calculated since they are not dependent on φ. The calculation of the through and drop response therefore only requires the recalculation of (4.10-4.12) which, assuming that φ is known, now only requires 1 cosine, 3 multiplications, 1 division, 1 subtraction and 1 addition.

4.3 RFit

The RFit tool, used for the parameter fitting of micro-resonator through and drop responses, was based on Equations (4.6-4.12). These allowed for a significant reduction (>10 times) of the fitting time compared Equations (4.4) and (4.5) because these equations are easily called several million times during the fitting process.
The fitting process uses a simple two-step brute force method that first fits the free spectral range and then the curve itself. When started the program requires a few approximate values to be set for α_{dB}, κ, n_g and R. The first three of these are not critical and are easily estimated by the user while the more critical value of the radius is almost always known from the design.
The free spectral range fit calculates the sum

$$\Sigma_{\lambda_m}\left[P_{Sim}(n_g, \Delta\lambda, \lambda_m) - P_{Meas}(\lambda_m)\right]^2 \tag{4.13}$$

for variations in the group index n_g and the response shift $\Delta\lambda$ within a range that has been defined by the program user. The latter variable is only used as a helper variable to shift the simulated response with respect to the measured response so that they are aligned correctly (i.e. resonances at the same wavelengths). It is added to the phase calculation of the simulated response using:

$$\varphi_r = \frac{(2.\pi)^2}{\lambda_m + \Delta\lambda} \cdot R \cdot n_g \tag{4.14}$$

The sum is only calculated for the wavelengths λ_m for which measurement data is available. The best fit is found for those values of n_g and $\Delta\lambda$ at which (4.15) is at its minimum.
The next step in the fitting process is then to scan the variables κ_1, κ_2 and α_{dB} across a user defined range and find the values for which the sum

$$\Sigma_{\lambda_m}\left[10\log(P_{Sim}(\kappa_1, \kappa_2, \alpha_{dB}, \lambda_m)) - 10\log(P_{Meas}(\lambda_m))\right]^2 \tag{4.15}$$

is at its minimum. A possible outcome of such a fitting process is given in Figure 4.4.

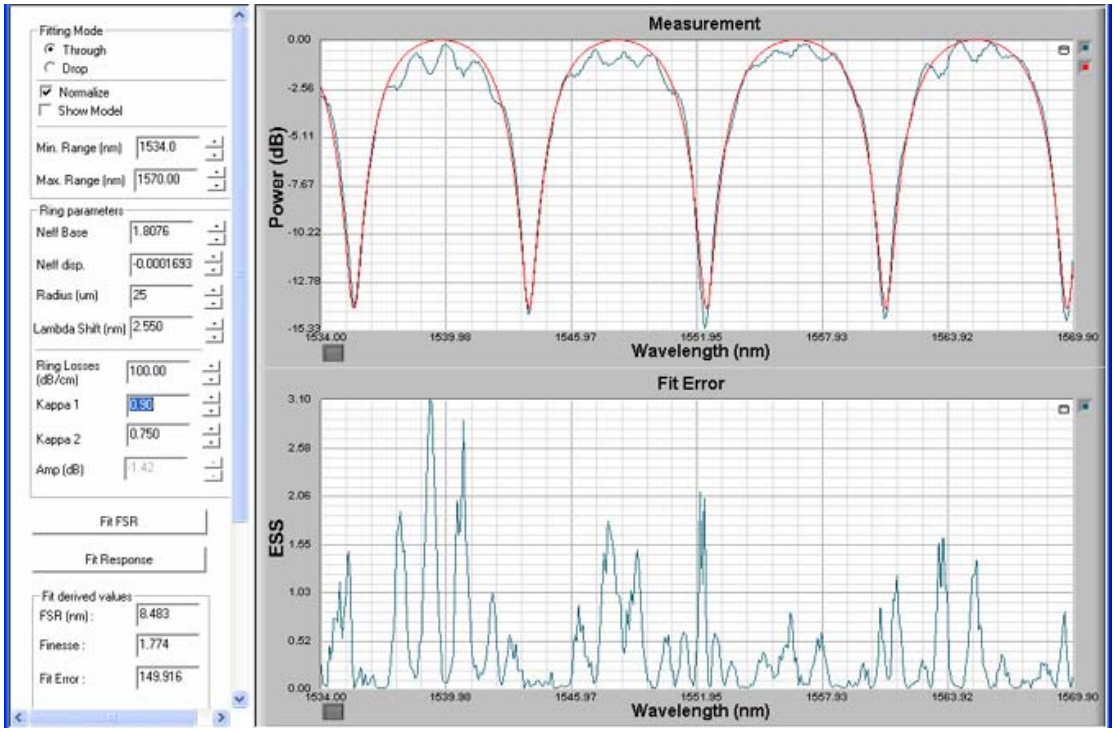

Figure 4.4. Screenshot of RFit showing a fit to a through response.

The upper graph in this screenshot of the RFit program shows a measured through response and the best fit that could be made to this response. The bottom graph gives the fit error (in dB):

$$ESS = \left[10\log(P_{Sim}(\kappa_1, \kappa_2, \alpha_{dB}, \lambda_m)) - 10\log(P_{Meas}(\lambda_m))\right]^2 \qquad (4.16)$$

made at each data point (wavelength λ_m) in the measurement data. It is important to note that the fit error is calculated using the logarithmic values of the simulated and measured responses. This ensures that a fit error in for instance the dip of a through response is given equal weight as an error elsewhere in the response and results in a better fit. In the given screenshot for instance, a Fabry-Perot like ripple, caused by reflections within the device, is seen in the measurement data. On a linear scale this ripple has a (normalized) amplitude of nearly 0.3 which is large in comparison with the amplitude of ≈0.95 of the actual through response. This makes a good fit difficult to achieve because the relatively large contribution of the ripple to the overall shape of the spectrum. On a logarithmic scale, however, the ripple of ≈1.5 dB is quite small when compared to the more than 15 dB dip of the through response which makes it possible, as the figure shows, to get a good fit.

In a measured signal that is not normalized it is impossible to separate the contribution of the insertion (IL_{Drop}) and waveguide losses in the overall shape of the response. However, for an accurate fit it is important to know the insertion losses, especially for resonators with high losses due to their inherently higher IL_{Drop}. The solution is then to normalize both the measured as well as the fitted response in order to remove the dependence in IL_{Drop} altogether. This option is therefore also provided by the RFit program and, as can be seen in the upper graph of Figure 4.4, was actually used in the given fit example.

4.4 DropZone

The brute force fitting process used by the RFit program can have some problems with very noisy measurements. While it is possible to filter some of this noise out of the measurement, for instance using a Fast Fourier-Inverse Fast Fourier transform (FFT-IFFT) based low-pass filter, this might also remove some important information from the measurement. The program is therefore best used interactively by combining computerized fitting with user experience to find the best possible fit.
For an experienced user, however, it is often relatively easy to estimate the depth of both the trough and drop responses, even if these signals are subject to a lot of noise. This is of importance since, for symmetric devices, the field coupling coefficients and resonator losses can be found analytically using only these depths as the input, thereby providing a very fast alternative fitting method. It is this method that was implemented in the DropZone tool. The user interface of this tool, shown in Figure 4.4 allows a user to determine the field coupling coefficients and waveguide losses from the through and drop responses or, if the drop response is not available, to at least estimate the waveguide losses.

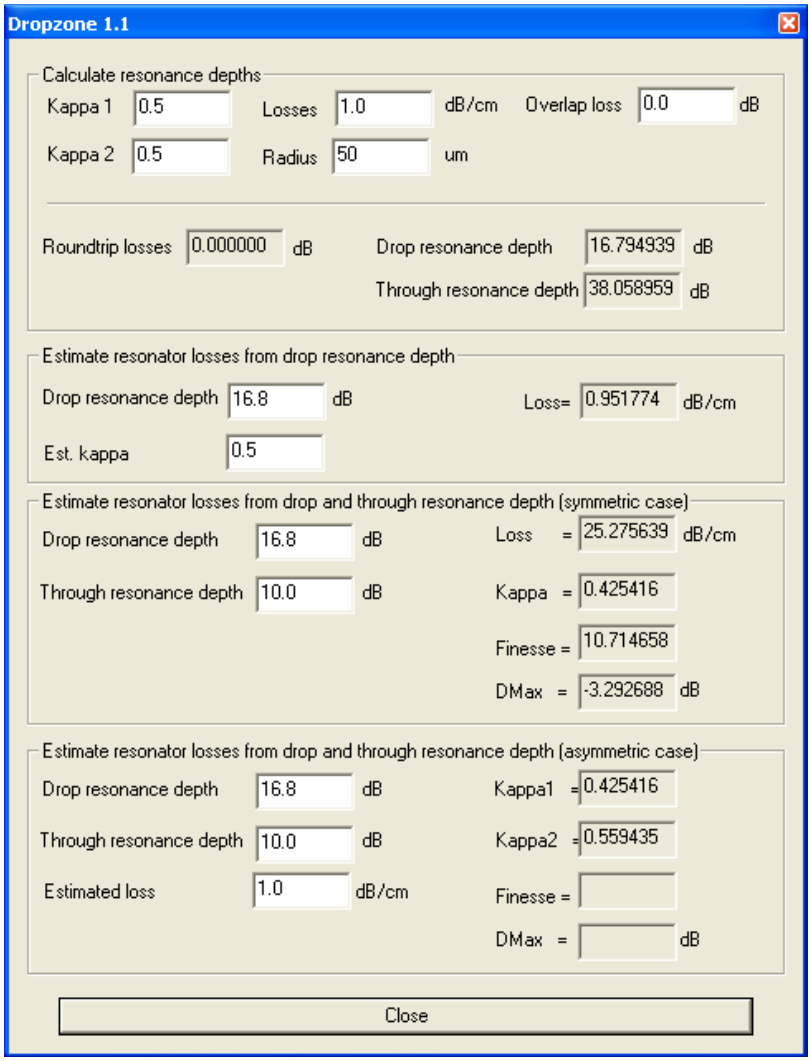

Figure 4.5. Dropzone user interface.

The equations required to find the values of α_{dB} and κ can be found by using the expressions that give the depth of the through and drop responses as a starting point. The depth of the drop response $\Delta OnOff_{Drop}$ (in dB) is equal to the resonator rejection ratio and was earlier defined in Chapter 3.2.2 as:

$$S_{RR} = \Delta OnOff_{Drop} = 10 \cdot \log\left(\frac{(1+\mu_1\mu_2\chi_r)^2}{(1-\mu_1\mu_2\chi_r)^2}\right) \tag{4.17}$$

This can be rewritten into:

$$\mu_1\mu_2\chi_r = \frac{\sqrt{M_{Drop}}-1}{\sqrt{M_{Drop}}+1} \tag{4.18}$$

where the drop response depth ratio M_{Drop} is given as:

$$M_{Drop} = 10^{\frac{\Delta OnOff_{Drop}}{10}} \tag{4.19}$$

The depth of the through response $\Delta OnOff_{Through}$ (in dB) can be found by combining Equations (3.6) and (3.7) into Equation 4.20:

$$\Delta OnOff_{Through} = 10 \cdot \log\left(\frac{P_{Off\,Res}}{P_{On\,Res}}\right) = 10 \cdot \log\left(\frac{\frac{(\mu_1+\mu_2\chi_r)^2}{(1+\mu_1\mu_2\chi_r)^2}}{\frac{(\mu_1-\mu_2\chi_r)^2}{(1-\mu_1\mu_2\chi_r)^2}}\right) \Leftrightarrow$$

$$\Delta OnOff_{Through} = 10 \cdot \log\left(\frac{(\mu_1+\mu_2\chi_r)^2}{(1+\mu_1\mu_2\chi_r)^2} \cdot \frac{(1-\mu_1\mu_2\chi_r)^2}{(\mu_1-\mu_2\chi_r{}^2)}\right) \tag{4.20}$$

Taking the square root of (4.20) and substitution with (4.18) then leads to:

$$\sqrt{M_{Through} \cdot M_{Drop}} = \frac{(\mu_1+\mu_2\chi_r)}{(\mu_1-\mu_2\chi_r)} \tag{4.21}$$

where the through response depth ratio $M_{Through}$ is given as:

$$M_{Through} = 10^{\frac{\Delta OnOff_{Through}}{10}} \tag{4.22}$$

By rearranging (4.21) the coupling coefficients and resonator roundtrip losses can be written as a function of the through and drop response resonance ratios:

$$\frac{\mu_2}{\mu_1}\chi_r = \frac{\sqrt{M_{Through} \cdot M_{Drop}}-1}{\sqrt{M_{Through} \cdot M_{Drop}}+1} \tag{4.23}$$

For symmetrically coupled ($\kappa_1 = \kappa_2$) resonators this reduces to:

$$\chi_r = \frac{\sqrt{M_{Through} \cdot M_{Drop}} - 1}{\sqrt{M_{Through} \cdot M_{Drop}} + 1} \tag{4.24}$$

which can be combined with Equation (4.18) to find the desired parameters.
For an asymmetrically coupled resonator, however, only κ_1 can be found directly and is given by:

$$\kappa_1 = 1 - \frac{(\sqrt{M_{Drop}} - 1)}{(\sqrt{M_{Drop}} + 1)} \frac{(\sqrt{M_{Through} \cdot M_{Drop}} + 1)}{(\sqrt{M_{Through} \cdot M_{Drop}} - 1)} \tag{4.25}$$

The other coupling coefficient, κ_2, can only be found if the losses are already known. This coupling coefficient can then be determined using:

$$\kappa_2 = 1 - \chi_r \frac{(\sqrt{M_{Drop}} - 1)}{(\sqrt{M_{Drop}} + 1)} \frac{(\sqrt{M_{Through} \cdot M_{Drop}} - 1)}{(\sqrt{M_{Through} \cdot M_{Drop}} + 1)} \tag{4.26}$$

In some devices accurate determination of the depth of the drop response might not be possible. Part of the measured drop response can for instance be below the detection limit of the measurement equipment or be overshadowed by stray light within the device. A measured response similar to the simulated drop response 4.6 may then for instance be found.

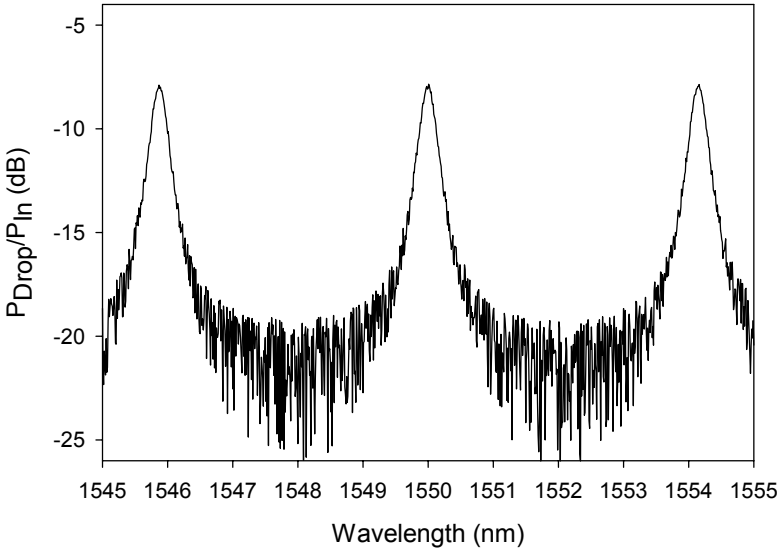

Figure 4.6. A simulated drop response to which random noise has been added, making it impossible to determine the depth of the drop response.

This is especially true if the devices incorporate micro-resonators that have high losses and relatively low coupling coefficients as this results in a large drop port insertion loss (IL_{Drop}) combined with a large filter rejection ratio (S_{RR}). In such cases, however, it is often still possible to determine the losses and coupling coefficients

using an approach based on the values of the FSR and the $\Delta\lambda_{FWHM}$, which is only slightly more difficult than the one used above. This is done by rewriting (2.31) into:

$$S_{RR} = 10.\log\left(\frac{2.FSR}{\pi\Delta\lambda_{FWHM}}\right)^2 + 1 \tag{4.27}$$

Substituting this Equation into (2.29) then gives:

$$\mu_1\mu_2.\chi_r = \frac{\sqrt{\left(\frac{2.FSR}{\pi\Delta\lambda_{FWHM}}\right)^2 + 1} - 1}{\sqrt{\left(\frac{2.FSR}{\pi\Delta\lambda_{FWHM}}\right)^2 + 1} + 1} \tag{4.28}$$

which is a drop in replacement for Equation (4.18). Combining this expression with (4.19) and (4.23) then leads to the desired values of the losses and the coupling coefficients.

4.5 Aurora

The Aurora program was developed over the course of several years. Initially it was created as a proof of principle of the underlying numerical simulation method. It soon became clear, however, that the method could also be used to quickly create and simulate complex optical circuits. It therefore proved a solution for problems related to the increasing complexity of new devices as these could no longer be implemented in the MRI tool.
While the equations that describe simple optical components such as the switch which is discussed in Chapter 6 could easily be formulated (see Chapter 2.6 for instance) and programmed into the MRI program the time required to do the same for more complex devices became a real problem. In a simple router as shown in Figure 4.7 and further described in Chapter 7, for instance up to eleven resonators may influence the signals passing through an individual resonator. If all signals are assumed to travel in only one direction it is still possible to find a practical analytical description of this device. However, if bi-directional propagation through the waveguides is required, for instance to include back reflected light, the interactions between the resonators also need to be considered. The very high order filter interactions that result from this then make it impossible to find a practical analytical solution.

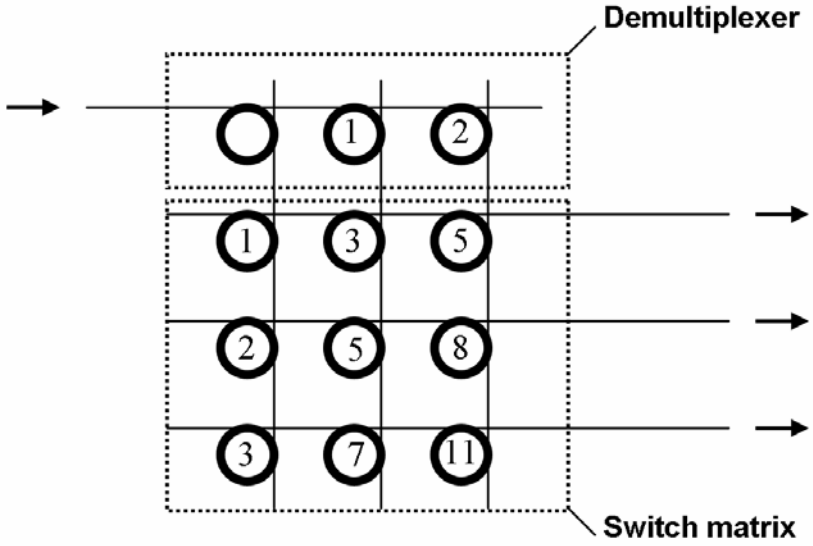

Figure 4.7. Resonator interaction in a 1x3x3 optical router. The numbers show the number of other MRs that affect the signals entering a certain MR.

The numerical method by the Aurora program, however, is relatively unaffected by such interactions as it can calculate each optical component individually based on well defined optical input signals. The “glue” between the components that takes the place of the higher order filter equations that would otherwise be required is instead provided by a time based scheduler that forwards optical signals in a parallel fashion between the components.

4.5.1 Architecture

The Aurora program, like the programs discussed in the previous paragraphs, was created using Microsoft Visual C++ [120]. The program was intentionally designed to be modular; relying heavily on object oriented programming to achieve this goal.
This is also reflected in the simplified architecture of the program, shown in Figure 4.8. All tasks of a certain nature, such as component management or simulation regulation have been assigned to a specific manager module. These modules interact with the program user and, based on user input, regulate the internal flow of data or invoke other modules to perform specific operations on this data.

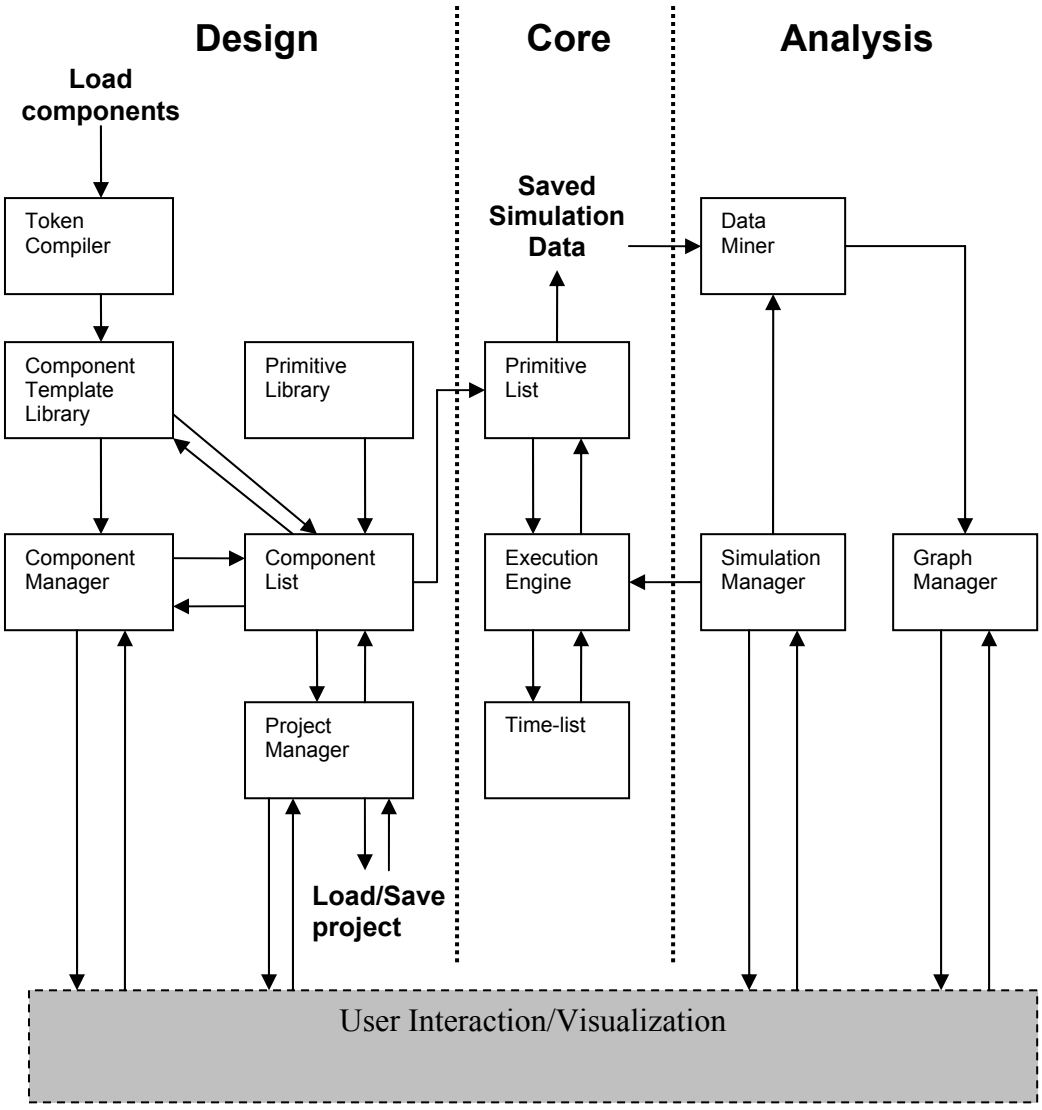

Figure 4.8. Aurora architecture.

On a super-modular level the program has been divided into three distinct parts that can be identified as design, core and analysis. Between these parts the interaction was intentionally kept to a minimum. Although this also provides a clear benefit to program maintainability the main reason for doing so lies in the nature of scientific simulation software. Typically such software is based on a comparatively small but highly complex algorithm or set of equations. These calculation algorithms are

generally required to be as fast a possible and should therefore be devoid of anything not related to the calculations. This is especially true for the user interface that is often required to change data that can be understood by the user into data that is easy to process by the algorithms. While the user interface and the simulation algorithms are sometimes intentionally placed in separate programs it is common practice to integrate these together in a single program. In addition to this a data visualization backend is often included to provide a user easy access to the output data of the algorithms.
The three parts of the Aurora program also reflect this strong separation of tasks:

- The design section serves as the main user interface. It allows the user to create a complex optical circuit out of "components". At the most basic level these components can represent single waveguides or couplers but higher level components, comprised of several other components are also possible.
  The components are essentially no more than localized user interfaces that are dynamically created from a template and added to an internal list when the user creates the component. They provide both the visualization of a component (e.g. show a circle for a resonator) as well as easy access, through the use of variables, to the actual mathematical representation of these components. This representation resides externally of these components in so called "primitives" that will be discussed in detail in Paragraph 4.5.2. In addition, a component takes care of the linkage between these primitives if the user connects one or more components. Although the primitives are created and maintained by the components they are separate entities that belong to and are part of the actual simulation algorithms.
- The core section of Aurora, which currently makes up less than 1% of the overall code, contains all the algorithms and management routines required to perform a time domain simulation. The core was designed to operate as a separate entity that takes the primitives created by the user interface and, after simulating the optical circuit represented by these, saves all relevant data to disk.
- The analysis section has a dual task. It serves both as a simulation manager, setting up the simulation core for a certain type of simulation, as well as a data-miner that extracts useful information from the output of a simulation and displays it to the user. Although it might seem cumbersome to put the simulation setup in the analysis section rather than combining it directly with the simulation core there is in fact a very good reason for doing so based on computational performance.
  The simulation algorithms that are used by the core are fundamentally time-domain based. It is therefore only possible to find the frequency response of an optical circuit by combining the results of several of these simulations. However, because the individual time-domain simulations have no interdependencies, it is possible to calculate all these simulations in parallel on different threads, processors or even computers which makes the calculation method used by Aurora extremely fast. In light of this distributed calculation it makes more sense to place the management of the simulation outside of the core. Based on the simulation settings by the user the simulation manager can then create a number of cores in different threads (on the same or other computers) that each simulate a small number of wavelengths and combine their outputs into a single result.

4.5.2 Simulation method

As was already shown in Chapters 2.3 a complex optical device such a micro-resonator can be reduced into a combination of basic optical constructs such as waveguides and couplers that are calculated individually. As long as the results of the individual calculations are properly forwarded between the constructs their combined behavior will be identical to that of the original component as was shown in Paragraph 4.2.1.
It is this observation that forms the fundamental principle behind the simulation method used by Aurora. Because many calculations are combined to simulate a component the simulation method is quite different from a simulation method in the traditional sense. Usually a simulation method refers to the type of algorithm that is used to perform the simulation (e.g. BPM, FDTD or Transfer Matrix). However, the simulation method of Aurora does not use any specific algorithm but leaves it up to the individual optical constructs to provide their own simulation algorithms. The simulation method can therefore be classified as a meta-algorithm that creates a framework in which many different simulation algorithms can be properly combined rather than providing a simulation algorithm itself. It is then these algorithms that together act as a single (but distributed) algorithm that can be used to simulate the component.

4.5.2.1 Primitives

In the simulation of the transient drop response all the basic optical constructs were still combined into a single algorithm for which the step time was fixed and pre-calculated. As mentioned in the above, however, Aurora treats these constructs as separate entities that forward the results of their internal calculations between one another.
The entities that are used to represent the basic optical constructs, such as waveguides or couplers, within Aurora are the so-called “primitives”. These primitives have a dual function:

1. The primitives are used to represent constructs, the links between them as well as their characteristics (coupling length, attenuation etc.). They are therefore comparable to data in that they completely describe a certain component.
2. The primitives are used to encapsulate the calculations (equations) that describe the operation of the constructs that they represent. This makes that they are also an integral part of the simulation algorithm with which the component is simulated.

Because the simulation method used by Aurora is based on the individual calculation of the optical constructs, and therefore of the primitives, there is a very large flexibility in the nature of these calculations. This gives it a large advantage over other simulation methods. A simulation method based on transfer matrices for instance would require that all individual constructs are defined using these matrices as they are all combined into a single large matrix that describes the entire optical component. The calculations encapsulated by the primitives, however, may contain any type of calculation (BPM, Transfer matrix etc.) as long as the in and output of these calculations consist of a complex number (representing the light that enters and exits the optical construct). It is therefore possible to optimize the individual

calculations in the best possible way instead of being forced to use a single (such as the mentioned transfer matrix method) approach that might be sub-optimal in some cases.

Because the primitive has to be combined with many other primitives and operate as part of the simulation algorithm there are certain requirements placed on its implementation:

- Each primitive has one or more nodes. These nodes maintain the connections between the primitives. The primitives are only aware of these connections, not of the type of the primitives they connect to. On the input side the nodes store the complex data (phase amplitude) forwarded from the primitives that these nodes are connected to. On the output side the nodes point out the nodes of the connected primitive where the results of the calculations are to be stored.
- Each node is input sensitive. A calculation routine may (should) be attached to each input node. When data is placed on this node the correct calculation routine is called. This ensures bi-directional propagation of the signals in the system when implemented correctly.
- There is a single calculation function that is called after a signal has been placed on a node. Any kind of implementation of the calculation function is allowed as long as there is a calculation method for all ports. As the input for the calculation the complex data present on all nodes may be used as well as the contents of several variables that have been set through the user interface provided by the components.
- If other primitives are connected to the outputs of a primitive the results of the internal calculations have to be forwarded to these primitives.
- Each primitive provides an initialization function that is called at the start of a simulation by the scheduler. While these functions can be used for the pre-calculation of internal variables they are mainly intended as a starting point for signals in a simulation as will be explained in the next paragraph.

The method used to forward the calculation results between the primitives depends entirely on the type of construct that the primitive represents. As was already mentioned in Paragraph 4.2.1 optical constructs can be classified as being either instantaneous or time propagating. The results of instantaneous constructs can be forwarded immediately while the results of time propagating constructs can only be forwarded after a certain time delay.

If the primitive represents an instantaneous optical construct as shown in Figure 4.9 then a calculation is performed for each signal change on one of the inputs I_i. The results of this calculation are placed directly into the nodes of the connected primitives after which their calculation functions are executed.

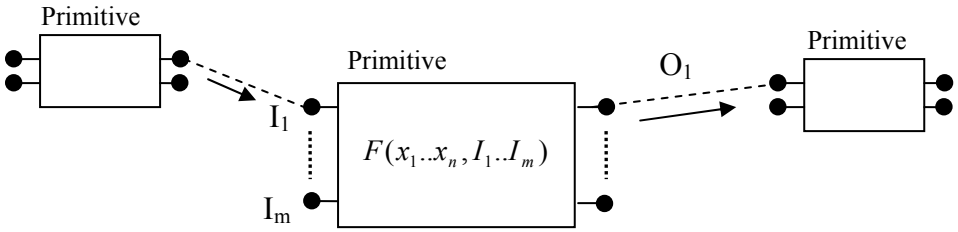

Figure 4.9. A Primitive with instantaneous result forwarding.

A pseudo code implementation of a coupler with a port configuration as shown in Figure 4.10 is given in Listing 4.2. The coupler is typically an instantaneous optical construct as was pointed out in Chapter 4.2.1. This is reflected by the code where, after the actual calculation, the calculation functions of the connected primitives are called directly. Although only one direction of the signal forwarding is shown in Figure 4.9 the data between the primitives is actually allowed to be forwarded in any direction as dictated by the implementation rules. In Listing 4.2 this bi-directionality is implemented using two separate calculations where one is called for data entering port 1 or 2 and the other for data entering port 3 or 4.

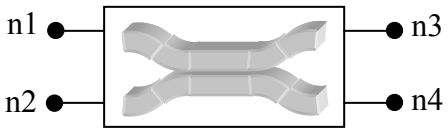

Figure 4.10. A coupler primitive and its nodes.

Listing 4.2. Pseudo code for the calculation function of coupler primitive. (instantaneous primitive)

```
Calculate()
{
        If a new value has been placed on ports 1 or 2
        {
                Calculate the values at ports 3 and 4 the  using the coupler
                propagation matrix (eq. 2.8);

                Find the ports that are connected to ports 3 and 4 and place the values
                calculated for port 3 and 4 in these ports;

                Call the Calculation() function of the primitives that are the parent of these ports
        }

        If a new value has been placed on ports 3 or 4
        {
                ……
        }
}
```

If the primitive represents a time propagating construct then a time delay has to be taken into account between the instant that a signal enters one of the inputs I_i and the moment when the results of the calculation can be forwarded to the next primitive. Instead of calling the calculation function of the next primitive directly this call is therefore redirected through a scheduler as shown in Figure 4.11. This scheduler will then ensure that at the correct time the result data belonging to output O_1 is placed on the port connected to this output. After this the process is finalized by once again calling the calculation function of the parent of this port.

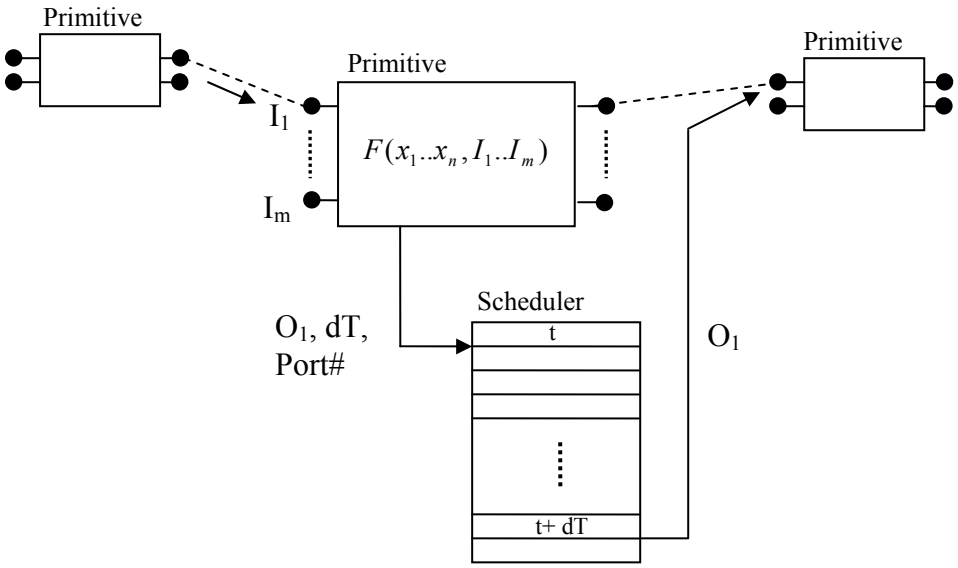

Figure 4.11. A Primitive with delayed (through the scheduler) result forwarding.

The pseudo code implementation of a waveguide, being a typical example of a time propagating element, is given in Listing 4.3. The time propagating section of the calculation is code written out in bold and is largely dedicated to gathering all the data required to build a "call" for the scheduler. As was the case for the coupler the waveguide also uses a split calculation for each direction of the signal through the waveguide (entering n1 or n2).

Listing 4.3. Pseudo code for the calculation function of waveguide primitive. (time propagating primitive)

```
Calculate()
{
        If a new value has been placed on port 1
        {
                Multiply the value at port 1 with the waveguide attenuation and the phase delay
                (eq. 2.9) to obtain the value 'V2' at port 2;

                Calculate the time delay dT of the signal within the waveguide;

                Find the port 'C2' that is connected to port 2;
                Find the primitive 'P2' that is the parent of this port;

                Tell the scheduler to put the value V2 into port C2 after expiration time
                delay dT; //The scheduler will call Calculate() of primitive P2
        }

        If a new value has been placed on port 2
        {
                ……
        }
}
```

4.5.2.2 The execution engine

Although the primitives perform all the important calculations the scheduler is critical to the flow of these calculations. The scheduler performs only three simple but very important tasks:

- **The initialization of the dataflow**.
  One of the main strengths of the simulation method used by Aurora is that it only reacts to changes within the optical system that is being simulated. Each primitive can only call (directly or through the scheduler) the calculation functions of the primitives that are connected to it. A change in a signal on one of the ports of a primitive (followed by calling the calculate() function of that primitive) will therefore only ever affect the signals going through all the primitives that are directly or indirectly connected to this primitive. This makes the method highly efficient at simulating large components or even large optical networks where there may be many subsections that are not connected in any way.
  Because the simulation is change driven this also implies that a simulation can only start after an initial signal change is made on one of the nodes in the optical system that is being simulated. At the start of a simulation the execution engine therefore gives an initial change to designated nodes to initialize the flow of data.
- **Callback storage and execution.**
  When the simulation is running the execution engine accepts the calls of all timed primitives and stores these calls in order in a list as shown in Figure 4.12. In this list all the calls are sorted by time. When the simulation time has progressed to a time that is equal to the call-time of these calls the engine

executes all the calls of equal time simultaneously and calls the calculation functions of the proper primitives.

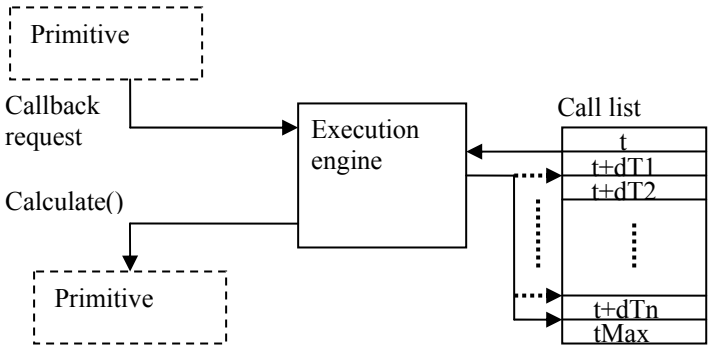

Figure 4.12. Diagram of the dataflow within the scheduler. A primitive asks the execution engine to place call in the call list. After a certain time has elapsed (equivalent to the propagation time of the light through the primitive) the execution engine places this call in the next primitive and calls its calculate() function.

- **Timekeeping.**
  The primitives intentionally do not store the current time data but only notify the execution engine of the delay in the signal they cause. It is therefore up to the execution engine to calculate the actual execution time of the call from this delay. In addition to this task the current time is also continuously checked against a maximum execution time at which the simulation needs to end. For the same reason that the simulation requires an initial change to start the simulation process it is also, under certain circumstances, unable to stop by itself. Since each primitive calls (directly or indirectly) the calculation function of a primitive it is connected to, feedback loops can be created for certain components such as the micro-resonator in which initial signal changes can be forwarded infinitely. This is in a way an integral part of the simulation method as it allows the simulation of optical components that contain many feedback loops. As was mentioned in Chapter 4.2.1, however, the output values of a resonant system are usually stable after a certain time T_{Max}. The execution engine therefore allows the simulation to end at that time (this has to be determined by the user).

In Listing 4.4 a highly simplified version of the execution engine is given in pseudo code. The algorithms shown in this code consists of two functions. The first, AddCall() is used by the primitives to place a call into the call list. The second, Simulate() is the actual simulation algorithm.
When a simulation is started all the primitives are first initialized. This initialization is important as the flow of signals within the simulation originates here through the use of source primitives. These primitives do not operate differently from the other primitives except that they already create a call (with time delay zero) in the call list when their initialization functions are executed. As can be seen in the core loop of the algorithm these first calls are crucial as the simulation would simply end without them.

Listing 4.4. Pseudo code implementation of the execution engine.

```
AddCall(dT, V, C)
{
        Create the call with value V and port target C to the call list at time T_Curr+dT;
}


Simulate()
{
        Set the current time T_Curr to 0;
        Initialize all the primitives;
        Find the first call in the call list;
        T_Curr is now equal to the time in this call;

        loop //Simulation loop
        {
            Execute all the calls that have time T_Curr by
                First placing the forwarded signal values V in these calls on their
                target nodes C;
                Then calling the Calculate() functions of the parent primitives of these nodes;
            Find the first call that has a time> T_Curr in the call list;
            T_Curr is now equal to the time in this call;
        } until T_Curr>T_Max or until there are no more calls;
}
```

With these first calls, however, the core loop of the algorithm becomes self sustaining: If the algorithm executes the calculate functions of the primitives that these first calls refer to, these in turn will either generate one or more new calls themselves or, if they are instantaneous, call another primitives that do so. When the core loop has finished executing all the calls placed at T_{Curr}=0 it can then simply continue with the newly created calls that are next on the time line. These calls in turn will then generate their own new calls and so forth and so on.
Once the core loop has started itself there are only two ways in which the simulation can be ended. In optical circuits that have no feedback loops, like the fictitious circuit shown in Figure 4.13, the signals and calls will simply propagate from the point where the change in signal originated (the wave source) to where they can propagate no further (the right coupler in this example). After these last calls have been executed the call list will be empty and the core loop will terminate by itself.

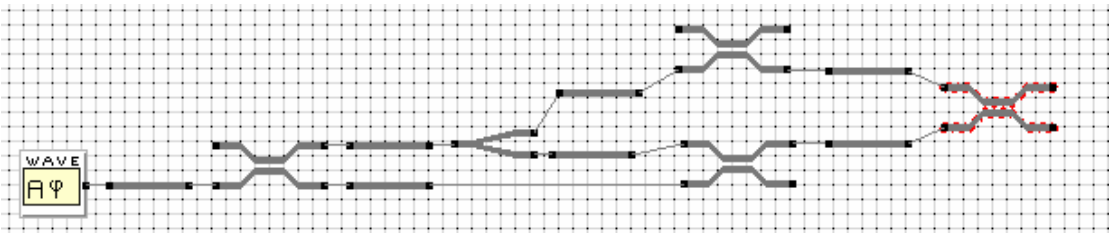

Figure 4.13. Self terminating optical circuit. (*Image created from an Aurora screenshot*). Unused ports in the simulation do not participate in the simulation.

In circuits with feedback loops, however, like the one shown in Figure 4.14 new calls are continuously generated, allowing the inner loop to continue forever. In such cases

the simulation is therefore forced to end at a predefined maximum simulation time T_{Max} as has already been explained in the preceding text.

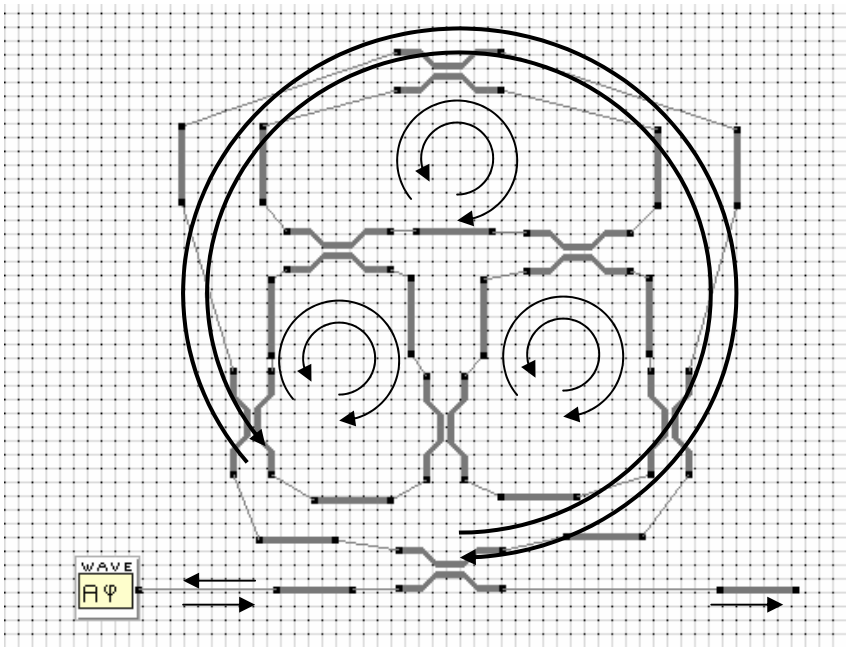

Figure 4.14. Self perpetuating optical circuit with many feedback loops.
(the arrows show the internal propagation directions of the light)

4.5.3 Validation of the simulation method

In order to test the stability and correctness of the numerical solutions given by Aurora some optical devices for which the analytical solutions were available (in MRI) have been compared with their Aurora counterparts. These comparisons were so far only performed in the frequency domain as the time-domain visualization functions of Aurora were not yet fully stable (i.e. the program crashed) at the time of this writing. Also, whereas the frequency spectra could be compared with the analytically calculated responses of MRI, no such comparison could be made for the transient response.
Four components, each allowing the testing of a different aspect of the simulation method, have been used to test the correctness of the method. These were:

- A Mach-Zehnder Interferometer to test an optical circuit without a feedback loop.
- A single micro-resonator to test a circuit with a single feedback loop.
- A second order micro-resonator to test a circuit with multiple feedback loops. The simulation of a second order filter differs significantly from a first order filter in that it can generate a large number of calls that need to be executed simultaneously without creating errors.
- A reflector based on a single micro-resonator to test the bi-directional propagation of signals.

The MZI test.
The MZI was created as shown in the Aurora screenshot in Figure 4.15 The upper waveguide branch has a length of 400 μm while the lower has a length of 100 μm. Both waveguides have an effective refractive index of 1.5. Figure 4.16 shows the

simulated output spectra calculated for the lower and upper branch of this device. This simulation, which calculated the response across 20 nm at 0.01 nm intervals, took only 0.093s (timed using the internal clock on an Athlon 64, 3000+ based system).

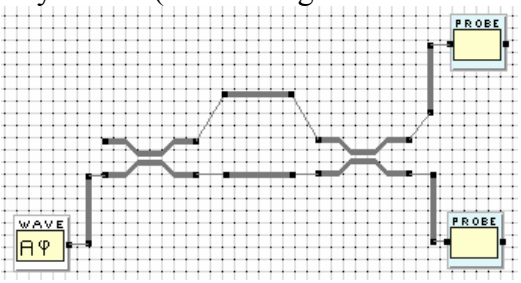

Figure 4.15. MZI circuit.

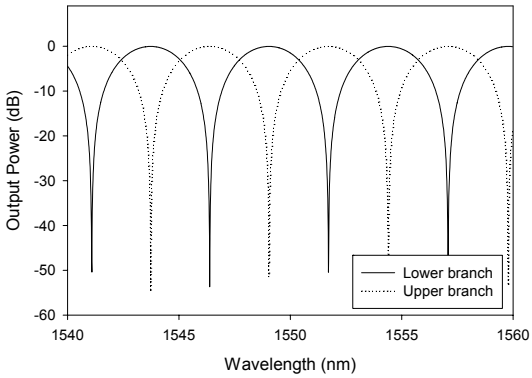

Figure 4.16. MZI simulation results.

Although these results have not been compared with an analytical solution the shape of the responses conforms to that of an MZI and its free spectral range of 5.33 nm is equal to that given by theory:

$$FSR = \frac{\lambda^2}{\Delta L \cdot Neff} \tag{4.29}$$

The Single micro-resonator test.

The correct simulation of a circuit with a single feedback loop was tested using the optical circuit shown in Figure 4.17. This circuit is equivalent to a resonator with a radius of 50 µm, κ_1=κ_2=0.55 and α_{dB}=1 dB/cm. Figure 4.18 compares the drop response of this circuit, simulated across 2000 wavelength points in 0.12s, with the analytical response calculated using MRI. As can be seen the two responses are identical. A comparison of the raw simulation data showed a mean error ≈0.02 dB, with a standard deviation σ = 0.057, between the two simulations. This difference is partly due to the numerical method used by Aurora which can accumulate errors made in individual calculations. The major part of the difference is, however, due to the fact that the two simulation results are not perfectly wavelength-aligned. The analytical results are shifted by about -0.02 nm with respect to the Aurora results.

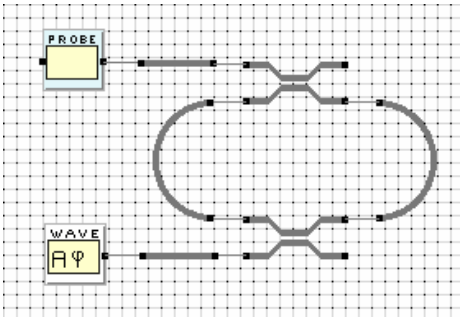

Figure 4.17. Single micro-resonator circuit.

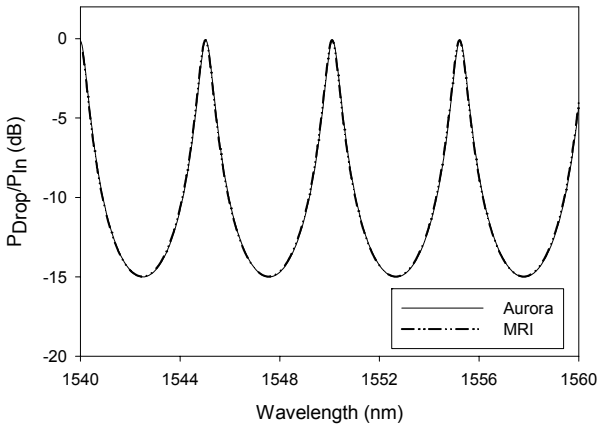

Figure 4.18. Comparison of the single MR drop responses produced by MRI (analytical) and Aurora.

The Second order micro-resonator test.
The MZI and single resonator simulations can be seen as validations of the equations used to calculate the individual optical constructs. However, the second order micro-resonator is also a test of the ability of the scheduler to correctly handle multiple signals that enter a single construct. In the second order resonator circuit shown in Figure 4.19 for instance two calls (signifying a change in the signal) may arrive at the middle coupler at the same time. The interaction between the light resonating in the upper ring with that which resonates in the lower ring is crucial to the operation of the filter as a whole. Therefore any error or incorrect handling of these two calls, that in effect link the signals (light) between the two resonators, will immediately have an effect in the simulated response.
Figure 4.20 shows, however, that this situation is well handled. The response of the second order MR, with R_1=R_2=50 µm, κ_1=κ_3=0.5, κ_2=0.143 and α_{dB}=1 dB/cm simulated by Aurora is nearly identical to the response returned by the analytical simulation in MRI. The mean difference (error) between the two simulations was a mere 0.024 dB with a standard deviation σ = 0.044.

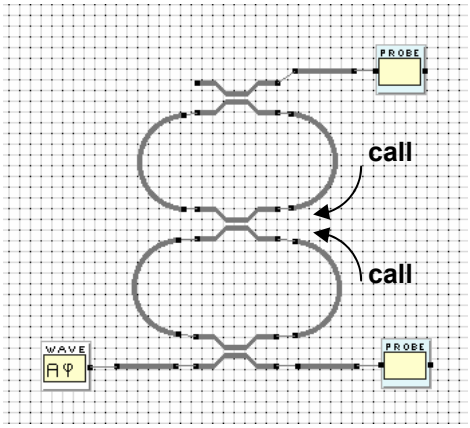

Figure 4.19. The second order MR circuit.

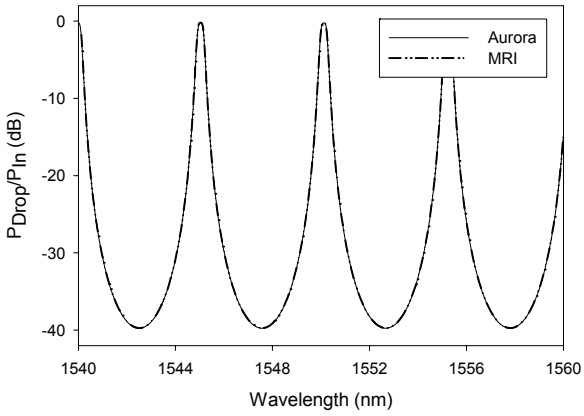

Figure 4.20. Comparison of the 2nd order MR drop responses produced by MRI (analytical) and Aurora.

The Reflector test.
The reflector is a single micro-resonator based device in which an input signal is divided by a y-splitter and coupled into the resonator in opposing directions as shown in Figure 4.21. If the bi-directional propagation is not handled correctly by the Aurora simulation then the reflected calls (optical signals) might not, or not at the same time, appear at the right side of the splitter. This would instantly show up in the response measured at the left side of the splitter by the probe.
A proper frequency response of the light that is reflected by this device is identical to the drop response of a single MR. The correctness of the bi-directional simulation can therefore be assessed by comparing the response of the reflected light, as simulated by Aurora, with the analytical single MR drop response given by MRI. If, for instance, there is an error in the bi-directional propagation these responses would not be the same. The results of this comparison, for a resonator with a radius of 50 µm, κ_1=κ_2=0.55 and α_{dB}=1 dB/cm are, as can be expected, identical to those shown in Figure 4.18. With a mean difference of 0.051 dB and a standard deviation σ = 0.057 found between these simulations it can be concluded the bi-directional propagation offered by the Aurora simulation method also works properly.

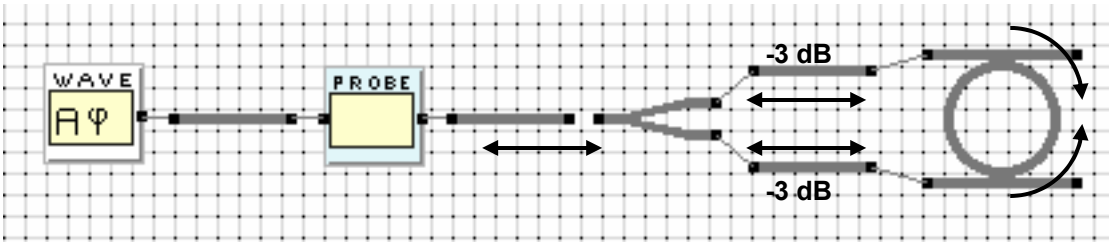

Figure 4.21. The reflector MR circuit.

It would be wrong to state that, based on these four tests, the simulation method used by Aurora performs flawlessly. However, the tests do address all the critical aspects of the simulation method and the underlying engine and would have exposed many if not all problems. Because complex optical circuits composed of a huge number of optical constructs are not much different from simple circuits from the perspective of the engine (since all calculations are localized), the results of the simulations performed on such circuits can also be trusted to a high degree. Nonetheless, since it is impossible to test every possible optical circuit for correct behavior, the program user should always be careful when interpreting the results, as is the case for nearly all (scientific) simulation software.
If incorrect behavior of simulations in Aurora does occur it is relatively easy to detect. Incorrect behavior can be categorized under two types: simulation core failure and incorrect simulation timing. A failure in the simulation core is exclusively the result of bad programming and should be detected while debugging the program. Incorrect simulation timing however is the result of bad simulation settings by the user.

- A failure in the simulation core can be detected quite easily using the four tests given above. The nature of the simulation method makes that these tests are either a success or go horribly wrong as for instance shown in Figure 4.22. This figure should have shown the drop response of a new optical construct that was introduced into the program to simulate an analytical drop response. This construct was for instance used in the OADM simulation discussed in Chapter 4.5.4.1. Due to a few minor mistakes made while programming the construct, however, the response showed only “noise”.

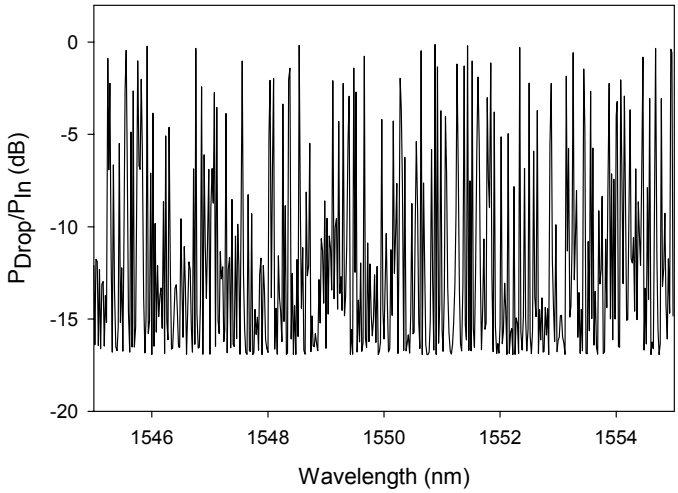

Figure 4.22. The result of a failed simulation.

- A flaw in the simulation timing is the direct result of a simulation that is not allowed to run long enough. It can affect the simulation results to varying degrees, ranging from quite subtle to severe. However, the timing problem can only occur in resonant devices. As pointed out in Chapter 4.2.1 a frequency-domain response, created by combining multiple time-domain responses simulated at different wavelengths, is only valid when the time-domain responses have converged to a stable value. Since the time-domain responses of resonant devices will only converge to a stable value after a certain simulation time has passed, erroneous results will therefore be returned if the simulation time is too short. If the time domain simulation of a resonator at maximum resonance ($\varphi_r = m.2\pi$), shown in Figure 4.23, ends prematurely at T=20 for instance then the maximum dropped power reported by the frequency response will be systematically too low. For wavelengths off-resonance even stranger effects can be observed. Because the time-domain responses at these wavelengths might oscillate before they stabilize, as shown in Figure 4.24 the frequency response may show both higher as well as lower dropped power values depending on the end-time of the simulation. At time $T = T1$ for instance certain values will be too low whereas they might be too high at time $T = T2$.

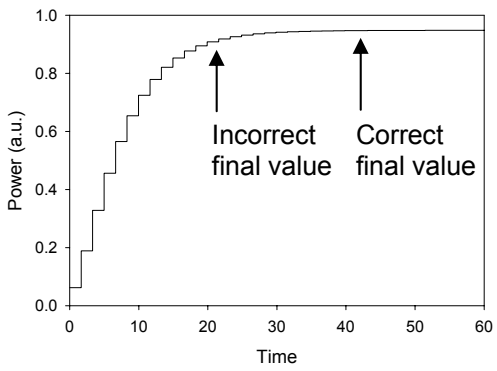

Figure 4.23. Time-domain drop response for a resonator at full resonance.

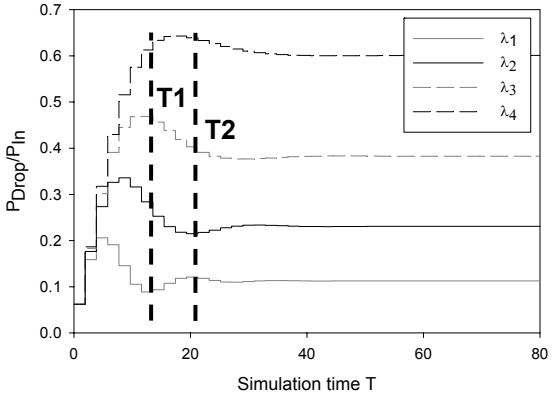

Figure 4.24. Time domain drop responses at off-resonance wavelengths showing oscillatory behavior.

These oscillations in the time-domain simulations are transferred to the frequency response as high frequency oscillations such as those shown in the MR drop response in Figure 4.25. As might be expected the magnitude of these oscillations is dependent on the maximum simulation time and becomes more severe for shorter simulations.

Behavior of the frequency response such as that shown for the drop response in Figure 4.25 is typical to a micro-resonator. However, similar behavior will also occur in other resonant devices such as gratings. Timing errors are therefore easy to detect for a user with experience in the field of integrated optics, for instance by running two simulations with different the maximum simulation time. If a simulation timing issue is found a suitable increase of the maximum simulation time will then suffice to create correct simulation results.

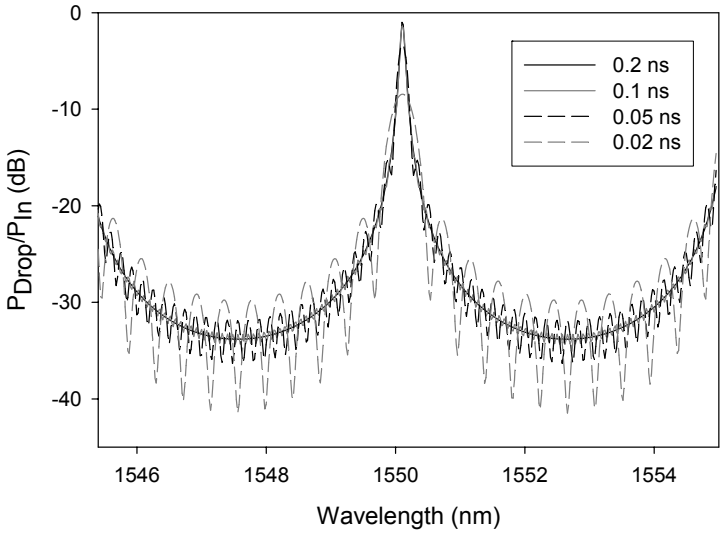

Figure 4.25. Drop response as a function of the user defined maximum simulation time.

4.5.4 Strengths and weaknesses of the simulation method

Although the basic concept behind the simulation method is quite simple it is nonetheless very powerful and possesses several strengths due to the distributed calculation by the individual primitives. However, the fact that some of the signals that are forwarded between these primitives need to be inserted into a call-list as explained in Chapter 4.5.2.2 also acts as an Achilles heel, causing the simulation run very slow under certain circumstances.

4.5.4.1 Simulation strengths

The strengths of the simulation method are largely due to the fact that each optical system automatically creates its own simulation algorithm and the fact that this algorithm is time-domain based. This creates several advantages that might not be available to other simulation methods:

Event driven calculation.
Because the algorithms are event driven, only those optical constructs of the system that are active during the simulation will be involved in the calculations. In fact, the non-active parts are totally invisible. This is a clear advantage over a transfer matrix based simulation that needs to consider (and therefore calculate) all the constructs since it is difficult to predict in advance which constructs will or will not be active. The "removal" of certain parts of the optical system can lead to significant reductions in simulation time.

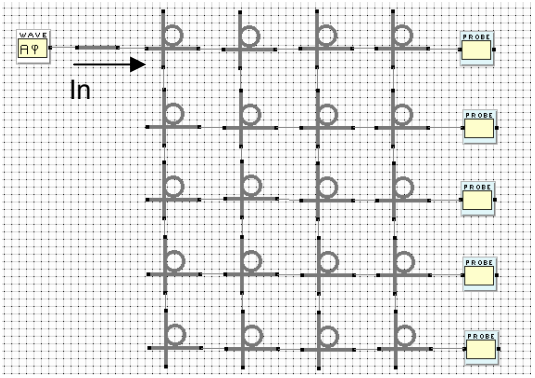

Figure 4.26a. Router calculated from left to right.

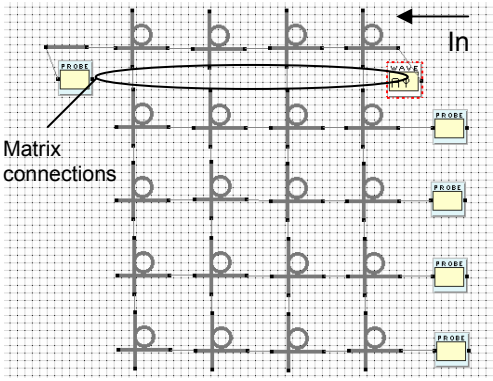

Figure 4.26b. Router calculated from right to left.

For instance, a simulation of the router configuration shown in Figure 4.26a will take ≈20.3s to calculate 50 wavelength points if a signal enters the matrix from the left. However, if the probe used to record the signal on the express port and the wave source are swapped, as show in Figure 4.26b, the simulation will take only ≈0.1s to complete. This is because it is impossible for the signal to enter the lower four rows of the matrix from this direction. These are therefore automatically excluded from the simulation. The simulation in this case is in fact similar to that of a 4-resonator OADM as the removal of the matrix connections indicated in the figure does not alter the 0.1s simulation time.

Freedom of construct calculation algorithms.

Each optical construct defines its own calculation algorithms. Since the simulation method requires that only the in-and output values of these calculations are well defined, the actual calculations can be implemented using whatever algorithm performs the most optimal for a given situation. This offers great flexibility, allowing the use of for instance BPM in one construct and a transfer matrix in another. Some constructs may even be optimized for a specific task in order to decrease the calculation time of the simulation. That such a targeted optimization can reduce the simulation time quite considerably is for example shown by comparing two different OADMs built in Aurora.

The Aurora screenshot in Figure 4.27a shows the optical circuit of a regular OADM. The individual resonators in this circuit are high level components that are internally comprised of several waveguides and couplers. A simulation using this layout would therefore be able to return both the time- as well as the frequency domain response as all the required timing is handled by the internal optical constructs. However, it is easily seen that if a correct time domain response is not required the individual micro-resonators might just as well be described by their analytical expressions (in this case where there is no higher order interaction between the resonators). This offers an alternative way of creating the OADM as shown in Figure 4.27b. The resonators used in this circuit do not contain the waveguides and couplers but instead implement Equations (2.13) and (2.23), that describe the resonator drop- and through responses, directly.

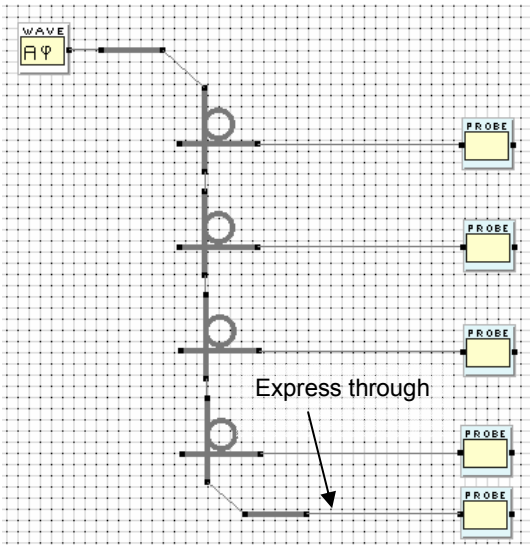

Figure 4.27a. OADM with resonators that are internally comprised of couplers and waveguides.

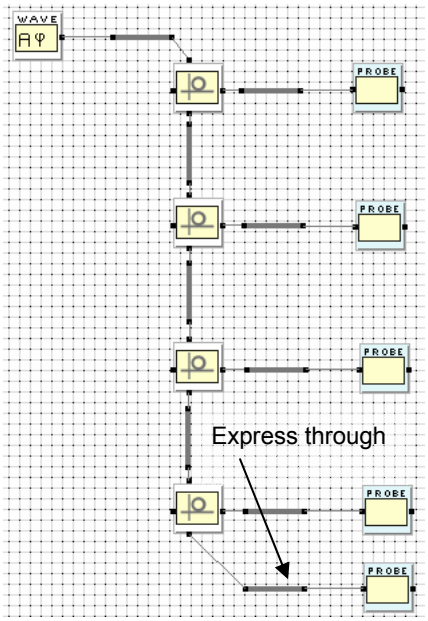

Figure 4.27b. Optimized OADM with resonators that directly implement the analytical through and drop response equations.

Figure 4.28a shows the simulated express through responses of both OADMs obtained for the configuration shown in Figure 4.28b. These two responses are virtually identical with a mean difference between the responses of only 0.013 dB.

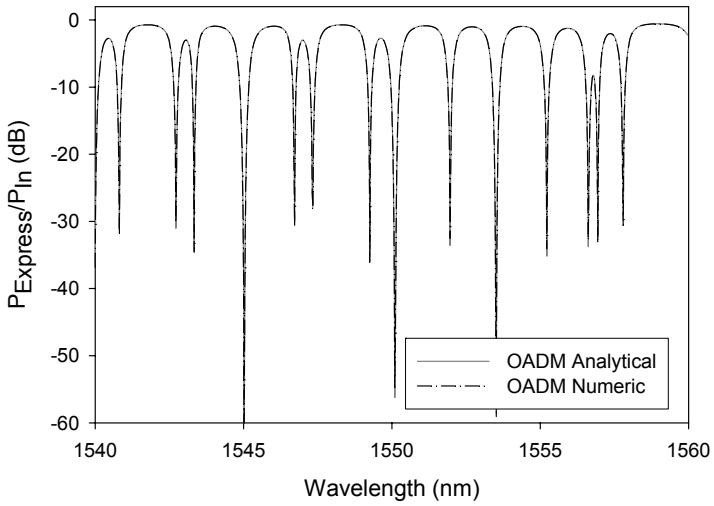

Figure 4.28a. Comparison between the express through response of an OADM in which the resonators are comprised of couplers and of an optimized OADM that uses analytically solved resonator responses.

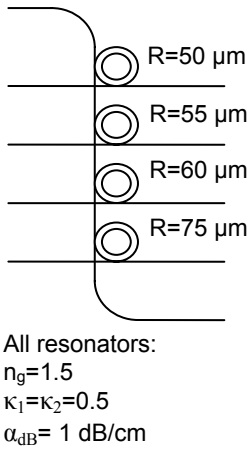

Figure 4.28b. OADM configuration used for the simulation in Figure 4.28a.

Although the frequency responses of both OADMs are identical, as can be expected, the time required to calculate this configuration differs quite substantially. Table 4.1 shows the calculation time required to calculate this and three other configurations. The beneficial effects of targeted optimization of a construct (in this case a micro-resonator) are clearly seen in this table. The OADM built with the optimized resonators (that internally use Eqs. (2.13) and (2.23)) simulates each of the given

configurations within 25 ms. The calculation time T_{reg} of the non-optimized OADM, however, is highly dependent on the radius of the resonators causing it to calculate up to 270 times slower. This makes that, if a correct time domain responses are not required, the optimized OADM is the preferred choice.

Table 4.1. OADM Calculation time comparison (calculation across 500 wavelengths, timed on an Athlon 64 3000+ system)

R_1 (µm)	R_2 (µm)	R_3 (µm)	R_4 (µm)	T_{Reg} (s)	T_{Ana} (s)
50	50	50	50	0.067	0.025
50	55	50	50	1.68	0.025
50	55	60	50	3.45	0.025
50	55	60	75	6.8	0.025

Parallel execution.
As was already stated in Chapter 4.5.1 the simulation method used by Aurora is intrinsically highly suitable for parallel computation when calculating the frequency response of an optical system. Because the method is based in the time-domain and creates its frequency-domain responses by combining multiple time-domain simulations at the very last stage of the simulation, the time-domain simulations are easily scaled to run on multiple processors. Apart from this shallow-level parallelization, deep-level optimization on the optical construct level is also possible due to individual calculation of these constructs. A construct may for instance represent a non-linear waveguide for which the calculation is offloaded to a separate micro-processor.

4.5.4.2 Simulation weakness

The simulation method used in Aurora is fundamentally dependent on the use of a call list in which calls, created by one primitive to forward a signal to another, are inserted in chronological order. The current algorithm used to insert a call is highly inefficient, however, as it simply traverses down the list until the right position for insertion is found. The time required to insert a new call therefore currently increases almost linearly ($T(n) \in O(n)$) with the number of calls in the list. As the insertion procedure can be called many times (e.g. the OADM simulation in the previous paragraph required >51.000 calls) during a simulation, it is easily seen that the overall calculation time is greatly dependent on the number of calls in the list.

That this dependency is currently a major weakness of the simulation method is clearly evidenced by the simulation calculation times given in Table 4.1. The table shows that the calculation time rises quite steeply with the number of resonators of unequal radius in the OADM. The reason for this is that an optical circuit with loops of differing optical path lengths will inevitably generate many more calls than an optical circuit in which the loops are of equal length. This can be explained by comparing two different second order MR filters: One in which the micro-resonators are of equal radius and one in which the radii are not equal.

In Figure 4.29 a second order resonator filter is shown in which the upper and lower resonators are of equal radius. If a signal enters this resonator at the first coupler it

will propagate through the first half of the lower resonator and will reach the second coupler at time $T=T_{d1}$ (with T_{d1} the time delay in one half of the resonator). From here the signal will now propagate into the lower as well as the upper resonator. After the signals have propagated a full roundtrip through the respective lower and upper resonators, however, each will return at the second coupler at exactly $T=3T_{d1}$ due to the identical roundtrip time of the resonators. This means that at $T=3T_{d1}$ two calls are present in the execution list. Each contains signal data that needs to be forwarded to the coupler and each requires that the coupler calculation procedure is executed afterwards.

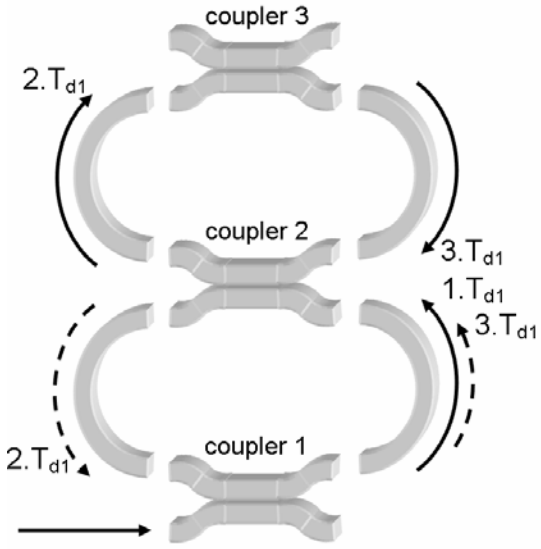

Figure 4.29. Call timing in a 2nd order resonator with rings of equal radius.

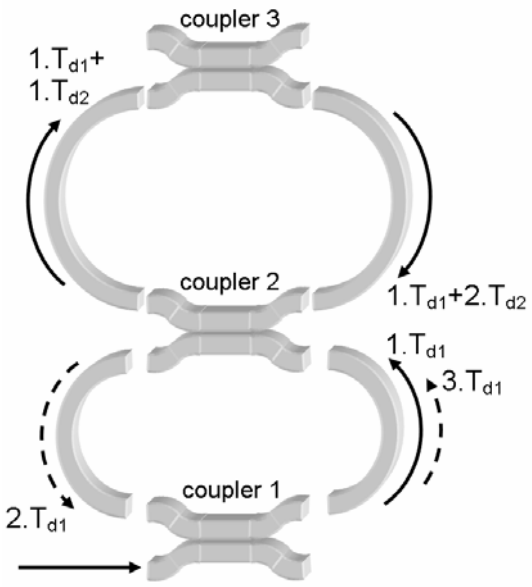

Figure 4.30. Call timing in a 2nd order resonator with rings that differ in radius.

At this point the call combiner of the execution engine comes into play to handle these two calls efficiently. This is important because of the behavior of multi-port constructs such as the coupler. For a single execution of this constructs will always create two or more calls to other constructs it is connected to. A coupler will for instance create two new calls at its outputs for each call at its input as shown in Figure 4.31a. Two calls that arrive simultaneously at different ports would therefore result in four new calls as shown in Figure 4.31b.

However, this is very inefficient because the two new sets of calls will have a time difference of zero between them. Since a change that takes place in 0 seconds is undetectable (and makes no sense) in the simulation of the optical system it is better that a construct sends out only one call for a specific time.

Even worse is the fact that this may also cause a massive increase in the number of calls. The resonator filter of Figure 2.29 would see a doubling of the calls after each roundtrip when the signals from the lower and upper resonator meet up in the second coupler.

In order to avoid this undesirable behavior the execution engine therefore detects and combines all the calls that arrive at a construct at the same time into a single new call. This guarantees that the calculation procedure of the construct is executed only once so that no redundant calls are created. This combining of calls works very efficient if many calls arrive at a construct at the same time. The resonator filter of Figure 2.29 is an almost ideal example of this because the two calls generated by the second coupler

can be combined again after every roundtrip. Due to this the total number of calls in the call list will never exceed four, making the simulation of this particular device very fast.

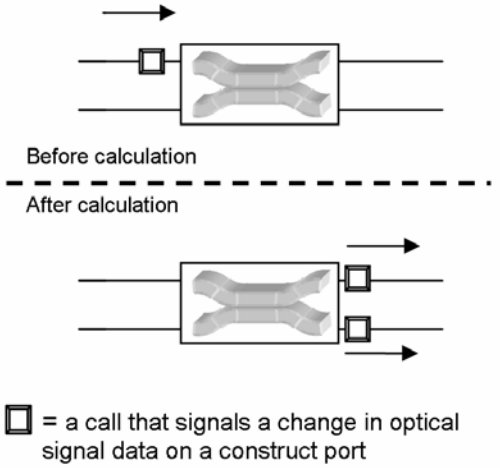

Figure 4.31a. A single call made to a coupler will result in two new calls.

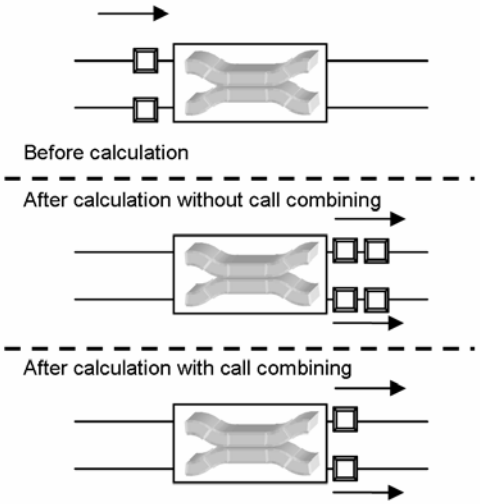

Figure 4.31b. Two calls that arrive simultaneously at a coupler are combined so that still only two new calls are generated.

If the radius of the resonators is not equal, however, far fewer calls can be combined. In Figure 4.30 for instance the signal returning from the upper resonator to coupler 2 will have a delay of T_{d1}+2.T_{d2} whereas the signal returning from the lower resonator will have a delay of 3.T_{d2}. In this second order MR therefore only those calls can be combined where

$$m.T_{d1} = n.T_{d2} \text{ with } m \in N, n \in N \tag{4.30}$$

Because fewer calls can be combined, more calls will be present in the call-list which results in longer list insertion times. The effect of this is clearly seen in Table 4.2 that shows the calculation time of this filter for variations in the radius of the top resonator. Only those radii of the top resonator for which Equation (4.30) is true for small values of m and n, such as for instance 25, 75 or 100 µm, calculate very fast whereas all other values show considerably longer calculation times.

Table 4.2. 2nd Order resonator calculation time for different radii of the upper resonator. The lower resonator is set at 50 µm (calculation across 500 wavelengths, timed on an Athlon 64 3000+ system)

Upper resonator radius (µm)	Simulation calculation time (s)
25	0.05
50	0.04
51	0.57
52	0.34
53	0.59
75	0.05
100	0.04

As demonstrated by these two second order micro-resonator filter examples the current simulation method is very sensitive to optical circuits with loops of differing optical path lengths. This sensitivity is largely due to the currently used call-insertion algorithm of which the time required for insertion scales with the number of calls in the call-list as $T(n) \in O(n)$. However, the use of more efficient algorithms, such as the B-Tree [121], the Binary tree [122] or Skip lists [123] that scale according to $T(n) \in O(\log n)$, can greatly reduce this sensitivity and easily improve the simulation time by an order of magnitude for complex optical circuits.

4.5.5 Simulations on complex structures

The strength of Aurora and other similar tools [124, 125] is that optical circuits can be evaluated with a minimum in effort and often in a fraction of the simulation time required by more rigorous methods. This also allows a user to quickly test a new idea and even stimulates "play-time": just try random optical circuits and see if any interesting effects occur.

4.5.5.1 The hyper-resonator

One optical circuit that emerged form this "play" is the "Hyper-resonator" which features on the cover of this thesis and shown again here in Figure 4.32a. While this device may seem quite simple at first glance, closer inspection reveals a highly complex high-order filter device in which light propagates in two directions in all waveguide sections. The complex behavior for such a seemingly simple geometry made this device a prime candidate for simulation in Aurora as such devices might display interesting and perhaps useful filter properties.
A simulation was therefore created as shown in Figure 4.32b. Although the ratio of the resonators radii in Figure 4.32a is by definition given by:

$$R_{Outer} = \frac{3+2\sqrt{3}}{3} R_{Inner} \approx 2.15 R_{Inner} \tag{4.31}$$

a ratio of 3 was chosen instead. This ratio is more realistic from the perspective of fabrication and removes any wide-range Vernier effects between the resonators that may obfuscate some of the more interesting effects in this device.

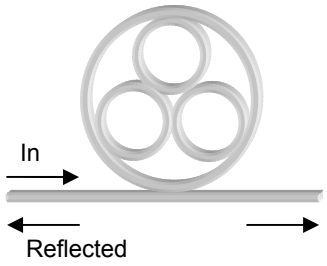

Figure 4.32a. "Hyper-resonator" layout.

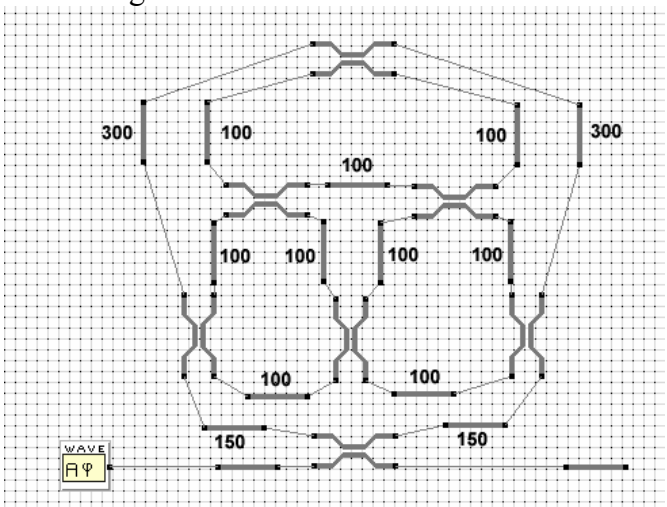

Figure 4.32b. Aurora simulation circuit to simulate the hyper-resonator. All lengths are in micrometers.

For the given waveguide lengths this translates to an inner ring radius of 47.7 μm and an outer ring radius of 143.2 μm. The coupling coefficients were all set at 0.707 and the waveguide losses at 1 dB/cm. Figure 4.33 gives the spectra resulting from the simulation of this device. The spectrum of the reflected light is particularly interesting as it shows that light is reflected across a wide band for certain wavelengths.

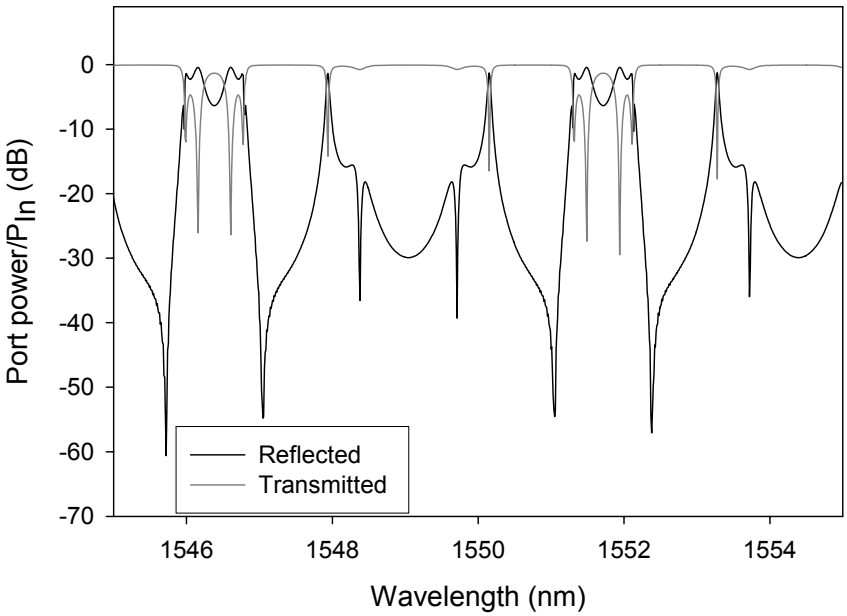

Figure 4.33. "Hyper-resonator" transmission and reflection.

The wide band reflection was further investigated by varying the coupling coefficient of all couplers in the circuit apart from the coupler with the port waveguide, which was held at a coupling of 0.707. Figure 4.34 shows that the returned signal becomes more flat for lower coupling coefficients at the expense of bandwidth and filter rejection ratio.

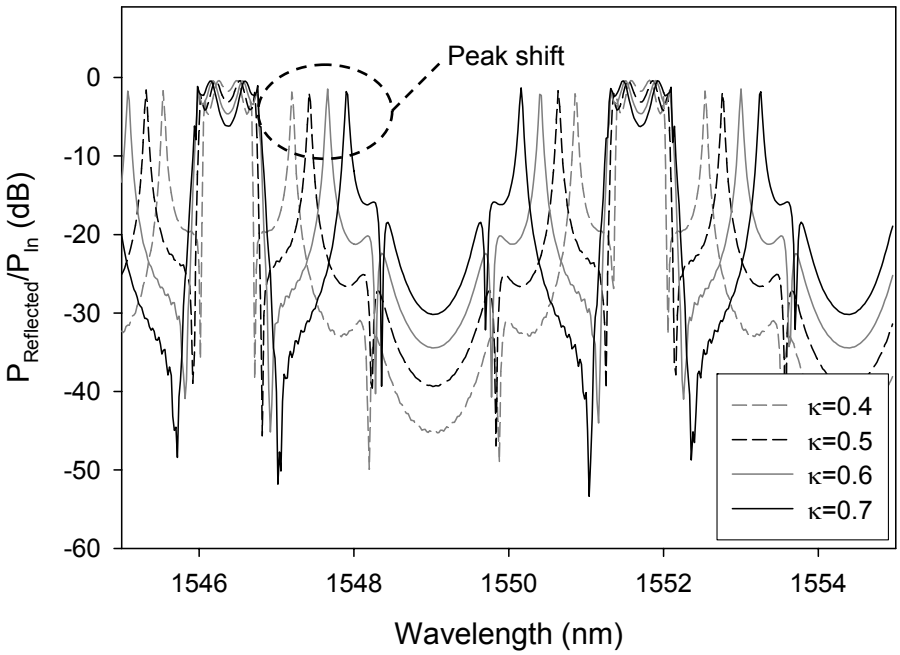

Figure 4.34. "Hyper-resonator" reflection as a function of the internal resonator coupling coefficients.

What is more interesting about the spectra, however, is the behavior of the sideband peaks. As indicated in the figure these peaks shift as a function of the coupling strength. This shift of the peaks is somewhat similar to the peak tuning effect seen in a second- (and also higher) order filter. As was shown in Figure 2.15 two peaks appear when the resonator is over coupled. While these peaks also shift as a function of the coupling coefficient of the center coupler, the peak shift and the rejection ratios that can be achieved are not as high as shown in the circuit presented here.

In Figure 4.35a a different simulation setup is given. Here the assumption was made that, at least to some degree, the internal resonators could be seen as three paired resonators. The internal coupling coefficients were therefore set equal to the critical coupling of a second order filter (κ=0.143). Figure 4.35b shows that the spectra are now quite different from those given in Figures 4.33 and 4.34. A wider reflection or "stop" band is now occurring. This may indicate that, given the proper settings of the couplers, this circuit can act as a wide-band reflector.

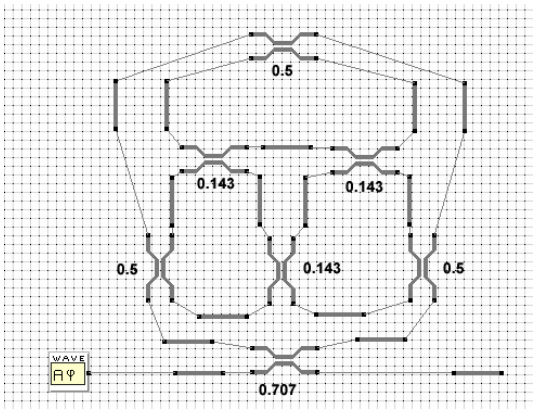

Figure 4.35a. Aurora simulation circuit showing coupler settings.

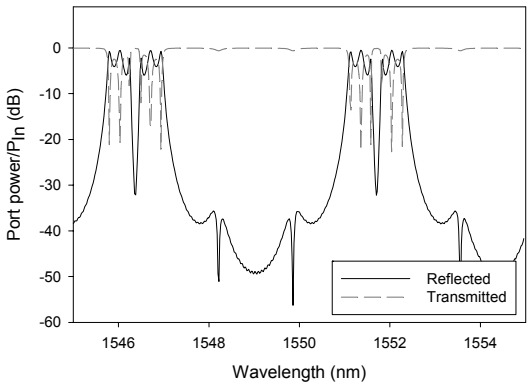

Figure 4.35b. Aurora simulation results for the circuit on the left.

The overall behavior of this device was quite unexpected and, due to its complexity, has so far not been investigated in more detail (although it certainly warrants further examination). The early simulation tests have already been presented here, however, in part because of the interesting properties of this device but also because it shows how a program like Aurora can quickly identify novel and interesting devices.

4.5.5.2 Simulation of a waveguide grating

Another complex device of interest is the waveguide grating shown in Figure 4.36.

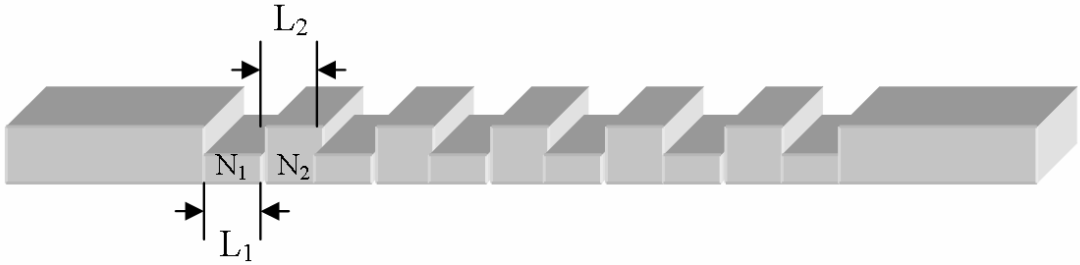

Figure 4.36. Schematic representation of a waveguide grating.

The light propagation through this device can be simulated in 2D or 3D using a number of simulation methods, such as FDTD, Finite Element (FEM), Bi-directional Eigenmode Propagation (BEP) or Coupled Mode Theory (CMT) [126, 127]. These methods can provide an accurate simulation of the grating in the time- as well as the frequency domain but are also computationally intensive and therefore slow. If the grating consists of a shallow etched waveguide, however, the propagating modes are weakly confined. This allows the grating to be approximated by a 1D Bragg stack [113]. This approximation replaces the alternating sections in the waveguide grating with a film that has a refractive index $\tilde{n}_i$ and thickness d_i equivalent to the respective effective refractive index N_i and length L_i of that section.

The transmission, reflection and absorption of a 1D Bragg stack can be calculated using the transfer matrix method. To do this each film of the Bragg stack is first described by its characteristic matrix [128]:

$$M_i = \begin{bmatrix} \cos\left(\frac{2\pi.\tilde{n}_i.d_i}{\lambda}\right) & -\frac{j}{N_i}\sin\left(\frac{2\pi.\tilde{n}_i.d_i}{\lambda}\right) \\ -jN_i\sin\left(\frac{2\pi.\tilde{n}_i.d_i}{\lambda}\right) & \cos\left(\frac{2\pi.\tilde{n}_i.d_i}{\lambda}\right) \end{bmatrix} \tag{4.32}$$

where $\tilde{n}_i$ is the complex refractive index $\tilde{n}_i = n - jk$ of the i-th layer. The matrix that describes the complete matrix is then found by multiplying the individual matrices:

$$M_{tot} = M_1 \cdot M_2 \cdots M_p = \prod_{i=1}^{p} M_i = \begin{bmatrix} m_{11} & m_{12} \\ m_{21} & m_{22} \end{bmatrix} \tag{4.33}$$

Using this matrix the transmitted (T), reflected (R) and absorbed (A) power in the Bragg stack are given by:

$$R = \left| \frac{(m_{11} + m_{12}n_s)n_a - (m_{21} + m_{22}.n_s)}{(m_{11} + m_{12}n_s)n_a + (m_{21} + m_{22}.n_s)} \right|^2 \tag{4.34}$$

$$T = \left| \frac{2n_a}{(m_{11} + m_{12}n_s)n_a - (m_{21} + m_{22}.n_s)} \right|^2 \tag{4.35}$$

$$A = 1 - R - T \tag{4.36}$$

where n_a and n_s are the refractive indices of the air and substrate respectively.
With these equations the frequency response of a Bragg stack, and therefore of a shallow etched grating, can be calculated in a very fast and memory efficient manner. The downside of the approach, however, is that it cannot be used to examine the behavior of the grating in the time-domain.

Alternatively, the grating can also be implemented using Aurora. Although the simulation of a grating in Aurora cannot calculate as fast as the given transfer matrix

method it does allow time domain simulations and will still outperform more rigorous simulation methods such as FDTD and BEP in calculation time.

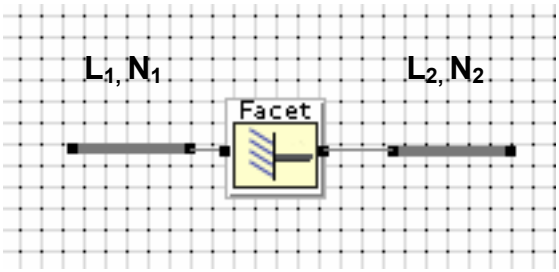

Figure 4.37. The implementation of a single grating period in Aurora.

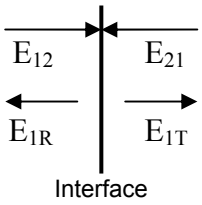

Figure 4.38. Definition of reflected and transmitted fields at an interface.

A single grating period of a grating can be implemented in Aurora as shown in Figure 4.37. Here the tooth and the groove section of the grating period are replaced by two waveguides of similar length and effective refractive index. The reflections that occur at the interface between the two sections are modeled by using the facet construct. This construct uses the transfer matrix:

$$\begin{bmatrix} E_{1R} \\ E_{1T} \end{bmatrix} = \begin{bmatrix} R_E & -j.T_E \\ -j.T_E & R_E \end{bmatrix} \cdot \begin{bmatrix} E_{12} \\ E_{21} \end{bmatrix} \tag{4.37}$$

where the fields E_{xx} are defined as shown in Figure 4.38.
The field reflection and transmission coefficients R_E and T_E are given by:

$$R = \left| \frac{n_1 - n_2}{n1 + n2} \right| \tag{4.38}$$

$$T = \sqrt{1 - R^2} \tag{4.39}$$

By combining several of these grating periods a grating circuit can be created as shown in Figure 4.39. This grating consists of 11 periods, has a period length Λ of 2 μm and a duty cycle of 50%. The indices of the grating periods, as indicated in the figure, were set at 1.5 and 3. It needs to be noted that these values are not in accordance with the condition of weak confinement that allows the 1D simplification of a 2D grating. However, a small index contrast would require a grating comprised of many more periods than the 11 used here to show a significant effect in the transmitted and reflected light. Since the user interface (not the underlying simulation method) of Aurora currently makes this nearly impossible a shortcut using a higher index contrast was opted for instead.

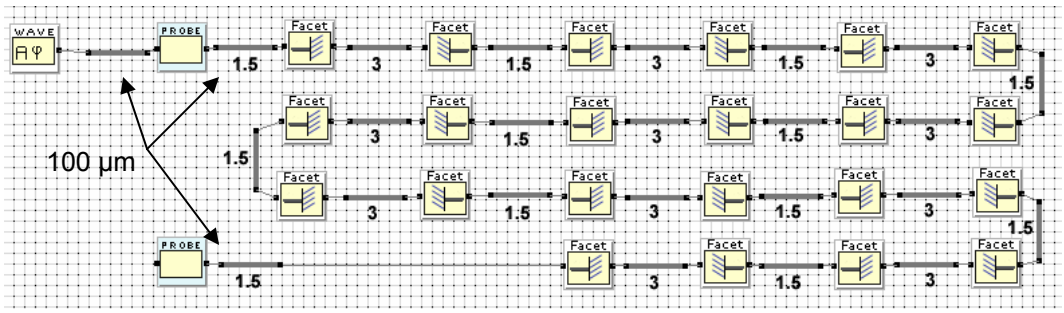

Figure 4.39. Implementation of an eleven period grating in Aurora.

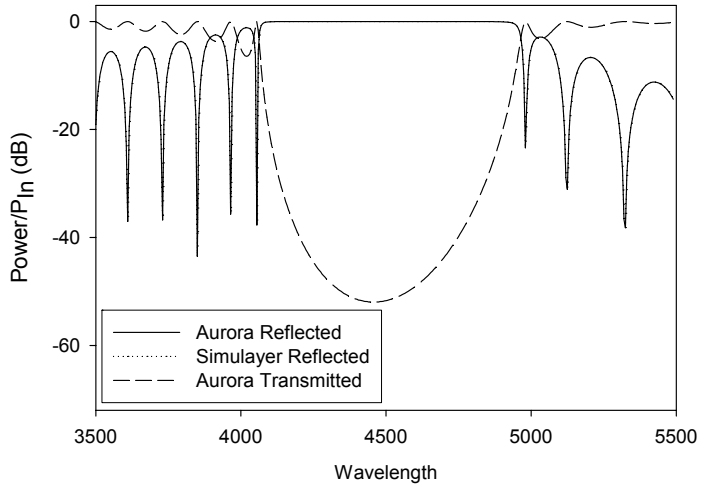

Figure 4.40. Grating transmission and reflection as a function of the wavelength (The simulated reflection spectra calculated with Aurora and SimuLayer lie perfectly on top of each other. Therefore only two curves can be discerned in the figure).

In Figure 4.40 the simulated transmission and reflection spectra of the grating circuit are given. The spectrum of the reflection has been calculated using Aurora as well as SimuLayer [129]. SimuLayer implements the transfer matrix method described in Equations (4.27-4.31), and can therefore be used to determine if the simulation results produced by Aurora are correct. By looking at the figure it can be concluded that this is clearly the case as the overlap between the reflection spectra is near perfect.

The simulations in Aurora of this particular grating (across 400 wavelength points) took 18 seconds to calculate. While this is several orders of magnitude slower than the time required by SimuLayer it is still fast in comparison with the other methods mentioned. The real advantage of Aurora, however, is in the simulation of the time-domain step responses of which the results are given in Figures 4.41 and 4.42. The first figure shows the step responses of the transmitted and reflected light at the second maximum in the transmission, located just below the bandgap of the grating at a wavelength of 3965 nm. The responses do not begin at T=0. This is mainly due to the fact that some waveguides in the circuit, as indicated in Figure 4.39, have a length of 100 µm. This results in a delay of the signals by ≈1.5 ps.

More interesting than the responses shown in Figure 4.41, are the step-responses shown in Figure 4.42 that were calculated for the center of the bandgap, at 4455 nm. Clearly, the interaction of the light within the grating at this wavelength is much more

complex than the interaction at a wavelength of 3965 nm, as can be concluded from the many oscillations in this figure.

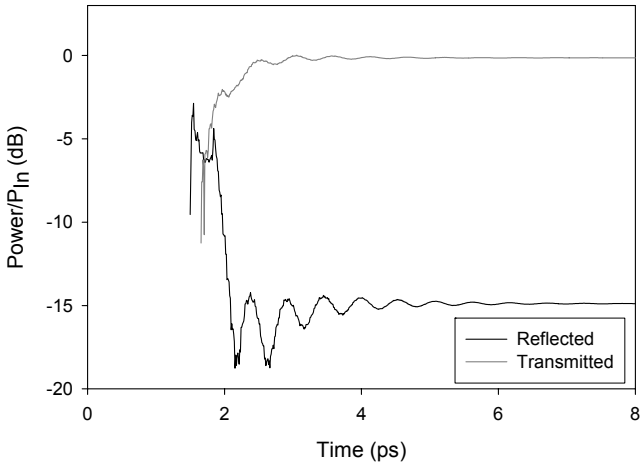

Figure 4.41. Step responses of the transmitted and reflected light outside the bandgap at 3965 nm.

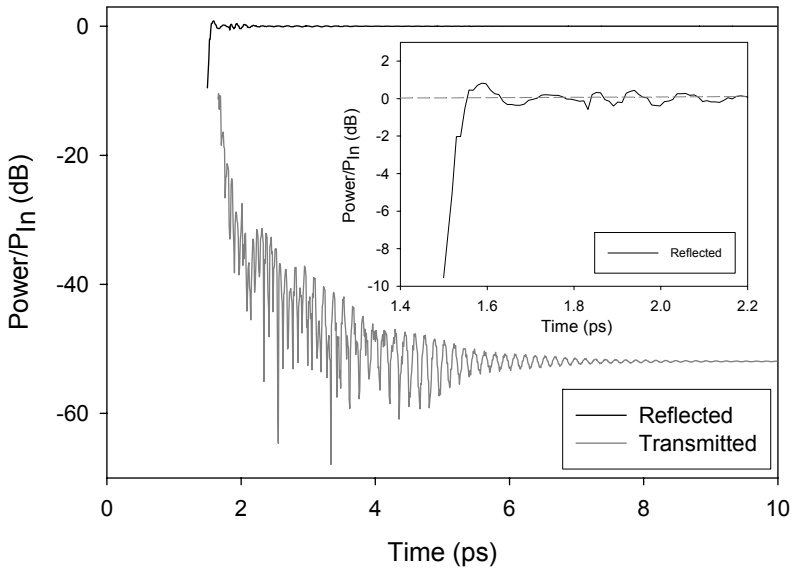

Figure 4.42. Step responses of the transmitted and reflected light in the middle of the bandgap at 4455 nm. Inset: a close-up of the reflected step response showing a slight signal overshoot.

Interestingly the reflected light reflects more power than is put into the grating for a short duration, as is shown in the inset. This might be an actual physical effect as it was for instance also seen in a different simulation that used grating indices of 1.5 and 4. However, none of the results of the time-domain simulations have currently been compared with the results of other simulation methods. The effect might therefore also be caused by unpredictable behavior of the simulation method used by Aurora, although this is not very likely.

For reasons of simplicity only the time domain responses at the in- and output of the grating have been recorded using the two probes placed in these locations. However, the probes are just as easily inserted at different locations in the grating. This could be used for instance, to analyze slow light or other phenomena within the grating. As such Aurora might prove to be a valuable tool in examining this particular class of complex optical devices.

Chapter 5

Fabrication

The majority of the devices that will be discussed in the following chapters have been realized in the Si_3N_4/SiO_2 materials system. Depending on the type of resonator that has been fabricated and the type of lithography that was used in this fabrication a different fabrication process was used. In this chapter three fabrication processes, one for lateral and two for vertically coupled resonators will be discussed. For the definition of the waveguides of the vertically coupled resonators contact as well as projection lithography has been used. The different requirements of these methods, both in mask design and fabrication, are also addressed.

5.1 Introduction

The material system in which most of the resonators presented in this thesis have been fabricated is the silicon nitride/silicon oxide system (Si_3N_4/SiO_2) [130]. The silicon nitride is used to fabricate the core of the waveguides while silicon oxide (e.g. thermal, TEOS or PECVD) is used in both the substrate and cladding layers. Both materials are highly compatible with CMOS technologies and can therefore benefit from all the advances made in these technologies.

Silicon nitride was chosen due to its high refractive index of ≈1.98 at 1550 nm which, combined with silicon oxide as substrate or cladding layer, allows for potentially very small resonators, down to a radius of approximately 15 μm. In addition, the material is optically transparent from 400 nm to 2 um which makes it suitable for a wide range of applications and allows for low-loss high index waveguides with reported losses lower than 0.1 dB/cm [131]. Silicon nitride can be deposited in multiple layers of which the thickness can be controlled to within a few nanometers. Also, because the silicon nitride precursor gasses can be chosen to react to form stoichiometric Si_3N_4, the process is very stable concerning the refractive index. This opposed to for instance the SiliconOxiNitride process (SiON) where the ratios of the various precursors need to be carefully controlled during layer deposition to obtain a uniform refractive index, and from deposition to deposition for reproducibility. The use of silicon nitride, however, does place a constraint on the thickness of the silicon nitride layer. Due to tensile stress within the material it will crack and become unusable. The maximum safe deposition thickness of a silicon nitride layer is therefore no more than ≈340 nm. This thickness, however, allows for resonators as small as 15 μm which is more than sufficient for many applications.

In total, three different fabrication processes have been used to realize different types of silicon nitride based devices. The characteristics of these processes have been summarized in Table 5.1. As shown, the process used to fabricate laterally coupled resonators is the simplest while the process that uses projection lithography to fabricate vertically coupled resonators is the most complex. The differences between these processes, however, are not limited to the processing itself but also have an effect on a higher level: in the layout of the masks and design choices made for the various devices. In the following sections the fabrication processes and their repercussions in the design of devices will be discussed in more detail.

Table 5.1. Comparison of the fabrication processes used to create Si_3N_4 based devices.

	Lateral	**Vertical I**	**Vertical II**
#guiding layers	1	2	2
#metal layers	Zero or 1	1	2 (Cr, Au)
Litho type	Contact	Contact	Contact + Projection
# mask exposure steps	1	3	6
Tapers	Horizontal	Horizontal	Horizontal, Vertical
CMP	No	No	Yes
#major processing steps	7 (etching, deposition, litho and anneal)	14 (etching, deposition, litho and anneal)	25 (etching, deposition, litho, CMP and anneal)

5.2. Fabrication and mask design of laterally coupled resonators

5.2.1 Fabrication

The most basic fabrication process is that which is used for the fabrication of devices based on laterally coupled resonators. Only contact lithography is used to define the waveguides and typically only two layers, a core and a cladding layer are required to build the device. This makes the process highly suitable for the testing of new MR based devices because a typical fabrication run can be performed in less than a week. The only critical step in the process lies in the accurate definition of the small coupler gaps typically associated with laterally coupled resonators. Good control of the lithography is therefore highly important.

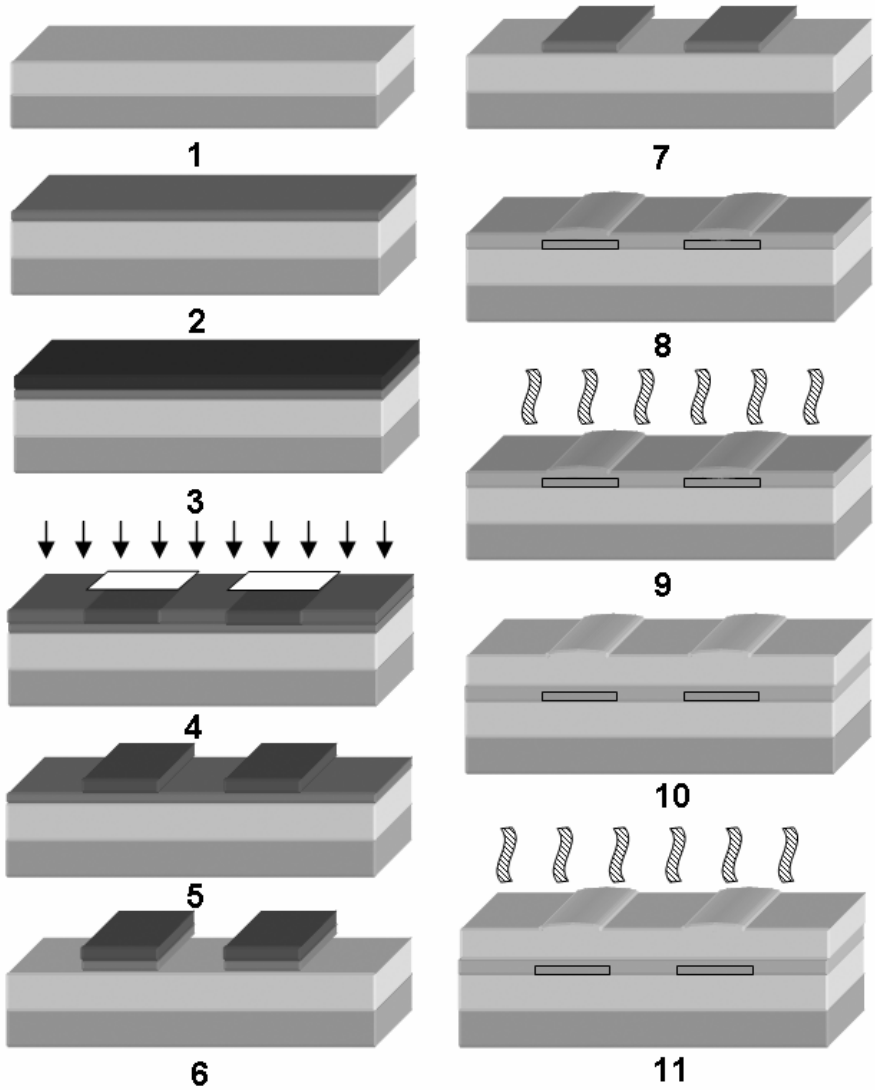

Figure 5.1. Process flow with the major fabrication steps required to fabricate laterally coupled Si_3N_4 microring resonators.

The process flow with the major fabrication steps used to fabricate a laterally coupled resonator is shown in Figure 5.1. As a substrate a thermally oxidized 4 inch silicon

wafer is used (step 1). The SiO_2, with a thickness of 6-8 µm, serves as a buffer layer between the waveguides and the silicon substrate to prevent leakage of light into the substrate. On top of the SiO_2 a 140-145 nm thick (varies slightly per application) layer of Si_3N_4 is deposited (step 2) using low-pressure chemical vapor deposition (LPCVD) at 800 °C. In this layer the waveguides are defined by first spinning a 1.5 µm thick layer of photoresist on top of the Si_3N_4 (step 3). After a pre-exposure bake of 1 minute at 95 °C this layer is exposed to UV light for 5.5 seconds through a chrome mask on a KARL SUSS MA 56M mask aligner (step 4). This mask, of which a small portion is shown in Figure 5.2 contains the definition of the waveguides, ring resonators, test structures and several supporting structures such as dice lines.

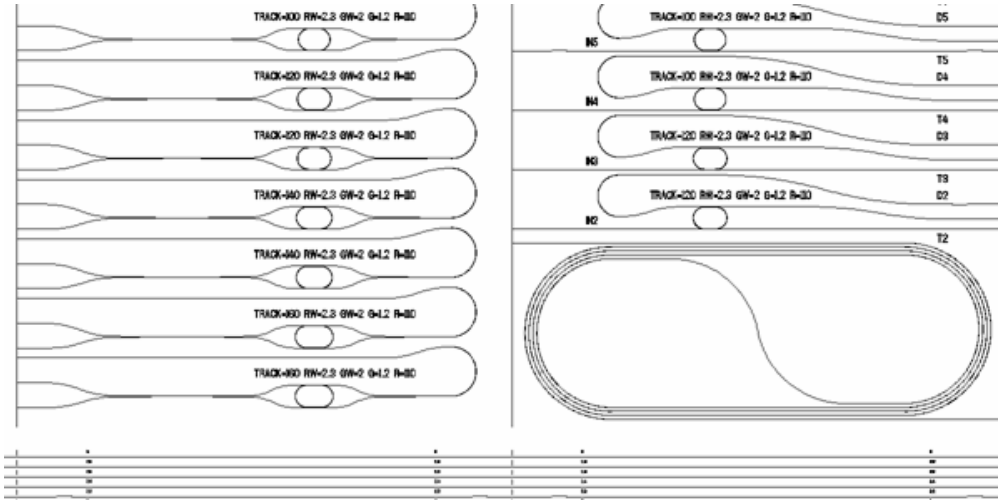

Figure 5.2. Small section of a mask that is used to define laterally coupled resonators. The layout shows reflectors (left), normal micro-resonators (right), waveguide test structures (loop and several straight waveguides) and dice lines (vertical)

After exposure the resist is baked at 120 °C for two minutes after which the resist is developed. The developed resist is then baked at 120 °C for 5 minutes to increase its resistance to dry plasma etching (step 5). Next the waveguides are created by completely etching through the Si_3N_4 in the areas not protected by resist using reactive ion etching (RIE) with a mixture of CHF_3/O_2 (step 6). After etching the resist is removed using fuming nitric acid (100% HNO_3) (step 7). A 1 µm thick layer of tetra-ethyl-ortho-silicate (TEOS SiO_2) is then deposited (step 8) at 700 °C. To densify the TEOS silicon oxide and anneal out loss-inducing NH and OH groups the wafer is annealed at 1100 °C for three hours (step 9). On top of the TEOS SiO_2 an additional top cladding of 3 µm SiO_2 is deposited (step 11) using plasma enhanced chemical vapor deposition (PECVD) after which the wafer is annealed for the second time at 1100 °C for three hours (step 11). As a final step the wafer with the completed devices is diced using a high precision dicing saw with a blade thickness of 50 µm.
In Figure 5.3 microscope images of a realized racetrack resonator and a racetrack based reflector are shown. The width of these devices is 220 µm. The inset in the image on the left shows a close-up of the coupling region of the racetrack resonator. The gap between the port waveguide and the resonator in the coupling region measures only 800 nm which is the minimum gap width which can be opened reliably using the fabrication process described above.

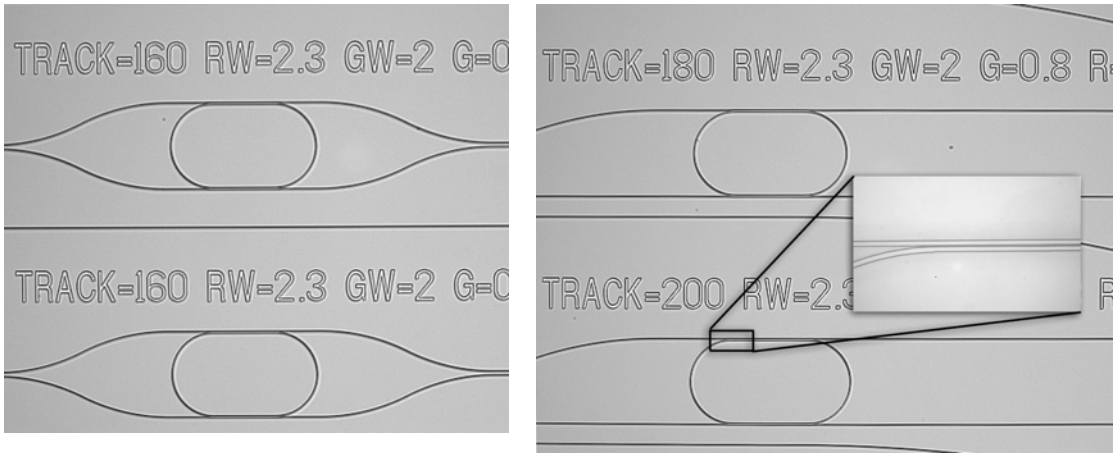

Figure 5.3. Realized MR based reflector (left) and a single resonator (right). The inset shows a close-up of the coupling region of the resonator. The gap between the waveguides is 800 nm.

5.2.2 Mask layout

Figure 5.4 shows the layout of a typical mask used to define laterally coupled resonators. This layout of this mask, like the masks used to define the vertically coupled resonators, follows a set of strict layout rules. The mask layout consists of several columns of which the width is an integer multiple of 5 mm. In each column there are 6 device groups and in each group are up to 20 individual microring-resonators, depending on the size of these resonators.

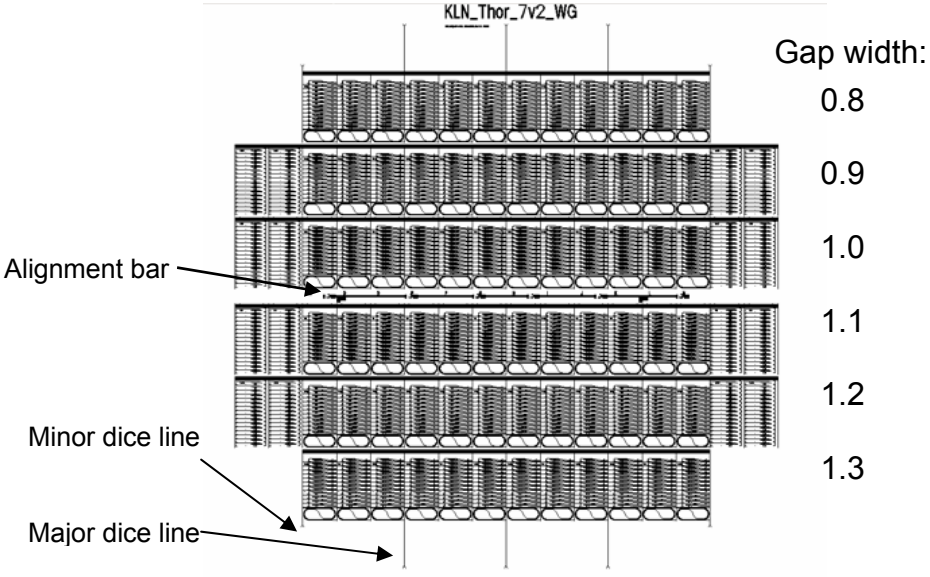

Figure 5.4. Mask layout used to define laterally coupled resonators.

Within the groups the devices are created in pairs (two of each for redundancy) and only one parameter is varied. The two racetrack resonators in the right image of Figure 5.3, for instance, are identical but for the length of their coupling regions: the upper resonator has a coupler length of 180 μm whereas the lower has a coupler length of 200 μm.

The groups within a single column are used to implement variation in the gap width but are otherwise identical. For laterally coupled silicon nitride racetrack resonators with a waveguide thickness of 140 nm a range in gap widths from 0.8 to 1.3 μm is used as shown in the Figure 5.4. Best performance of the resonators is usually in the

range of 0.9 to 1.1 µm. The 0.8 µm gaps are sometimes not fully opened while for gaps wider than 1.1 µm the coupling is normally too low. The addition of gap sizes beyond the useful range, however, makes the devices more resistant to variations (intentional or accidental) in the fabrication process.
The columns that contain the groups are used to implement different types of devices. The outer four columns in the mask layout, for instance, contain MR-based reflectors while the inner twelve columns contain several different types of racetrack resonators. Also shown in the mask layout are the major and minor dice lines and the center alignment bar. In the mask layouts used for laterally coupled resonators the major dice lines are placed every 15 mm while the minor lines are spaced at 5 mm. The center alignment bar contains the alignment markers and several test structures. In Figure 5.5 a small section of this bar is shown. The structures in grey belong to the waveguide layer while the structures in black belong to an additional design layer used to define chromium heaters.

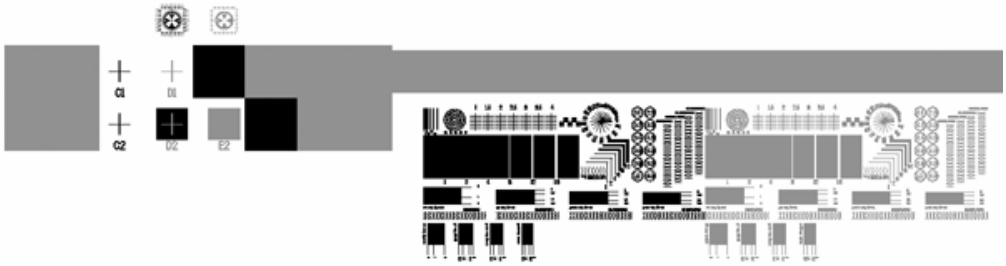

Figure 5.5. Close-up of the alignment bar. This bar contains the alignment markers (left) and several test structures (right).

As shown in Figure 5.5 each layer has its own set of test structures. These structures, shown in more detail in Figure 5.6, are used to monitor several aspects of the fabrication process such as the lithography and the etch process. The resonator gap test shown in Figure 5.7 for instance can instantly tell which resonator gaps (could) have been opened in the fabrication process.

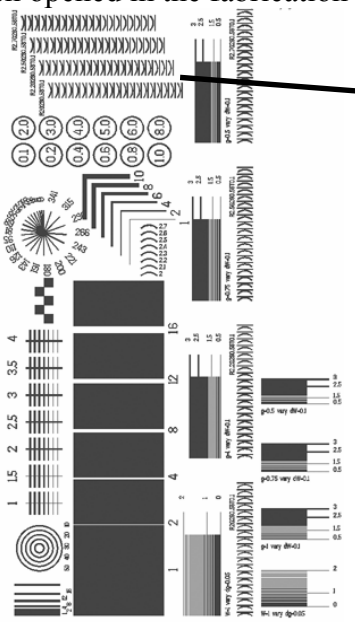

Figure 5.6. Test structure set with patterns to test the lithography and etching of straight waveguides, ring resonators and several other structures.

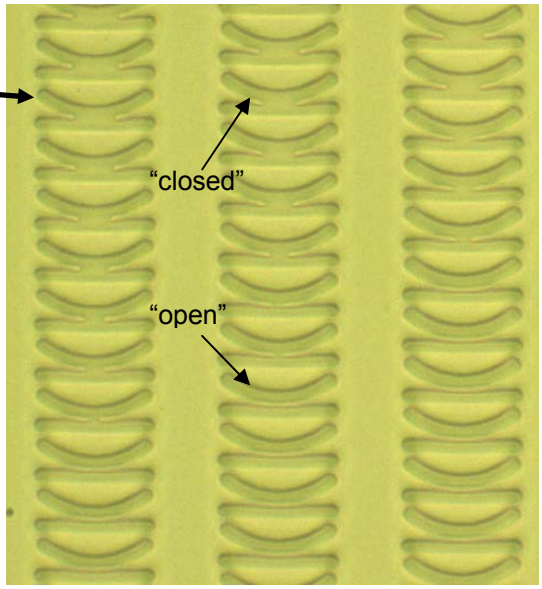

Figure 5.7. Resonator gap test.

5.3. Fabrication and mask design of vertically coupled resonators defined using contact lithography

5.3.1 Fabrication

The fabrication process used to build the first generation of vertically coupled resonators which is described here uses contact lithography to define the port waveguides and micro-ring resonators. Although the lithography for these devices is not as critical as that used for laterally coupled resonators, there are no small gaps between waveguides, this issue is replaced with the problem of correctly aligning the microring resonators to the port waveguides. This, combined with the fact that these devices consist of many more layers than devices based on laterally coupled resonators makes this process overall more complicated and time-consuming.

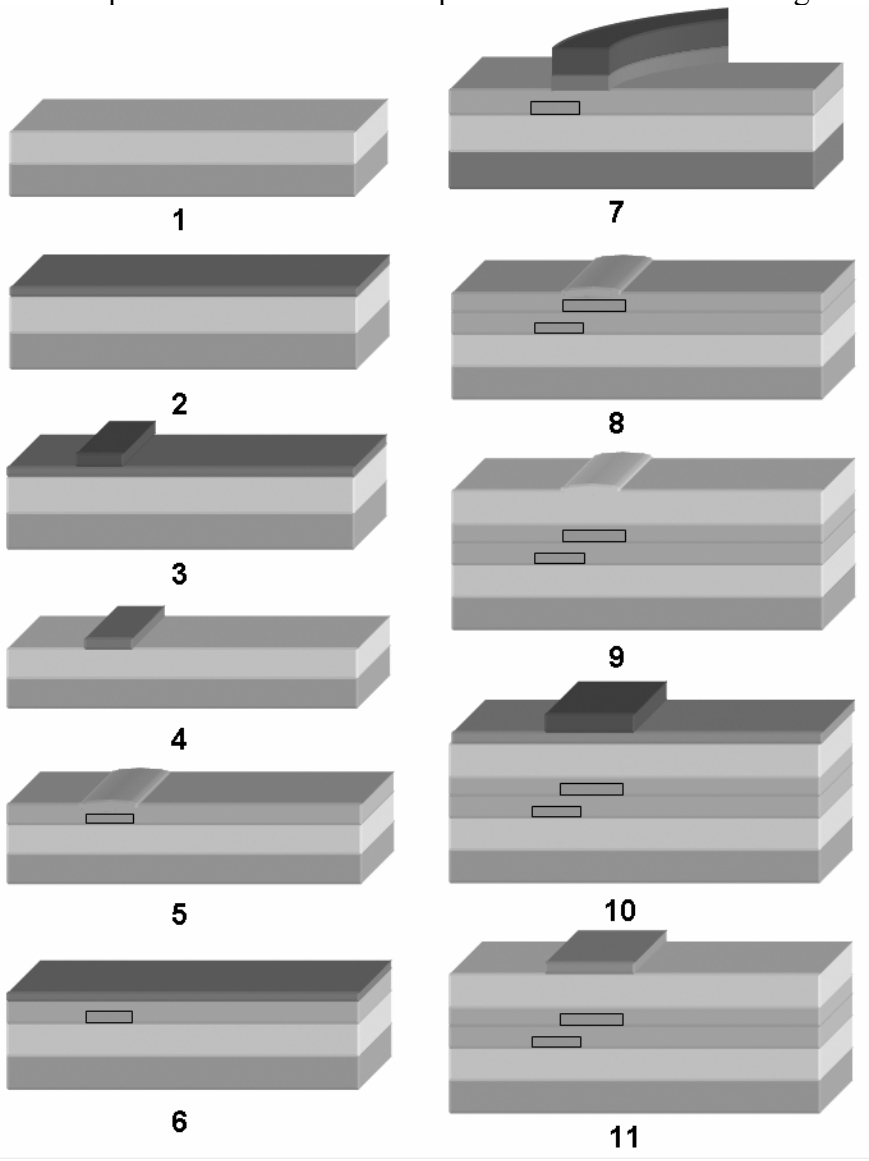

Figure 5.8. Process flow with the major fabrication steps required to fabricate vertically coupled Si_3N_4 microring resonators. (Vertical I, using contact lithography)

The process flow with the major fabrication steps used to fabricate a vertically coupled resonator is shown in Figure 5.8. As a substrate a thermally oxidized 4 inch silicon wafer is used (step 1). On top of the SiO_2 a 140 nm thick layer of LPCVD Si_3N_4 is deposited (step 2) at 800 °C. In this layer the waveguides are defined by contact lithography using the KARL SUSS MA 56M (for more details see Paragraph 5.2.1 and Figure 5.1) mask aligner (step 3) and by subsequent etching of the Si_3N_4 using reactive ion etching (RIE) with a mixture of CHF_3/O_2 (step 4). A 1 μm thick layer of TEOS SiO_2 is then deposited at 700 °C and annealed at 1100 °C for three hours (step 5). On top of the TEOS SiO_2 a 180-190 nm thick layer of LPCVD Si_3N_4 is deposited (step 6). In this layer the microring resonators are defined using contact lithography by subsequent RIE etching (step 7). An additional 0.5 μm thick layer of TEOS SiO_2 is then deposited and annealed (step 8). On top of the TEOS SiO_2 a top cladding of 3.5 μm PECVD SiO_2 is deposited after which the wafer is annealed for the third time (step 9). Next, a 200 nm thick layer of chromium is deposited on top of PECVD SiO_2 in which the heaters are defined using contact lithography (step 10) after which the heaters are etched using chrome etch (step 11).

5.3.2 Packaging

After completion of the fabrication process some of the vertically coupled resonator based devices have been “pigtailed” and packaged. The process of attaching one or more fiber arrays and packaging a device is shown in Figure 5.9. First, a wafer is glued below the wafer with the devices (step 1). Next, 4 mm wide glass rails are glued on top, centered on the dice lines (step 2). The bottom wafer and the glass rails provide the “body” to attach the fiber arrays to the side of the chip. The wafer assembly is then diced in single columns using a 300 μm thick dicing saw. These columns are then measured and a properly working device is selected. The column with the working device is then diced again below and above the working device to create a chip with a width of 7-10 mm (step 4). This chip is then placed in a special fiber pigtailing measurement setup. In this setup the fibers can be glued to the device whilst simultaneously optimizing the fiber-chip coupling loss (step 5). The chip with the attached fibers is then glued onto a ceramic carrier substrate (step 6) followed by the wire bonding of the chip using aluminum bond wires. A packaged chip is shown in Figure 5.10. Clearly visible are the fiber arrays that have been glued to both sides of the chip and the glass rails on top. Also the ceramic chip carrier and the bond wires that lead from the optical chip to the carrier can be identified. The small scale of the optical devices is also evident from this picture: the chip measures only 10 by 7 mm but already contains 10 individual devices. In the inset 3 devices consisting of 8 resonators each are shown. The bondpads measure 300 by 350 μm.

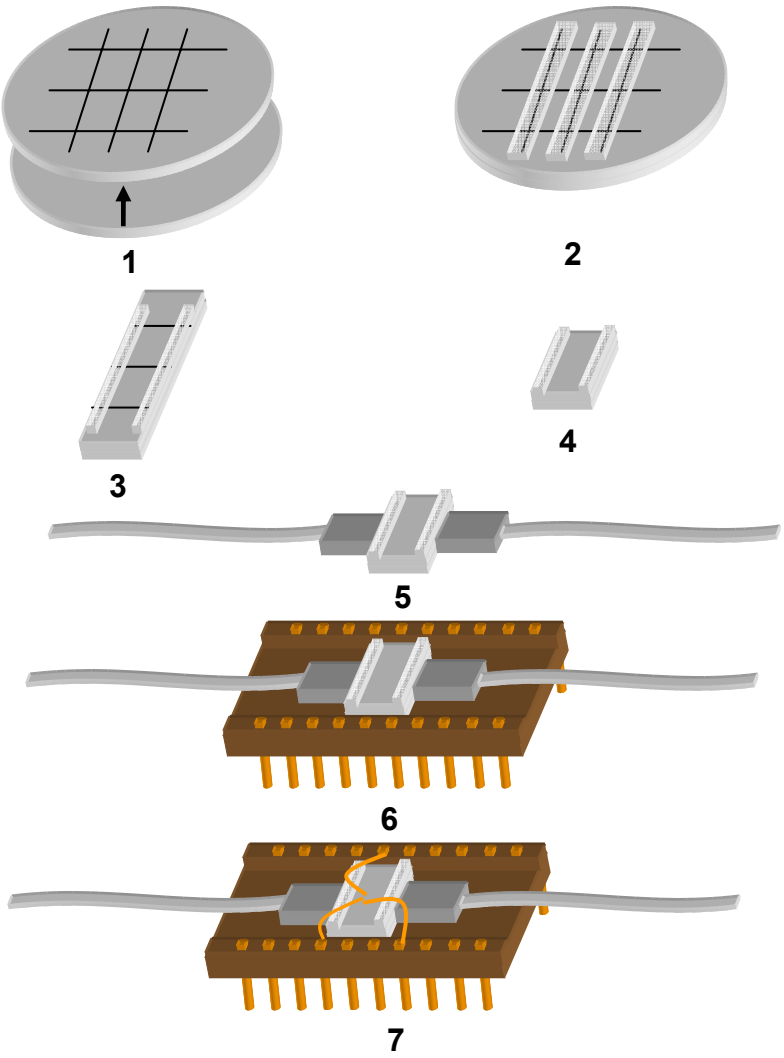

Figure 5.9. Pigtailing of an optical chip.

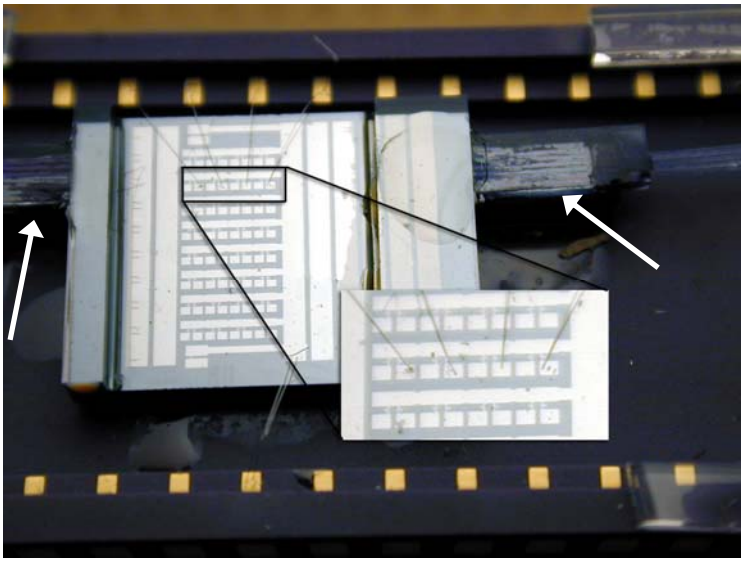

Figure 5.10. Pigtailed and packaged chip. The fiber arrays (white arrows) are glued to the glass rails on top of the chip. The inset shows a close-up of the wirebonds that connect to the carrier chip.

5.3.3 Mask layout

The biggest concern when fabricating vertically coupled micro-resonators using contact lithography lies in the alignment of the resonator to the port waveguides. With the KARL SUSS MA 56M mask aligner that was used for the lithography an alignment error of less than 0.5 μm can be achieved in theory (specification says 0.25 μm). This, however, often requires many attempts before succeeding, making it a very laborious and unreliable process. More often than not alignment errors in excess of 1 μm were obtained, and could be as bad as the 2 μm misalignment shown in Figure 5.11.

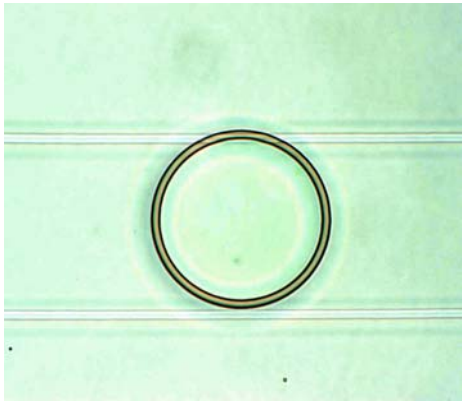

Figure 5.11. A misaligned microring resonator

The effect of this misalignment can be quite severe as shown in Figure 5.12a. If for instance the TEOS SiO_2 layer between the resonator and the port waveguide is 1 μm and the resonator power coupling coefficient ($=\kappa^2$) designed to be ≈0.5 then a misalignment of 0.5 μm can lead to a $\Delta\kappa^2$ as high as 0.3. In Figure 5.12b where the dropped power is plotted as a function of the two coupling coefficients for a resonator with R=50 μm and α_{dB}=1.5 dB/cm it can be seen that such differences can lead to a very large reduction of the dropped power.

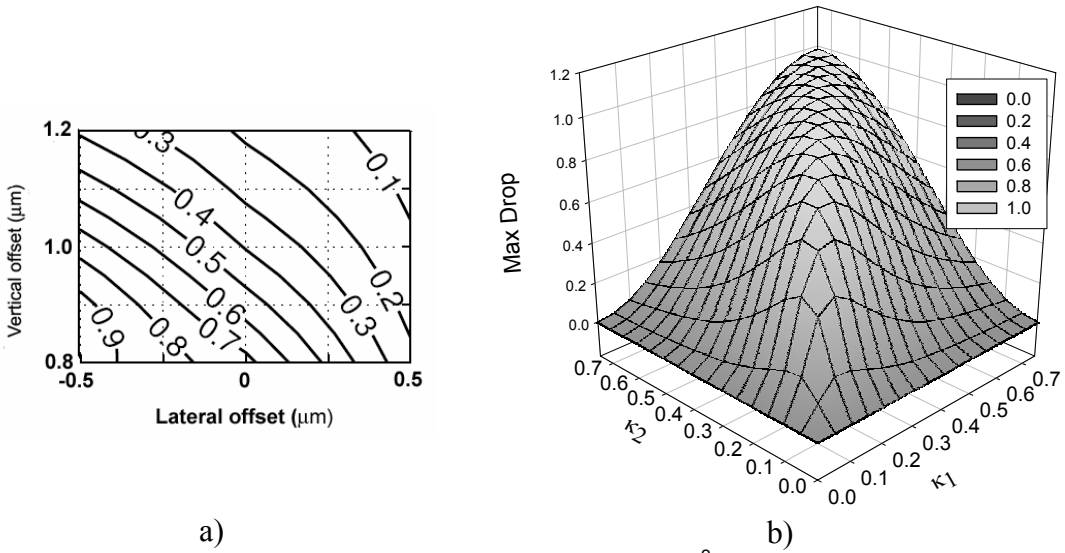

a) b)

Figure 5.12. Close-up of Figure 3.20a showing the coupling κ^2 as a function of the lateral and vertical offset a). A difference in coupling coefficients can have a detrimental effect to the maximum dropped power of the resonator b).

To reduce this problem a built in misalignment, where the resonator is offset in one direction with respect to the port waveguides, was introduced into the masks that were used to create the vertically coupled resonator devices. The layout of these masks, of which two types are shown in Figures 5.13 and 5.14, is similar to the layout used for the laterally coupled devices with a standardized column width and device group size, a central alignment bar with test structures, and dice lines. Instead of varying the gap for the 6 device groups in a single column, however, a variation in the alignment error is introduced. Within a single group the devices are all equal but for a variation of the lateral distance between the resonator and port waveguides called the "symmetric offset" which is also shown for reference in Figure 5.13b. In Figure 5.13a a mask is shown that was used to create resonators that have port waveguides on opposing sides as shown in Figure 5.13b. In this mask the alignment is varied in increments of 0.5 µm between -1.5 µm and 1.0 µm. Although this implies, by definition, that $5/6^{th}$ of the devices will always be misaligned it also reduces the misalignment for one set of devices in the column to 0.25 µm or better. However, due to the fact that there are four columns in the mask and the small size of the resonators, meaning that many are present in a single group, this can still lead to a substantial number of working devices. The same approach of using built in misalignments is also used in the mask layout of newer devices with port waveguides that are cross-coupled to the resonator as shown in Figure 5.14b. Due to that fact that the waveguides are now susceptible to alignment errors in the vertical as well as the horizontal direction, however, the alignment has to be varied in two directions as shown in Figure 5.14a. This means that although properly aligned devices can be fabricated these represent only $1/36^{th}$ of the total number of fabricated devices.

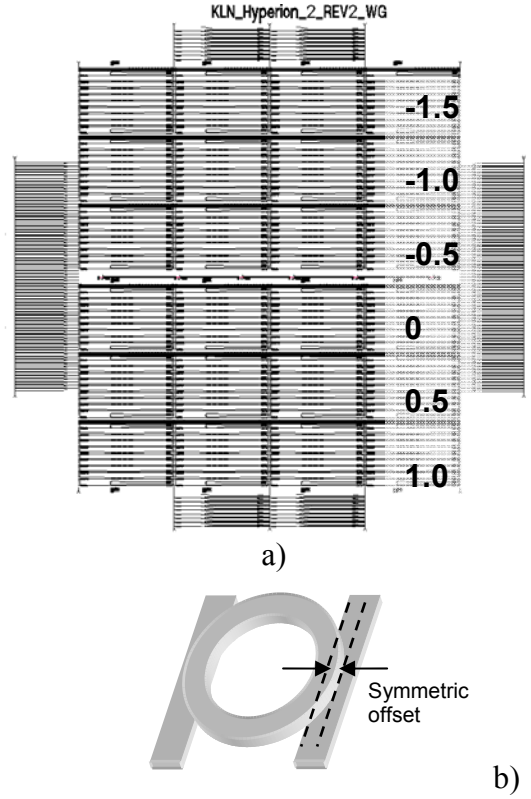

Figure 5.13. Mask layout a) for side coupled resonators b). Also shown is the definition of the symmetric offset of a resonator. This is the distance between the center of the resonator guide and the center of the port waveguides.

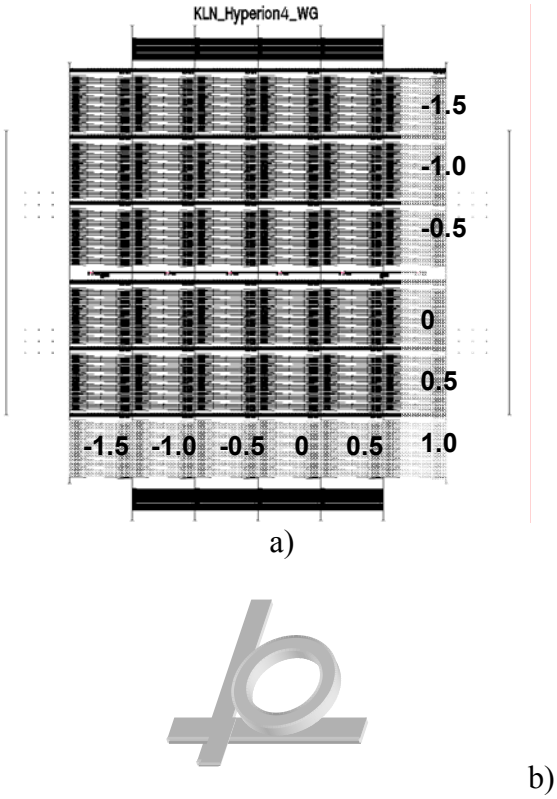

Figure 5.14. Mask layout a) for cross coupled resonators b).

5.4. Fabrication and mask design of vertically coupled resonators defined using stepper lithography

5.4.1 Stepper lithography and mask design

As pointed out in the previous section, only 1/36th of the total number of fabricated devices can be properly aligned when building cross-coupled micro-resonators using contact lithography. This is not necessarily a problem when small devices, consisting of one or two microring-resonators, are built. Assuming a realistic average device height of 500 μm then, when using 6 columns, 20 devices can fit in the 1 cm^2 area allotted to a single group. Because the devices are, on average, only 1.5 mm in width (largely due to bends, tapers etc), the number of columns can even be tripled to 18, giving a total number of 60 functional devices per wafer, which gives more than enough devices for redundancy and parameter variations. More complex devices such as for instance the later discussed OADM and λ-Router, have a height between 1.5 and 2 mm and a width of about 5 mm. At most 10 to 12 of these devices can therefore be put on 1 cm^2 which leaves almost no room for redundancy. Considering the fact that inevitably some of these devices will be damaged during fabrication [132], getting sufficient yield (or even functional devices) can be a problem.
In collaboration with ASML Netherlands B.V [133] a solution was therefore sought in the use of wafer stepper lithography. Contrary to contact lithography where a single mask exposes an entire wafer in a single step, a wafer stepper exposes only a small fraction of the wafer by projecting a selected area (the image) of the mask (the reticle) onto the wafer through a series of lenses as is shown in Figure 5.15. By moving the wafer in the x- or y- direction several locations on the wafer can by exposed in this fashion, producing many identical copies.

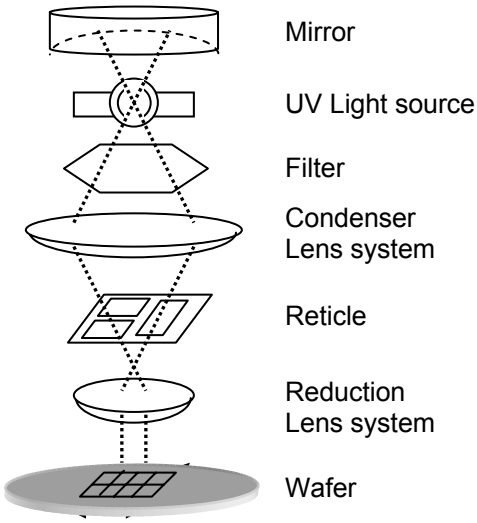

Figure 5.15. Wafer stepper concept: An image located on the reticle is reduced through a series of lenses and projected on a wafer. The wafer can be moved to expose several areas on the mask with this image.

The main benefits of using wafer stepper lithography for vertically coupled microring resonator devices lies in the alignment accuracy of the images projected onto the wafer and the high resolutions that can be achieved. The ASML PAS 5500/275 [134] stepper used to fabricate the OADM and router devices has a resolution better than

280 nm and an alignment accuracy better than 40 nm. The problems related to the accurate positioning of the resonator with respect to the waveguides are therefore essentially removed. The downside of using a stepper however lies in the maximum mask area that can be exposed. To achieve the high optical resolution the wafer stepper reduces the image(s) present on the reticle linearly by a factor of five. Due to this reduction and the image space available on the reticle the maximum area that can be exposed on the wafer is 22 x 27.4 mm for this specific stepper tool. This, however, is the maximum area that can be exposed in a single exposure step and uses up all the image space on the reticle. This poses a problem since the fabrication of a typical microring resonator based device with heaters requires at least three or four mask exposures. The solution is then to either use 4 expensive reticles or use a single reticle with 4 smaller images instead of a single large image. The latter solution then still allows for a roughly 10 by 10 mm area to be exposed by these images.

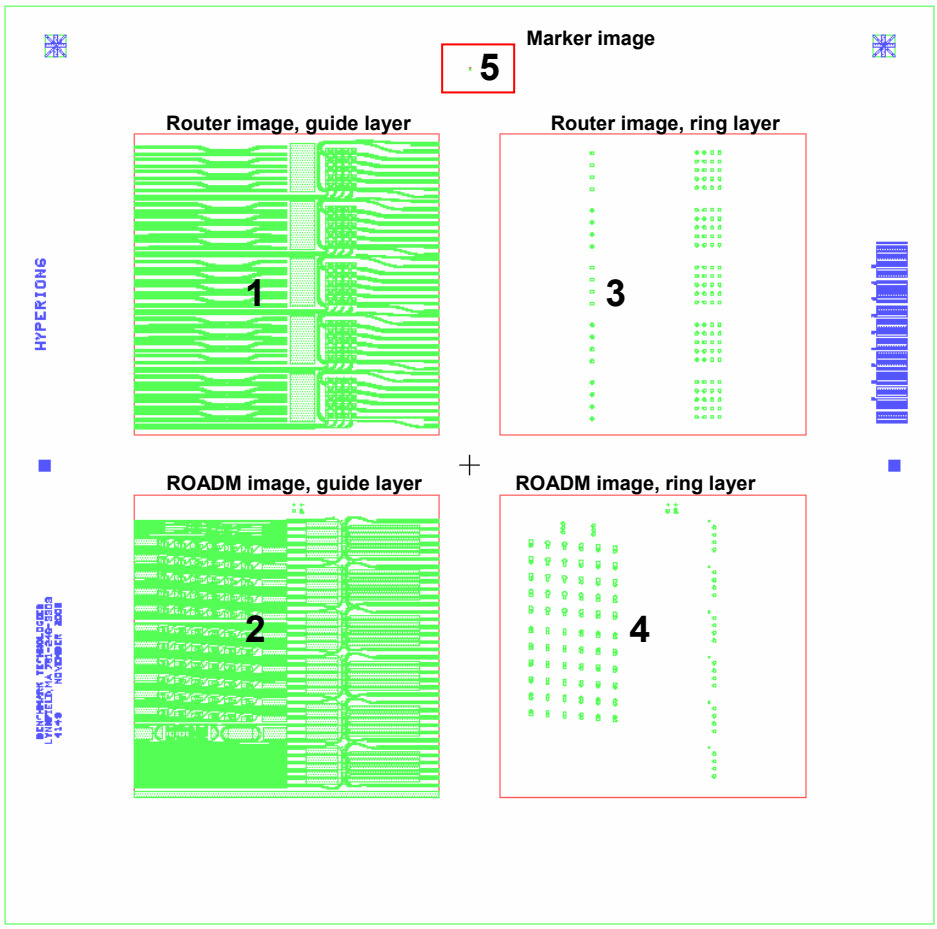

Figure 5.16. Layout of a mask (reticle) used in the PAS 5500/275 wafer stepper. In total 5 images are present in this reticle. The stepper can select one of these images to expose a certain area on a wafer.

Instead of using the stepper lithography for the definition of all layers in the device a more efficient method can also be found, based on alignment accuracy requirements. Based on the results of the OADM devices fabricated in the "Vertical I" process the decision was made to improve the OADM and router devices built using the stepper lithography by adding an additional gold electrode layer on top of the heaters. In addition the newer designs added vertical tapers to reduce the fiber–chip coupling losses. A total of 5 mask exposure steps are therefore required:

1. Definition of the vertical tapers
2. Port waveguide definition
3. Resonator waveguide definition
4. Definition of the chromium heaters
5. Definition of the gold electrodes

Of these five steps, however, only the alignment of the second and the third layers is critical. It is therefore possible to use a hybrid approach, using stepper as well as contact lithography. With this hybrid approach only two stepper wafer exposures are required per device. Using a total of four images on the reticle it is therefore possible to create two unique device groups that each measure 10 by 10 mm instead of only one of that size. The layout of the images on the stepper reticle is shown in Figure 5.16. Images 1 and 3 define the port waveguides and resonators of a device group that contains several routers respectively. Images 2 and 4 are used for a device group that contains several routers in addition to several types of test structures.

If in the original 5 mask exposure steps only step 2 and 3 use stepper litho then a problem will occur since the stepper cannot align to the vertical taper structures defined by the first exposure step. However, it is possible to do the reverse: aligning a contact mask to structures defined with the stepper. An additional exposure step is therefore added to create the exposure sequence written in Table 5.2.

Table 5.2. Mask exposure sequence. The router does not use vertical tapers. Exposure step 2 is therefore left open for the router.

	OADM	Router
1	Stepper reticle, Image 5	Stepper reticle image 5
2	Contact mask, Vertical tapers	--
3	Stepper reticle, Image 2	Stepper reticle, Image 1
4	Stepper reticle, Image 4	Stepper reticle, Image 3
5	Contact mask, Chromium heaters	Contact mask, Chromium heaters
6	Contact mask, Gold leads	Contact mask, Gold leads

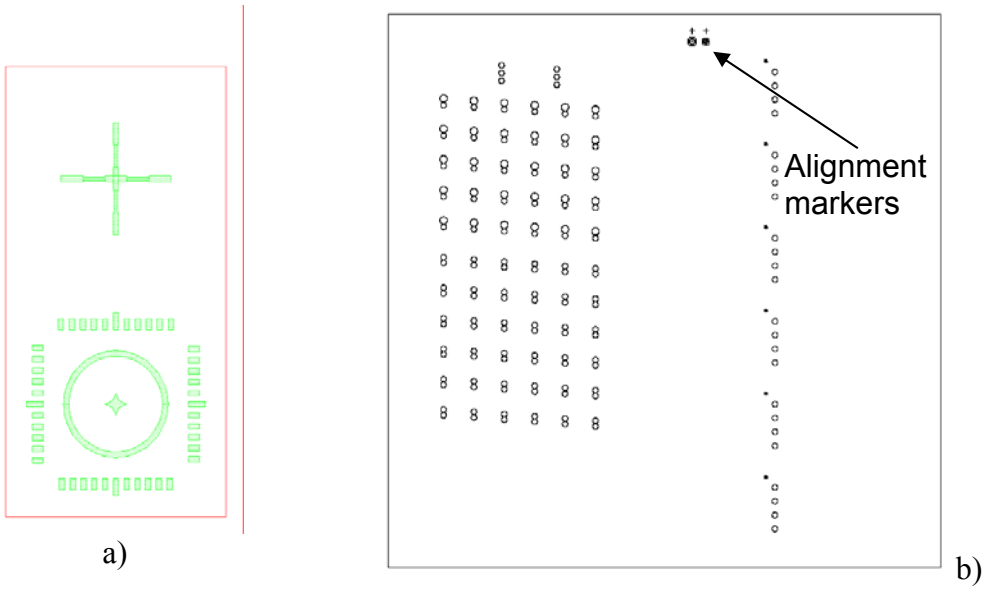

a) b)

Figure 5.17. Alignment markers in the reticle images help to align the contact mask.

In the first exposure step the wafer stepper is used to define ASML-specific alignment markers that are used to align all future images. In addition a special marker, located in reticle image 5 (see fig. 5.16) and shown enlarged in Figure 5.17a, is placed on the wafer in two locations: -25000, -500 and +25000, -500 (x,y-in microns, offset relative to the center of the wafer). To these markers the contact mask that defines the vertical tapers is then aligned.
During the second exposure step the contact mask, which defines the vertical tapers for the OADM devices, is aligned to these markers. The following two critical stepper exposure steps 3 and 4 that define the waveguide and resonator layers use the ASML markers created in step 1. Next, in the fifth exposure step, the mask used by the contact lithography to define the chromium heaters is aligned to the markers present in the OADM resonator reticle image which is shown enlarged in Figure 5.17b. The mask used in this step is also shown in Figure 5.18 to show how the various device groups are positioned across a wafer. Each of the squares visible on the mask represents a device group: 58 OADM groups and 2 router groups. The layout follows the typical pattern of a wafer stepper where many identical device groups are created adjacent to one another in consecutive exposure steps. The sixth and final exposure uses a similar mask to define the gold electrodes. In this instance the mask is aligned to alignment markers created in the chromium heater layer.

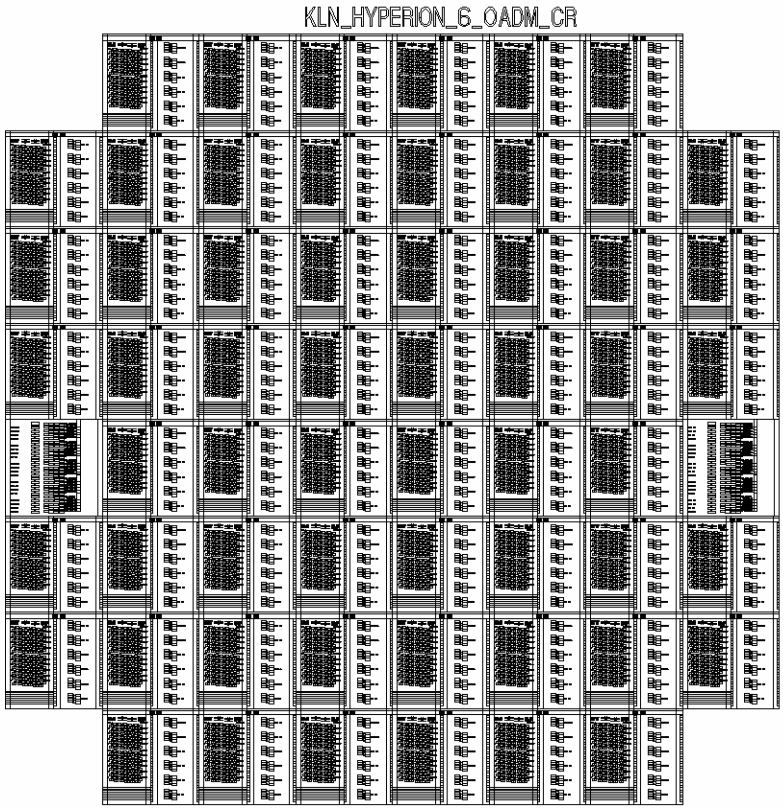

Figure 5.18. Layout of a mask used for contact lithography. The typical pattern produced by the stepper, creating many of the same images side by side which also dictates the layout of this mask, is clearly visible.

5.4.2 Fabrication

The fabrication process used to build vertically coupled resonators using stepper lithography is by far the most complicated due to the fact that the contact and stepper lithography have to be combined in a single process. In addition vertical tapers, an additional gold electrode layer and chemical mechanical polishing (CMP) have been added to improve overall device performance. Due to the many processing steps the fabrication flow described in the following text is separated into three sections. In the first section the processing steps for creating the initial alignment markers and vertical tapers are discussed. The second section discusses the steps required to create the port and resonator waveguides and in the final section the steps required to create the heaters and electrodes are described.

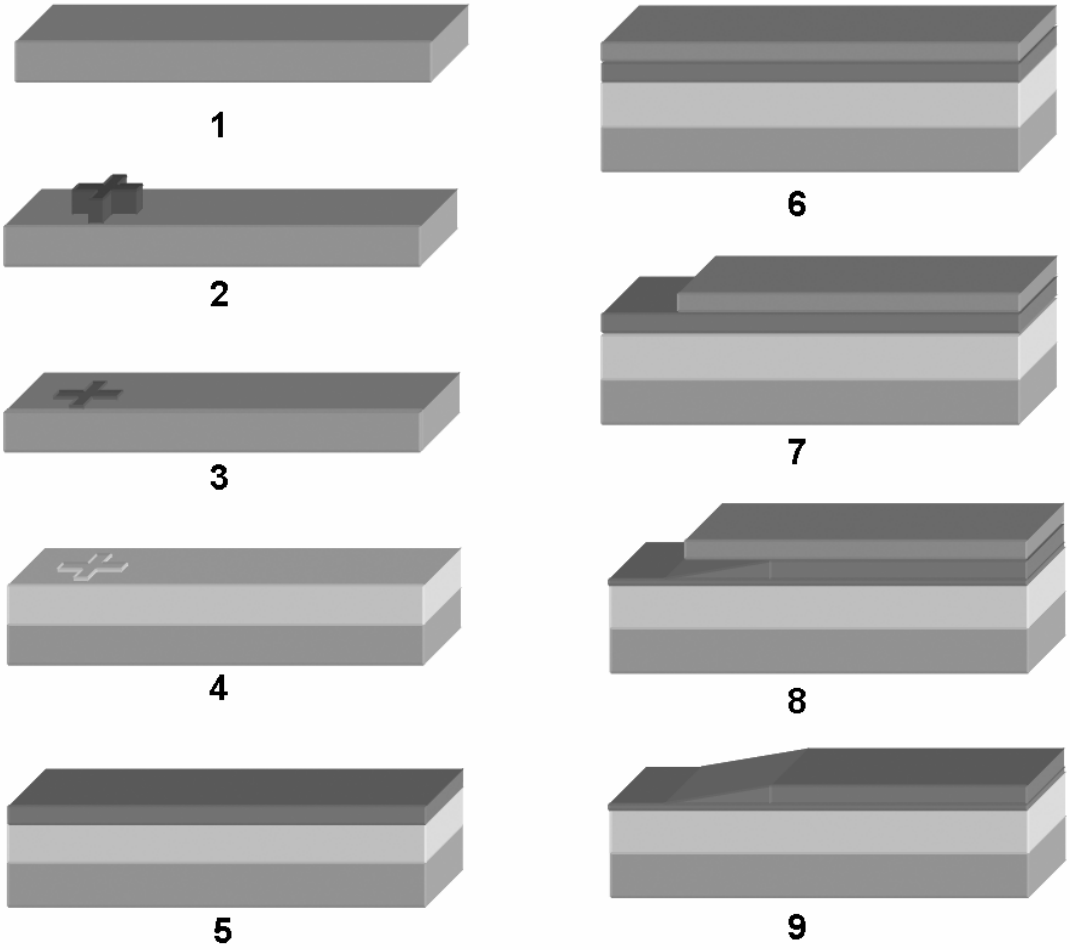

Figure 5.19. Process flow showing the steps required to make the alignment markers and the vertical tapers in the Si_3N_4 layer that will hold the port waveguides.(Process: Vertical II, using contact+stepper lithography)

Figure 5.19 shows the process flow to create the markers and vertical tapers.
The process commences with a 4 inch silicon wafer (step 1). Using the wafer stepper the ASML specific alignment markers and contact-to-stepper alignment markers are patterned in resist (step 2). These patterns are then etched to a depth of 120 nm using RIE on a PlasmaTherm 790 with a mixture of CHF_3/O_2 (step 3). The etch depth in the silicon is critical for the alignment performance of the wafer stepper. The alignment procedure uses the differences in optical path length between the etched and non-

etched regions in the marker, shown in Figure 5.20. A deviation of the 120 nm etch depth will therefore result in degraded alignment performance.

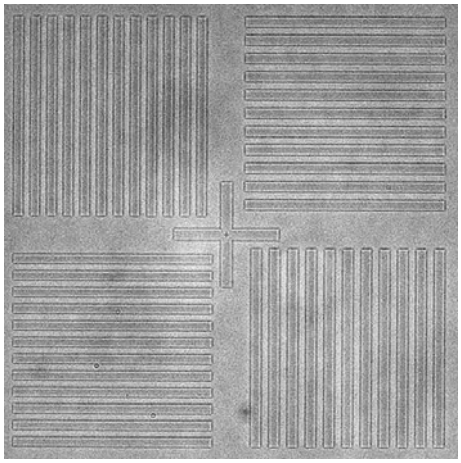

Figure 5.20. Optical microscope image of an ASML alignment marker etched in silicon used for the alignment of the wafer stepper.

After etching the markers the wafer is thermally oxidized at 1100 °C in a steam oxidation furnace until an oxide thickness of 6 μm is reached (step 4). Normally an oxide thickness of 8 μm is preferred to ensure that there is no leakage of light into the silicon substrate. However, alignment tests with the stepper showed a degraded performance of the alignment at this thickness. Since simulations showed no increase in leakage to the substrate for a thinner oxide buffer layer of 6 μm, this thickness was used instead of the 8 μm to improve the alignment accuracy. On top of the thermal SiO_2 a 140 nm thick layer of LPCVD Si_3N_4 is deposited (step 5). On top of this layer a sacrificial layer is then deposited (step 6). In this layer holes and slots are defined using contact lithography and subsequently etched down to the Si_3N_4 layer using wet etching (step 7). Wet etching of the Si_3N_4 is then used to create a slowly tapering region by under etching of the Si_3N_4 masked by the sacrificial layer (step 8). After removal of the sacrificial layer (step 9) the unmasked region of the Si_3N_4, which is etched down to a thickness of 70 nm, will form (after etching of the waveguides) a thin lead-in waveguide that is well matched to the modal field of a small core fiber. The tapered region etched in the masked Si_3N_4 then forms a vertical taper that, in combination with a horizontal taper, adapts this modal field to the modal field of the 140 nm thick port waveguides.

Figure 5.21 shows the next steps, used to create the port and ring resonator waveguides, of the fabrication process. In the Si_3N_4 layer with vertical tapers (the actual tapers are not shown in the figure) created in process step 9 the waveguides are defined in resist using stepper lithography (step 10). Subsequently the waveguides are etched by etching through of the Si_3N_4 using RIE (step 11). A 1 μm thick layer of TEOS SiO_2 is then deposited at 700 °C and annealed at 1100 °C for three hours (step 12). This layer is then chemically mechanically polished for 90 seconds using a colloidal suspension of ≈30% amorphous silica, with a diameter of 25 nm, stabilized in an acid medium (step 13). The CMP removes ≈33 nm of TEOS while smoothing the "bumps" in the TEOS, made by the Si_3N_4 waveguides underneath, from a height of ≈150 nm down to a height of ≈5 nm.

On top of the TEOS SiO_2 a 180 nm thick layer of LPCVD Si_3N_4 is deposited (step 14). In this layer the microring resonators are defined in resist using stepper lithography (step 15) and are etched using RIE (step 16).

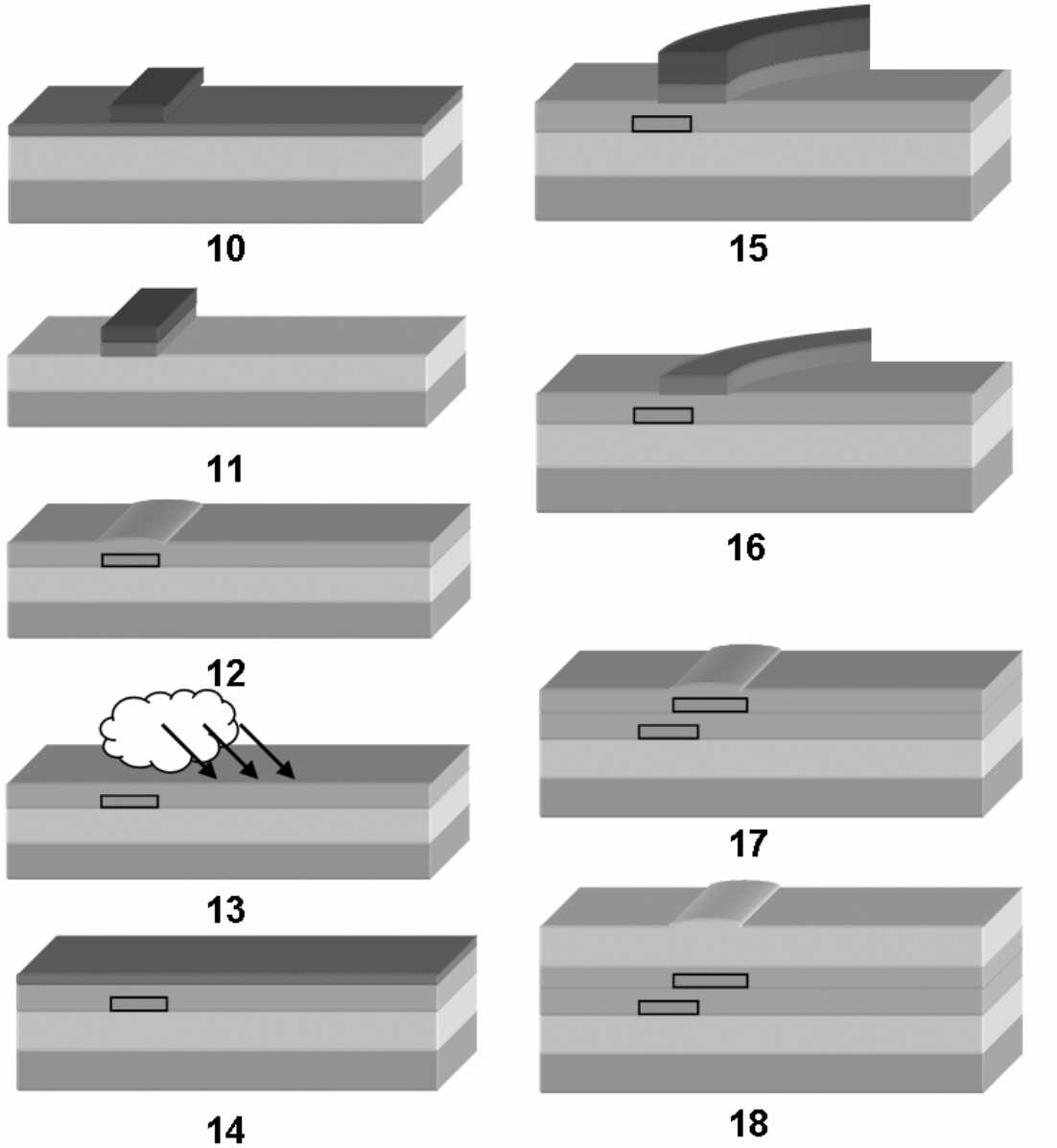

Figure 5.21. Process flow showing the steps required to make the port and resonator waveguides in Si_3N_4. (Process: Vertical II, using contact+stepper lithography)

A 0.5 μm thick layer of TEOS SiO_2 is then deposited and annealed (step 17). On top of the TEOS SiO_2 a top cladding of 3.5 μm PECVD SiO_2 is deposited after which the wafer is annealed for the third time (step 18).
In microscope images taken of the devices after processing step 15 the advantages of the stepper lithography are clearly visible. In Figure 2.22 a perfectly aligned microring resonator is shown which would be difficult to achieve when using only contact lithography. In Figure 2.23 the high resolution of the stepper is demonstrated: the gap between the two resonators measures less than 300 nm but is fully opened.

Figure 5.22. Stepper lithography provides perfect alignment of the resonator and port waveguides.

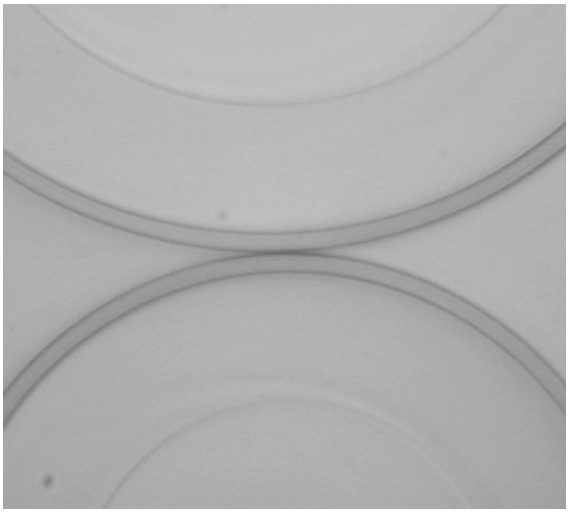

Figure 5.23. An open gap in the coupling region between two resonators of less than 300 nm can be created.

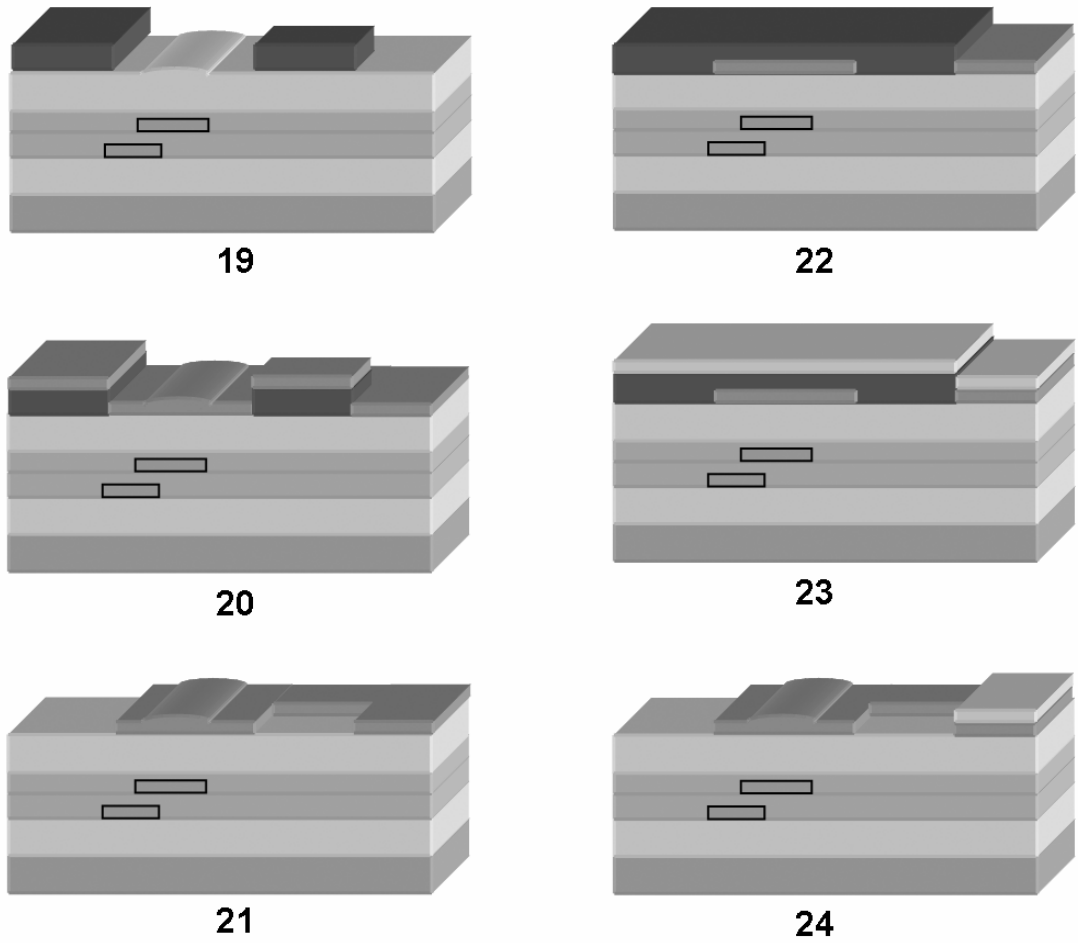

Figure 5.24. Final steps of the process flow showing the steps required to make the chromium heaters and gold electrodes. (Process: Vertical II, using contact+stepper lithography)

Figure 5.24 shows the final steps of the fabrication process. The chromium and gold metallization layers used to create the heaters and electrode wires are created using lift-off. For the chromium heaters the layout is first patterned in resist (step 19) using contact lithography. Next a 200 nm chromium layer is deposited (step 20) which is

removed using lift-off of the resist (step 21).The gold electrodes are fabricated in a similar fashion (steps 22-24) after which the fabrication process is completed.
The SEM micrograph in Figure 5.25a shows a top view of a second order microring resonator that has been realized using this process in which the heater and electrode metallization layers can be discerned. A close-up of the coupling region between the two resonators is given in Figure 5.25b. Here the different layers of the device, from thermal SiO_2 to chromium metallization are clearly visible.

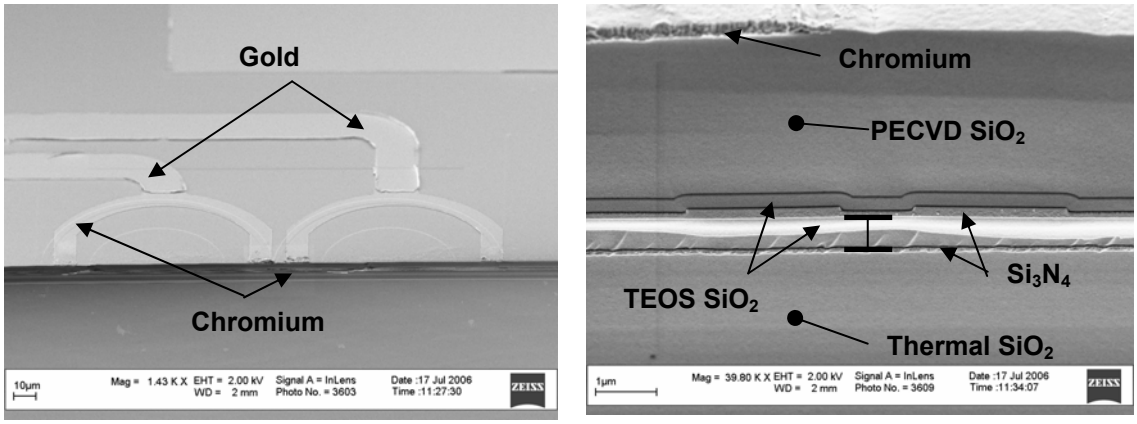

Figure 5.25. Top view of a second order resonator filter showing the metallization layers a) and a cross-section b) of the coupling region of this resonator showing the numerous layers in the device.

A top view of a completed wafer is shown in Figure 5.26. Some of the devices on this wafer, like those fabricated using only contact lithography, have been packaged. For this the same process was used as described in Section 5.3.2. However, due to the increased number of bondwires and the long distances that need to be made to connect these to the pads on the ceramic carried that are required for these devices an "extender board" was designed. This extender board, which is also visible in the pigtailed and packaged device shown in Figure 5.27, consists of several gold leads on a glass substrate. Because the bondwires only need to bridge the gap between the extender and router bondpads on one side and the extender and pads on the carrier on the other side the length of the bondwires remains small.

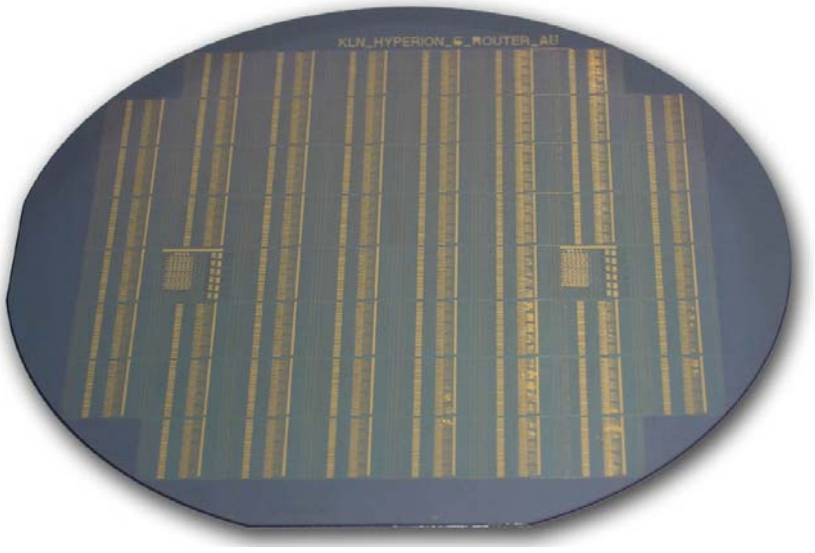

Figure 5.26. Fully processed wafer.

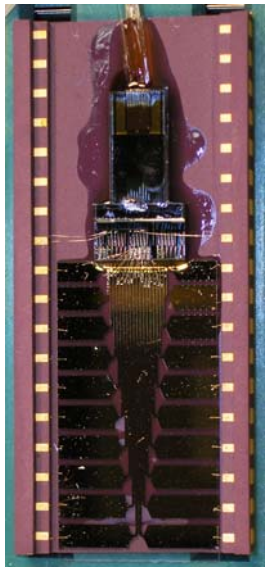

Figure 5.27. Pigtailed and packaged device.

Chapter 6

Microring-resonator building blocks

In this chapter the basic microring resonator building block is introduced. This building block forms the basis of more complex devices such as the ROADM and λ-router described in the following chapter. It is also used in the wavelength selective switch which, because it is used as a subcomponent in the NAIS transceiver and the λ-router, is a building block in its own right and is therefore also discussed in this chapter.

6.1 Introduction

About half of the work that is described in this thesis was carried out within the NAIS project. This project, which was previously described in Chapter 1.4.1, aimed to create an integrated optic WDM-Transceiver for application PON-Networks. As was already shown in Figure 1.5 this transceiver is a highly integrated, highly complex component that combines many functions, such as modulators, filters and switches on a single chip. A simple implementation of this device, able to receive and send data on four different channels (using a total of 8 channels), in which all functions have been implemented using microring resonators is given in Figure 6.1 [135] The main features on the chip are a λ-filter and modulator section used for outgoing (upstream) communication and a section with a channel selector comprised of several wavelength selective switches that can select a single channel from incoming (downstream) communication.
The section for upstream communication uses an array comprised of four MRs to filter out distinct wavelengths from a broadband light source. One or several of these wavelengths are then modulated to create the upstream signal.
For the downstream signal a point of concern is the fact that the polarization state of this signal is not known. This is no problem when the microring resonators used, have polarization independent behavior. However, it is difficult to make polarization independent microring resonators in silicon nitride, the material of choice for this device. The channel selector is therefore implemented using polarization diversity (also see Chapter 8) where the TE and TM polarization of the signal are operated on individually. To this end the polarizations are first separated after which the TM signal is converted to TE. The two TE polarized signals are then operated on by two identical switch matrices as shown in the figure.

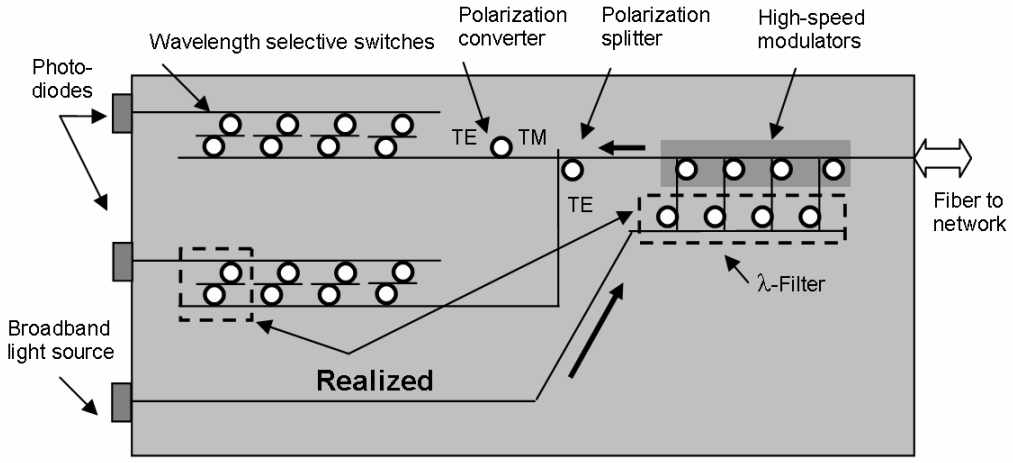

Figure 6.1. Implementation of the NAIS 4-channel WDM-Transceiver for use in PON Networks that is exclusively comprised of microring resonators.

The separation of the TE and TM polarization with a resonator is fairly straightforward since it only requires a resonator that cannot go in resonance for the TM polarization, for instance by ensuring very high cavity losses for the TM polarization. Making a polarization converter based on a microring resonator is more complicated, however, but can be achieved by using a microring resonator that has sloped resonator sidewalls [136-138]. Because of the polarization diversity approach the resonators only have to be optimized for the TE polarization, making the overall

design simpler and easier to fabricate. In fact, in the implementation that is shown most resonators, except those used for modulation and polarization conversion, can then be implemented using the same type of resonator.
This resonator is the basic "resonator building block" used in most devices described in this thesis. In Section 6.2 the design of this resonator is presented, followed by the characterization of a number of different resonators in Section 6.3. In this section the thermal tuning of these resonators is also investigated. In Section 6.4 the design and characterization of a wavelength selective switch are discussed. This switch is one of the realized sub-components of the NAIS transceiver, where it is used in the channel selector. The basic principle behind the switch, which is based on the overlap of the resonance wavelengths of two cascaded resonators, is also found in the λ-router which is presented in the next chapter. As such the switch can also be seen as a building block because the same considerations that go into the design of a single switch also largely apply to the switch matrix used in the router.

6.2 A vertically coupled microring resonator based building block

The basic microring resonator building block referred to in the introduction consists of a vertically coupled microring resonator that is made tunable using a thin-film metal heater. The ring and port waveguides of this resonator are made in Si_3N_4 embedded in SiO_2. As stated in Chapter 5.1 these materials were chosen for their high index contrast of ≈0.55, their low optical loss and high material stability.

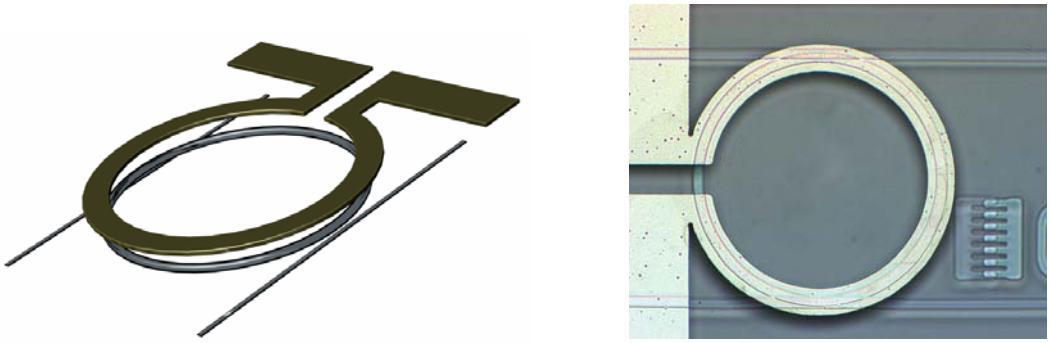

a) b)

Figure 6.2. Isometric rendering a) and a realized version b) of a vertically coupled MR building block that has side-coupled port waveguides. The marker next to the resonator is used to check the vertical alignment of the resonator.

a) b)

Figure 6.3. Isometric rendering a) and a realized version b) of a vertically coupled tunable MR building block that is cross-coupled to the port waveguides. The marker next to the resonator measures the vertical as well as the horizontal alignment of the resonator.

In early, comparatively simple devices such as the wavelength selective switch, the microring resonator in the building block used side-coupled port waveguides as shown in Figure 6.2. In more recent devices such as the OADM and the λ-router mainly cross-coupled resonators [25], as shown in Figure 6.3, have been used because of the ease with which these resonators can be placed in a compact *mxn* matrix configuration [139]. Aside from the coupling to the waveguides, however, the geometrical design of both resonators is identical.

The cross-section of the coupling region with all the relevant design parameters relating to the geometrical design of the microring resonator building block is shown in Figure 6.4. A description of these parameters is given in Table 6.1 and Table 6.2 gives the refractive index of the materials that are used. In the following sections the choices made to arrive at the values of these parameters are discussed in more detail.

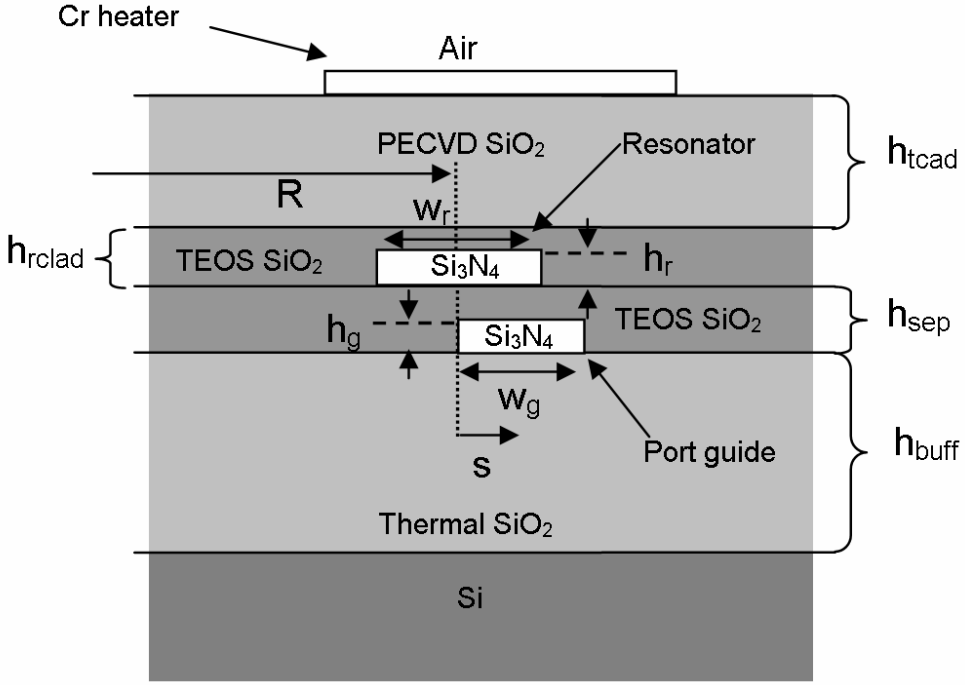

Figure 6.4. Si_3N_4/SiO_2 microring resonator cross-section across the coupling region. All relevant parameters and materials are depicted.

Table 6.1. Microring resonator design parameters used for the building block

Parameter	Description	Typical value (μm)
h_{tclad}	PECVD top cladding thickness	3.5
h_{rclad}	TEOS top cladding thickness	0.5
h_{sep}	TEOS separation layer thickness	1.0
h_{buff}	Thermal SiO_2 Buffer layer thickness	>5.0
h_g	Port waveguide thickness	0.14
w_g	Port waveguide width	2.0
h_r	Ring resonator waveguide thickness	0.18 – 0.19
w_r	Ring resonator waveguide width	2.5
s	Offset between ring resonator and port waveguide	1.0 -2.5
R	Ring resonator radius	50

Table 6.2. Refractive index of the materials used in the microring resonator building block

Material	Refractive index @1550 nm
Silicon	3.47
Thermal SiO_2	1.452
Si_3N_4	1.979
TEOS SiO_2 (Annealed)	1.45
PECVD SiO_2	1.46
Chromium (for heater)	4.13+j5.03
Gold (for electrodes)	0.357+j10.4

6.2.1 Dimensions of the oxide layers

The vertically coupled microring resonator consists of several layers of silicon oxide in which the Si_3N_4 ring and port waveguides are embedded. The thickness of the various layers of silicon oxide is largely independent of the resonator design as the thickness of these layers is mainly determined by materials constraints and the need to avoid leakage to the substrate and heater.

The thermal oxide buffer layer between the port waveguide and the silicon substrate has to be thick enough to prevent leakage. For the given port waveguide dimensions this leakage becomes noticeable (i.e. significant change in propagation loss) for the TE mode at a thickness of ≈4 μm and for the TM mode at t_{buff}≈4.5 μm. At the facets, where these waveguides are tapered and the mode expands this distance becomes even larger. To be on the safe side it is therefore a rule of thumb to use a thermal oxide buffer layer with a thickness >5 μm. All devices discussed in this thesis used a buffer with a thickness of 8 μm with an exception of 6 μm made for the devices fabricated in the "Vertical II" fabrication process due to stepper requirements. An even thicker thermal oxide layer was not used because it has little effect on the losses while significantly increasing the time to grow the layer by wet oxidation of the silicon.
For the resonator there is a similar problem with leakage due to the chromium thin film metal heater on top. Due to the higher confinement of the field in the resonator, a combined thickness of the TEOS and PECVD SiO_2 top cladding layers of >3 μm is sufficient in this case and has been used in some older building block realizations. However, because leakage from the port waveguides also needs to be considered, an additional 1 μm was added to this for safety in more recent building blocks, used in the OADM and router for instance. The top cladding should not be too thin, but also not too thick because this will adversely affect the heater efficiency. The thickness of the top cladding is therefore to a certain extent dependent on the design of the resonator because a more confined field allows a thinner cladding and thus higher efficiency.
In the design TEOS SiO_2 is used as the intermediate layer between the resonator and port waveguides as well as on top of the resonator because of the high optical quality and very good step coverage of this material. This avoids the "voids" directly near the waveguide that may occur when growing other materials such as PECVD SiO_2 and which may increase the propagation losses in the waveguide. As can be seen the total thickness of the two TEOS layers combined is 1.5 μm which is because of the fact

that the TEOS has a very high material stress which may cause cracking at a larger thickness.
The coupling between the resonator and port waveguide is largely determined by the lateral offset s, the radius R of the resonator, and the thickness h_{sep} of the separation layer. As shown in Table 6.1 a thickness of 1 μm was chosen for the separation layer. Although this layer can be thinner, experiments on a number of fabricated devices have shown that this thickness usually gives the best MR performance in the range of lateral offsets that are also given in the table. In addition, if for some reason the coupling of turns out to be lower than expected then it is still possible to increase the coupling by reducing h_{sep} and no new mask design is required.

6.2.2 Dimensions of the resonator and port waveguides

As discussed in Chapter 3.5.1 the design of the waveguide dimensions in a vertically coupled resonator starts with the design of the resonator and then tries to match this resonator to a port waveguide with well chosen dimensions. This design strategy assumes that the dimensions of the port waveguide can be adjusted such that its effective refractive index can be made to match that of the ring resonator.

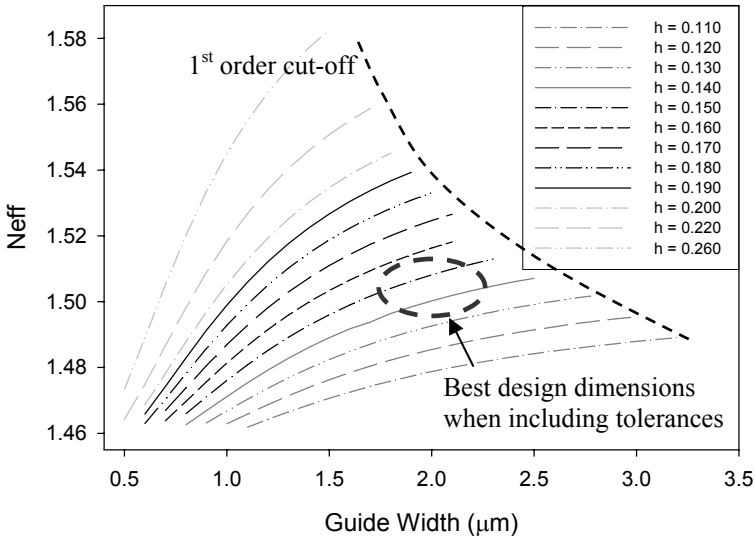

Figure 6.5. Port waveguide *Neff* versus the waveguide height and width. The indicated areas show the dimensions for best phase matching and the best dimensions when tolerances are included.

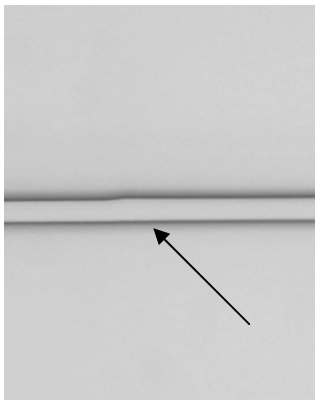

Figure 6.6. Waveguide stitching.

Figure 6.5 shows that, in theory, it is indeed possible to design a monomodal waveguide for a wide range of effective refractive indices. In practice, however, the useful design range was much more limited for several reasons:

- Most of the devices that have been fabricated use masks made at the MESA+ institute for the lithography. One problem of these masks is that stitching in the waveguides may occur, as shown in Figure 6.6. Because the additional waveguide losses induced by this stitching are proportional to the waveguide width, the waveguides should not be chosen too narrow. Another reason for doing so is the fact that, for widths in the order of 1.5 μm, defects sometimes occurred in the masks which can be avoided for larger dimensions.
- Bi-modality in the waveguides needed to be avoided at all cost. For fabricated waveguides a deviation in width and height with respect to the original design

of 0.2 µm and 5 nm respectively is not uncommon. This should therefore be taken into account in the design of the waveguide so that there is some tolerance in the dimensions before the waveguide becomes bi-modal.

- Tests with waveguides of 150 nm and a width of 2.0 µm had shown bimodal behavior in some cases. Although part of this could be attributed to a widening of the waveguides during fabrication, the simulations used to design the waveguide are also not to be trusted completely. The plots shown in Figure 6.5 have been created using the Film Mode Matching solver of Selene. This solver finds a cut-off for the first order mode for a waveguide with a thickness of 140 nm near a width of 2.6 µm. However, the FD generic solver of the same program already shows a first order occurring for a width of 2.2 µm.

Taking all these reasons into account the useful design range, offering sufficient tolerance in the design as well as an *Neff* that is as high as possible, is roughly for a width of 1.7 to 2.2 µm and a height of 130 and 150 nm as indicated in Figure 6.5. In particular a waveguide with a height of 140 nm and a width of 2 µm was chosen out of this range as it offers sufficient tolerance in the waveguide dimensions and still has a reasonably high effective refractive index of ≈1.50. These dimensions also allow for a fairly small bend radius of the port waveguide. As shown in Figure 6.7, the optimum bend radius for this waveguide is around 170 µm. A small radius, as was discussed in Chapter 3.7.3, can be important for the miniaturization of the devices. In most designs, however, instead of the 170 µm radius a more conservative radius between 220 to 250 µm was used. This is because of the fact that a fabricated waveguide can not only be thicker than designed, potentially causing bimodality, but also thinner. As shown in Figure 6.7 for a waveguide with a thickness of 130 nm and a width of 2 µm this can lead to a considerable increase in bend loss if a radius of 170 µm is used. For a radius between 220 to 250 µm, however, the increase in loss is much less severe.

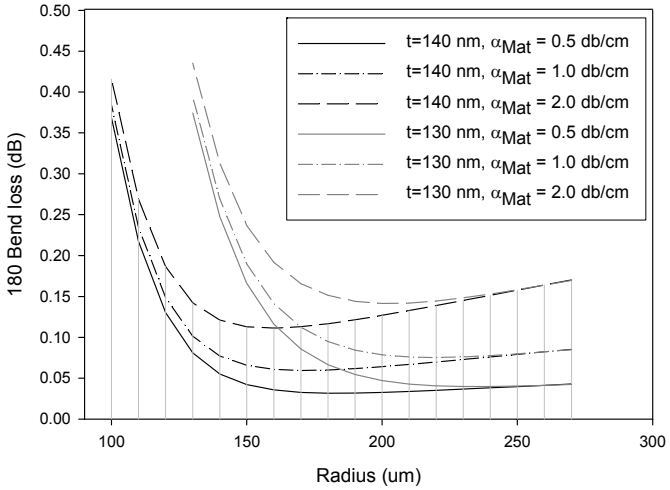

Figure 6.7. Port waveguide 180 degree bend losses as a function of the bend radius for a number of intrinsic waveguide losses (material + scatter loss).

Because the port waveguide has effectively reached its maximum effective refractive index of ≈1.50 at the dimensions of 0.14 by 2 µm it is not possible to follow the design strategy given in Figure 3.17 because the *Neff* cannot be raised without sacrificing the tolerances in the design. Therefore, the ring resonator for the thermally tunable resonator building block had to be designed to match the port waveguide instead of the other way around.

The most important aspect in the design of the ring resonator was to achieve good phase matching with the port waveguide. This is important because it allows for more freedom in the design, due to the fact that a wider range of coupling coefficients is available. Another strong benefit, as was previously discussed in Chapter 3.5.3, is that good phase matching can also reduce the sensitivity to an error in the alignment of the resonator to the port waveguides.
In Figures 6.8a and 6.8b the *Neff* and bend loss of several resonators, with a width of 2.5 μm and a thickness between 175 and 195 nm are given as a function of the bend radius. When looking purely at the phase matching and the bend losses the resonator waveguides with a thickness of 175 nm and a radius of 65 μm would be a good option as these dimensions allow for Δ*Neff* 0.012 and a bend loss of ≈2 dB/cm. However, in the design of the building block it was also important to have a large FSR and therefore a resonator with a small radius. A resonator with a radius of 50 μm and a thickness between 180 nm and 190 nm was therefore chosen instead.

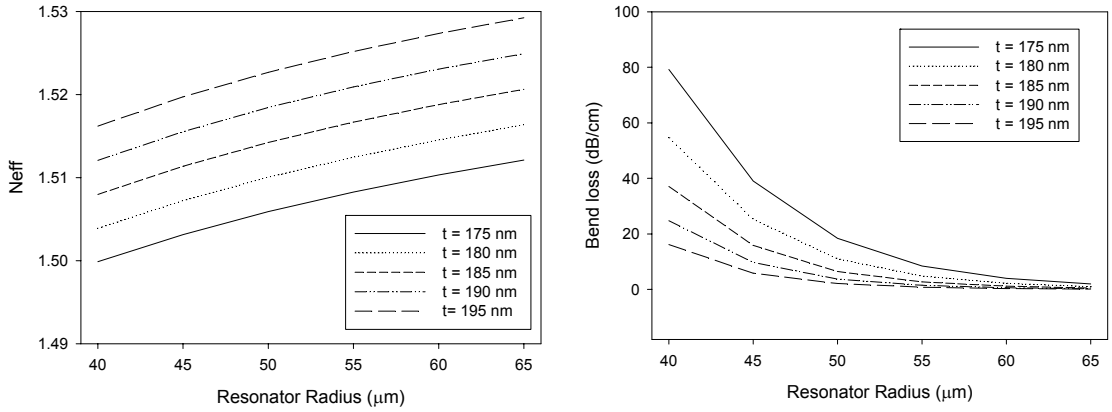

a) b)

Figure 6.8. Ring resonator effective refractive index a) and bend loss b) as a function of its radius and thickness.

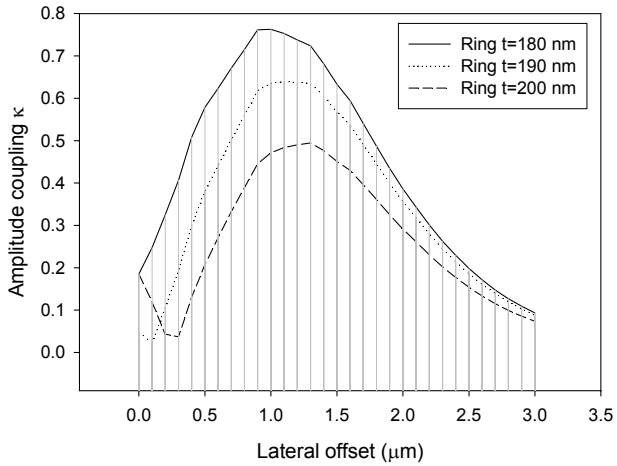

Figure 6.9. Amplitude coupling coefficient as a function of the lateral offset s for a resonator with a thickness of 180, 190 and 200 nm. All resonators have a width of 2.5 μm and a vertical distance to the port waveguide h_{sep} of 1 μm.

Figure 6.9 shows that for both the 180 nm as well as the 190 nm thick resonator an amplitude coupling of at least 0.6 can be achieved. This is important since one of the goals in the design of the building block was to use it for the transmission of 40 Gbit/s signals which, at a radius of 50 μm, requires a κ of at least 0.4. (As a simplification it

is assumed that the maximum capacity of a signal that is sent through the MR is roughly equivalent to the $\Delta\lambda_{FWHM}$ bandwidth of this resonator which, for κ=0.4 is ≈40 GHz. In practice, however, the actual bitrate will also depend on the signaling scheme that is used.)
For the 180 nm thick resonator a coupling higher than this can be achieved across a range for the lateral offset of 1.8 μm while this is 1.4 μm for the 190 nm thick resonator.

Although the usable range of the lateral offset is fairly large for both resonators the 180 nm resonator is the slightly more attractive option since it allows for more variations of the coupling coefficient, through a variation in the symmetric (lateral) offset s as discussed in Chapter 5.3.3, to be implemented in the design. Typically values of s in the range of 1.0 to 2.5 um have been used which, as shown in Figure 6.9, results in a variation of the coupling coefficients of the realized devices between 0.2 and 0.75. In addition the 180 nm resonator is more tolerant to the variations in width and height that inevitably occur in fabricated devices. For instance, if the thickness of the 190 nm resonator is increased by 10 nm then the range in which the coupling of 0.4 can be achieved becomes very small as shown in the figure. When this is combined with a possible misalignment error then a working device at 40 Gbit/s is nearly impossible to obtain. Conversely, when the 180 nm waveguide is reduced in thickness to 170 nm this would increase the bend loss from 10 dB/cm to 34 dB/cm. Although this does for instance increase the insertion loss from 1.1 dB to 3.1 dB (at κ=0.5) this is acceptable because the increase of 2 dB is small compared to the total loss in a device. This loss is typically in excess of 14 dB and is predominantly caused by the not yet optimized fiber chip coupling losses. For these reasons the 180 nm resonator was used as the basic resonator in the thermally tunable resonator building block.

The group index of the resonator waveguide with dimensions of 2 x 0.180 μm is ≈1.747. For the designed resonator with a radius of 50 μm this corresponds to a FSR of ≈4.37 nm (using eq. 2.21). Although this fits the initial design requirement to have the largest FSR possible for the resonator, in retrospect a radius of 55 μm would have been a better choice. At this radius the FSR is 4 nm (500 GHZ) which allows the resonator to be positioned exactly on the 100 GHz channel grid that has been defined for the OADM and Router within the Broadband Photonics project.
In addition the stepper lithography used to fabricate these devices makes the majority of the reasons for designing the port waveguide with the 0.140 x 2 μm dimensions invalid. This is because of the fact that the stepper can image much smaller features in a much more controlled manner (i.e. no large variations in width of the waveguides). It would therefore have been possible to raise the *Neff* of the port waveguide by going to narrower and higher waveguides, thus allowing for smaller resonators.
The reason why neither of these design changes were made in the OADM and Router devices is that, in order to learn from a certain change in the design or fabrication of a device, the number of changes made in this device should remain small. Doing so ensures that at least some devices may work or, if no device works, that the problem can be easily located. Since the OADM and Router were already fabricated in a process that introduced many changes such as vertical tapers, stepper lithography and CMP (which already resulted in a large number of problems during the fabrication of these devices), making further changes to the design of the resonators was considered to be unwise.

6.2.3 Chromium heater design

The devices in which the vertically coupled microring resonator building blocks have been used typically required a tuning range equal to their free spectral range to allow for the selection of any wavelength within this range. Of all the methods of tuning that have been discussed in Chapter 2.8 only thermal and mechanical tuning allow for such large tuning ranges. Of these two methods thermal tuning has been chosen because of the fact that it is considerably easier to implement than MEMS based tuning. In addition the telecom devices such as the OADM and the Router that use these resonators will rarely be reconfigured (change or switch channels) more than a few times per second (or even in a day). The millisecond switching times offered by thermal tuning are therefore more than sufficient.

Heaters used on top of optical waveguides generally consists of a thin-film metal resistor [70] but can also be made using heavily doped poly-silicon [72] for instance. When designing a heater for a ring resonator the general requirements are the same as those for heaters used for straight waveguides:

- The use of a heater should not introduce additional losses in the microring resonator. Since the presence of a metal in the field of a mode introduces very high losses the heater should be placed outside the field of the propagating mode. As shown in Figure 6.9 the losses in the resonator start to noticeably increase below a cladding thickness of 2 μm. With the addition of 1 μm for safety a cladding thickness of ≈3 μm can then be considered as the minimum cladding thickness that is required.

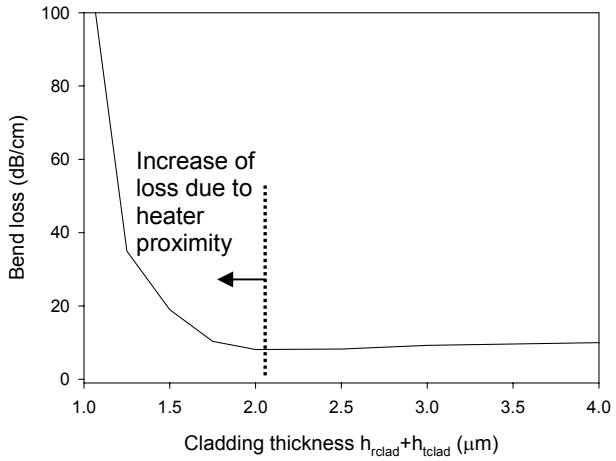

Figure 6.9. Bend losses in a 180 nm thick resonator with a radius of 50 μm as a function of the total upper cladding thickness.

- The heater should also be low power. This means that the change $\Delta Neff/\Delta T$ should be as high as possible in order to reduce the power required to induce a certain change in *Neff*. The low-power criterion is not of essential importance in devices consisting of only a few resonators such as for instance a micro-resonator based switch. However, it does become an issue in designs of greater complexity, such as for instance in the WDM router proposed in the Broadband Photonics project, where multiple resonators need to be tuned simultaneously. The power dissipated in the heaters can then cause problems, such as the heating of the device as a whole (requiring temperature

compensation), or increased requirements for the electronics that drive the heaters. Also, the effects of thermal crosstalk, which may occur when two or more devices with heaters are located in close proximity of each other, are reduced when less power is dissipated in the heaters.

- The thermal tuning should be reasonably fast. Although, as mentioned in the preceding text, fast tuning is not an absolute requirement it does widen the application range of a device if it offers faster tuning of switching. Fast tuning, however, can come at the price of power consumption. A very efficient heater will most likely use some means, such as for instance trenching, to limit the flow of heat away from the waveguide that is tuned. Due to this the cool-down time will also be slower. In the design the need for speed and the low-power requirements will therefore have to be balanced.
- The heater should be reliable: the heater characteristics should not change over time. The choice of the heater material is therefore important as it should allow for high heater temperatures without breaking down and have a good adhesion to the silicon oxide cladding layer. A material that allows for a higher heater temperature can also increase the available tuning range.
- In order to achieve a large tuning range and tuning efficiency it is also important that the heater on top of the heater has a uniform heating distribution. This is because the heater can only be heated up to a certain temperature without damage. The hottest locations in the heater therefore determine the maximum tuning range.

When the heaters were designed the use of a polymer instead of the PECVD and TEOS SiO_2 top cladding was shortly considered due to the high thermo-optic coefficients found in these materials. Typically, polymers have a thermo-optic coefficient that is an order of magnitude larger than the thermo-optic coefficient of silicon oxide or silicon nitride [140]. Since the thermo-optic coefficient of the cladding material influences the total ΔN_{eff} that may be obtained for a certain heater temperature, it is therefore worth investigating these materials. The main problem with the use of polymers as a cladding layer, however, is that they generally exhibit higher losses than $Si_xO_yN_z$ materials. In addition the thermo-optic coefficient of these materials is negative. When combined with $Si_xO_yN_z$ materials that have a positive thermo-optic coefficient, the changes in the index of the layers may then cancel each other out, effectively creating a temperature insensitive device.
In order to find the effects of using a polymer for the cladding layer a simulation was performed in TempSelene [50] using the geometry described in Figure 6.3 where the PECVD and TEOS oxide cladding were replaced with a PMMA layer (n=1.47). The heater width used in this simulation was 10 μm. The simulation showed a change in effective refractive index of approximately $-5.4\ 10^{-4}$ for a heater with a temperature of 100 °C (the silicon substrate, serving as a heatsink, was set at 0 °C in the simulation). The negative sign shows that the polymer has not only cancelled out the positive changes in index in the silicon nitride core and oxide substrate, but in fact dominates the tuning of the effective index of the waveguide. Although the change in N_{eff} is substantial it was still smaller than the $7.6\ 10^{-4}$ change that could be obtained using an oxide cladding. The polymer option was therefore discarded. Even if the polymer cladding had resulted in a change equal to or slightly higher than that of a silicon oxide cladding the latter would have been a more favorable option. This is because most polymers have a low glass transition temperature. (100-160 °C for PMMA).

Therefore, even if the silicon dioxide had had a lower change in refractive index, this would have been offset by the larger possible thermal tuning range for this material.

For the actual geometry a number of heater geometries were investigated [141]. This resulted into two viable heater candidates, shown in Figure 6.10a and 6.10b. Both heaters geometries have a radius R equal to the radius of the resonator underneath and a heater width of 10 μm.

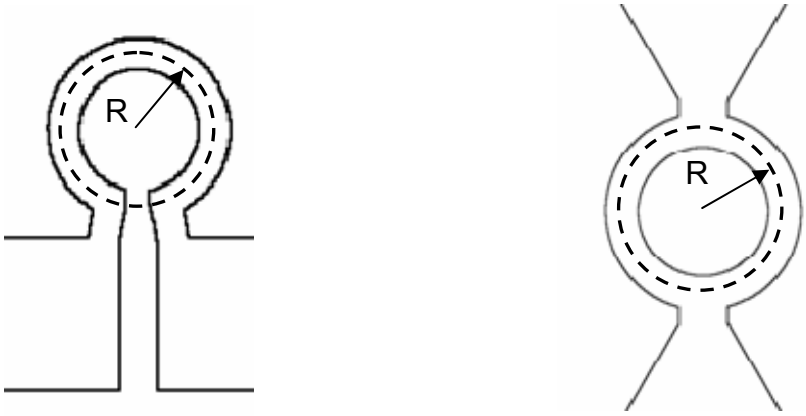

Figure 6.10. An omega a) and circular b) shaped heater geometry for use on top of a microring resonator.

The omega shaped heater shown in Figure 6.10a consists of a single metal strip that is lain out in the shape of the letter Ω. Due to the fact that the strip has a uniform width, the current that runs though it will heat up the strip to the same temperature in all locations. Therefore also most of the resonator underneath, except the part underneath the small gap in the foot of the Ω, will be heated uniformly.
The heating of the resonator underneath the circular heater shown in Figure 6.10b is less uniform. This is because the circular heater is connected from both sides with leads that necessarily have to be twice as wide as the rest of the heater in order to avoid hotspots in the location of the lead connection. Because most of the current in these locations will flow along the edges of this connection, the center part of the connection is heated less. This results in an uneven heating of the heater and the resonator underneath, as is well illustrated by Figure 6.13b. This is especially a problem when the circular heater is used on top of small resonators, for instance with a radius of 25 μm. Here the heater connection can cover a large portion of the resonator. The reduced heating at these locations can then significantly affect the overall tuning performance of the resonator. For larger resonators, however, this is less of an issue. In fact, the positioning of the leads makes the circular heater type more easy to use than the omega heater in certain designs such as the second order resonator filter that was shown in Figure 5.25 or in the racetrack resonator based tunable reflector discussed in Section 6.5.

The omega shaped heater is used as the default heater in the resonator building block design because it is more efficient than the circular heater. One point of concern in the geometry of this heater, however, is the small gap between the two leads. If this gap is too small then the heater may malfunction due to dielectric breakdown, causing sparking between the two leads, when a high voltage is applied to the heater. This can be avoided by careful design of the gap between the leads, however, which can be

chosen such that the heater will melt long before the dielectric breakdown threshold is reached. For instance, if a gap of 10 μm is chosen then the dielectric breakdown will occur at 30 V (the dielectric strength of air is 3 x 10^6 V/m [142]). At this voltage a heater with a resistance of 200 Ohm would theoretically dissipate 4.5W. This, however, is well beyond the point where parts of the heater start to melt.

6.2.4 Heater characterization

Both heater geometries have been implemented using chromium [143]. This material was chosen for its good adhesion properties to silicon oxide and its high melting point of 1907 °C. In addition it has a relatively high resistivity of 1.25 10^{-7} Ω/m (at 20 °C), making it a highly suitable material for use as a heater.
Before using the heaters on actual microring resonator devices they were first fabricated separately, on a test wafer. By testing the maximum allowed heat dissipation in these heaters before the heaters would be damaged a safe operation range could be determined to avoid damaging thermally tunable resonator devices in the future. In addition these heaters were used to determine the temperature dependent resistance of the heaters. This is useful since it is very difficult to measure the temperature of the heaters in situ, on top of a resonator. However, because the resistance of the chromium of the heater changes as a function of its temperature it is possible to measure the temperature indirectly.

To make this possible the test wafer was first heated indirectly in a controlled fashion on top of a hot plate, using thermal paste for improved heat conduction. The temperature of the wafer, and therefore also of the heaters, was measured using an infrared thermometer.
Simultaneously the resistance of a heater was measured using a multimeter. Figure 6.11 shows the measured change in heater resistance relative, normalized to the resistance on an unheated heater, as a function of the applied temperature.

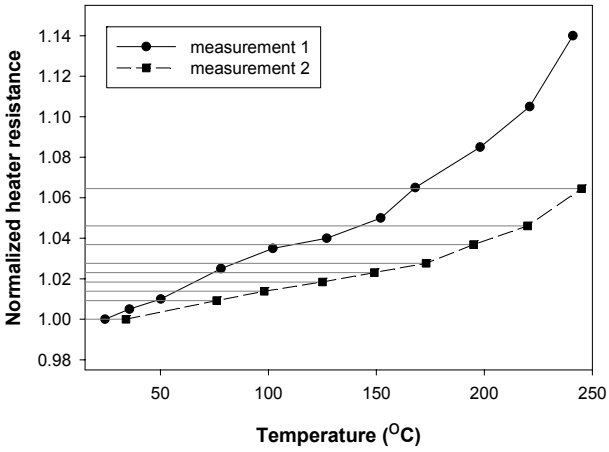

Figure 6.11. Normalized change in heater resistance as a function of its temperature.

As shown in the figure, the change in temperature in the first measurement of the heater is much larger than in the second measurement of the same heater. This change is due to the passivation of the heater during the first measurement run. After this initial "burn-in", however, the heater response is largely stable.

Next, the heater was heated directly, by connecting it to an adjustable power supply. The dissipation in and resistance of the heater were determined by measuring the current through and voltage across the heater. Figure 6.12a shows the measurement results of several measurement runs performed on the same omega shaped heater with a radius of 50 µm. As was the case for the indirect heating, the resistivity increases between the first and the second run due to passivation of the heaters but is then stable for the subsequent third and fourth runs. In the fourth run the power dissipation in the heater was increased beyond 300 mW (equivalent to ≈1 mW/µm heater length) at which a further passivation effect was observed, this time decreasing the resistance as shown by the fifth measurement run.

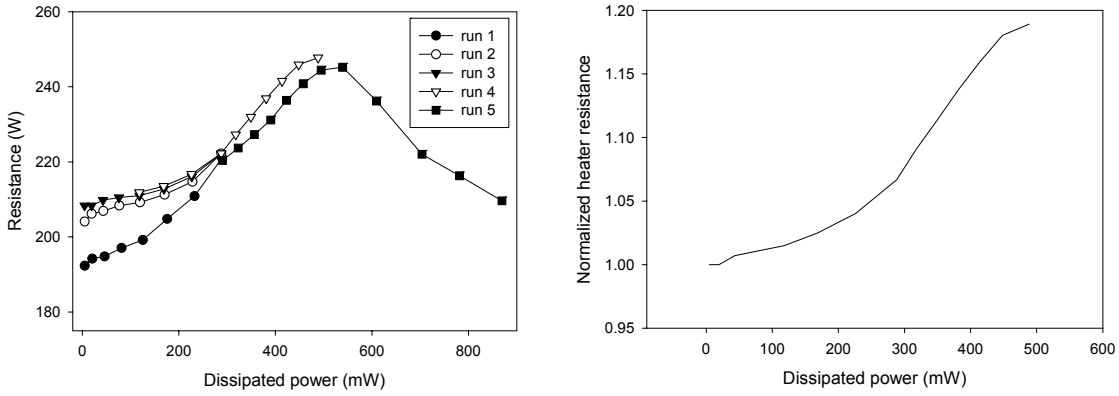

Figure 6.12. Measured a) and normalized b) heater resistance as a function of the heater dissipation.

In the fifth run the limits of the heater were tested by increasing the applied voltage until heater breakdown. Until a dissipation of 500 mW (≈0.63 mW/µm) the heater showed no signs of breaking down. Beyond this value, however, the resistance was seen to decrease, resulting in a runaway increase of the heater dissipation until the heater finally broke down at 870 mW in this case.

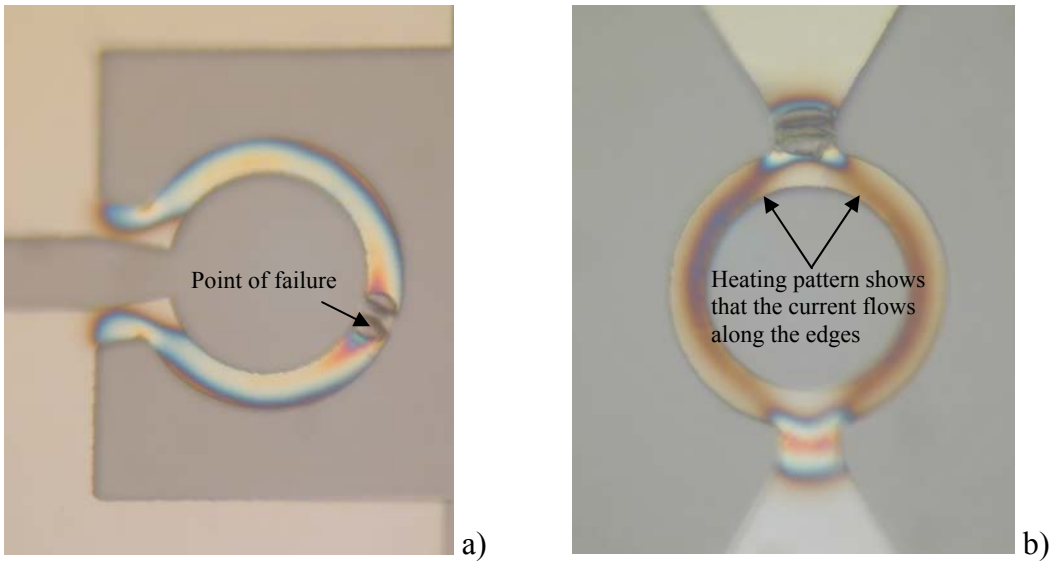

Figure 6.13. Microscope images of a broken down omega a) and circular b) heater showing the heat distribution and the points of failure.

All breakdowns in the heaters were the result of single point failures as shown in Figure 6.13a and 6.13b for the omega and circular heater respectively. These pictures

also clearly show the distribution of the heat by means of the discoloration. Using the data from the thirds and fourth measurement run the plot in Figure 6.12b was compiled. This plot shows the normalized heater resistance as a function of the dissipated power in the heater. By finally combining the data in this plot with the measurement data given earlier in Figure 6.11 the plot in Figure 6.14 can drawn, which gives a rough estimate of the temperature of the heater as a function of the dissipated power.

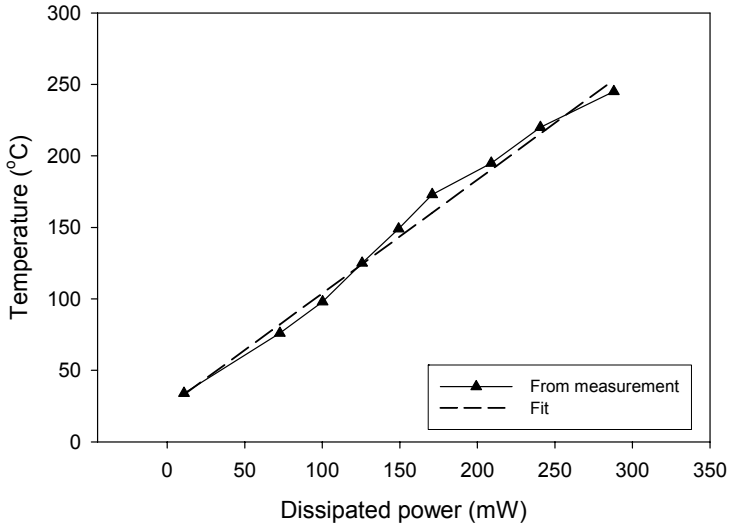

Figure 6.14. Temperature in the measured heater as a function of the power dissipation in the heater.

A fit to the curve in this figure gives a temperature dependence of ≈0.79 K/mW for this heater. Therefore, using the $\Delta Neff/\Delta T$ of ≈7.6 10^{-6} K^{-1} calculated for the resonator waveguide in the preceding section, the tuning of the effective refractive index of the waveguide resonator can be predicted to be 6.0 10^{-6} mW^{-1}. This, using Equations 2.11 and 2.41, corresponds to a shift in resonance frequency of. 6.1 pm/mW

6.3 Characterization of single, vertically coupled microring resonators

Apart from the resonator building block of which the design was described in the preceding section other vertically coupled microring resonators, with for instance a different radius or cladding thickness, have also been realized. In this section several measurements performed on these devices will be presented. These measurements were specifically chosen to illustrate certain important or interesting aspects in the design and application of the resonator:

- The importance of phase matching and the ability to identify a misalignment of the resonator through extraction of the basic parameters from the resonator measurements.
- The effect of cladding layer thickness on the heater efficiency and a method to improve the thermal tuning speed.

First, however, the measurement setups used to perform these measurements will be discussed.

6.3.1 Measurement setup

The lens setup shown in Figure 6.15 is mainly used for "difficult devices" i.e. those devices that are hard to couple into. This may for instance occur for experimental devices where no tapers have been added or in devices that have damage facets. By choosing the right input objective it is then often still possible to characterize the device.

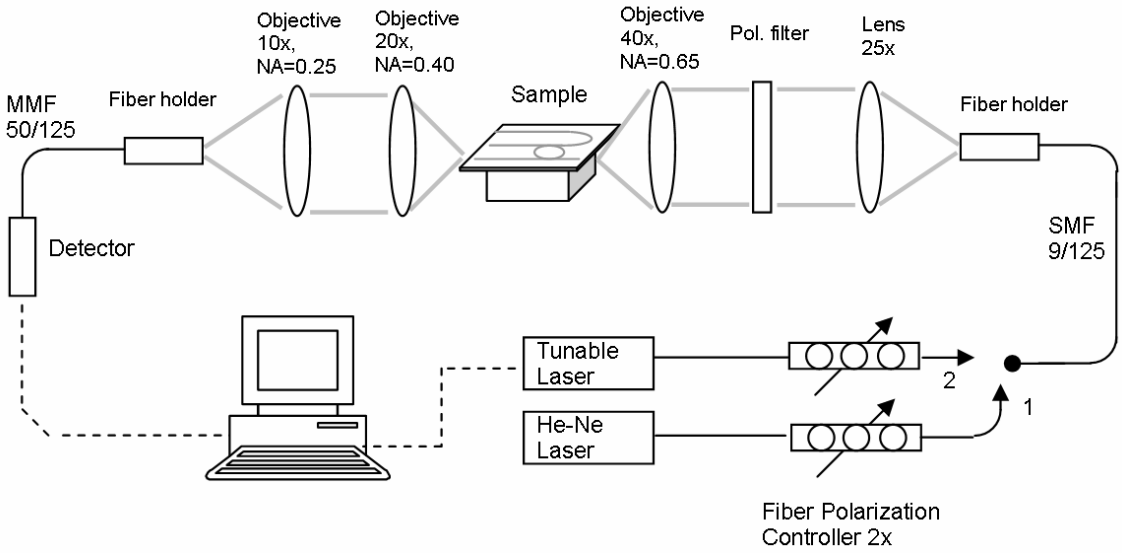

Figure 6.15. Measurement setup for the characterization of optical devices using lenses.

For the characterization of a device first a HeNe laser is used to align the sample. A switch is then made to a Hewlett Packard 8168C tunable laser, with a maximum resolution of 1 pm, to perform the actual measurement. The light from the lasers is first polarized and then focused on the input facet of the devices using a 40x objective. The light at the output facet is collected using a 20x objective and focused

on a 50 μm wide multi mode fiber. The light is then measured using a HP 81521B photo-detector.
Aside from the measurements with the tunable laser this setup was also used in combination with a Sensors Unlimited 320 MX-1.7 RT infrared camera. The camera provides unique information that cannot be obtained through other means, e.g. by measuring the different ports of a device. Figure 6.16a and 6.16b for instance, show an infrared image of a cross coupled microring resonator. The orientation and heater placement in these images is similar to that of the resonator shown in Figure 6.3b. In Figure 6.16a the resonator is off-resonance. Most of the light propagates past the resonator to the through port and only a minor fraction of the light is coupled into the drop port.

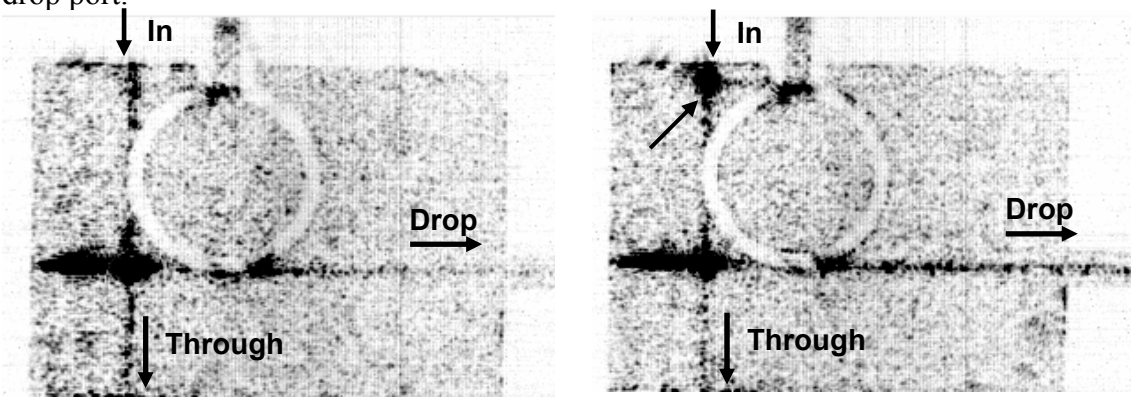

Figure 6.16. Infrared image (inverted) of a vertically coupled resonator in the off a) and on-resonance b) state.

In Figure 6.16b where the resonator is in the on-resonance state the reverse can be seen. Most of the light propagates through the resonator to the drop port and only a minor fraction of the light is present in the through port. Of special interest in this image is the "scatter" point that appears near the input (pointed to by the diagonal arrow). This point is only seen when the resonator is in resonance and is caused by light that radiates out of the resonator and then hits the port waveguide where it scatters to all directions. Another scatter point, seen in both images, is located at the crossing between the two waveguides.
Although the lens setup is highly useful for the measurement of devices that would otherwise be difficult to characterize, the adjustment of the lenses to off-axis port waveguides, i.e. waveguides that are not in the same line from input to output, can be quite difficult. Also it is not possible to measure an output port that is on the same side as the input. In these cases or when devices are relatively easy to measure then it is useful to use a fiber setup as shown in Figure 6.17a. This setup can be equipped with single fibers or fiber arrays which are relatively easy to align to port waveguides, thereby speeding up the measurements. Also, the fiber arrays make it possible to measure ports that are on the same side of a device. Where possible small core fibers have been used to coupled light into the devices in order to reduce the fiber-chip coupling loss. The setup, of which a photograph is shown in Figure 6.17b, uses a HeNe laser for the alignment of the fibers to the port waveguides. Two laser sources have been used in this setup, depending on the resolution required. The previously mentioned tunable laser source in combination with the power meter is used for slow but high resolution measurements down to 1 pm. The Erbium Doped Fiber Amplifier with Amplified Spontaneous Emission Source (EDFA ASE) in combination with an Optical Spectrum Analyzer (OSA) on the other hand is used for near real-time measurements with a resolution down to 100 pm. On the input port of the device a

polarization maintaining fiber (PMF) is used in combination with a polarization filter to ensure that only one polarization is coupled into the device. This, however, was only a requirement for devices with a port waveguide that allows, besides the TE, the propagation of the TM mode, either by design or due to enlargement of the waveguide during fabrication. For devices where the design did not allow for the propagation of the TM mode and where the fabrication process was more tightly controlled, such as in the OADM and the λ-Router, no polarizer was required.

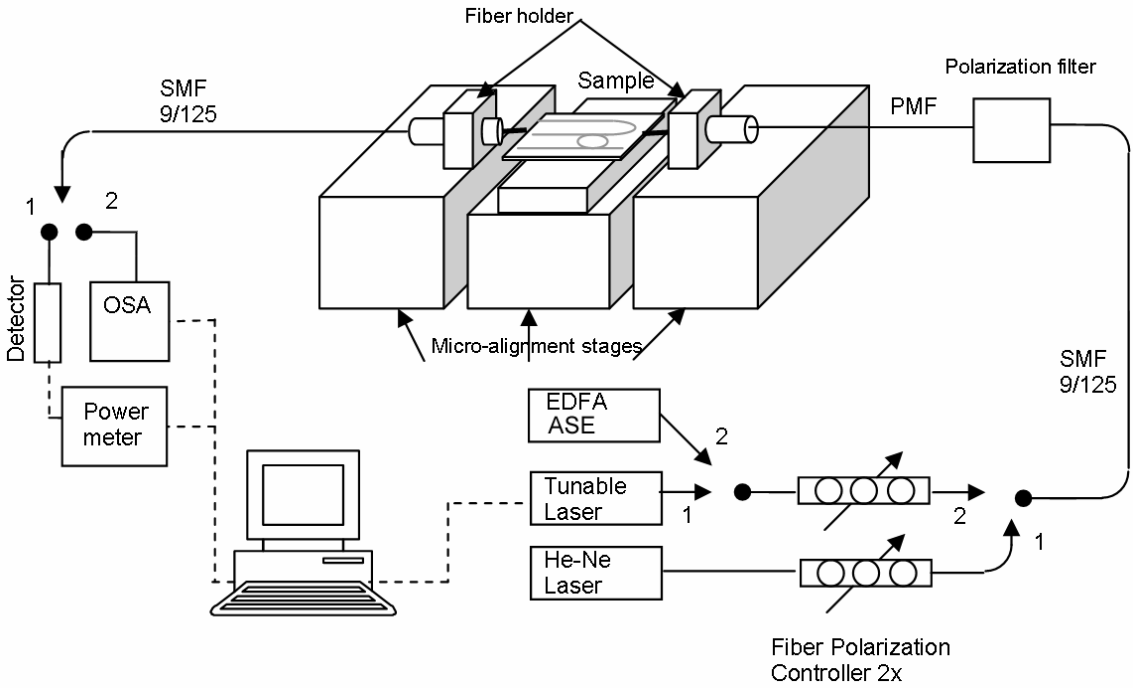

a)

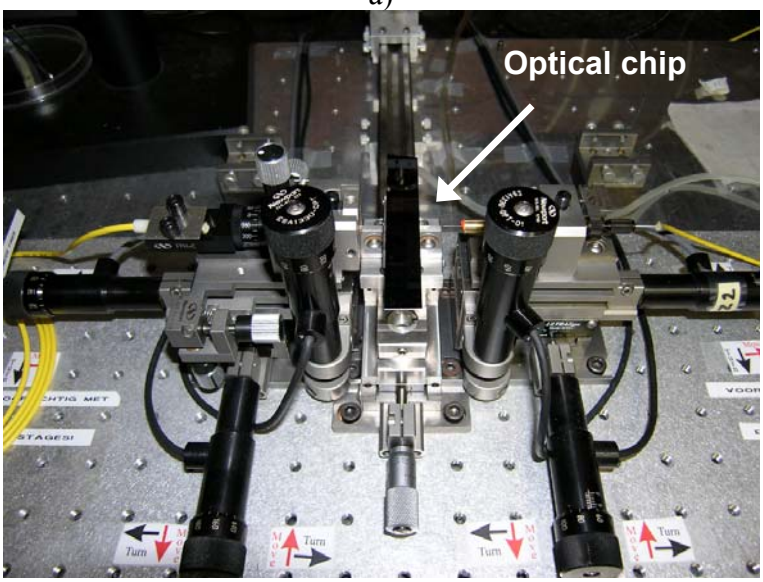

b)

Figure 6.17. Measurement setup for the characterization of optical devices using fiber butt-coupling a). The photograph b) shows the part of the setup with the piezo-actuated alignment stages. An optical chip is placed on the stage in the middle.

6.3.2 The importance of phase-matching and the fitting of resonator responses

In Figure 6.18 the shift in the through response of a resonator is shown as a function of the applied heater voltage. This measurement was of one of the very first tunable microring resonators to be realized, in the first year (2002) of the NAIS project. The Si_3N_4 resonator had a radius of 25 μm and bend waveguide dimensions of 2.5 x 0.3 μm, giving it a *Neff* of ≈1.58. The resonator combined with the standard Si_3N_4 port waveguide measuring 2 x 0.14 μm.
Although these measurements conclusively showed that an omega heater on top of a resonator could be used to tune the resonance frequency, the performance of the resonator was very poor in all other respects. The main reason for the poor performance of this device was the phase mismatch of ≈0.08 between the ring resonator and port waveguides. Although the importance of phase matching was known at the time, its effects on the coupling coefficients could not yet be quantified due to the lack of suitable simulation software. Hence it was not foreseen that such a phase mismatch would for these resonators result in a maximum coupling coefficient well below 0.1, as was shown by simulations performed at a later stage. Due to the bend loss of ≈ 10 dB/cm in these resonators it was therefore not possible to achieve a power extraction of more than ≈0.3 at resonance.

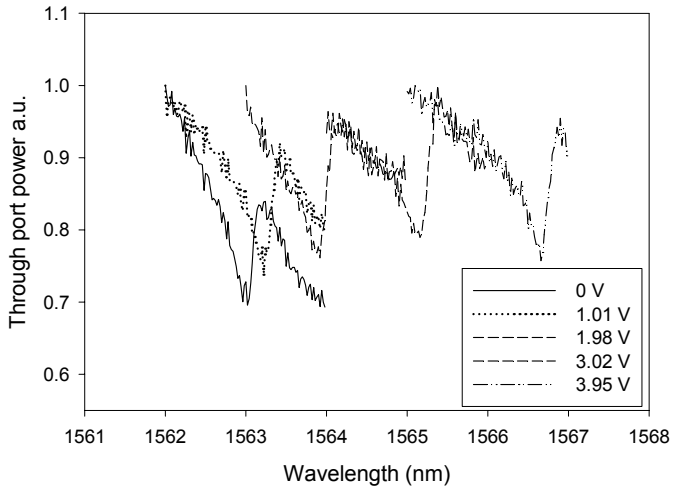

Figure 6.18. A tuning measurement performed on one of the very first tunable microring resonator in the NAIS project. The resonance wavelength in the through responses shifts as a function of the applied heater voltage

The significance of phase matching became fully clear when a resonator that was fabricated using the same design was accidentally fabricated with a resonator waveguide thickness of only 200 nm. Although this increased the bend loss to ≈200 dB/cm, corresponding to a roundtrip loss of 3.1 dB, it also decreased the phase mismatch to ≈0.006. The high coupling coefficients that this phase matching allowed could fully compensate for the high losses, making it possible to achieve through and drop responses with a depth up to 14 and 12 dB respectively. These measured responses, plotted as a function of the port waveguide offset s, are given in Figure 6.19. All these measurements were taken from devices in the same device group, of which the mask design is shown in Figure 6.20. Therefore the (mis)alignment of all

the resonators in this group is identical and it becomes possible to not only determine the resonator parameters κ_1, κ_2 and α_{dB} for a given response but also its alignment.

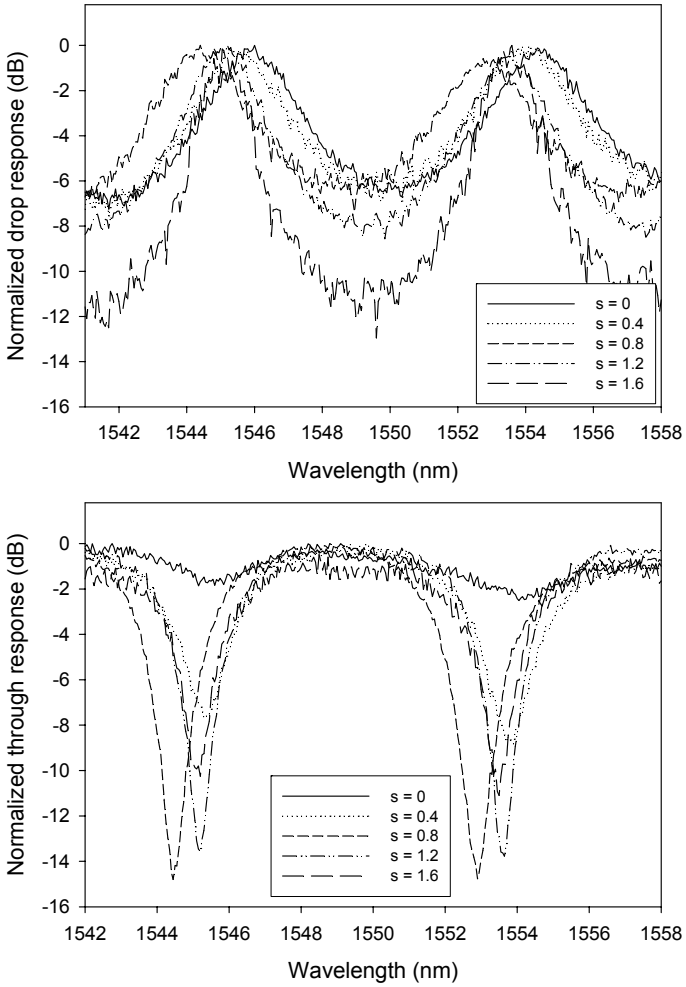

Figure 6.19. Through (bottom) and drop (top) response as a function of the port waveguide offset s for a Si_3N_4 microring resonator with a radius of 25 µm.

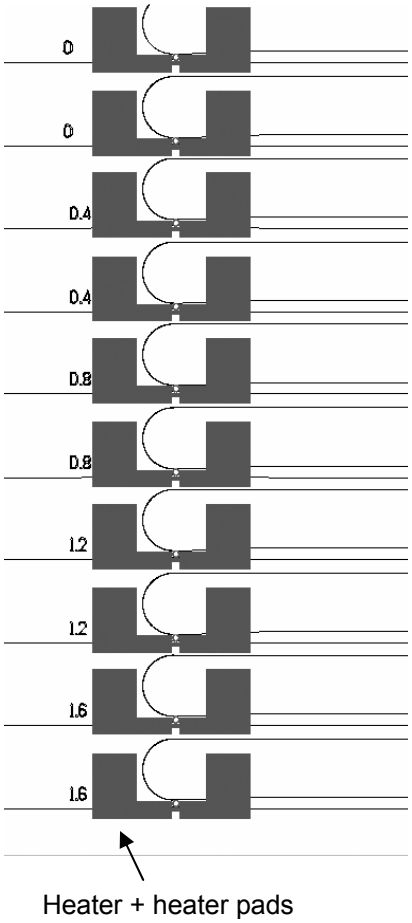

Figure 6.20. Mask layout of the group of resonators that was measured.

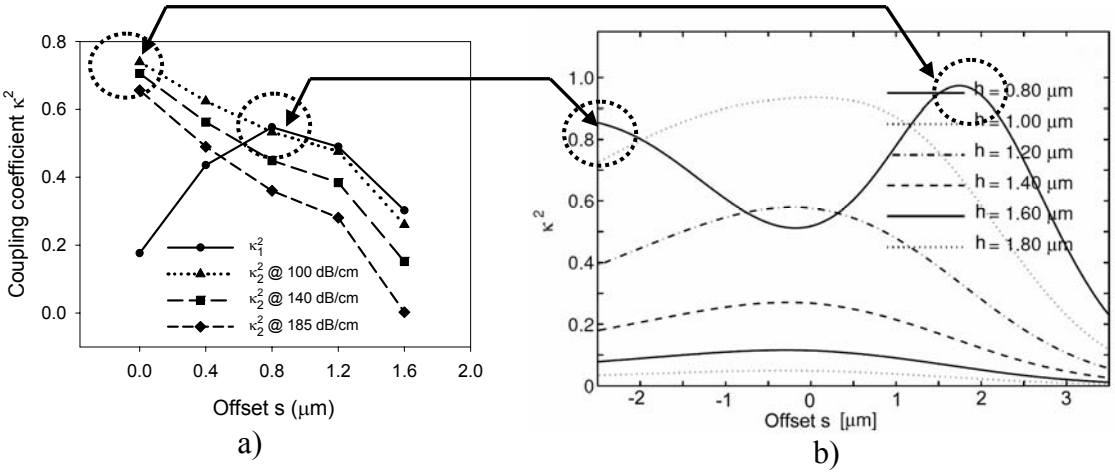

a) b)

Figure 6.21. Fitted coupling coefficients κ_1 and κ_2 ($\kappa_1 \neq \kappa_2$) as a function of the offset *s* of the fabricated resonator (that has a misalignment) a). In b) the coupling coefficients of a simulated resonator have been calculated as a function of the offset *s* for a resonator that is perfectly aligned ($\kappa_1=\kappa_2$). The arrows indicate offset positions that are roughly equivalent in the fabricated and simulated resonators.

In Figure 6.21a the values of the coupling coefficients κ_1 and κ_2 are given as a function of the port waveguide offset s. To obtain these values the DropZone tool was used to solve Equations 4.22 and 4.23. As was previously discussed in Chapter 4.4, only κ_1 can be determined directly. In order to determine the other coupling constant, κ_2, an estimate of the losses has to be made. Using the Selene mode solver these losses were determined to be 200 dB/cm. However, when fitting the responses for the offset of 1.6 μm, the maximum limit for the loss is 185 dB/cm because κ_2 then becomes zero. Therefore the actual losses have to be at least below 185 dB/cm but, considering the Selene simulation results, probably not far below that value. Figure 6.21a shows the fitted values of κ_2 for the maximum loss of 185 dB/cm as well as for two lower bend losses of 140 and 100 dB/cm. As can be seen in the figure, there is a spread of 0.3 in the values of κ_2 at s=1.6 μm. However, at s=0 μm there is a convergence for all bend losses to a value of ≈0.7, making the uncertainty in the fitted value κ_2 less for this offset.

Interestingly, the maximum values of κ_1 and κ_2 are not equal, as might be expected based on resonator symmetry, but show values of 0.5 and 0.7 respectively. In fact, the maximum of κ_2 is likely to be even higher for a negative offset but no resonators with that offset were available. The difference can be explained by examining the CMT simulations of this resonator shown Figure 6.21b where the coupling coefficient is plotted as a function of the offset s and the thickness of the separation layer h_{sep}. These simulations show that when to coupling between the resonator and port waveguides is very high, which in these simulations occurs for h=0.8 μm, there can be more than one maximum. The reason for this is that within a certain range of offsets the coupling length is so long that part of the power is coupled back into the port waveguide. Although this effect is seen only for a thickness of 0.8 μm in the simulations and the thickness of the separation layer in the fabricated device was 1.0 μm, neither the device not the simulations are perfect. For the fabricated device there will always be a variation in thickness and, since many approximations are used in the CMT simulation tool, coupling coefficients predicted by the simulation also been seen as an indication rather than solid fact. Keeping this in mind it is then possible to estimate the offset of the resonator from the measurement data. Assuming that the maximum in the curve of κ_2 at s=0 μm corresponds to the simulated offset of 2 μm and that the maximum of κ_1 at s=0.8 μm corresponds to the simulated offset of -3 μm as indicated by the arrows, then the misalignment can be estimated to be ≈2.1 μm towards the second coupler. To give a better idea of this misalignment it is illustrated by the drawing in Figure 6.22. For reference the arrows indicate the positive axis of all parameters.

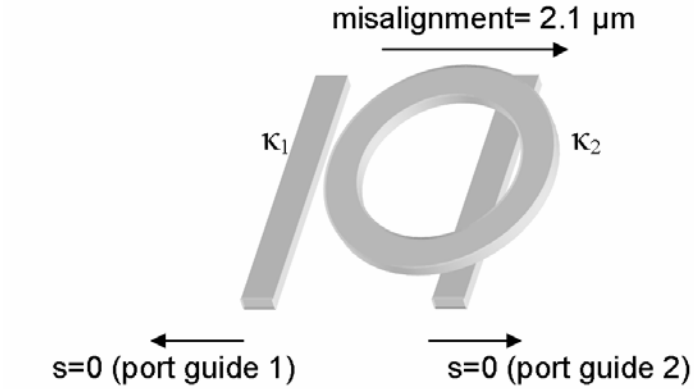

Figure 6.22. Exaggerated drawing of a resonator with a misalignment of 2.1 and an offset s=0 for both port waveguides.

Although the fitted coupling coefficients seem to indicate a shift of 2.1 μm, this could not be verified due to the heaters on top of the resonators (removal of the heaters was not an option). This was partly the reason why later microring resonator based devices also included alignment marker structures like those shown in Figures 6.2 and 6.3.

Apart from being able to determine the coupling coefficients and resonator alignment from measurements shown in Figure 6.19, these measurements also give information about how similar the dimensions of the resonators on a given wafer are. By comparing the resonance frequencies of the resonators it is possible to determine the differences in n_g or the radius between the resonators using:

$$\Delta R \cdot \Delta n_g = \frac{\Delta\lambda \cdot R \cdot n_g}{\lambda} \tag{6.1}$$

For the given through and drop responses the maximum resonance shift $\Delta\lambda$ is 0.75 nm. If it is assumed, for simplicity, that this shift is caused entirely by a variation in the radius of the resonator then this shift corresponds to a change in radius of only 21 nm. Considering that the maximum on-chip distance between the measured resonators was almost 0.8 mm this value indicates a very high uniformity in the fabrication process. This result was in fact quite surprising since these particular devices had resonators with considerable roughness as shown in Figure 6.23. It is suspected, however, that although the localized roughness can be quite considerable, this roughness averages out on the scale of the circumference of the resonator.

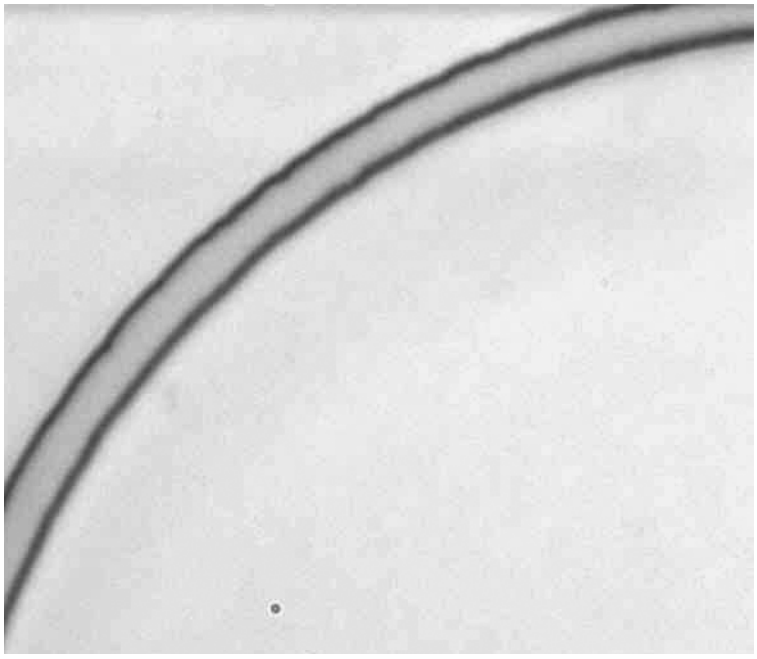

Figure 6.23. Part of a ring resonator, showing a considerable waveguide roughness.

6.3.3 Microring resonator thermal tuning and modulation frequency

A number of measurements have been made to investigate the resonance tuning as a function of the applied heater power for different types of tunable resonator geometries. The results of these measurements have been summarized in Figure 6.24. For the resonator with a 25 µm radius and a top cladding of 3 µm, of which the tuning measurements were presented earlier in Figure 6.18, the shift in the resonance wavelength is approximately 21 pm/mW. In Figure 6.25 the tuning of a 200 nm thick resonator, which was also discussed in the previous section, is shown. This resonator was fabricated with a slightly thicker cladding layer of 4 µm. Because of this the tuning of the resonance wavelength of this resonator was reduced to 16 pm/mW.

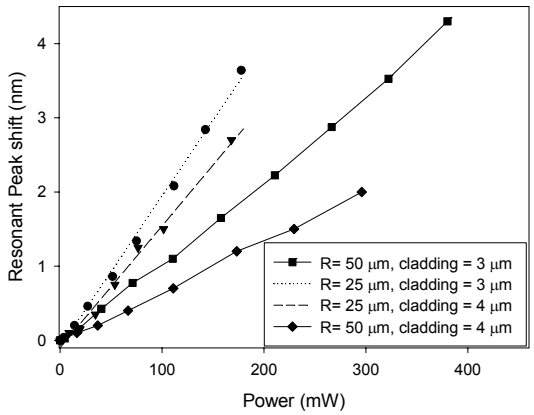

Figure 6.24. Resonance shift versus heater power dissipation for four different resonators.

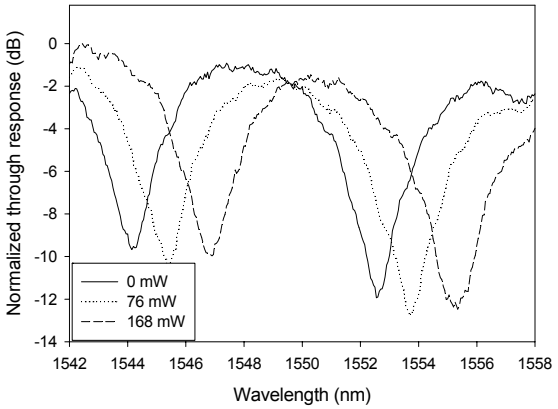

Figure 6.25. Tuning of the through port response of an MR with a 25 µm radius and a top cladding of 4 µm.

According to Equation 2.41 the only factor that determines the tuning is the change in effective index that can be achieved by the tuning method that is used. In the case of thermal tuning the change in the resonance frequency is therefore dependent on the power density in the heater and not on the overall power that is dissipated. This means that for an omega heater that is twice as long, twice as much power will be dissipated to achieve the same shift in resonance frequency.

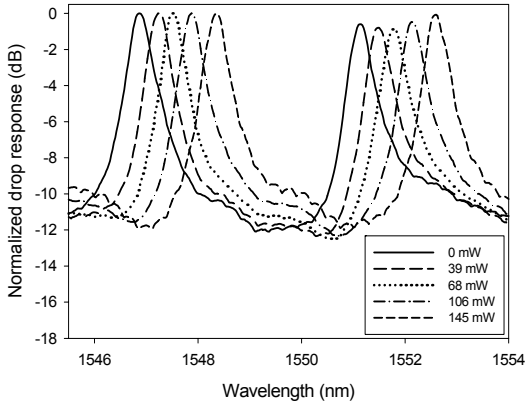

Figure 6.26. Tuning of the drop port response of an MR with a 50 µm radius and a top cladding of 3 µm.

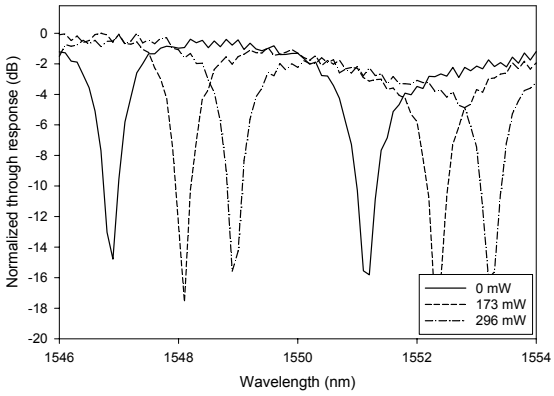

Figure 6.27. Tuning of the through port response of an MR with a 50 µm radius and a top cladding of 4 µm.

This was verified by the measurements given in Figures 6.26 and 6.27. The first figure shows the tuning of the drop response of a resonator with a radius of 50 µm and

a cladding thickness of 3 µm. The shift in the resonance frequency is 10 pm/mW for this resonator which is about half the shift that was found for the resonator with a radius of 25 µm. The second figure shows the shift in the through response of the same resonator with a cladding thickness of 4 µm. In this case a shift of 7 pm/mW was found which is almost half the shift obtained for the 25 µm resonator. This value is also very close to the value of 6.1 pm/mW that was predicted for this resonator in Section 6.2.4.

Besides the tuning efficiency and the tuning range, which was more than 4.3 nm for all these resonators, the maximum thermal modulation frequency was also analyzed [75]. Typically, thermal modulation is limited by the heat capacity and thermal resistance of the layers that make up the device: the lower the resistance and heat capacity, the faster the modulation will be. In the microring resonator geometries that have been discussed the heater is placed at a small distance of 3 to 4 µm from the waveguide. Therefore, even though the thermal conductivity of the SiO_2 is only 1.4 $Wm^{-1}K^{-1}$, the waveguide can be heated quite rapidly. Likewise the silicon substrate allows for a fast cooling of the waveguide due to its very high conductivity of 150 $Wm^{-1}K^{-1}$.
It is possible to maximize the modulation frequency by decreasing the thickness of the various layers so that the heat is transferred as fast as possible or to choose layers with a high thermal conductivity. However, decreasing the layer thickness is often not an option due to leakage of the light in the waveguides to the heater or the silicon substrate and suitable optical materials with a higher conductivity are most likely not available. Even if such materials can be found they might still not be desirable because the increased conductivity would decrease the heater efficiency.
Another, more suitable, method of increasing the modulation frequency is to drive the heater with an overshoot in the modulation signal. The principle behind the overshoot is that a high voltage burst, that would otherwise damage the device if used for a prolonged time, is used for a short period on the rising flank of the drive signal. This allows the heater temperature to increase more rapidly without damaging it because the overshoot can be proportioned such that the maximum temperature in the heater does not rise above the temperature that would have occurred for a normal, square wave, signal.

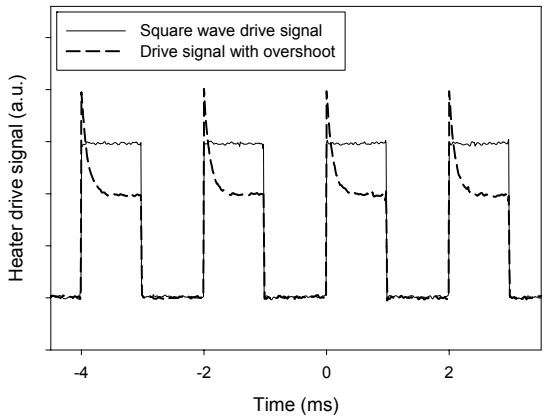

Figure 6.28. A normal rectangular drive signal and a signal containing an overshoot on the rising flank.

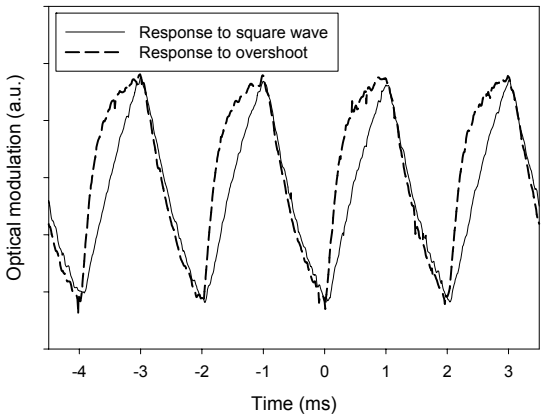

Figure 6.29. Optical modulation measured for the rectangular drive signal and the signal with an overshoot.

In Figure 6.28 the square wave signal and the signal with the overshoot are shown. Both signals have a frequency of 500 Hz. In Figure 6.29 the corresponding optical responses are given. As can be seen the rising flank of the response created using the overshoot in the drive signal is much steeper. The rise time has decreased from 0.93 to 0.54 ms., an improvement of 42%. In addition the drive voltage after the initial peak can be much lower, although the same modulation depth is reached which leads to a 44% improvement in the power consumption.
Besides increasing the rise time it is also possible to decrease the fall time. This requires a biased drive signal as shown in Figure 6.30. This bias makes it possible to also have an overshoot on the falling edge of the modulation signal. As can be seen in Figure 6.31 this can decrease the fall time quite significantly.

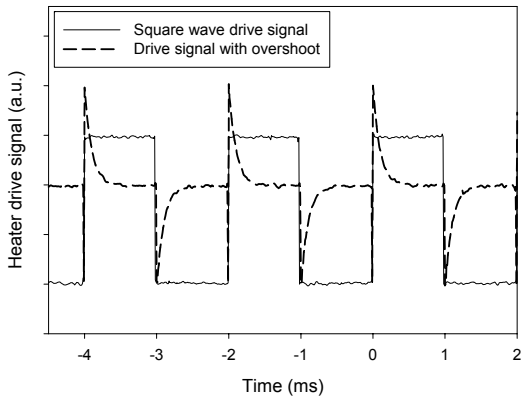

Figure 6.30. A normal rectangular drive signal and a biased drive signal containing an overshoot on the rising flank and falling flank.

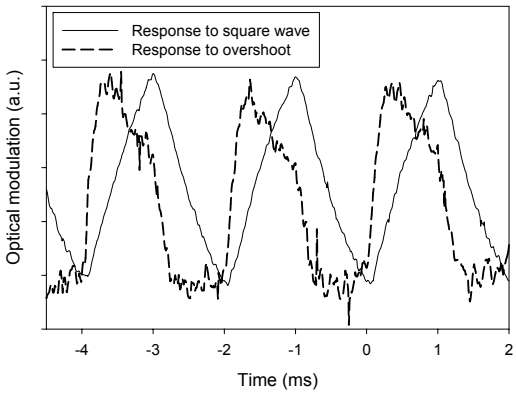

Figure 6.31. Optical modulation measured for the rectangular drive signal and the biased signal with an overshoot.

In fact, by optimizing the overshoots and the bias voltage of the drive signal it was possible to increase the modulation frequency to 10 kHz, as shown in Figure 6.32.

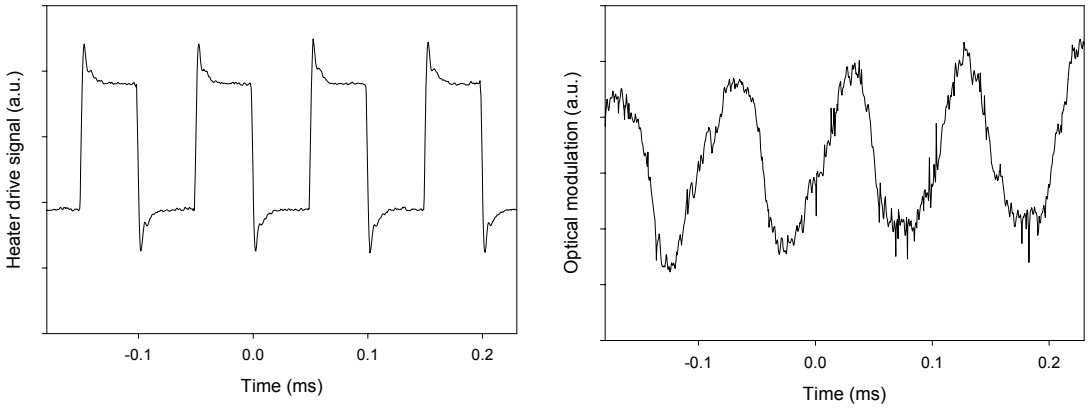

Figure 6.32. Heater drive signal a) and the measured optical modulation for this signal b).

6.4 A wavelength selective optical switch based on microring resonators

The vertically coupled microring resonator building block with a radius of 50 μm has been used to implement a number of different devices. The simplest of these devices is the wavelength selective optical switch. As was shown in Figure 6.1 this switch can for instance be used as part of a channel selection array in a transceiver.
The switch is based on the first order resonator cascade filter comprised of two resonators that was discussed in Chapter 2.6. The first resonator of the switch, which is shown in Figure 6.33a, is used to select a certain wavelength channel from a WDM input signal and drop it to the waveguide between the resonators. If the resonant wavelength of the second resonator matches that of the first, the signal on the channel will be transported to the drop port of the switch. The switch is then in the "on" state. However, if the resonance frequencies are shifted with respect to each other then less power will be dropped. The least power is dropped when the shift between the resonance frequencies is equal to half the FSR of the resonator. The switch is then in the "off" state. The "on", "off" responses of the switch as well the response for an intermediate state, where the shift $\Delta\lambda$ between the resonances is ≈1.46, are given in Figure 6.33b.

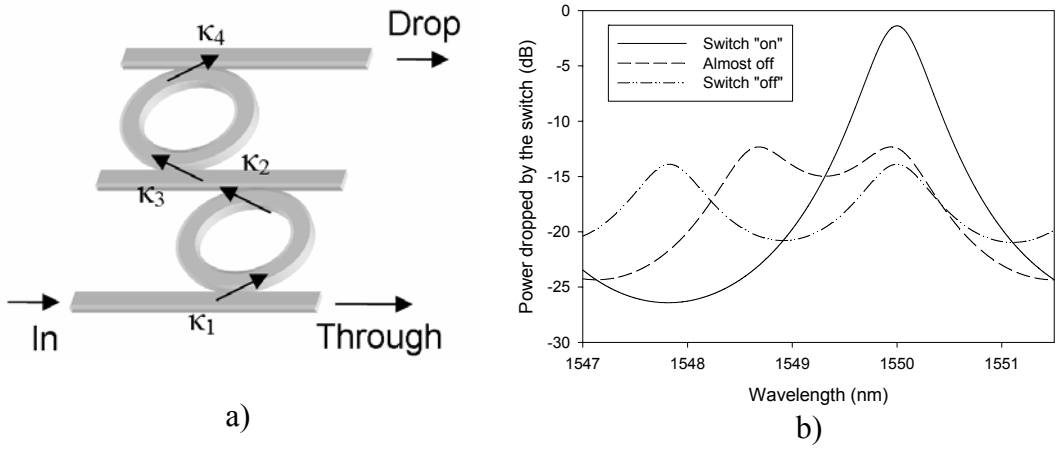

Figure 6.33. Schematic drawing of an MR based switch a) and simulated responses for this switch b).

6.4.1 Switch design

The filter rejection ratio S_{RR} which was discussed in Chapter 2.5 is an important parameter for the switch since the difference between the "on" and "off" state of the switch is equal to the S_{RR} of the first resonator in the switch. Increasing this parameter, for instance by lowering the coupling coefficients, will therefore improve the "on/off" attenuation of the switch. Lowering the coupling will also increase the steepness of the response. This is beneficial to the power consumption of the device since it reduces the shift in the resonance wavelength that is required to reach a certain "on/off" attenuation. There is, however, a trade-off to be made since lower coupling will also reduce the bandwidth of the switch. In addition it has to be taken into account that the bandwidth of two cascaded resonators combined will be approximately ≈0.7 [149] of the bandwidth of a single resonator.

In Figure 3.34 the filter bandwidth is given as a function of the "on/off" attenuation for a number of effective radii ($R.n_g$). The values were calculated using Equation 2.31 and multiplying the results with ≈0.7.

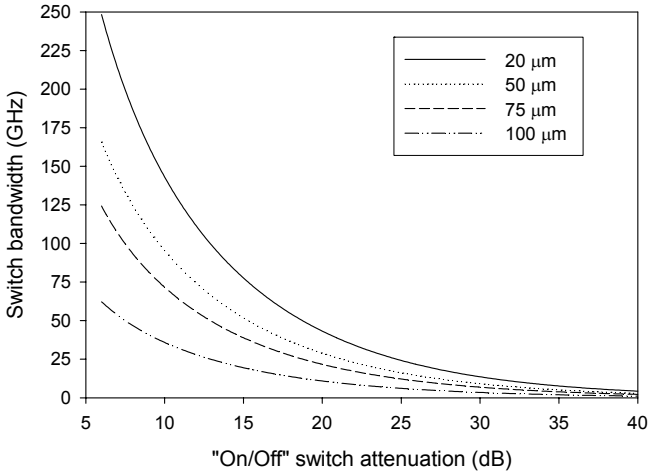

Figure 6.34. Maximum achievable bandwidth as a function of the switch "On/Off" attenuation for a number of effective radii (simulated for λ_0=1550nm)

For the design of the MR based switch the goal was to have a -3 dB band width of 50 GHz. The switch was based on the "standard" building block with the parameters as described in Table 6.1. The resonator in the building block has an effective radius of ≈87 μm. Therefore the maximum "on/off" attenuation is ≈12 dB. If it is assumed that the bend loss in the resonator is 10 dB/cm, then field coupling coefficients of ≈0.6 are required.

6.4.2 Characterization

The switch was fabricated using the "Vertical I" fabrication process that was discussed in Chapter 5. A photograph of the realized switch is shown in Figure 6.35a. The size of the switch is about 200 x 200 μm excluding the heaters. The measured responses for the "on" and "off" state of the switch are given in Figure 6.35b.
To switch the device off, 225 mW was dissipated in the heater of the first resonator which was used for the tuning. For the observed shift in the resonance frequency of 1.46 nm this implies a tuning of 6.5 pm/mW, which is close to the value predicted for these resonators. A comparison with the simulated curve in Figure 6.33b which was also shifted by 1.46 nm shows that the simulated and measured values look very similar apart from a difference in the insertion loss.
The responses have been normalized to the measured power in the through port while the switch was in the "off" state. The responses therefore also show the drop-port insertion loss. The "on/off" attenuation of the switch is 12 dB. When the switch is "on" the crosstalk with the adjacent channels is ≈-20 dB (channel spacing of 0.8 nm). The on chip insertion loss of the switch is around 5 dB. Using the DropZone tool the bend loss and coupling coefficients were determined to be in the order of 44 dB/cm and 0.54 respectively. For these parameters the insertion loss of a single resonator can be calculated to be about 3.2 dB which fits quite well with the 6 dB measured for the two resonators combined.

A possible explanation for the considerable bend losses might be sought in a resonator waveguide that either has a lot of roughness or has been fabricated too thin. More likely, however, these losses are due to the "lifting" of the resonator in the coupling region as is shown in Figure 3.36 for a different resonator. Here the required modal adjustment can cause significant losses.

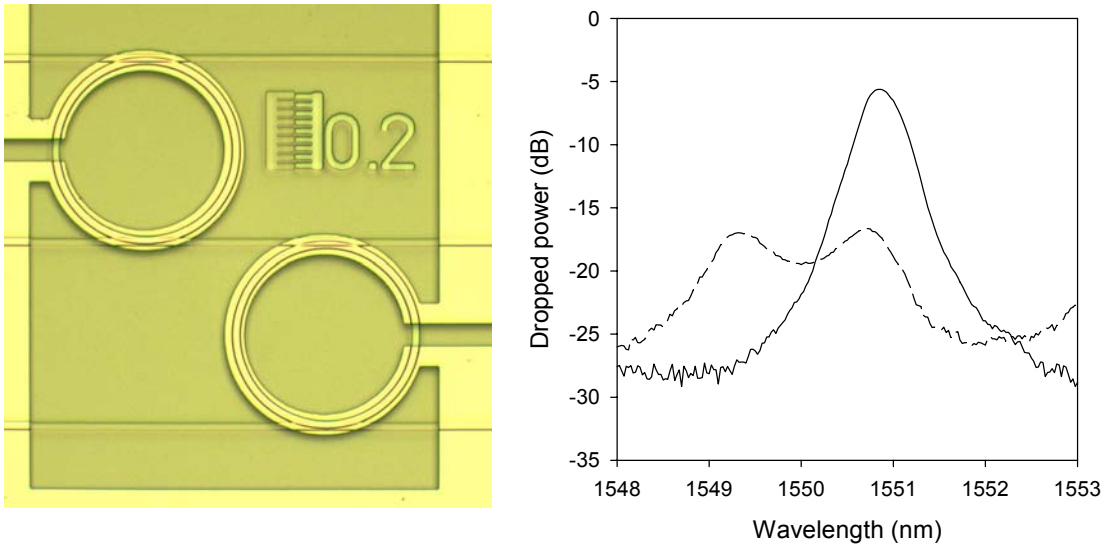

Figure 6.35. Microscope image of a realized switch a) and the "on" and "off" responses b) measured for this device.

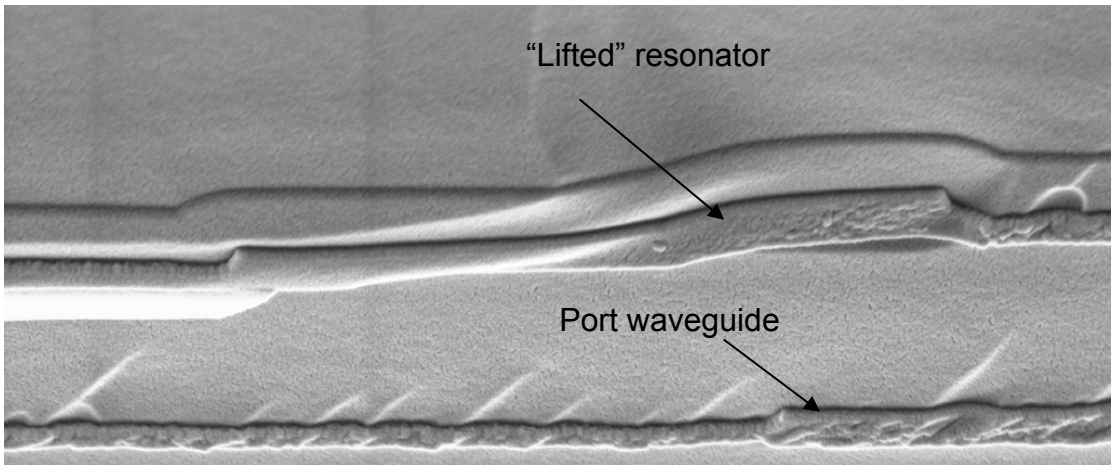

Figure 6.36. The lifting of the resonator in the coupling region due to the waveguide underneath. This lifting can increase the losses considerably.

6.4.3 Vernier switch

One of the problems of the presented switch is that the 12 dB "on/off" attenuation is too low for practical applications. As shown in Figure 6.34, however, nothing can be done about this for the given configuration. The only possible solutions are then to decrease the radius, which is not possible for this resonator, or go to higher order filters [53-68]. Another problem is that the free spectral range of 4.2 nm of the switch

is also limited. By introducing the Vernier effect as was discussed in Chapter 2.7, however, the FSR can be increased significantly. In order to test this, a switch-like device was fabricated with two different resonators. The resonators in this device, which is shown in Figure 6.37a have a radius of 46 µm and 55 µm. This corresponds to a FSR of 4.66 and 4 nm respectively. The combined FSR, which can be calculated using Equation (2.36) is therefore ≈28 µm. The measurement of the drop response of this Vernier switch shows that this FSR was indeed obtained. Although this Vernier resonator is clearly not state-of-the-art it clearly demonstrates the problem of the side-lobes that typically occurs for Vernier-type devices. These side-lobes that are typically close to the main resonance peak can significantly interfere with device operation if, for instance, adjacent channels of a certain wavelength band are also dropped to a certain extent.

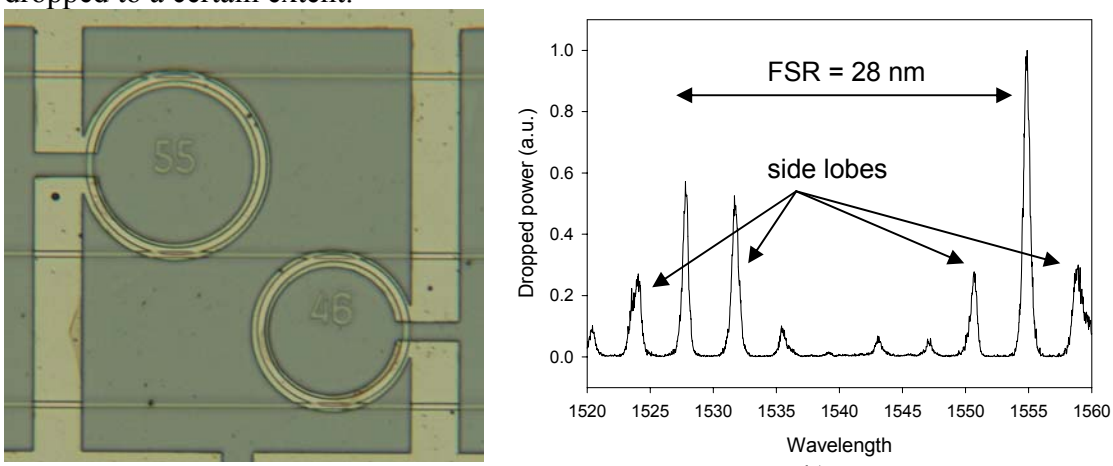

Figure 6.37. Realized Vernier resonator comprised of two microring resonators with a radius of 46 and 55 µm. The drop measured response b) has a FSR of 28 nm.

Chapter 7

Densely integrated devices for WDM-PON

In this chapter the design and characterization of two types of optical add-drop multiplexer and a λ-router are discussed. These devices combine a large functionality with a small footprint and are therefore promising candidates for making WDM-PON networks more cost-effective.

7.1 Introduction

In Chapter 1 the WDM-PON was introduced as a possible successor of traditional passive optical networks. In a traditional PON, as shown in Figure 7.1, only two wavelengths are used to transport data. This severely limits the bandwidth available to each user because the information going to- and coming from multiple users has to be multiplexed onto a single wavelength. Another problem is that when the network is upgraded, it is likely that all connected users have to upgrade as well because they all share the same wavelength channels.

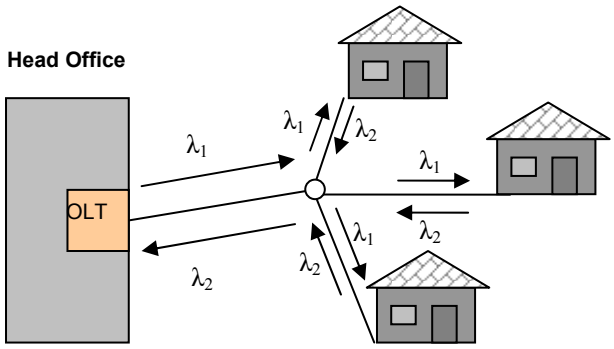

Figure 7.1. Traditional PON architecture.

A WDM-PON uses multiple wavelengths, as shown in Figure 7.2. Since the network is still based on a passive splitter all users receive the downstream wavelengths. However, the ONUs at the user's premises can now filter out a specific wavelength with a service for which they have a subscription. This allows the provider to run many services, for instance providing different bandwidths, side by side. In addition, if an upgrade is required, this can be run on a different wavelength to which the users can then migrate gradually.

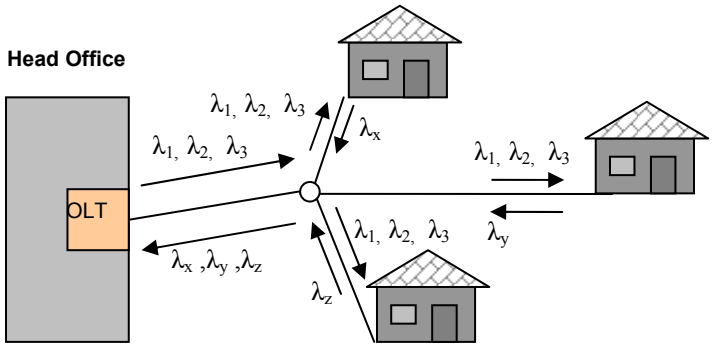

Figure 7.2. WDM PON architecture using a passive splitter (for use with the NAIS transceiver).

The WDM-PON therefore has the potential to be more cost effective than the traditional PON. Currently, however, the cost of the required optical components is one of the factors limiting the adoption of the WDM-PON. This is especially true for the ONUs for which the cost cannot be shared amongst multiple users. The WDM-PON ONUs can be very expensive because they have to be able to receive and send data in multiple wavelengths which requires optical filtering and a tunable laser

source. The NAIS and Broadband Photonics projects, within which the work presented in this thesis was carried out, have in common that they both approach the problem of cost (amongst other issues) through the miniaturization and integration of the required network components. The approach to the actual implementation of the ONUs, however, is quite different, even though both are intended for the WDM-PON, and has implications for the rest of the components in the network.
The transceiver at the ONU proposed in the NAIS project takes an active approach. Each user receives all downstream channels as shown in Figure 7.2. From these channels a single channel is then selected. For the upstream signal a single wavelength channel is used which has to be set explicitly (by the user or the Head Office H.O.), through the hardware configuration of the transceiver. The light of the required wavelength for this channel is then generated on chip, by spectral slicing of a broadband source. This has the advantage that old PON networks are easily upgraded because the passive splitters can still be used.
The Broadband Photonics project on the other hand has a semi-passive approach using colorless transceivers. From the head-office each ONU transceiver receives two paired wavelength channels. One channel contains the downstream data signal while the other is a continuous wave (CW) signal which is amplified (using a SOA), modulated and returned as the up stream data signal as is shown in Figure 7.3.

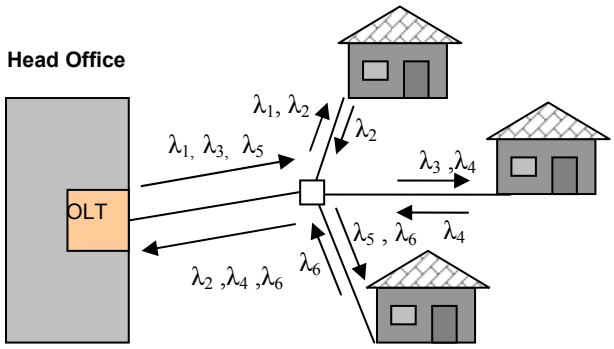

Figure 7.3. WDM PON architecture using a wavelength filter (AWG, OADM etc.) in combination with reflective SOA transceivers.

The main advantage of this is that the wavelength can be changed transparently, without the need to reconfigure the transceiver because the transceiver will modulate and reflect any wavelength that is sent down stream (with the exception of the designated downstream wavelengths). This also poses a problem, however, since each transceiver should receive no more than two wavelengths which is not possible when passive splitters are used.
In order to send only specific channels to a transceiver the Broadband Photonics network therefore uses reconfigurable optical λ-routers instead of the passive splitters (in the strictest sense of the word this network is no longer a PON network but is nonetheless regarded as such in the following text). These optical routers are useful for several reasons. First of all only those channels that are used by a specific user are sent to that user. This is not only a requirement for the use of the colorless transceiver but it also improves the power budget since no power is wasted in sending a signal to a user that does not require it. It is also beneficial to the network security as a whole since it is more difficult if not impossible for users to “eavesdrop” on signals destined for other users. Another important reason is the fact that, since the device can be reconfigured, the network can be better balanced. It is for instance possible to allocate

more channels (i.e. bandwidth) to work office locations during the day, while at night more are allocated to domestic areas. In its most fundamental form the router is no more than an optical add-drop multiplexer which can drop (or add) a single channel per port. Even with such a simple router, however, a complex network as shown in Figure 7.4 becomes possible. In this network a traditional PON network is used side by side with a WDM-PON network. Customers 2 through 4 are all connected to the PON network where data on λ_3 is sent downstream and data is returned on λ_4. Customers 1, 5 and 6 on the other hand all use a colorless transceiver and therefore have 2 wavelengths sent downstream. For customers 1 and 5 the router is using multicasting to send the same wavelengths to both users that do not require a lot of bandwidth. For customer 6 the network can be regarded as being no different than a point to point network with all its benefits.

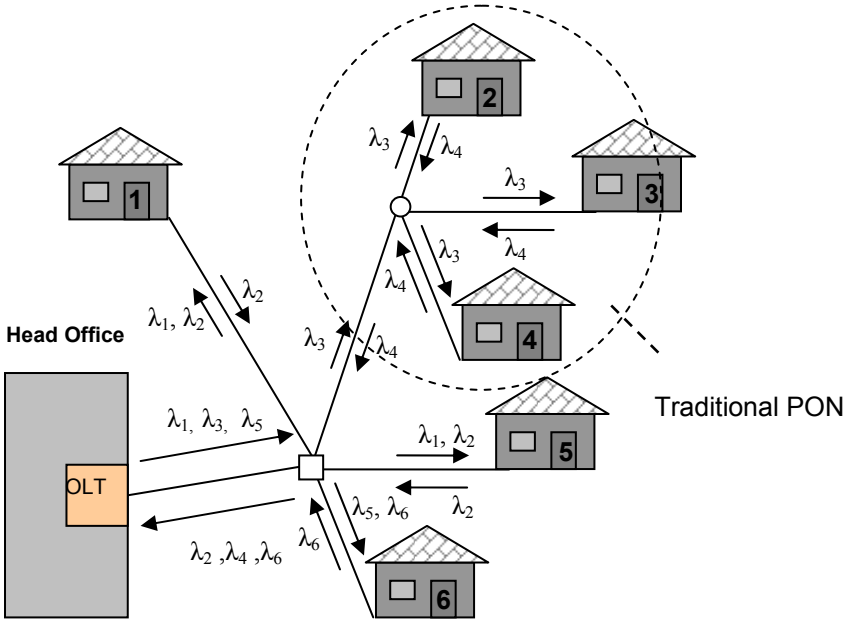

Figure 7.4. A possible complex network topology that is made possible when a (reconfigurable) OADM is used.

In Section 7.2 the design and characterization of a reconfigurable 1x4 OADM are discussed. This OADM has the required functionality to operate as a simple router. The design and characterization of a more complex 1x4x4 router, capable of sending up to four channels to a single customer, are discussed in Section 7.3.

7.2. A reconfigurable Add-Drop Multiplexer based on microring resonators

An OADM can be implemented using for instance arrayed waveguide gratings or Mach-Zehnder interferometers (MZI). However, OADMs based on AWGs are generally large devices since AWGs can only split one channel into multiple channels or vice versa. An OADM based on AWGs would therefore require additional components like optical switches. Likewise, a considerable number of MZIs would be required to drop even a few channels [144]. An OADM based on microring resonators [145] with radii in the order of tens of μm, however, allows for extremely small–area devices. Due to the highly selective MR filter characteristic a minimum component implementation of a 4-channel OADM can already be realized with four microring resonators while additional switching functionality is easily implemented.

7.2.1 Design and fabrication

The OADM was designed as shown in Fig. 7.5 It consists of a central bus waveguide (with the ports I_{In} and I_{Out}) and four add-drop port waveguides that intersect the bus waveguide at right angles with a single MR placed at each intersection. In addition to the waveguides that are shown, an alignment waveguide, as discussed in Chapter 3.7.1, was also included to aid in the alignment of fiber arrays.
The cross-grid (Manhattan) [139] arrangement of the bus and add-drop waveguides allows for a very efficient and simple design, requiring only two bends in the central bus waveguide. All other waveguides can be implemented using straights.

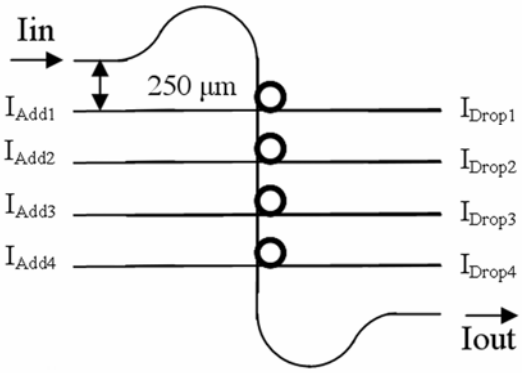

Figure 7.5. Schematic layout of a 4-channel OADM.

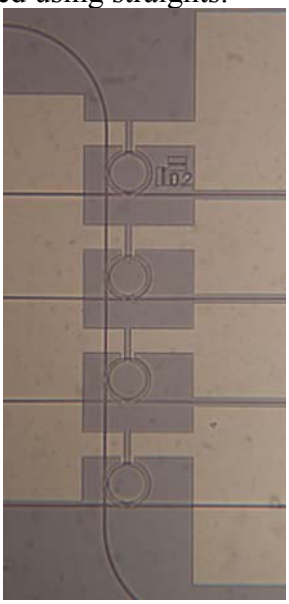

Figure 7.6. Close-up of a realized OADM. The waveguides and the omega shaped heaters on top of the four resonators can be discerned.

A downside to the cross-grid approach, however, is that minor losses and reflections occur at the intersections between the bus and add-drop waveguides. In addition some crosstalk between the signals propagating in these waveguides may occur. This can be

largely solved, however, by placing the bus and add-drop waveguides in different layers [146] The vertical distance between the add-drop and bus waveguides is 250 μm so that the device can be used in combination with standard fiber-arrays. The size of the OADM, 1.5 mm by 0.2 mm, is mainly determined by this spacing. All waveguides are horizontally tapered down to 1.5 μm at the facets. As shown in Figure 7.7 this can reduce the fiber chip-coupling losses from 6.5 to 6.0 dB for a standard (SMF, Mode Field Diameter 10.2) fiber and from 4.3 to 3.9 dB for a small-core (HI-1060, MFD 5.6) fiber.
For the resonators in the OADM the standard vertically coupled microring resonator building block described in Chapter 6 was used, following the design parameters described in Table 6.1 except for the thickness of the resonator which was set at 190 nm.

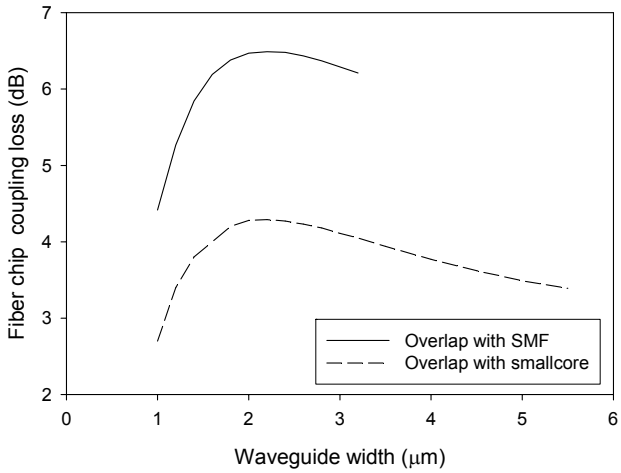

Figure 7.7. Fiber-chip coupling loss with a standard or a small-core fiber as a function of the waveguide width for a Si_3N_4 SiO_2 waveguide with a thickness of 140 nm.

The OADM was fabricated using the "Vertical I" fabrication process and subsequently pigtailed and packaged so that the device could be fully characterized [147]. Figure 7.6 shows a close-up of a fabricated OADM. The four add/drop and central waveguides are clearly discernable as well as the omega shaped heater elements on top of the four micro-ring resonators.
Two photographs of the pigtailed OADM chip are given in Figure 7.8 In these photographs the fiber arrays, glued to both sides of the chip, can be seen. Also discernable are the glass rails on top of the chip as well as the bond wires. The chip measures 10 mm by 9 mm. Although the actual OADM measures only 10 mm by 1.5 mm, the width of 9 mm is required to provide the fiber arrays with enough space to be glued onto. The chip that is shown therefore actually contains 4 OADMs.

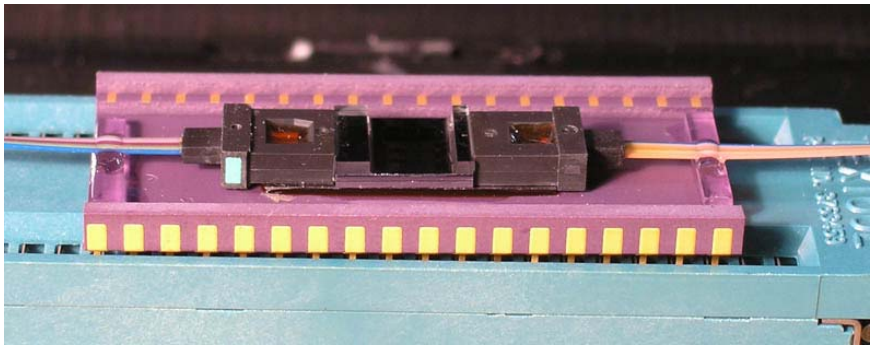

a)

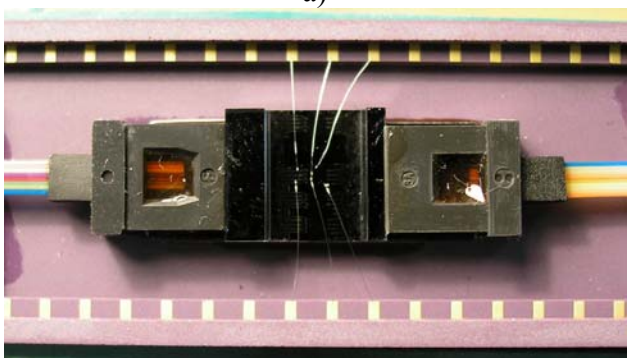

b)

Figure 7.8. Side a) and top view b) of a pigtailed OADM.

7.2.1 Spectral measurements

The pigtailed OADM was measured using an EDFA ASE broadband source and an OSA with a resolution of 0.1 nm. For the responses shown in Figure 7.9 the EDFA ASE was connected to the I_{In} port of the OADM. The OSA was connected to the I_{Out} port. In this configuration the OADM acts as a de-multiplexer by dropping the channels present on I_{In} to the drop ports I_{Drop1}-I_{Drop4}. These dropped channels are visible as dips in the I_{Out} port. The two different responses that are shown in the figure were created by tuning the resonators so that 1) they either all had the same resonance wavelength, or 2) that the resonance wavelengths of the individual resonators were all different.

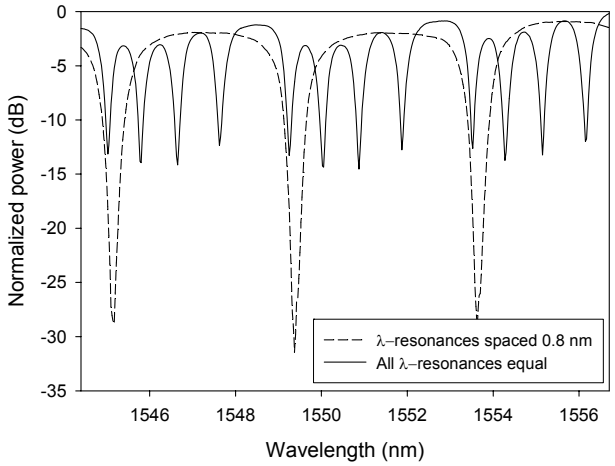

Figure 7.9. OADM through responses measured at I_{Out} for two different OADM configurations, set by the thermal tuning of the resonance wavelength of the MRs

To obtain the response that shows four distinct resonance dips, a total heater power of 446 mW was required in order to tune the MR resonance wavelengths to a 100 GHz ITU Grid (spaced at 0.8 nm). The minima of the individual MR through responses are ≈12dB below the normalized input power level.
For the configuration that shows the single large dip the resonance wavelengths of the individual MRs were carefully tuned to overlap each other. This increased the power extracted from the channel to give a minimum of -30 dB relative to the normalized input power level. This configuration could be set while dissipating only 20 mW due to the fact that the un-tuned MRs already had nearly overlapping resonance frequencies. This indicates a good fabrication uniformity of the microring resonators in the OADM (and potentially across the wafer). The change between the two configurations could be made in < 1 ms.
For the configuration where the resonators were tuned to different wavelengths the responses at the drop ports I_{Drop1}-I_{Drop4} were also measured with the OSA. In Figure 7.10 the normalized drop responses, measured at the four drop ports are shown. The depth of the individual MR drop responses is ≈12dB. As can be expected some drop responses also show the (filtered) through responses of the preceding resonators. This effect is especially pronounced in the drop response measured at the fourth drop port in which the through port resonances of three other resonators can be discerned.
The responses of the add-ports, shown in Figure 7.11, were measured by connecting the EDFA ASE to the I_{Add1}-I_{Add4} ports and measuring the wavelength response at the I_{Out} port using the OSA. As can be seen, the overall behavior of the OADM when adding or dropping signals is the same. However, a direct comparison between the individual responses cannot be made because the measured add response of a certain resonator is quite different from the drop response of that resonator. The response of the fourth drop port for instance shows three dips because the broadband input signal first has to pass three other resonators before it can be dropped by the fourth MR. Conversely, when a signal is added to the fourth add port which is connected to the same MR no such dips are present because the added signal passes no other resonators.
By fitting the individual MR drop- and through responses to a MR model (using RFit) the field coupling constants κ_1 and κ_2 were determined to be 0.56 ±0.04 and 0.44 ±0.04 respectively. For the loss in the resonator a value of 1.5±0.5 dB/cm was found. Using these parameters the channel crosstalk of the device was calculated to be -11.7 dB. The measured FSR and Finesse were 4.18 nm and 10.3 respectively, giving the MRs in the OADM a $\Delta\lambda_{FWHM}$ of 0.41 nm (=51 GHz).

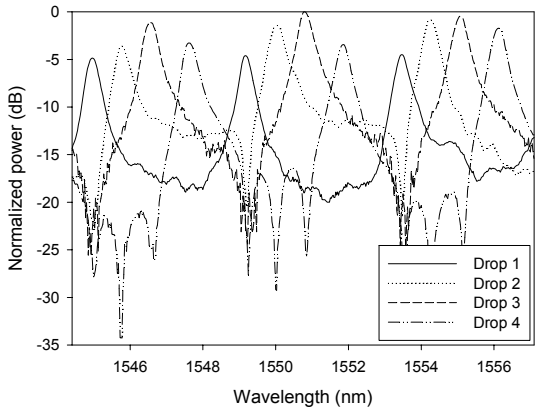

Figure 7.10. Measured OADM drop responses.

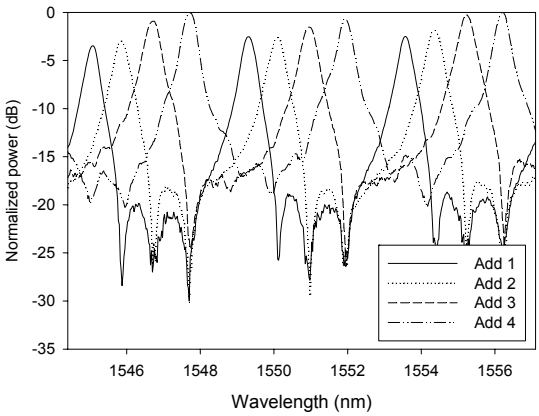

Figure 7.11. Measured OADM add responses.

7.2.2 Spectral measurements

In addition to the spectral measurements the operation of the OADM was also characterized at bitrates of 40 Gbit/s to determine the eye patterns and BER [148]. For this a measurement setup as shown in Figure 7.12 was used. The setup consists of a high-speed Pseudo-Random-Bit-Sequence (PRBS) generator that generates to generate a random data pattern at 40 Gbit/s. This data pattern is then used to drive a high-speed (Electro-Absorption) modulator which modulated the output of a tunable CW source. The modulated signal which is amplified using an EDFA, is then fed into the OADM. The output signals of the OADM are amplified and detected using a high-speed (U2T) photodetector. The modulated and amplified input signal is also measured via a high-speed photodetector. From the photodetectors the signals can be sent to an wide- bandwidth Agilent 86100B oscilloscope to visualize the eye diagrams or to a Bit-Error-Rate-Tester (BERT) to measure the BER.

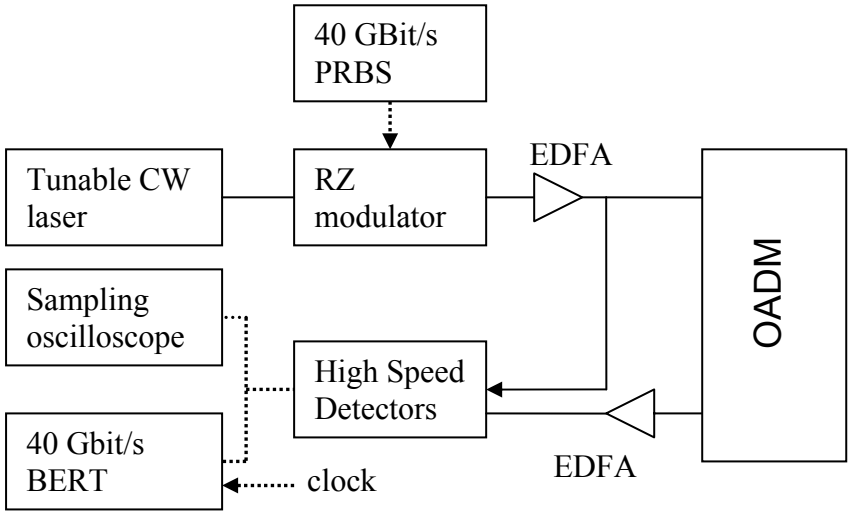

Figure 7.12. Measurement setup for the analysis of 40 Gbit/s RZ signals.

To measure the eye pattern of a dropped signal an optical 40 Gbit/s PRBS return-to-zero (RZ) data signal with a bit word sequence of 2^{31}-1 was encoded via the modulators onto the CW laser source which had a wavelength of 1550 nm. If Figure 7.13 the eye diagrams of the amplified signal measured at I_{Drop1} (bottom) as well as the input signal (top), which was connected to I_{In}, are shown. For this measurement the resonance wavelength of the first resonator was tuned to match the wavelength of the tunable laser (so the input signal is dropped by the resonator). Although the eye pattern of the signal at I_{Drop1} shows an increase in noise, which is caused by the EDFAs, the eye clean and is open, allowing for error free detection at this bitrate. This was corroborated by BER measurements that showed error free detection down to 10^{-9} with a minor power penalty of 1 dB [149, page 102]. When the resonator was tuned out of resonance, as shown in Figure 7.14, the eye was almost completely closed. The difference between the on- and off resonance amplitudes of the eye pattern was 11 dB which is close to the 12 dB drop response resonance depth that was determined in the spectral measurements.

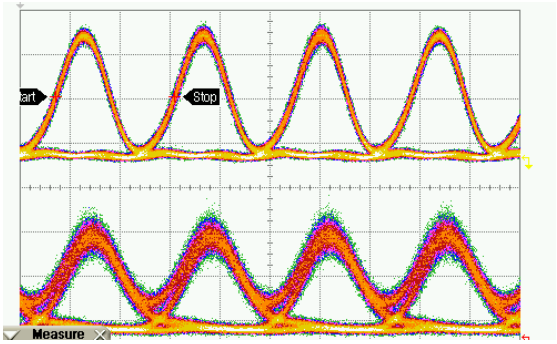

Figure 7.12. Measured eye patterns of the input signal (top) and the signal at I_{Drop1} (bottom). The resonator is tuned "on resonance".

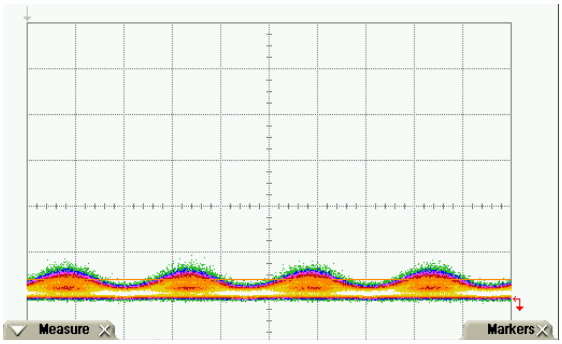

Figure 7.13. The Measured eye patterns of the signal at I_{Drop1} when the resonator is tuned "off resonance".

The multicasting feature of the OADM as it was shown in Figure 7.4 (for customers 1 and 5) was tested by tuning the first two resonators in the OADM such that each drops an equal part of the input signal as is illustrated in Figure 7.14 (the figure is idealized, typically MR1 is tuned so that it drops 50 % while MR2 is tuned to be on-resonance to drop the rest of the signal). Figure 7.15 shows the two eye patters that were measured at I_{Drop1} and I_{Drop2} and for this configuration. Although the amplitude of the measured signals was lower compared to a single dropped signal, as can be expected, the eye-patterns are still open. This shows that, at a bitrate of 40 Gbit/s, this OADM is indeed capable of multicasting.

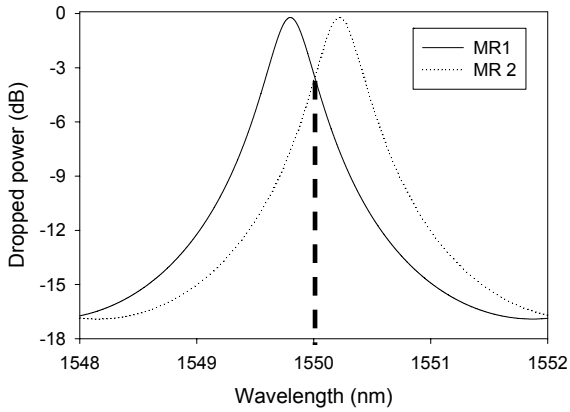

Figure 7.14. Multicasting principle: Each resonator is tuned such that only part of the signal (at λ=1550 nm) is dropped.

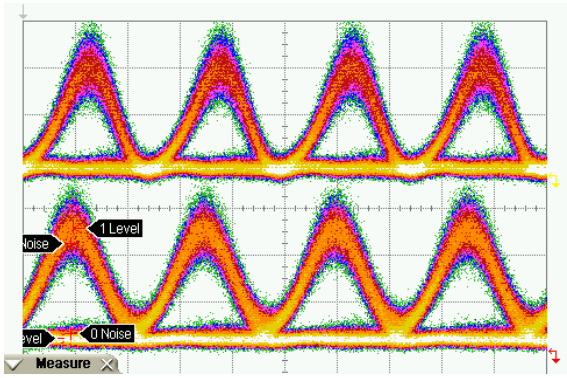

Figure 7.15. Multicasting principle: Each resonator is tuned such that only part of the signal (at λ=1550 nm) is dropped.

7.3 Flexible λ-multicasting Router for use in Access networks

The OADM that was described in the previous section can only be used to drop a single channel to a certain customer. It may, however, be useful to be able to drop multiple channels to a single customer. For instance, multiple channels may be combined to offer a higher overall bandwidth to that customer. Also, different channels could be used for different services. One channel may be used to provide all customers with the same data, such as digital television, while other channels are used by one, or only a few customers. In stead of a $1 \cdot m$ demultiplexer such as the OADM a more general $1 \cdot n \cdot m$ router solution (i.e. a router with a single input and express output that can drop n channels to m drop ports) is then required which can drop not one channel but any combination of channels to a single node (e. g. a customer).

Such a router was developed within the context of the Broadband Photonics project [14]. This router is to become part of the reference network architecture as shown in Figure 7.16. The architecture consists of up to 4 routers (3 shown) that each connect up to 256 users to a ring network.

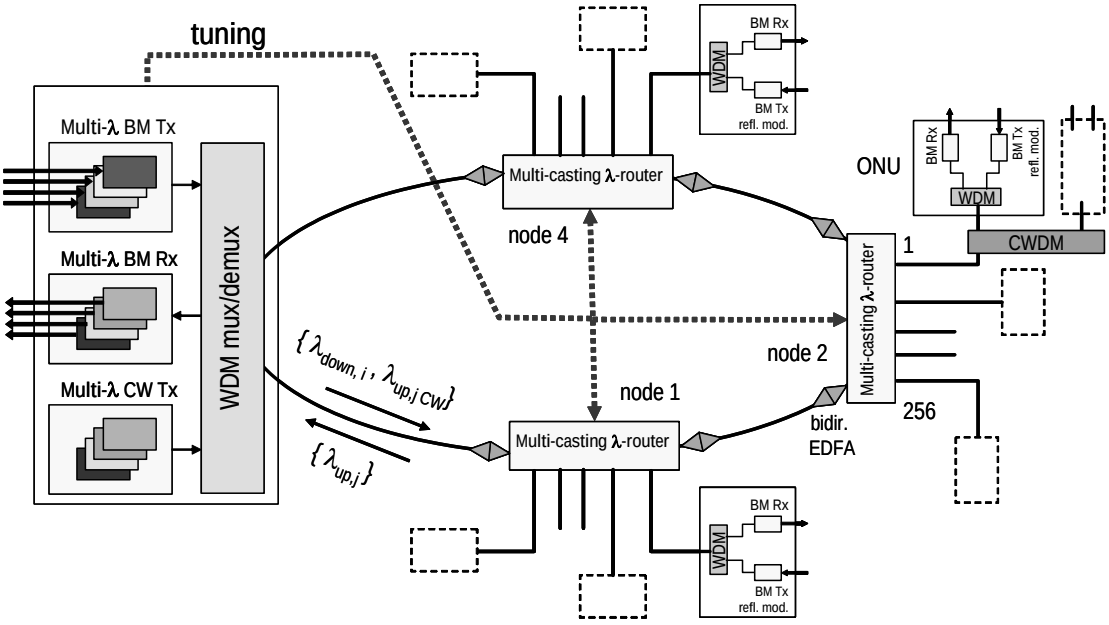

Figure 7.16. The Broadband reference network architecture.

7.3.1 Router implementation using micro-resonators

The typical (targeted) characteristics of the reference network are given in Table 7.1. The parameters of highest importance to the design of the router are the insertion loss, the multicasting insertion loss, the number of users per node (router) and the number of frequency pairs.

Table 7.1: access network key characteristics

Parameter	Value
Fiber type	Standard Single-mode (e.g. ITU G.652)
Ring circumference	Typical 20 km
Inter-node distance	< 20 km
Maximum number of users per head-end	1024
Maximum number of users per node	256
Distance node to user	< 5 km
Number of frequencies/wavelengths	20 on a 200 GHz grid
Number of frequency pairs	10
Maximum wavelength window	1530 - 1561 nm
λ-Router insertion loss	6 dB
λ-Router multicasting loss (256 ch.)	24 dB

Of the parameters that are of importance to the router the number of nodes is the most difficult parameter to meet, especially when using conventional optical components. Figure 7.17, for instance, shows a 1x20x256 router implementation using Arrayed Waveguide Gratings (AWG) [150] and switch matrices [151]. This implementation consists of 258 1x20 AWG's and 20 1x256 switch matrices. Given the relatively large size of these components it is evident that this implementation is difficult to realize.

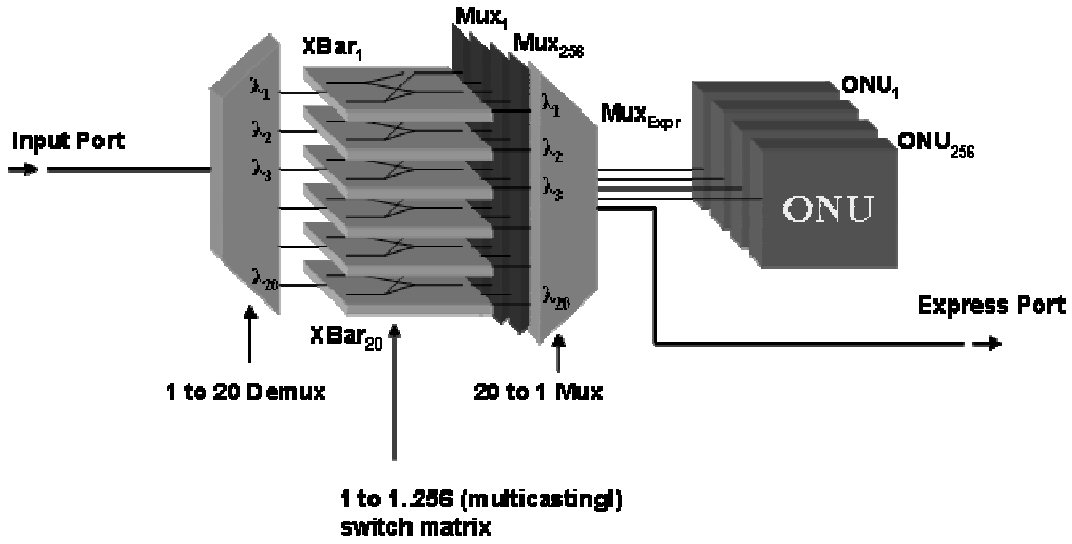

Figure 7.17. A 1x20x256 router implementation using conventional components

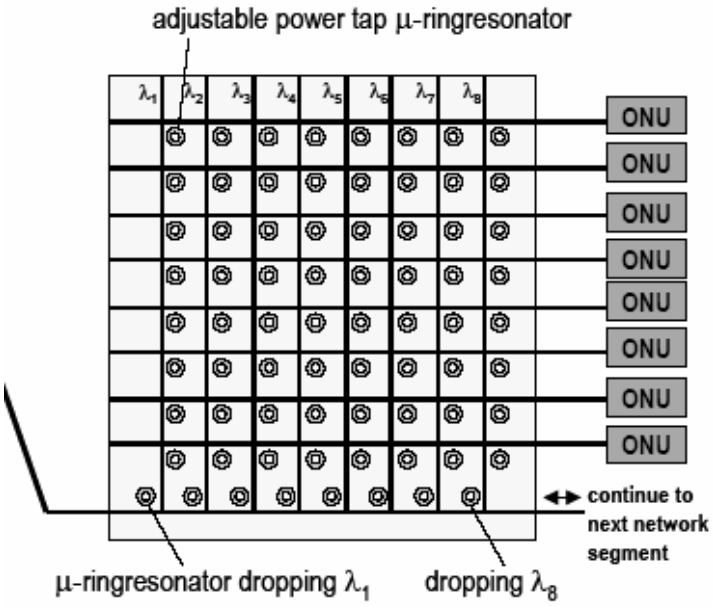

Figure 7.18. A 1x8x8 router implementation that uses micro-resonators

As an alternative the router can be realized using microring-resonators [139, 152]. An implementation of a 1x8x8 router that uses micro-resonators is shown in Figure 7.18. In this router a WDM signal enters the bottom row from the left side. The microring-resonators on this row demultiplex this signal so that a single channel is dropped to each of the columns in the routing matrix. The micro-resonators located in each of in these columns can then switch the channel onto one of the outputs (to the ONU's). If it is assumed that one micro-resonator "cell" in the matrix measures 250x250 µm then the full router will measure only 2.0x2.25 mm. In fact, the 1x20x256 router can be implemented ≈1x2 cm. The micro-resonator based router thus offers a clear advantage over more conventional implementations.

7.3.2 Router design

Although a 1x20x256 router is practically feasible when micro-resonators are used, the implementation still requires >2500 micro-resonators. Such a router is therefore extremely complex to design and fabricate. In addition, if all resonators require tuning, the power consumption would be prohibitively high if thermal tuning is used (see Chapter 6). On grounds of feasibility it was therefore decided that, as a first prototype, a relatively simple 1x4x4 router would be designed and fabricated. With this router any combination of 4 channels can be sent to 4 output ports. The choice for a 1x4x4 router had the added advantage part of the router had already been characterized, in the form of the OADM described in the previous section. As shown in Figure 7.19 five of these OADMs can be combined to form the 1x4x4 router.

According to the original network specifications [153] that were drawn up for the Broadband reference network, the router should have been designed for a channel spacing of 200 GHz (1.6 nm) with up- and downstream channels placed in adjacent positions as shown in Figure 7.20. However, this scheme proved to highly impractical when combined with the MR building block that, because it had proven itself in the OADM, was also seen as the best MR design to use in the router.

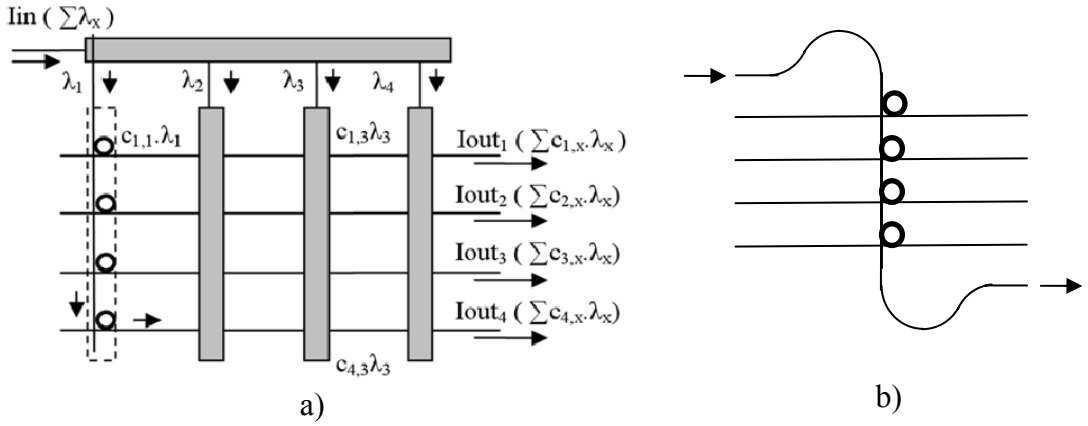

Figure 7.19. A 1x4x4 router a) can be implemented using five 4-channel OADMs b).

Because this resonator has a FSR of ≈4 nm the channel spacing scheme would have limited the number of channels within the FSR of a single resonator to at most 3 channels (i.e. two up and one downstream channel). The maximum number of channels that can be uniquely addressed using this scheme is therefore limited to three. A possible solution to this problem is to increase the FSR of the micro-resonators but, due to technological constraints, this is only possible through the use of Vernier-like schemes that utilize multiple micro-resonators and is therefore not very efficient.

An alternate solution however is found by realizing that the channels are always used in pairs. For instance, if a user requires more bandwidth then two additional channels are routed to the user: one upstream and one downstream. It is therefore possible to use one ring resonator to switch the up- and downstream channels simultaneously providing that the distance between them is equal to the FSR of the micro-resonator. A new channel configuration that uses the FSR in such a fashion was therefore proposed [154]. This new channel configuration, shown in Figure 7.21 has 8 up and downstream channels placed in pairs at a distance of 500 GHZ (utilizing the 4 nm FSR of the MR). The spacing between the individual channels is 50 GHZ, leaving 150 GHz for a guard band between up/downstream. The added bonus of the new configuration is that the number of required ring resonators in the router is effectively halved compared to the original channel configuration because each resonator is now used to drop two channels instead of one. Under the new scheme the 1x4x4 router shown in Figure 7.19 therefore effectively operates as a 1x8x4 router and is therefore referred to as such in the rest of this discussion.

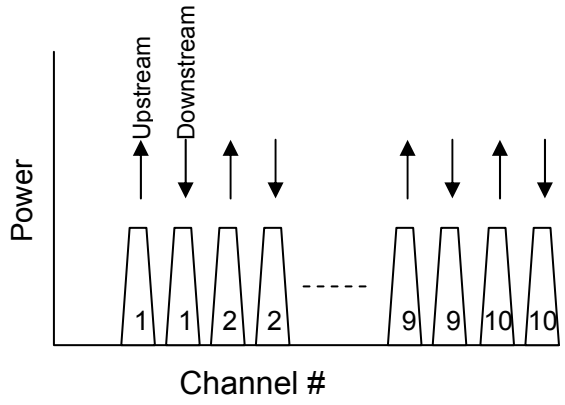

Figure 7.20. Original channel configuration with alternating up and downstream channels spaced at 200 GHz.

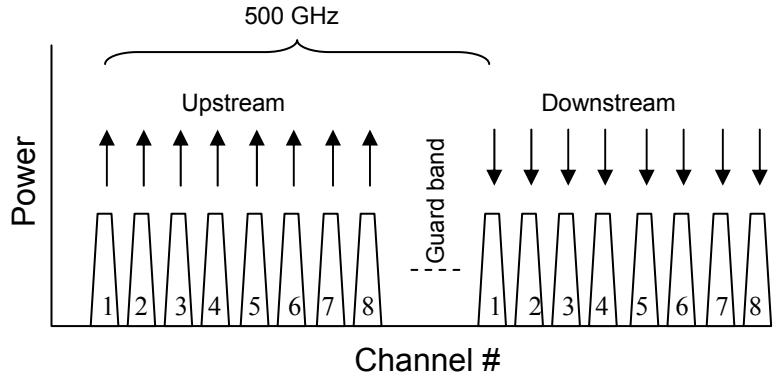

Figure 7.21. New channel configuration with 8 alternating up and downstream channels which have a 50 GHz channel spacing.

The schematic layout and the mask design of the 1x4x4 (1x8x4) router are shown in Figure 7.22. The router consists of a 4x4 microring-resonator router matrix and a 4 microring-resonator demultiplexer. For the individual resonators in the design the basic building block described in Chapter 6 was used with a resonator waveguide thickness of 180 nm. Because the router essentially consists of a large number of wavelength selective switches the individual resonators in the matrix can be designed using the same design rules as described in Chapter 6.4.1. Therefore, in order to achieve a bandwidth of ≈50 GHz, the target for the coupling coefficients in the design was ≈0.6.

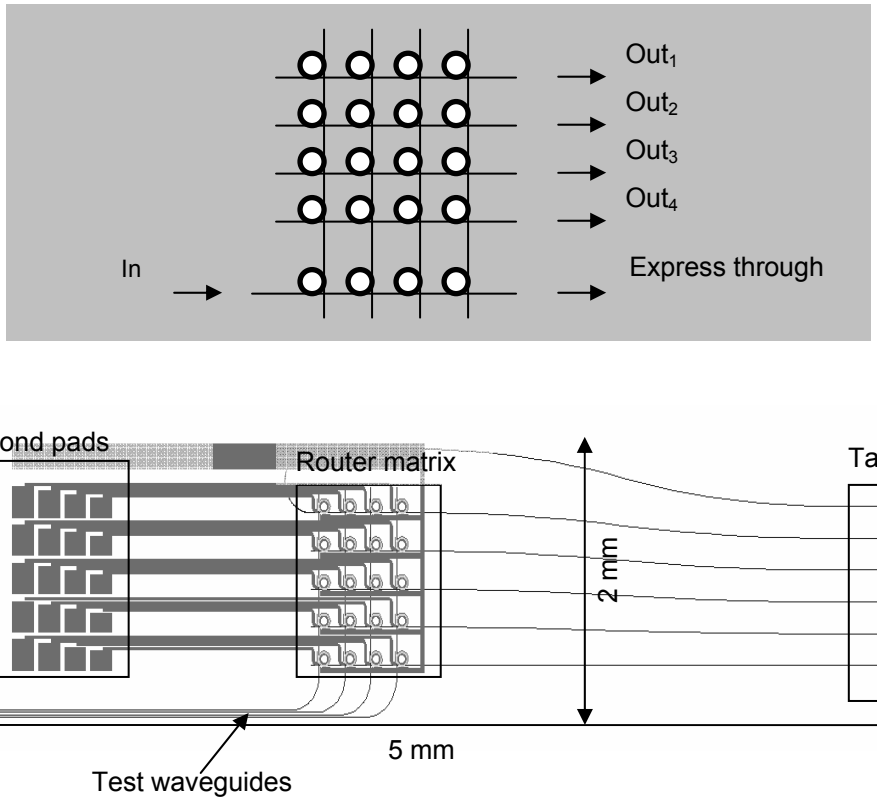

Figure 7.22. Schematic layout of the 1x8x4 router (top) and the equivalent mask design (bottom).

As indicated in the mask design the router matrix is situated in the center of a chip that measures only 5 x 2 mm. The vertical distance between the resonators in the

matrix is 300 μm and the horizontal distance is 250 μm. These distances were required to be able to fit the wiring of all the electrodes. Also, having some distance between the resonators will reduce the thermal crosstalk between the resonators. Also indicated in the figure are the horizontal taper sections and the electrode bonding pads. From the bond pads gold on chromium wires extend to the chromium heaters on top of the resonators in the router matrix. Because many of the resonators in the matrix interact with each other it can be difficult to interpret initial measurement results. Additional test waveguides were therefore incorporated in the design to help determine the resonance frequencies of the individual micro-resonators in each column.

7.3.3 Improved OADM design

The router design was to be fabricated in the new "Vertical II" fabrication process that used stepper lithography for the alignment and exposure of the resonator and port waveguides. Since not all of the image space on the reticle had been used for the router design the rest of the available image space was not only filled with several test structures but also with a new, slightly improved OADM design. This design, of which a schematic is shown in Figure 7.23, is largely identical to the OADM discussed in Section 6.2. In the new layout, however, the in- and output ports are placed on the same side of the OADM (compare, for instance, with fig.7.5). Therefore, if the OADM is only used as a de-multiplexer in a test-network situation, only one side requires pigtailing, saving considerable time in the fabrication process. By the wrapping around of this waveguide as shown in the figure it performs a dual function: it is both an in- and output as well as an alignment waveguide. A similar alignment waveguide is also present on the left side of this device. Vertical tapers were also for the first time implemented in this design.

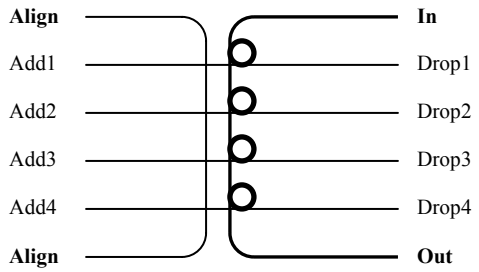

Figure 7.23. Re-designed OADM schematic

7.3.4 Characterization

The OADM and the router were both fabricated in the "Vertical II" fabrication process. However, due to a currently not yet fully understood interaction of the resist used for the stepper lithography (which is normally not used within MESA+) with the gasses used in the RIE etching process the etch rate of the nitride dropped dramatically. Regrettably this was not detected on time.
As a result most waveguides were only etched to a depth of 70 nm. Therefore, in stead of having rib waveguides for the resonators only a ridge was etched in stead. This is clearly visible in Figure 7.24b where a cross-section is shown of coupling region between two resonators of the second order microring resonator filter in Figure 7.24a. Also visible in this figure is a thin slab of Si_3N_4 underneath the resonator waveguides This is the layer used for creating the port waveguides which normally would have been etched away completely in this location.

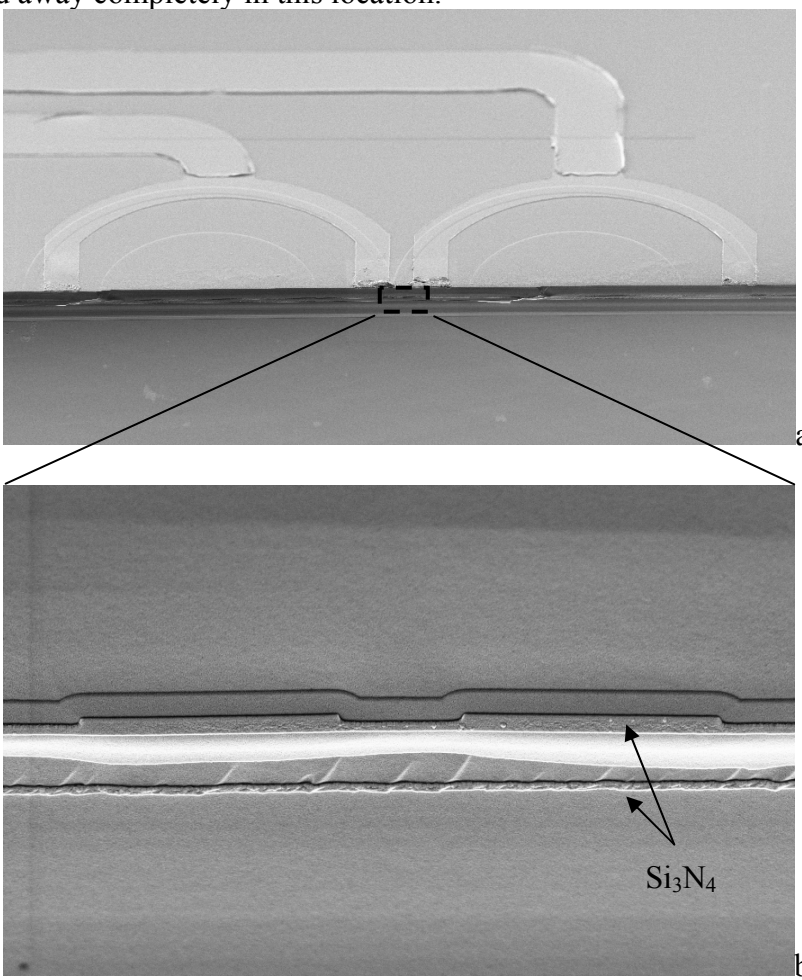

Figure 7.24. Top view a) and zoomed in cross-section of the coupling region of two microring resonators in a second order filter.

The etching down of the resonator waveguides proved to be especially dramatic in the case of the resonator which should have been etched down 180 nm. Therefore, instead of a bend loss in the order of ≈10 dB/cm at 1550 nm, measurements performed on single (test) resonators showed a bend loss in excess of 400 dB/cm, which made these resonators unusable at this wavelength. At 1310 nm, however, the results were relatively good due to the significant decrease in bend loss at this shorter wavelength

From the through and drop responses of single resonators that were fabricated along side of the OADM and Router devices a bend loss of ≈34 dB/cm was determined for these devices at this wavelength. In Figure 7.25 the drop responses measured around 1310 nm are shown for a number of resonators for a number of different port waveguide offsets *so* (and therefore for different field coupling coefficients). The resonators have a FSR of 3 nm and a finesse between 5.5 (for *so*=1.0 µm) and 15 (for *so*=2.0 µm). Using DropZone the resonator losses were determined to be 33 ±3 dB/cm.

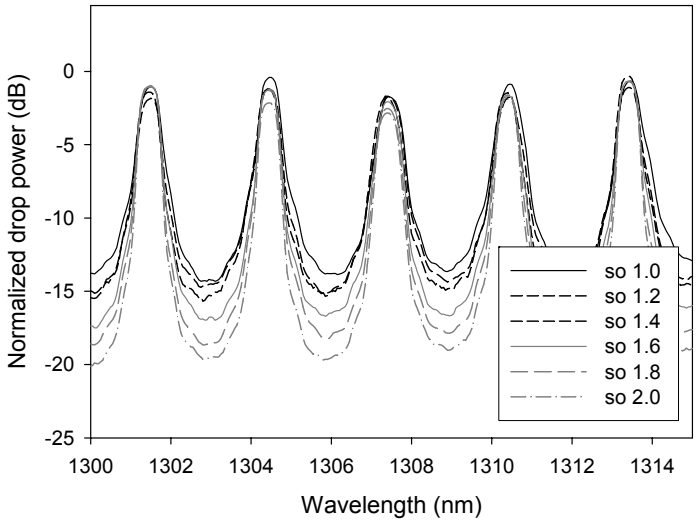

Figure 7.25. Drop responses measured for a number of resonators having different port waveguide offsets so (in µm).

7.3.4.1 Characterization of the OADM

The realized OADM, of which a picture is shown in Figure 7.26, was measured using a broadband source and an optical spectrum analyzer with a resolution of 0.05 nm. Figure 7.27 shows the normalized drop responses measured when the broadband source was connected the "In" port of the OADM (see Figure 7.23). The resonance frequency of each resonator has been tuned to a different wavelength to demonstrate the dropping of four different channels. In the drop responses of the resonators the individual effects of the adjacent MRs can be observed, for instance in the response at the fourth drop port. The three dips in the response of this port are the through responses of the three preceding resonators as has been shown previously in the measurements of the 1550 nm router. For the drop port responses shown, the filter rejection ratio of the individual resonators is ≈16.7 dB. From the measurements the amplitude coupling constants of the individual resonators were determined to be $\kappa_1=\kappa_2=0.40 \pm 0.01$ at resonator losses of 33 ±3 dB/cm. The FSR and Finesse are 3.0 nm and 10.6 respectively, giving a $\Delta\lambda_{FWHM}$ of 0.28 nm (=46 GHz @1310 nm). The channel crosstalk for channels spaced at 100 GHz (0.6 nm @1300 nm) is ≈-12dB. The on-chip insertion losses of the resonators are ≈5 dB which is due to the relatively high losses in the resonator. The consecutive drop responses from $Drop_1$ to $Drop_4$ show a steady decline of the maximum output power of around 0.25 dB per resonator that is passed.
With the known parameters of $\kappa_1=\kappa_2=0.40 \pm 0.01$ and $\alpha_{dB}=33 \pm 3$ dB/cm a simulation of the OADM was created in Aurora. The results from this simulation are given in

Figure 7.28. As can be seen the measured and simulated responses look very similar, showing the good quality of the fabricated OADM as well as the usefulness of Aurora as a simulation tool. In the Aurora simulations The steady decline of dropped power from $Drop_1$ to $Drop_4$ is also seen. However, here it is about 0.2 dB for each resonator that is passed. In Aurora these losses are due to the fact that there is some crosstalk between the channels which lowers the dropped power from one resonator to the next. In the measured OADM this same effect is occurring but also the losses incurred by each waveguide crossing (of the center bus waveguide with a port waveguide) between the resonators need to be taken into account. Since these losses were not included in the simulated OADM this leads to the conclusion that around 0.05 dB is lost at each waveguide crossing. It has to be noted, however, that there is significant uncertainty involved in this number since the simulated and measured OADM are not exactly identical.

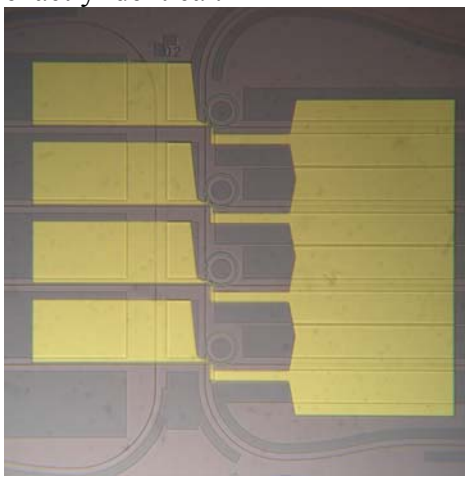

Figure 7.26. Realized OADM.

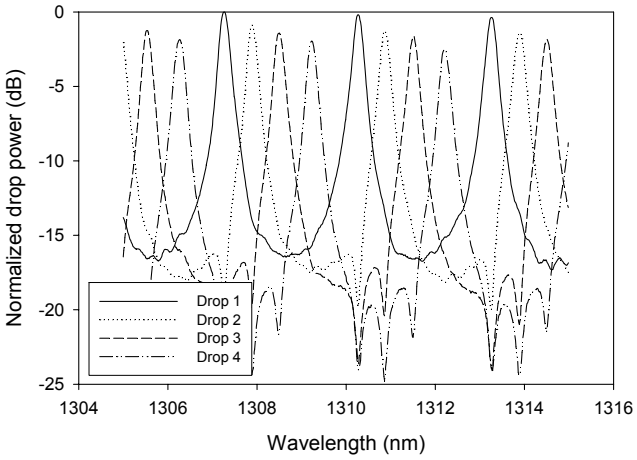

Figure 7.27. Drop Responses of $Drop_1$-$Drop_4$ (see Fig 7.23) for a broadband source connected to the "In" port.

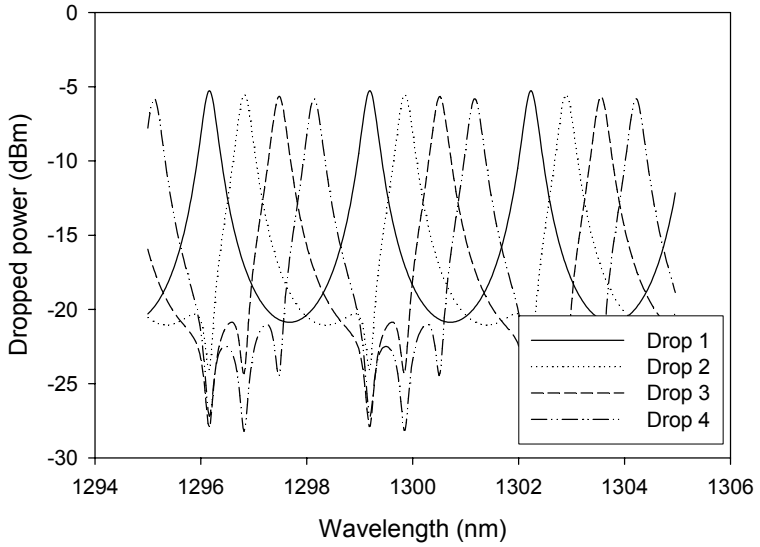

Figure 7.28. The drop responses of the OADM simulated using Aurora

A system level measurement at 1.25 Gbit/s was also performed on this OADM by Patryk Urban of the TUE. For this measurement, a reference measurement was first performed using the setup as shown in Figure 7.29a in order to find the sensitivity of the receiver. The extinction ratio of the modulator that was used is 7,7dB at 1305.2

nm. Next, the setup as shown in Figure 7.29b was used to measure a signal going through the $Drop_1$ port of the OADM. As can be seen in the BER (PRBS = 2^{31}-1 @ 1,25Gb/s) measurement results of these two setups shown in Figure 7.30 no significant power penalty was measured. As can be seen in eye patterns shown in Figure 7.31 the OADM has no significant effect on the opening of the eye.

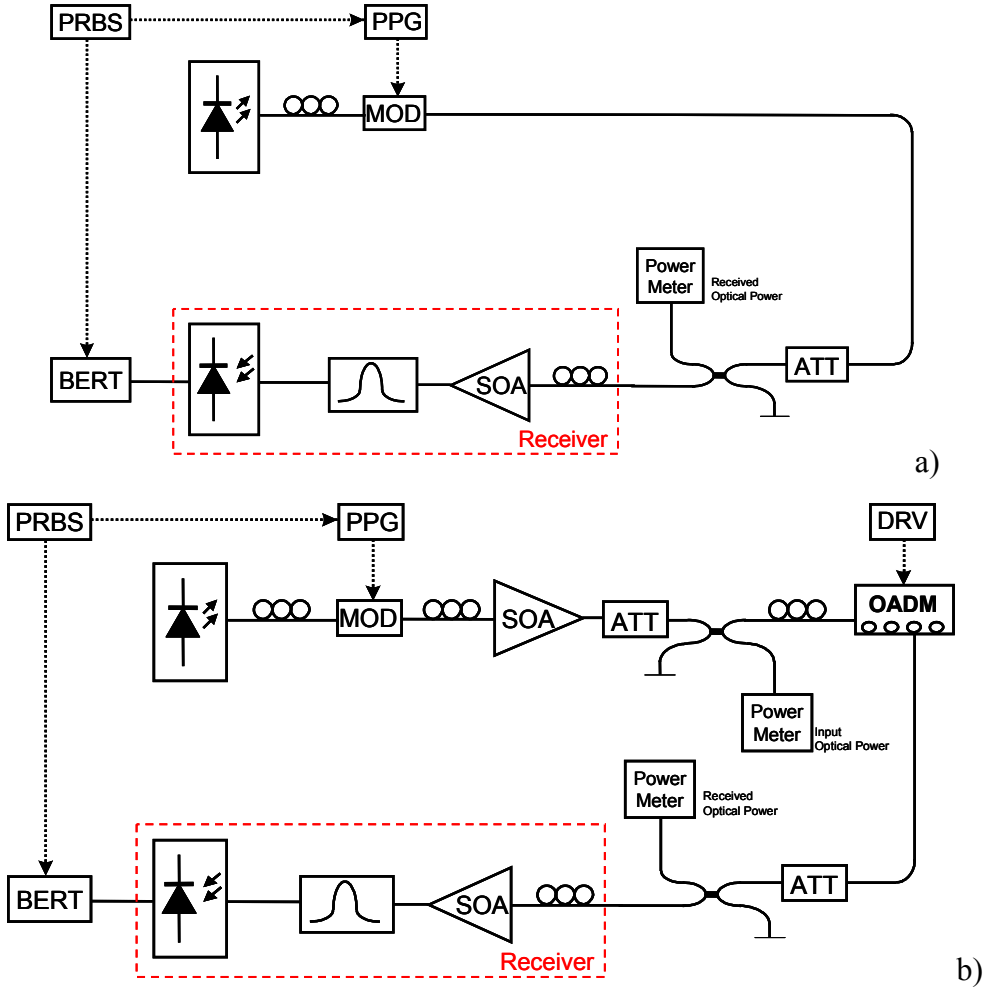

Figure 7.29. Reference measurement setup a) and the setup with the OADM inserted b) that was used to measure the BER at 1.25 Gbit/s.

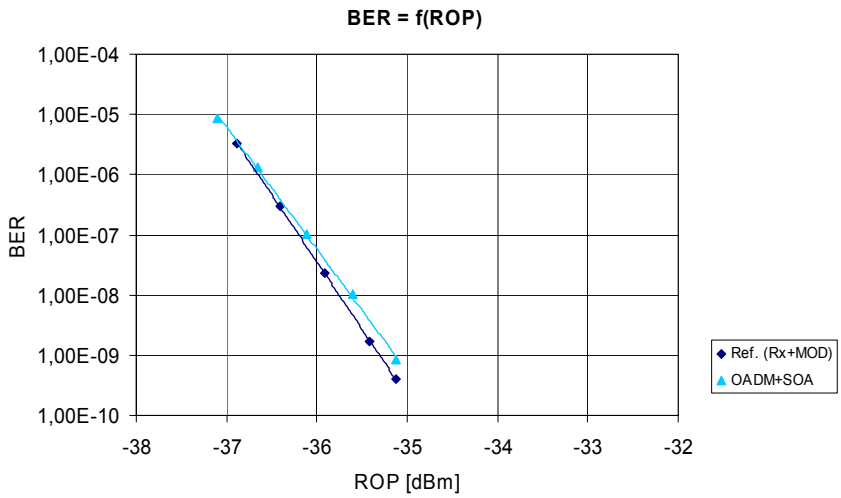

Figure 7.30. BER at 1.25 Gbit/s.

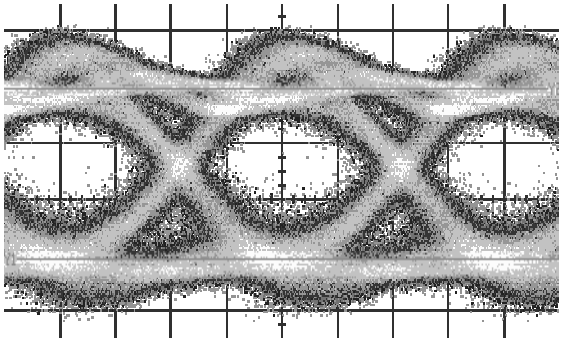

Figure 7.31a. Eye pattern of the reference setup.

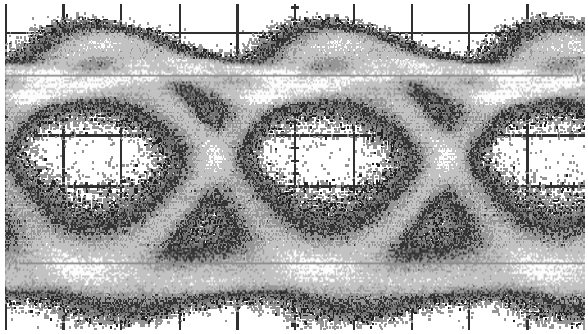

Figure 7.31b. Eye pattern of the setup with the OADM.

7.3.4.2 Characterization of the Router

The λ-router, shown in Figure 7.32, was also characterized using the broadband source at the input and the OSA to measure the wavelength response of the first drop port as indicated in Figure 7.33.

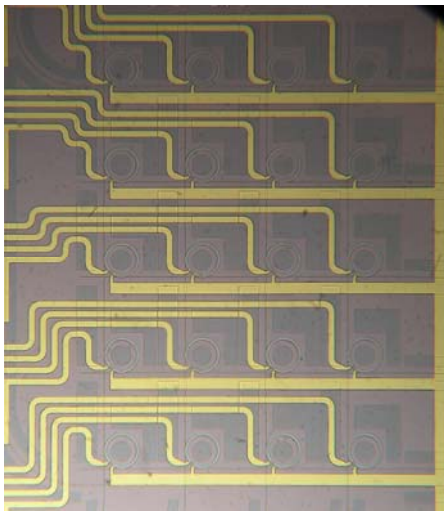

Figure 7.32. Realized 1x4x4 λ-router.

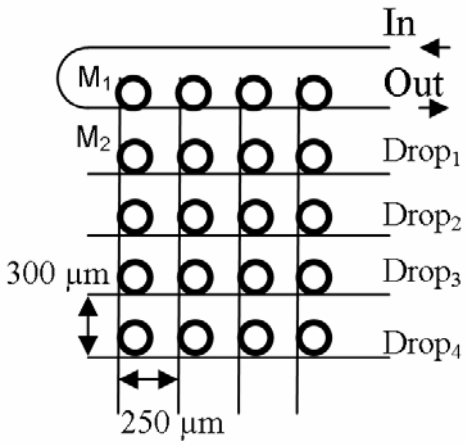

Figure 7.33. Router layout

In Figure 7.34a the responses measured at this port are given for three different "tuning" configurations of the router. In the first configuration the heaters on all resonators are switched off and all resonators are in resonance at the same wavelength. The spectral response of this configuration shows a single broad peak, with a FSR of 3 nm. This peak is predominantly the result of the power dropped by the first resonator in the de-multiplexer section of the router (M1 in Figure 7.33). The minor dip in the center of the peak is due to the interaction with the (smaller) power fractions dropped by subsequent resonators in the de-multiplexer. For the second configuration the first resonator was tuned half a FSR. The power dropped by this resonator shows up as the minor peak in the response. The major peak is now the result of the power dropped by the second resonator in the de-multiplexer and the interactions with the third and fourth resonators. For the third and final router configuration resonator M2 was tuned to the same wavelength as M1. This causes the channel selected by M1 to be dropped by M2 onto the first drop port. The channel is therefore effectively switched "on" on this port for this configuration as is shown by

the large peak in the response measured for this configuration. A comparison with the response of the second configuration shows that the "on" / "off" switch ratio that can be obtained for this router is ≈15 dB. The $\Delta\lambda_{FWHM}$ of the dropped channel is 0.22 nm (=37 GHz @1310 nm).

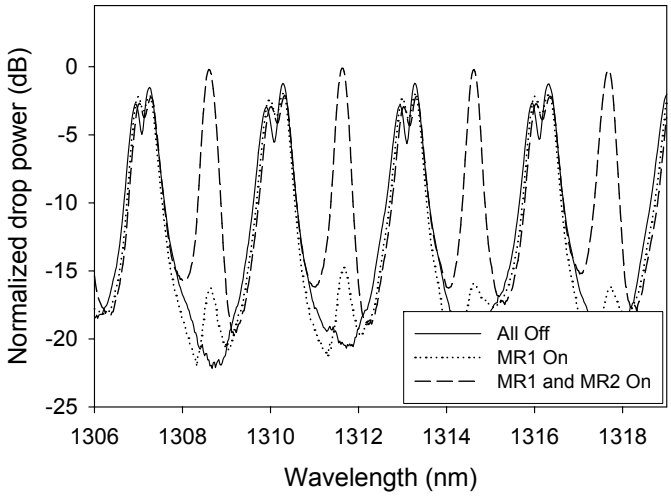

Figure 7.34. Switching of a single channel in the router.

Following these measurements the router was pigtailed, wirebonded and packaged in a compact box as shown in Figure 7.35. This box contained all necessary hardware to drive control the router via USB.

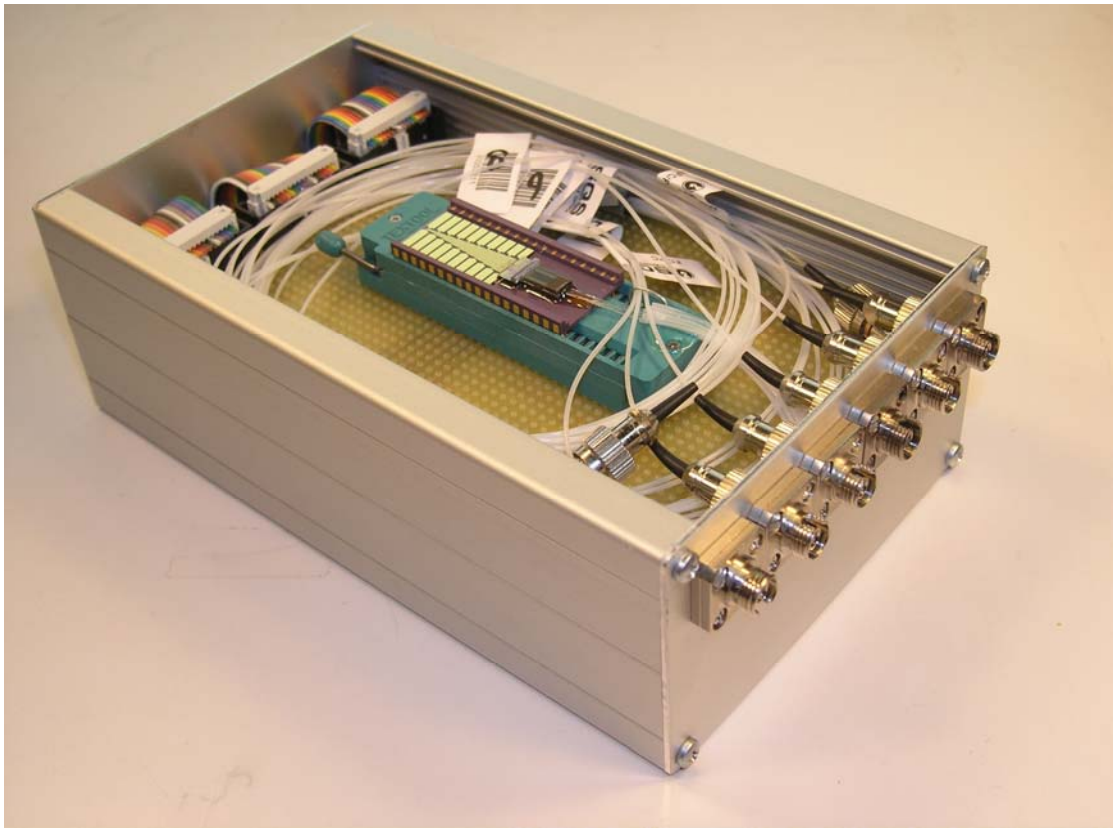

Figure 7.35. The 1300 nm router packaged in a compact box.

After packaging all heaters on the router could be driven on more complex switching measurements could be performed. Unfortunately, however, some heaters were damaged in the initial router tests. In addition, the high power output of the broadband source damaged the glue after prolonged measurements, resulting in a drop in the

measured power of more than 15 dB. The preliminary measurement results shown in Figure 7.36 that show the switching of two or three channels to the first drop port of the router are therefore quite noisy. Nonetheless, these measurements do show the powerfull capability of the router to select and switch multiple channels to a certain output channel.

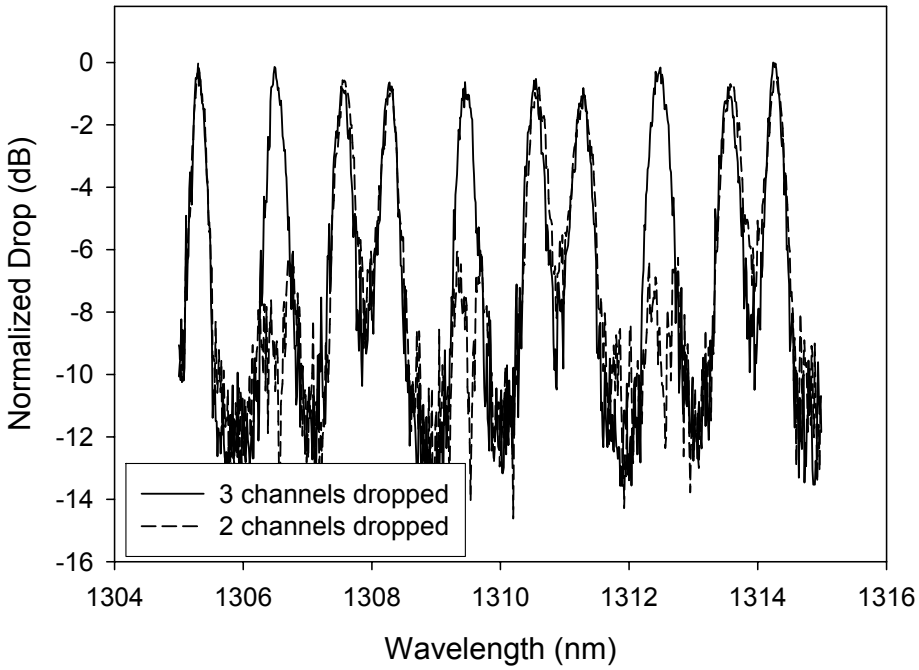

Figure 7.36. Output spectra measured at the first drop port of the router showing the dropping of 2 and 3 channels.

Chapter 8

Polarization independent devices

One of the greatest concerns in the design of optical devices that have an application in Telecom is that these devices need to be polarization independent. This property is especially hard to achieve in micro-resonator based devices as their design and fabrication tolerances often don't allow for a practical solution. In this chapter an approach based on polarization diversity is discussed. The strength of the proposed solution lies in the fact that only a minor increase in the number of components is required instead of the traditional doubling normally associated with the diversity scheme. The main ideas presented in this chapter have been filed at the US patent office.

Chapter 8

8.1 Introduction

In most optical communication networks, fibers are used to connect between the optical nodes. The polarization state of the transported optical signal in these fibers is undefined and often changes over time. However, for reliable operation of the network the behavior of the nodes should not vary with the state of the polarization. Therefore, polarization-independent performance of the (integrated) optical devices at the nodes of the network is of major importance.

In devices without microring-resonators that have relatively low birefringence, in the order of 10^{-3}, several techniques have been proposed to reduce the birefringence.
Stress induced birefringence has for instance been reduced by using stress releasing grooves [155] or stress compensating layers [156, 157]. Other techniques use carefully designed polarization independent ridge waveguides [158, 159]. Also birefringence compensating layers of high index materials have been incorporated in the waveguide geometry [160, 161].
In devices based on high index contrast microring resonators, however, the birefringence and polarization dependent loss (PDL) can be quite substantial. The standard resonator building block that was described in Chapter 6, for instance has a birefringence of ≈0.04 and TM mode propagation losses that are about 3 orders of magnitude larger the losses for the TE mode. In addition, the coupling strength of the couplers of a resonator is also highly polarization dependent.
The high birefringence and PDL in these devices are mainly the result of choices made in the design of the resonator. Merely compensating for stress induced birefringence is therefore insufficient, as well as the use of compensating layers. Altering the waveguide of the resonator geometry can, in theory, improve the birefringence. However, there are a number of problems with this.
Firstly not all materials allow the resonator to be fabricated in the dimensions that are required for polarization independence. This might for instance be due to material stress, its refractive index or technological constraints such as lithographical resolution or maximum etch depth.
Furthermore, even if the materials pose no problem, it may be highly challenging to find waveguide dimensions for which:

a) the port and resonator waveguides have zero birefringence,
b) the resonator is phase-matched to its port waveguides, and
c) the coupling coefficient of the directional couplers is polarization independent.

The design of polarization independent racetrack resonators is slightly less complicated in this respect as these devices are intrinsically phase-matched. Proposed solutions [162-164] for these resonators, however, often result in a substantially higher resonator radius which is often undesirable.
Even if these two problems can be overcome there is still the issue of fabrication tolerance. Micro-resonators with a small radius have to be fabricated in high index-contrast materials. This, on the basis of mono-modality, implies small waveguides that are far less tolerant to variations in the fabrication process. It may therefore be very difficult to fabricate devices in which the microring resonator waveguides and couplers consistently show polarization independent behavior.

8.2 Polarization diversity

Instead of designing a resonator in such a way that its behavior is polarization independent, it is also possible to use a polarization diversity approach [135, 165]. In a polarization diversity device, such as for instance the polarization diverse implementation of a single microring resonator shown in Figure 8.1, the TE and TM polarized signals are separated at the input of the optical device. The polarization of one signal is then converted (for instance TM to TE) after which both signals are led through two identical parts of the device. The main advantage of this is that the resonators need to be optimized for one polarization only, thereby solving many of the problems related to the design and fabrication of polarization independent devices.
At the output of the device the polarization of one signal is again converted –to avoid interference between the signals- after which the TE and TM polarized signals are combined.

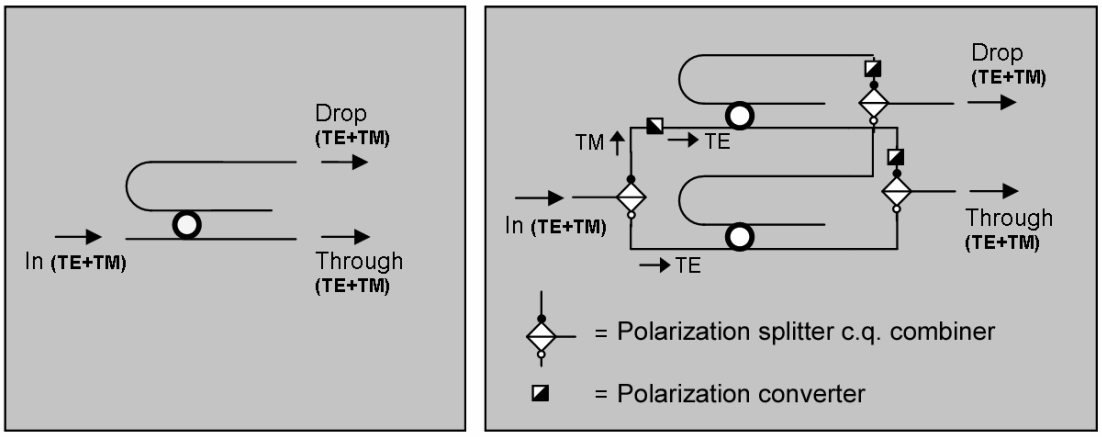

Figure 8.1. The polarization diverse implementation of a single resonator filter (right) consists of two copies of the original non-diverse implementation (left). Each resonator is then used to filter only one polarization of the light that enters the device.

Although polarization diversity has clear advantages over non-polarization diverse approaches it also introduces several new problems.
The polarization diverse approach effectively doubles the number of resonators and requires the use of polarization converters. While the larger number of resonators might increase the footprint, it is generally not a problem due to the small size of the resonators. Also, as discussed in Chapter 3.7, factors other than the size and number of the resonators determine overall device size at high levels of integration. In addition, polarization diversity requires the use of polarization converters which add to the complexity of the circuit in both design and fabrication. However, several converters have been proposed that can be integrated efficiently, using for instance half-wave plates [166], angled waveguides [167, 168], bends [169], gratings [170, 171] and micro-resonators [136-138].

A problem of greater concern, especially in devices with a large number of resonators, is controlling the resonance wavelength of each micro-resonator.
Micro-resonators with a predefined resonance wavelength are difficult to fabricate and therefore nearly always require some form of “tuning” to make them resonate at the desired wavelength. In addition the “tuning” might also be required to implement some form of functionality, e.g. switching or modulation. This tuning requires an electronic driver for each individual micro-resonator and in each resonator a certain

amount of power will be dissipated. The power requirements and the number of drivers for a polarization diverse implementation are therefore roughly twice that of an implementation that uses polarization independent micro-resonators. A larger number of devices that require tuning will also increase the pin count of the devices (since each micro-resonator has to be connected to a driver) which can add significantly to the manufacturing costs. Furthermore the polarization diversity scheme requires that the resonance frequencies of the micro-resonators that perform identical functions in the TE and TM polarized light sections of the device are perfectly matched in order to avoid signal degradation (e.g. due to Polarization Mode Dispersion or Polarization Dependent Loss). These strict requirements increase the complexity of the driver electronics and add to the number of device parameters to be validated during manufacturing, resulting in an overall increase in cost.

8.3 Polarization independence through bi-directional use of the micro-resonator

The problems associated with the tuning, matching, power consumption and packaging can severely limit the usefulness of the polarization diversity approach, especially in large scale integrated optical devices that consist of many components. Under the right conditions it is possible, however, to implement polarization diversity in such a way that the required number of resonators is only slightly higher than that used by non-diverse approaches whilst completely removing the matching problems. The solution is found in the fact that the micro-resonator (or any four port element with equivalent functionality) can be used bi-directionally for two signals at the same wavelength without having these signals interfere with each other. This is illustrated in Figure 8.2 where two signals, both with wavelength λ_1, enter the micro-resonator from opposite sides. The signal originating from port 1 will propagate through the micro-resonator in the counter clockwise direction and (when in resonance) will be dropped to port 3. A signal that originates from port 2, however, will propagate through the micro-resonator in the clockwise direction and will be dropped onto port 4. As the two signals within the microring-resonator propagate in opposite directions, there is no interference between these signals, even though they are of the same wavelength.

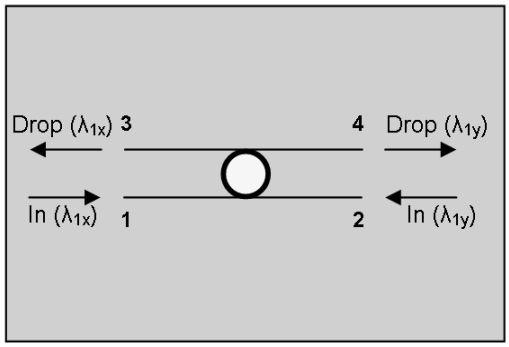

Figure 8.2. Bidirectional use of the same micro-resonator by two signals x and y, each having wavelength λ_1. (The through ports of input ports 1 and 2 are ports 2 and 1 respectively but are not shown to keep the figure simple)

Although this concept can be applied to any two signals of equal wavelength that require the same optical operation it is especially useful for implementing polarization diversity. This is due to the fact that, by definition, the TE and TM polarized signals

are of equal wavelength and require exactly the same optical operations under the polarization diversity approach. Instead of making use of one resonator per filter function per polarization it is therefore possible to implement polarization diversity using only one resonator per filter function for both polarizations.

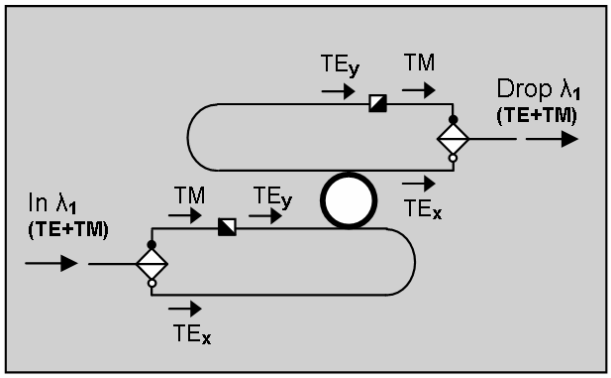

Figure 8.3. Polarization diversity using a single resonator.

Figure 8.3 shows how this new approach can be applied to a single resonator filter. In this filter an incoming signal is separated into the TE and TM polarization states. The TM polarized light is converted into TE polarized light (TE_y) and then enters the micro-resonator from the left side. The TE polarized light (TE_x) enters the micro-resonator from the right side. At the backend of the micro-resonator TE_y is converted back to TM polarized light and combined with TE_x.

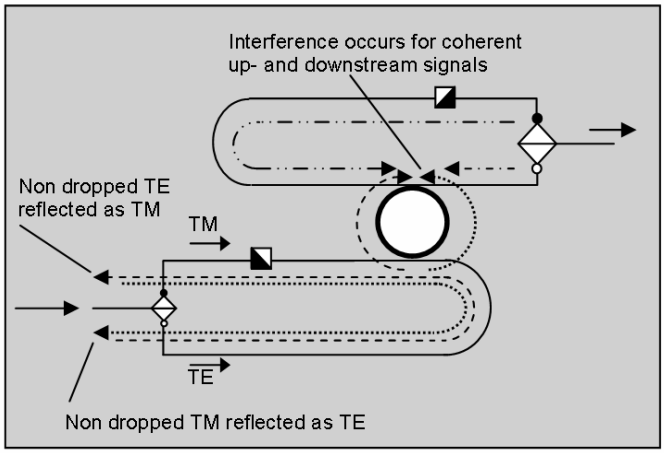

Figure 8.4. Possible problems when using the bi-directional approach to polarization diversity: reflections and up/downstream signal interference.

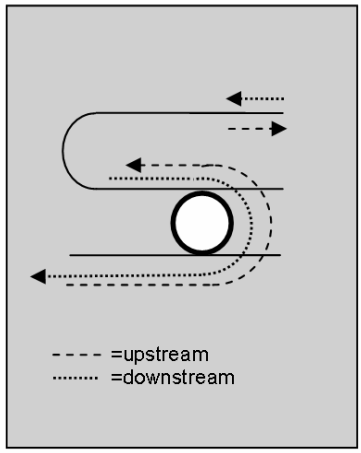

Figure 8.5. Up- and downstream propagate in different directions through the MR

The approach can significantly reduce the total number of resonators in addition to solving several other problems. However, it is not without its limitations. One problem, as shown in Figure 8.4, is that light that is not dropped by a resonator will inevitably propagate back to the input of the device, in effect creating a reflection. This is even true for light that is dropped because, as was discussed in Chapter 3.2.6, a minor fraction of the input light of a resonator will always remain in the through port at resonance. The returned light does not have to be a problem, however, because many implementations of optical networks already include optical isolators to filter out unwanted reflections.

Another problem that may occur is when the device is intentionally used in an up- and downstream configuration. In a normal resonator, as shown in Figure 8.5, the up- and downstream signals circulate in opposite directions through the resonator, making interference between the signals impossible. However, in a polarization diverse resonator signals from one direction already circulate in two directions. Since the downstream signal will also circulate in both directions interference may therefore occur if these signals are coherent.

It also needs to be noted that not all devices are equally suitable for implementation using the bi-directional diversity approach: some devices can be implemented very efficiently while the required functionality of other devices makes it impossible.
The regular polarization diverse implementation of a 1xn multiplexer shown in Figure 8.6, for instance, can be implemented very efficiently using the bi-directional approach as shown in Figure 8.7. This is because in the de-multiplexer the signals only need to be dropped from a central bus waveguide. It is therefore possible to create an optical circuit in which the two polarizations (TE and the converted TM) can enter the resonator from opposing directions by adding the "loops" indicated in the figure.

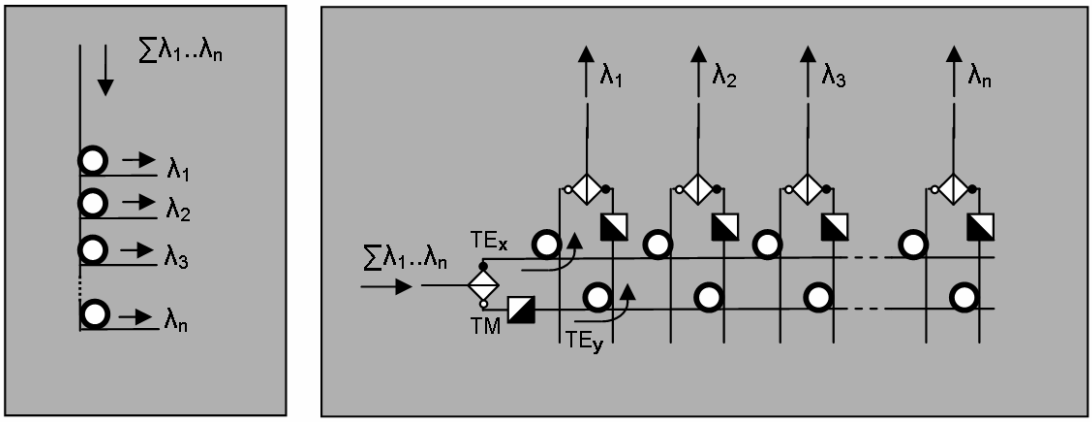

Figure. 8.6. A polarization independent 1x*n* de-multiplexer (left) and the regular polarization diverse alternative that uses unidirectional micro-resonators (right).

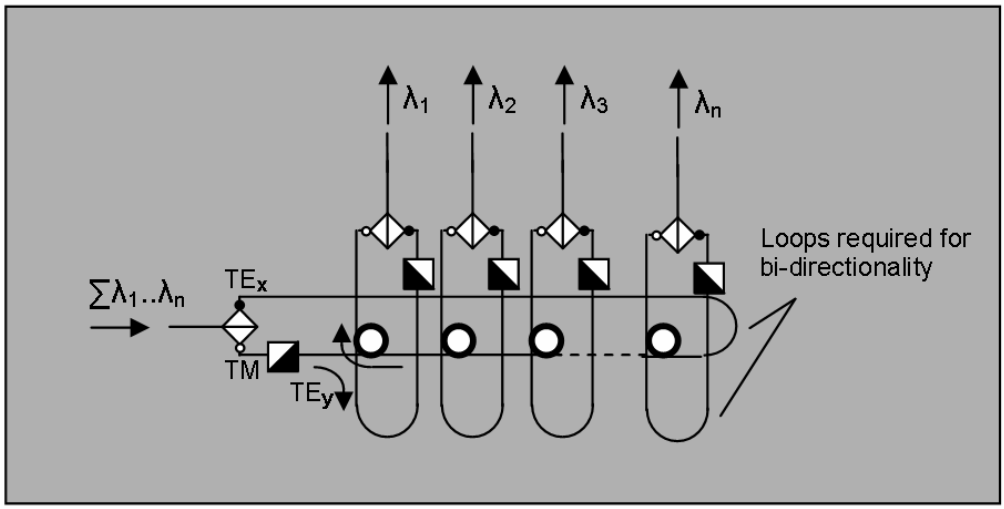

Figure 8.7. Bi-directional polarization diverse implementation of a 1x*n* wavelength de-multiplexer.

If signals also need to be added to the bus waveguide, however, as is the case for the 1xn optical add-drop multiplexer, the bi-directional use of the resonators is no longer possible. This is because it is impossible to create the add- and express through ports without opening the loops that were added in Figure 8.7 to create the bi-directional propagation through the resonators. The OADM therefore needs to be implemented as shown in Figure 8.8, using the unidirectional polarization diversity approach.

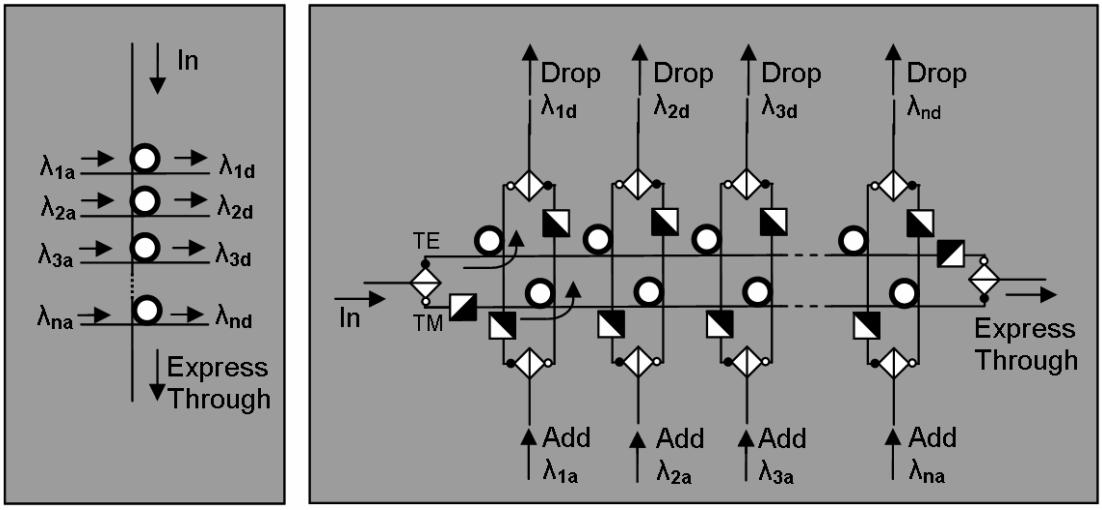

Figure. 8.8. A polarization independent 1xn Add-Drop multiplexer (left) and the polarization diverse alternative that uses unidirectional micro-resonators (right).

8.4 Polarization diverse Router

Fortunately the router is one of the components that can benefit significantly from bi-directional polarization diversity. Figure 8.9 shows the unidirectional polarization diversity implementation of a $1 \cdot m \cdot n$ router. The router consists of two identical

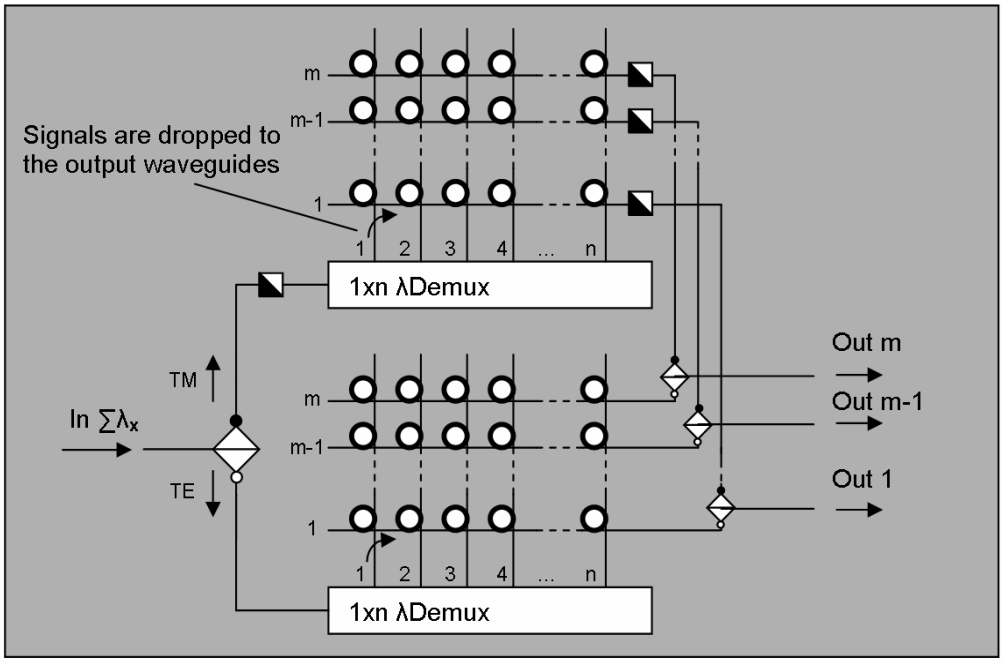

Figure 8.9. Polarization diverse implementation of an $1 \cdot m \cdot n$ wavelength router that uses unidirectional micro-resonators.

halves that are each comprised of a de-multiplexer, which can be implemented using for instance micro-resonators or an AWG, and a routing matrix as was discussed in Chapter 7. The de-multiplexer filters out the *n* individual channels on the input port and directs these into the routing matrix. In the routing matrix these channels can then be combined in any required combination and sent to one of the *m* output ports. Because the individual channels are only dropped to an output waveguide and no adding of channels is required as was the case for the OADM, it is possible to redesign the router for bi-directional use of the resonators, resulting in the implementation given in Figure 8.10.

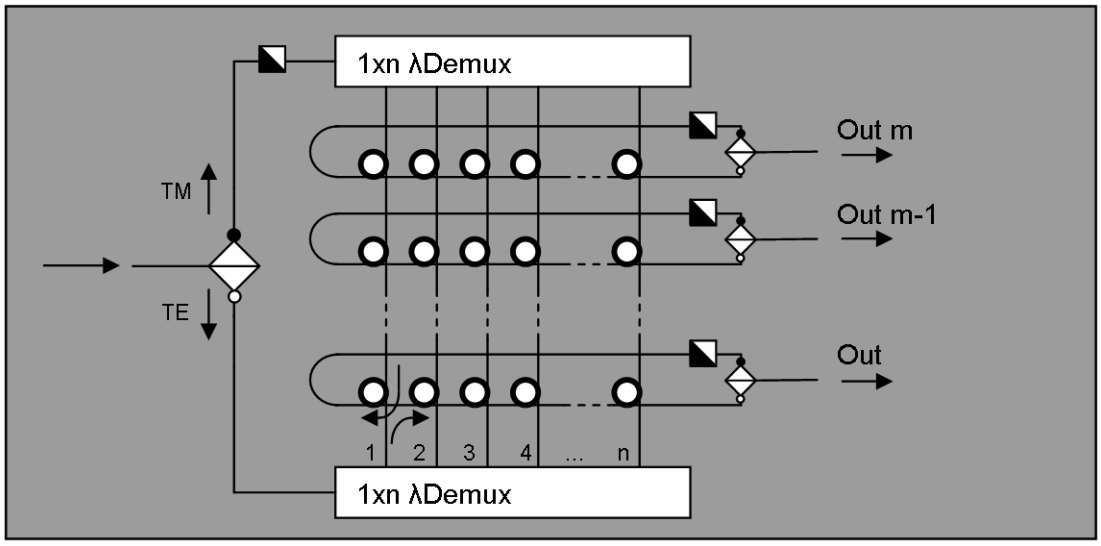

Figure 8.10. Polarization diverse implementation of a $1 \cdot m \cdot n$ wavelength router that uses bi-directional micro-resonators.

This router uses only a few more optical components than a polarization independent implementation. Assuming that the de-multiplexers are created using resonators the additional number of components (MR+ pol. splitters/combiners + pol. converters) will scale as $Num_{comp} = 2(1+m)+n$. A 16 by 16 router would therefore have a component overhead of only ≈18% with respect to a router implemented using polarization independent resonators.

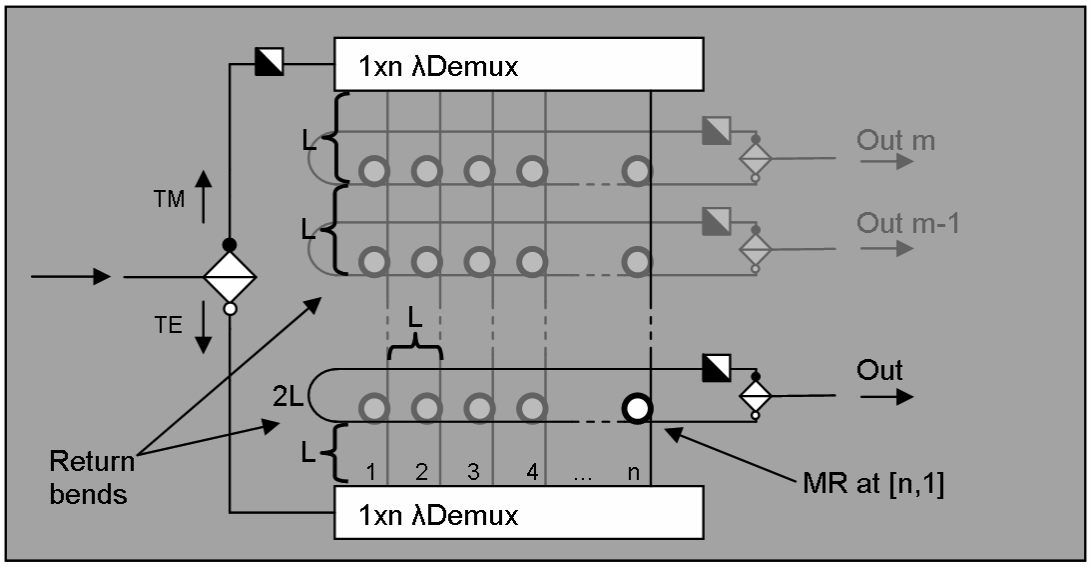

Figure 8.11. Polarization diverse implementation of a $1 \cdot m \cdot n$ wavelength router that uses bi-directional micro-resonators.

While this router implementation guarantees that signals for each polarization are filtered by the resonators in the matrix in exactly the same way, there is still a time-delay between the arrivals of the two polarizations at the output of the router. This polarization mode dispersion (PMD) can be quite high depending on which channel is dropped and which output port it is dropped to. For instance, it can be assumed that a router design can be created where the grid spacing between the resonators in the horizontal and vertical directions is L. If it is then also assumed that the return bends can be created with length $2L$, as shown in Figure 8.11, then the path length difference between the polarizations is $\Delta Path = L(m + 2(n-1) + 1)$ for the resonator at position [n,1]. For L=250 μm and m=n=4 this is a difference of 2750 μm or, assuming an effective refractive index of 1.5 for the waveguides, a PMD of ≈6.1 ps. For convenience, the PMD that might be incurred by the polarization splitters and converters is not taken into account. The high PMD can significantly affect the bit-error rate in high bandwidth applications. It can be compensated for, however, as is shown in the $1x3x3$ router example given in Figure 8.12. Here the waveguides that exit the lower de-multiplexer, as well as the return bends, have been given additional length so that the path lengths from the de-multiplexers to the outputs are identical for both polarizations.

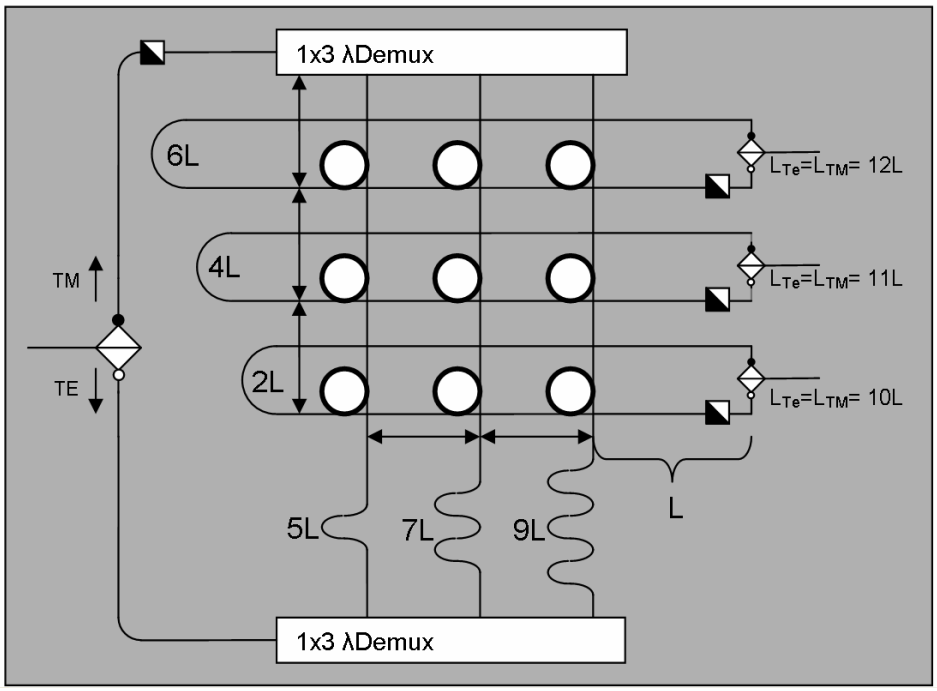

Figure 8.12. Polarization diverse implementation of a $1x3x3$ wavelength router that uses bi-directional micro-resonators and has PMD compensation. (The arrow markers indicate equal grid distances)

Generalizing the example it can be said that, for a router matrix with m outputs, n channels, a grid-size L and a minimum return bend length of $2L$ a PMD compensated matrix can be created when the length of the return bends is set following the rule:

$$L_{\mathrm{Re}turn\_bend\_i} = 2i \quad (i=1..m) \tag{8.1}$$

and the length of the waveguides at the lower de-multiplexer as:

$$L_{Demux\_guide\_j} = m + 2 + 2j \quad (j=1..n) \tag{8.2}$$

Chapter 9

Discussion and Conclusions

During the four years in which the work presented in this thesis was carried out the quality and complexity of the microring resonators steadily progressed from single resonators showing very bad responses (see for instance Figure 6.18) to multi-resonator devices such as the OADM and router presented in Chapter 7 that show spectra that nearly look like simulations. In this thesis an attempt was made to not only show the results obtained from the devices that have been fabricated but to also give most of the tools and information required to continue the work on even more complex devices.

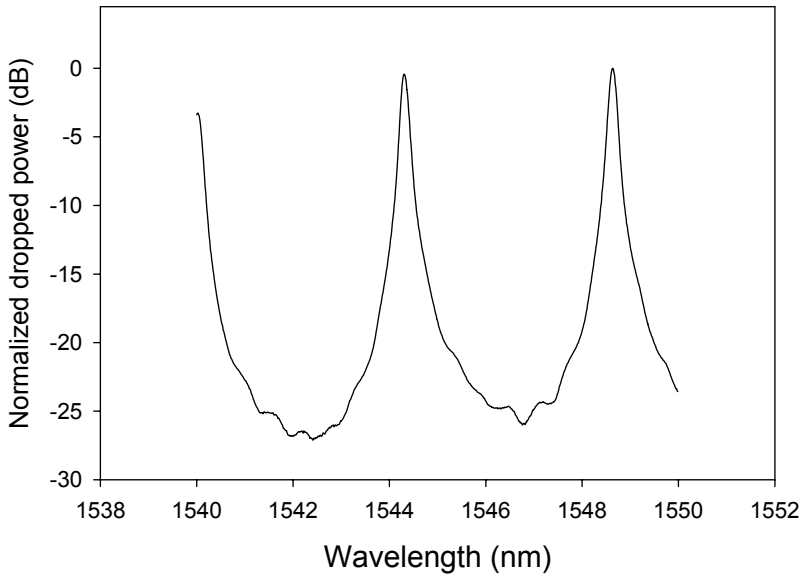

Figure 9.1. Response measured at the drop port of a 1550 nm OADM fabricated in the Vertical II fabrication process.

Regrettably the problems with the fabrication of the router, although resulting in a few highly interesting devices in the 1300 nm telecom window, caused such a delay devices that the intended devices, designed to operate at 1550 nm, were not yet

available for full characterization and are therefore absent from this thesis. Many of the technology and design improvements made when moving from the Vertical I to the Vertical II fabrication process could therefore not yet be verified to work as intended. A last minute measurement, shown in figure 9.1, made on a drop port of an OADM from a new batch of 1550 nm devices however, shows the best drop response ever measured (and this is not a typical best result) in a Si_3N_4/SiO_2 OADM. This therefore holds great promise for the operation of the complete OADM and Router devices in the 1550 nm window.

Concerning the work presented in this thesis the following conclusions and recommendations can be made:

- Silicon nitride is a highly suitable material for the fabrication of microring resonator based components. Although it does not allow for the fabrication of resonators as small as is possible in for instance silicon this will often not be a problem because it is more likely that the size of the devices is limited by external factors such as the fiber chip coupling with a fiber array than by the size of the resonators. Also, given the right technology, very low loss waveguides can be made (<0.1 dB/cm) and, because it can be deposited in multiple layers, also allows for dense integration in the third dimension.
- Stepper lithography is absolutely essential when making vertically coupled resonators. Although error compensation schemes as discussed in this thesis are possible these are ultimately impractical because of the reduced yield. Also, when moving to higer order resonator configurations, stepper lithography will be required to image small features such as the small coupler gaps that are typically present in these devices.
- When carefully examining the various performance parameters in Chapters 2 and 3, however, it is easily seen that it will be difficult if not impossible to create an OADM or router with specification that are good enough for even current optical networks when only single resonators are used. Higher order resonators will therefore be required in future devices.
- Also essential is the use of CMP in the fabrication process to reduce the losses in the resonator caused by the abrupt lifting of the resonator at the port waveguides. Although a quantitave measurement to see the improvements in the resonator loss has not yet been made, the measurement in figure 9.1 seems to indicate a definite improvement.
- For the design but also the interpretation of measurements of complex devices containing multiple resonators a tool like Aurora can be very useful as was shown in the comparison between the measured and simulated responses of the 1310 nm OADM.
- Currently thermal tuning for the resonators. Although it is estimated that the current power consumption can be reduced by at least a factor of five, thermal tuning will ultimately not be practical in devices that incorporate a large number of heaters such as the router. A good alternative can probably be found in MEMS based devices or, even better, in tuning using liquid crystals.
- The practical feasibility of the polarization diversity scheme presented in chapter 8 still has to be proven. In theory, however, it provides a robust alternative to current methods to create polarization independence for a wide range of microring resonator based devices.

Appendix A. Mason's rule

Several optical components have been solved using Mason's rule [172, 173]. Mason's rule can be used to find the transfer function of a linear system by representing this system as a signal-flow graph in which each node is a variable. The transfer function H_{ij} between two nodes x_i and x_j is given by:

$$H_{ij} = \frac{\sum_k P_{ijk}\Delta_{ijk}}{\Delta} \tag{A.1}$$

where:

P_{ijk} = the k^{th} path that leads directly from variable x_i to x_j,
Δ = the determinant of the graph,
Δ_{ijk} = the co-factor of the patch P_{ijk}.

The summation is taken over all possible k paths from x_i to x_j. The co-factor Δ_{ijk} is the determinant of the system that remains when direct path P_{ijk} is removed. The determinant Δ is given by:

$$\Delta = 1 - \sum L_1 + \sum L_2 - \sum L_3 \cdots \tag{A.2}$$

where L_n is the product of n loops in the graph that do not touch. Loops do not touch when they have no node (variable) in the loop in common. In words (A.2) can be written out as:

Δ=1-(sum of all the individual loop gains)
+(sum of the products of all combinations of two loops that don't touch)
- (sum of the products of all combinations of three loops that don't touch)
+ …..etc.

Appendix B. Crosstalk Derivation

The adjacent channel crosstalk is the relative power fraction of a signal that is present on a channel adjacent to the channel on which this signal is transmitted and is defined as:

$$CT = 10\log\left(\frac{P_{Drop}(\lambda = \lambda_c + \Delta\lambda_{cs})}{P_{Drop}(\lambda = \lambda_c)}\right) \tag{B.1}$$

where λ_c is the wavelength of the channel for which the resonator is in full resonance and $\Delta\lambda_{cs}$ is the separation between the channels.
Then with φ_1 the roundtrip phase of a resonator in resonance:

$$\varphi_1 = \frac{(2\pi)^2}{\lambda_c}.R.Neff \tag{B.2}$$

and φ_2 the roundtrip phase of the adjacent channel:

$$\varphi_2 = \frac{(2\pi)^2}{\lambda_c + \Delta\lambda_{cs}}.R.Neff \tag{B.3}$$

Combined with the drop response of the resonator:

$$P_{Drop} = \frac{H}{1 + F_C.\sin^2(\varphi/2)} \tag{B.4}$$

The expression for the crosstalk then becomes:

$$CT = 10\log\left(\frac{\frac{H}{1 + F_C.\sin^2(\varphi_2/2)}}{\frac{H}{1 + F_C.\sin^2(\varphi_1/2)}}\right) = 10\log\left(\frac{1 + F_C.\sin^2(\varphi_1/2)}{1 + F_C.\sin^2(\varphi_2/2)}\right) \tag{B.5}$$

The phase φ_2 is equal to $m.2\pi$ because λ_c is the resonance frequency. In addition F_C can be written as:

$$F_C = \frac{1}{\sin^2(\pi/2F)} \tag{B.6}$$

Combining (B.5) with (B.6) then gives the expression:

$$CT = 10\log\left(\frac{1}{1 + \frac{1}{\sin^2(\pi/2F)}.\sin^2(\varphi_2/2)}\right) = 10\log\left(\frac{\sin^2(\pi/2F)}{\sin^2(\pi/2F) + \sin^2(\varphi_2/2)}\right) \tag{B.7}$$

Then, since

$$\varphi_2 = \varphi_1 + \varphi_{ITU} = m.2\pi + \varphi_{cs} = \varphi_{cs} \tag{B.8}$$

and realizing that φ_{cs} can be written in terms of the FSR and the cannel separation $\Delta\lambda_{cs}$ as:

$$\varphi_2 = \varphi_{ITU} = (2.\pi / FSR).\Delta\lambda_{cs} \tag{B.9}$$

The crosstalk CT can be written as:

$$CT = 10\log\left(\frac{\sin^2(\pi/2F)}{\sin^2(\pi/2F) + \sin^2(\pi.\Delta\lambda_{cs}/FSR)}\right) \tag{B.10}$$

Simplifying this equation then leads to:

$$CT = -10\log\left(1 + \frac{\sin^2(\pi.\Delta\lambda_{cs}/FSR)}{\sin^2(\pi/2F)}\right) \tag{B.11}$$

List of Acronyms

ADSL	-	Asymmetric Digital Subscriber Line
AN	-	Access Network
ASE	-	Amplified Spontaneous Emission
AWG	-	Array Waveguide Gratings
BEP	-	Bi-directional Eigenmode Propagation
BER	-	Bit Error Rate
BPM	-	Beam Propagation Method
BW	-	Bandwidth
CAGR	-	Compound Annual Growth Rate
CMT	-	Coupled Mode Theory
CT	-	Cross Talk
CW	-	Continuous wave
DMT	-	Discrete Multi-Tone
DOS	-	Digital Optical Switch
DSL	-	Digital Subscriber Line
DWDM	-	Dense Wavelength Division Multiplexing
EDFA	-	Erbium Doped Fiber Amplifier
FEM	-	Finite Element Method
FDTD	-	Finite Difference Time Domain
FP	-	Fabry-Perot Resonator
FSR	-	Free Spectral Range
FTTB	-	Fiber To The Building
FTTC	-	Fiber To The Curb (or Cabinet)
FTTH	-	Fiber To The Home
FTTS	-	Fiber To The Squirrel
FWHM	-	(also $\Delta\lambda_{FWHM}$) Full Width at Half Maximum
HDTV	-	High Definition Television
HNA	-	High Numerical Aperture (fiber), also called smallcore fiber
HO	-	Head Office
IL	-	Insertion Loss
LPCVD	-	Low-Pressure Chemical Vapor Deposition
MAN	-	Metropolitan Area Networks
MEMS	-	Micro Electro-Mechanical Systems
MFD	-	Mode Field Diameter
MMI	-	Multi-Mode Interferometer
MR	-	Microring Resonator
MRI	-	Micro-Resonator Investigator tool
MZI	-	Mach-Zehnder Interferometer
NAIS	-	Next-generation Active Integrated-optic Subsystems
NRZ	-	Non Return to Zero
NTT	-	Nippon Telegraph and Telephone Corporation
OLT	-	Optical Line Termination
ONU	-	Optical Network Unit
OSA	-	Optical Spectrum Analyzer
OXC	-	Optical (WDM) Cross Connect
PDL	-	Polarization dependent loss
PMD	-	Polarization mode dispersion

PON	-	Passive Optical Network
PECVD	-	Plasma-Enhanced Chemical Vapor Deposition
RIE	-	Reactive Ion Etching
ROADM	-	Reconfigurable Optical Add-Drop Multiplexer
SiON	-	Silicon Oxy-Nitride
SOA	-	Semiconductor Optical Amplifier
SOI	-	Silicon on Insulator
TDM	-	Time Division Multiplexing
TE	-	Transverse Electric
TEOS	-	Tetra-Ethyl-Ortho-Silicate (An SiO_2-like material)
TFF	-	Thin Film Filter
TM	-	Transverse Magnetic
VLSI	-	Very Large-Scale Integration
VDSL	-	Very high bit-rate Digital Subscriber Line
WAN	-	Wide Area Networks
WDM	-	Wavelength Division Multiplexing
xDSL	-	ADSL, ADSL2, ADSL2+, VDSL, VDSL2 etc.

List of Symbols

Q	-	Quality Factor	[-]
κ_c	-	Coupling constant	[m^{-1}]
κ	-	Field coupling coefficient (cross)	[-]
μ	-	Field coupling coefficient (bar): $\mu^2=1-\kappa^2$	[-]
α_{dB}	-	Waveguide losses	[dB/m]
α_r	-	Resonator roundtrip loss	[dB]
χ_c	-	Directional coupler loss	[-]
χ_r	-	Resonator roundtrip loss factor	[-]
λ	-	Wavelength	[m]
R	-	Radius	[m]
F	-	Finesse	[-]
F_C	-	Finesse Factor	[-]
P	-	Power	[W]
Neff	-	Effective refractive index	[-]
T, t	-	Time	[s]
n_g	-	Group index	[-]

Bibliography

[1] Dan Schiller, "*End of the telecom revolution*," Le Monde Diplomatique, August 2003.

[2] Lawrence Gasman, "*Who killed Telecom*?," Cato Institute, Executive Summary No. 533, February 7, 2005.

[3] Paul Starr, "*What Killed the Boom*," The *American Prospect Online Edition*, September 10th 2001.

[4] Eli M. Moam, "*The Telecom bust? Get ready for the next one,*" Telecom Asia, October 2003.

[5] Alain Puissochet, "Do we need Fiber to the home?," *Communications & Strategies*, No. 57, 1st quarter 2005, pp. 187-194

[6] "VDSL Tutorial, Fiber – Copper access for the information highway," http://www.dslforum.org/aboutdsl/vdsl_tutorial.html

[7] Aware Inc, "ADSL2 and ADSL2+ the new ADSL standards," http://www.dslprime.com/a/adsl21.pdf

[8] "ADSL2 en ADSL2+. Wat moet je ermee?," http://www.tekstenuitleg.net/artikelen/adsl2/1

[9] Richard Sekar, "New VDSL2 standard will bring fiber fast Broadband," *Ikanos Communications*, January 2005.

[10] Wikipedia, http://en.wikipedia.org/wiki/Passive_optical_network

[11] Barry Kantner, "The FTTP Battlefield: Active Ethernet vs. PON," *Lightwave Online*, July 6th, 2004.

[12] Meghan Fuller, "Industry mulls over WDM-PON technology," *Lightwave*, August 1st, 2006.

[13] A. Driessen, "NAIS: Next-generation Active Integrated-optic Subsystems," Project introduction, http://www.mesaplus.utwente.nl/nais.

[14] H. de Waardt, "Dynamically reconfigurable broadband photonic access networks," http://www.freeband.nl/uploadedFiles/Projectflyer%20BBPhotonics%20EN.pdf.

[15] E. A. J. Marcatili, "Bends in optical dielectric waveguides, " *BSTJ*, Vol. 48, pp. 2103-2132, 1969.

[16] K. Jackson, S. Newton, B. Moslehi, M. Tur, C. Cutler, J. Goodman and H. Shaw, "Optical Fiber Delay-Line Signal Processing," *IEE Trans. Microwave Theory Techniques*, Vol. 33, No. 7, pp. 909-930, 1984.

[17] N. Ngo and L. Binh, "Novel Realisation of Monotonic Butterworth Type Lowpass, Highpass, and Bandpass Optical Filters Using Phase-Modulated Fiber-Optic Interferometers and Ring Resonators," *Journal of Lightwave Technology*, Vol. 12, No. 5, pp. 827-841, 1994.

[18] L. Collot, V. Lefe`vre-Seguin, M. Brune, J.-M. Raimond, and S. Haroche, ''Very high-Q whispering gallery modes resonances observed on fused silica microsphere,'' *Europhys. Lett.,* Vol. 23, 327–333, 1993.

[19] M. L. Gorodetsky and V. S. Ilchenko, "Optical microsphere resonators: optimal coupling to high-Q whispering-gallery modes," *J. Opt. Soc. Am. B*, Vol. 16, No. 1, pp. 147-154, January 1999.

[20] H. C. Tapalian, J.-P. Laine, and P. A. Lane, "Thermooptical Switches Using Coated Microsphere Resonators," *IEEE Photonics Technology Letters*, Vol. 14, No. 8, pp. 1118-1120, August 2002.

[21] W. Bogaerts, P. Dumon, D. Taillaert, V. Wiaux, S. Beckx, B. Luyssaert, J. Van Campenhout, D. Van Thurhout, R. Baets, "SOI nanophotonic waveguide structures fabricated with deep UV lithography," *Photonics and Nanostructures: Fundamentals and Applications*, Elsevier, 2(2), pp. 81-86, September 2004.

[22] A. Morand, Y. Zhang, B. Martin, K. P. Huy, D. Amans, P. Benech, J. Verbert and E. Hadji, "Ultra-compact microdisk resonator filters on SOI substrate," *Optics Express*, Vol. 14, No. 26, pp. 12814-12821, 25 December 2006.

[23] A. Driessen, D. H. Geuzebroek, H. J. W. M. Hoekstra, H. Kelderman, E. J. Klein, D. J. W. Klunder, C. G. H. Roeloffzen, F. S. Tan, E. Krioukov, C. Otto, H. Gersen, N. F. Van Hulst, L. Kuipers, "Microresonators as building blocks for VLSI Photonics" in "Microresonators as building blocks for VLSI Photonics," F. Michelotti, A. Driessen, M. Bertolotti (Eds.), *Proceedings International School of Quantum Electronics*, Melville, New York, USA : American Institute of Physics (ISBN 0-7354-0184-5), pp. 1-18, 2004.

[24] B. E. Little, "A VLSI Photonics platform," OFC 2003.

[25] B. E. Little, S. T. Chu, W. Pan, and Y. Kokobun., "Microring resonator arrays for VLSI photonics," *IEEE Photonic Technology Letters*, Vol. 12, No. 3, pp. 323-325, 2000.

[26] B. E. Little, S. T. Chu, "Toward Very Large Scale Integrated Photonics," *Optics and Photonics News,* November 2000.

[27] Robert W. Boyd and John E. Heebner, "Sensitive disk resonator photonic biosensor," *Applied Optics*, Vol. 40, No. 31, pp. 5742-5747, November 2001.

[28] I. M. White, H. Zhu, J. D. Suter, N. M. Hanumegowda, H. Oveys, M. Zourob, and X. Fan, "Refractometric Sensors for Lab-on-a-Chip Based on Optical Ring Resonators," *IEEE Sensors Journal*, Vol. 7, No. 1, pp.28 -35, January 2007.

[29] P. K. Pattnaik, Bh. Vijayaaditya, T. Srinivas and A. Selvarajan, "Optical MEMS Pressure and Vibration Sensors Using Integrated Optical Ring Resonators," *Sensors*, 2005 IEEE, 30 Oct-3 Nov 2005, pp.636-639.

[30] A. Yalcin, K. C. Popat, J. C. Aldridge, T. A. Desai, J. Hryniewicz, N. Chbouki, B. E. Little, O. King, V. Van, S. Chu, D. Gill, M. Anthes-Washburn, M. S. Ünlü, and B. B. Goldberg, "Optical Sensing of Biomolecules Using Microring Resonators," *IEEE Journal of selected topics in Quantum Electronics*, Vol. 12, No. 1, pp. 148-155, 2006.

[31] P. Rabiei, W. H. Steier, C. Zhang, and L. R. Dalton, "Polymer Micro-Ring Filters and Modulators," *Journal of Lightwave Technology*, Vol. 20, No. 11, November 2002.

[32] A. Leinse, M. B. J. Diemeer, A. Rousseau, and A. Driessen, "A Novel High-Speed Polymeric EO Modulator Based on a Combination of a Microring Resonator and an MZI," *IEEE Photonics Technology Letters*, Vol. 17, No. 10, pp. 2074-2076, October 2005.

[33] Q. Xu, B. Schmidt, S. Pradhan and M. Lipson, "Micrometre-scale silicon electro-optic modulator," *Nature*, Vol. 435, pp. 325-327, May 2005.

[34] T. Sadagopan, S. J. Choi, S. J. Choi, K. Djordjev and P. D. Dapkus, "Carrier-Induced Refractive Index Changes in InP-Based Circular Microresonators for Low-Voltage High-Speed Modulation," *IEEE Photonics Technology Letters*, Vol. 17. No. 2, pp. 414-416, February 2005.

[35] K. Djordjev, Seung-June Choi, Sang-Jun Choi, and P. D. Dapkus, "Vertically Coupled InP Microdisk Switching Devices With Electroabsorptive Active

Regions," *IEEE Photonics Technology Letters*, Vol. 14. No. 8, pp. 1115-1117, August 2002.

[36] R. Grover, K. Amarnath, T. A. Ibrahim, P. Ho, "Nonlinear and active optical III-V semiconductor micro-resonators," *Optical Fiber Communication Conference*, Technical Digest (ISBN: 1-55752-783-0), Vol.5, pp. 3, March 2005.

[37] J. P. Hohimer, D. C. Craft, G. R. Hadley, G. A. Vawter, and M. E. Warren, "Single frequency continuous-wave operation of ring resonator diode lasers," *Applied Physics Letters,* Vol. 59, No. 26, pp. 3360-3362, December 1991.

[38] B. Liu, A. Shakouri, and J. E. Bowers, "Wide Tunable Double Ring Resonator Coupled Lasers," *IEEE Photonics Technology Letters,* Vol. 14, No. 5, pp. 600-602, May 2002.

[39] K. Amarnath, R. Grover, S. Kanakaraju, and P. Ho, "Electrically Pumped InGaAsP–InP Microring Optical Amplifiers and Lasers With Surface Passivation," *IEEE Photonics Technology Letters*, Vol. 17, No. 11, pp. 2280-2282, November 2005.

[40] G. Griffel, J. H. Abeles, R. J. Menna, A. M. Braun, J. C. Connolly, and M. King, "Low-Threshold InGaAsP Ring Lasers Fabricated Using Bi-Level Dry Etching," *IEEE Photonics Technology Letters*, Vol. 12, No. 2, pp. 146-148, February 2000.

[41] T. F. Krauss, R. M. De La Rue, and P. J. R. Laybourn ," Impact of Output Coupler Configuration on Operating Characteristics of Semiconductor Ring Lasers," *Journal of Lightwave Technology*, Vol. 13, No. 7, pp. 1500-1507, July 1995.

[42] D. G. Rabus, Z. Bian, and A. Shakouri, "A GaInAsP–InP Double-Ring Resonator Coupled Laser," *IEEE Photonics Technology Letters*, Vol. 17, No. 9, pp. 1770-1772, September 2005.

[43] H. Takahashi, R. Inohara, K. Nishimura, and M. Usami, "Expansion of Bandwidth of Tunable Dispersion Compensator Based on Ring Resonators Utilizing Negative Group Delay," *Journal of Lightwave Technology*, Vol. 24, No. 6, pp. 2276-2286, June 2006.

[44] G.L. Bona, F. Horst, R. Germann, B.J. Offrein, D. Wiesmann, "Tunable Dispersion Compensators Realized High-Refractive-Index-Contrast SiON Technology," *Proceedings ECOC 2002*, European Conference on Optical Communications, Vol. 2, 8-12 September 2002.

[45] C. G. H. Roeloffzen, L. Zhuang, R. G. Heideman, A. Borreman, and W. van Etten, "Ring resonator-based Tunable Optical Delay Line in LPCVD Waveguide Technology," *Proceedings Symposium IEEE/LEOS Benelux Chapter*, Mons, pp. 79-82, 2005.

[46] A. Takagi, K. Jinguji and M. Kawachi, "Silica-Based Waveguide-Type Wavelength-Insensitive Couplers (WINC's) with Series-Tapered Coupling Structure," *Journal of Lightwave Technology*, Vol. 10. No. 12, pp. 1814-1824, December 1992.

[47] M. Hammer, "Coupled mode model for 3D directional couplers", NAIS internal manuscript, September 2002.

[48] M. Lohmeyer, N. Bahlmann, O. Zhuromskyy, and P. Hertel, "Radiatively coupled waveguide polarization splitter simulated by wave-matching based coupled mode theory," *Optical and Quantum Electronics*, Vol. 31 pp 877-891, 1999.

[49] WMM based coupled mode theory: Adiabatic directional couplers. http://www.math.utwente.nl/_hammerm/Nais/WmmCmt/.
[50] OlympIOs Integrated Optics Software. C2V, P.O. Box 318, 7500 AH Enschede, The Netherlands. http://www.c2v.nl/software/.
[51] F. Xia, L. Sekaric and Y. A. Vlasov, "Mode conversion losses in silicon-on-insulator photonic wire based racetrack resonators," *Optics Express*, Vol. 14, No. 9, pp. 3872-3885, May 2006.
[52] C.K. Madsen and J. H. Zhao, "Optical Filter Design and Analysis: A Signal Processing Approach," John Wiley & Sons (ISBN: 0-471-18373-3), May 1999.
[53] B. E. Little, S. T. Chu, P. P. Absil, J. V. Hryniewicz, F. G. Johnson, F. Seiferth, D. Gill, V. Van, O. King, and M. Trakalo, "Very High-Order Microring Resonator Filters for WDM Applications," *IEEE Photonics Technology Letters*, Vol. 16, No. 10, pp. 2263-2265, October 2004.
[54] J. V. Hryniewicz, P. P. Absil, B. E. Little, R. A. Wilson, and P.-T. Ho, "Higher Order Filter Response in Coupled Microring Resonators," *IEEE Photonics Technology Letters*, Vol. 12, N0. 3, pp. 320-322, March 2000.
[55] R. Orta, P. Savi, R. Tascone, and D. Trinchero, "Synthesis of Mu1tiple-Ring-Resonator Filters for Optical Systems," *IEEE Photonics Technology Letters*, Vol. 7, No. 12, pp. 1447-1449, December 1995.
[56] D. G. Rabus, M. Hamacher, H. Heidrich, "Resonance frequency tuning of a double ring resonator in GaInAsP/InP:Experiment and simulation," *Japanese Journal of Applied Physics*, Vol. 41, No. 2b, pp. 1186-1189, February 2002.
[57] C. K. Madsen and J. H. Zhao, "A General Planar Waveguide Autoregressive Optical Filter," *Journal of Lightwave Technology*, Vol. 14, No. 3, pp. 437-447, March 1996.
[58] A. Melloni and Mario Martinelli, "Synthesis of Direct-Coupled-Resonators Bandpass Filters for WDM Systems," *Journal of Lightwave Technology*, Vol. 20, No. 2, pp. 296-303, February 2002.
[59] K. Oda, N. Takato, H. Toba, "A Wide-FSR Waveguide Double-Ring Resonator for Optical FDM Transmision Systems," *Journal of Lightwave Technology*, Vol.9, No. 6, pp. 728-736, June 1991.
[60] A. Melloni, "Synthesis of a parallel-coupled ring-resonator filter," *Optics Letters*, Vol. 26, No. 12, pp. 917-919, June 2001.
[61] S. T. Chu, B. E. Little, W. Pan, T. Kaneko, and Y. Kokubun, "Second-Order Filter Response From Parallel Coupled Glass Microring Resonators," *IEEE Photonics Technology Letters*, Vol. 11, No. 11, pp. 1426-1428, November 1999.
[62] R. Grover V. Van, T. A. Ibrahim, P. P. Absil, L. C. Calhoun, F. G. Johnson, J. V. Hryniewicz, and P.-T. Ho, "Parallel-Cascaded Semiconductor Microring Resonators for High-Order and Wide-FSR Filters," *Journal of Lightwave Technology*, Vol. 20, No. 5, pp. 900-904, May 2002.
[63] G. Griffel, "Synthesis of optical filters using ring resonator arrays," *IEEE Photonics Technology Letters*, Vol. 12, No. 7, pp. 810-812, July 2000.
[64] G. Griffel, "Vernier effect in asymmetrical ring resonator arrays," *IEEE Photonics Technology Letters*, Vol. 12, No. 12, pp. 1642-1644 December 2000.
[65] C. J. Kaalund and G. Peng, "Pole-Zero Diagram Approach to the Design of Ring Resonator-Based Filters for Photonic Applications," *Journal of Lightwave Technology*, Vol. 22, No. 6, pp. 1548-1559 June 2004.

[66] B. E. Little, S. T. Chu, J. V. Hryniewicz and P. P. Absil, "Filter synthesis for periodically coupled microring resonators," *Optics Letters*, Vol. 25, No. 5, pp. 344-346, March 2000.

[67] S. T. Chu, B. E. Little, V. Van, J. V. Hryniewicz, P. P. Absil, F. G. Johnson, D. Gill, O. King, F. Seiferth, M. Trakalo and J. Shanton, "Compact full C-band tunable filters for 50 GHz channel spacing based on high order micro-ring resonators," *Optical Fiber Communication Conference*, 2004. OFC 2004, 23-27 Feb. 2004.

[68] S. T. Chu, B. E. Little, W. Pan, T. Kaneko and Y. Kokubun, "Cascaded Microring Resonators for Crosstalk Reduction and Spectrum Cleanup in Add–Drop Filters," *IEEE Photonics Technology Letters*, Vol. 11, No. 11, pp. 1423-1425, November 1999.

[69] Z. Wang, W. Chen and Y. J. Chen, "Unit cell design of crossbar switch matrix using micro-ring resonators," ECOC 2004, Page We 3.7.2.

[70] Y. Inoue, M. Katoh and M. Kawachi, "Polarization Sensitivity of a SilicaWaveguide Thermooptic Phase Shifter for Planar Lightwave circuits," *IEEE Photonics Technology Letters*, Vol. 4, No. 1, pp. 36-38, January 1992.

[71] D.J.W. Klunder, "Thermo-optical tuning of Mach-Zehnder interferometers," Internship report, IBM, Zurich, Switzerland, 1997.

[72] P. Heimala, P. Katila, J. Aarnio and A. Heinämäki, "Thermally tunable Integrated Optical Ring Resonator with Poly-Si Thermistor," *Journal of Lightwave Technology*, Vol. 14, No. 10, pp. 2260-2267, October 1996.

[73] M. B. J. Diemeer, "Polymeric thermo-optic space switches for optical communications," *Optics Materials*, Vol. 9, pp. 192-200, 1998.

[73] D. H. Geuzebroek, E. J. Klein, H. Kelderman, and A. Driessen, "Wavelength tuning and switching of a thermo-optic resonator," *Proceedings ECIO 2003*, pp. 395-398, 2003.

[74] P. Rabiei and W. H. Steier, "Tunable Polymer Double Micro-Ring Filters," *IEEE Photonics Technology Letters*, Vol. 15, No. 9, pp. 1255-1258, September 2003.

[75] R. Meijerink, D. H. Geuzebroek, E.J. Klein, H. Kelderman, R. Dekker, M. B. J. Diemeer, A. Driessen, "Optimization of driving signal forthermal modulation of a microring resonator," *Proceedings 8th annual symposium IEEE/LEOS Benelux Chapter*, pp. 85-88, 2003.

[76] G. Cocorullo, M. Iodice, I. Rendina and P. M. Sarro, "Silicon Thermooptical Micromodulator with 700-kHz - 3-dB Bandwidth," *IEEE Photonics Technology Letters*, Vol. 7, No. 4, pp. 363-365, April 1995.

[77] Wikipedia, http://en.wikipedia.org/wiki/Kerr_effect.

[78] A. Schneider, I. Biaggio and P. Günther, "Teraherz-induced lensing and its use for the detection of teraherz pulses in a birefringent crystal," *Applied Physics Letters,* Vol. 84, No. 13, pp. 2229-2231, March 29, 2004.

[79] M. J. B. Diemeer, "Polymeric Components for Optical Communications," PhD Thesis, University of Twente, ISBN 90-365-1869-5, 2003.

[80] A. Leinse, M. B. J. Diemeer, A. Rousseau and A. Driessen, "High speed polymer e-o modulator based on a combination of a microring resonator and an MZI," *Proceedings European Conference on Integrated Optics*, Grenoble, France, 2005.

[81] I.L. Georma, "Fundamental limitations of optical resonator based high-speed EO modulators," *IEEE Photonics Technology Letters*, Vol 14, No. 6, pp. 795-797, 2002.

[82] A. Leinse, M. B. J. Diemeer, A. Rousseau and A. Driessen, "A novel high speed polymeric EO modulator based on a combination of a microring resonator and an MZI," *IEEE Photonics Technology Letters*, Vol. 17, No. 10, pp. 2074-2076, October 2005.

[83] S. Lee, S. M. Garner, V. Chuyanov, H. Zhang, W. H. Steier, F. Wang, L. R. Dalton, A. H. Udupa and H. R. Fetterman, "Optical Intensity Modulator Based on a Novel Electrooptic Polymer Incorporating a High μβ Chromophore," *IEEE Journal of Quantum Electronics,* Vol. 36, No. 5, pp. 527-531, May 2000.

[84] R. Dekker, A. Driessen, T. Wahlbrink, C. Moormann, J. Niehusmann and M. Först, "Ultrafast Kerr-induced all-optical wavelength conversion in silicon waveguides using 1.55 μm femtosecond pulses," *Optics Express*, Vol. 14, No. 18, pp. 8336-8346, 2006.

[85] Wikipedia, http://en.wikipedia.org/wiki/Liquid_crystal

[86] B. Maune, R. Lawson, C. Gunn, A. Scherer and L. Dalton, "Electrically tunable ring resonators incorporating nematic liquid crystals as cladding layers," *Applied Physics Letters*, Vol. 83, No. 23, pp. 4689-4691, December 2003.

[87] S. Wua, C.-S. Hsu and K.-F. Shyu, "High birefringence and wide nematic range bis-tolane liquid crystals," *Applied Physics Letters*, Vol. 74, No. 3, pp. 344-346, January 1999.

[88] R. A. Soref and B. R. Bennett, "Electrooptical effects in silicon," *IEEE Journal of Quantum Electronics*, Vol. 23, pp. 123–129, 1987.

[89] P. D. Hewitt and G. T. Reed, "Improved Modulation Performance of a Silicon p-i-n Device by Trench Isolation," *Journal of Lightwave Technology*, Vol. 19, No. 3, pp. 387-390, March 2001.

[90] T. A. Ibrahim, W. Chao, Y. Kim, J. Li, J. Goldhar, P.-T. Ho and C. H. Lee, "All-optical switching in a laterally coupled microring resonator by carrier injection," *IEEE Photonics Technology Letters*, Vol. 15, No. 1, pp. 36-39, 2003.

[91] V. R. Almeida, C. A. Barrios, R. R. Panepucci and M. Lipson, "All-optical control of light on a silicon chip," *Nature*, Vol. 28, pp. 1081-1084, October 2004.

[92] C. Manolatou, M. Lipson, "All-Optical Silicon Modulators Based on Carrier Injection by Two-Photon Absorption," *Journal of Lightwave Technology*, Vol. 24, No. 3, pp. 1433-1439, March 2006.

[93] F. C. Blom, D. R. van Dijk, H. J. W. M. Hoekstra, A. Driessen and T. J. A. Popma, "Experimental study of integrated-optics microcavity resonators: Towards an all-optical switching device," *Applied Physics Letters*, Vol. 71, pp. 747-749, 1997.

[94] J. Niehusmann, M. Först, H. Kurz, R. Dekker, T. Wahlbrink, C. Moormann. "Sub-picosecond all-optical switching via cross-phase modulation in silicon-on-insulator waveguides," *submitted to IEEE Photonics Technology Letters*, 2006.

[95] P. V. Lambeck, " Integrated optical sensors for the chemical domain," *Measurement Science & Technology*, Vol. 17, No. 8, pp. 93-116, August 2006.

[96] E. Krioukov, D. J. W. Klunder, A. Driessen, J. Greve and C. Otto, "Sensor based on an integrated optical microcavity," *Optics Letters*, Vol. 27, No. 7, pp. 512-514, 2002.

[97] H. Haeiwa, T. Naganawa and Y. Kokobun, "Wide range center wavelength trimming of vertically coupled microring resonator filter by direct UV radiation to SiN ring core," *IEEE Photonics Technology Letters*, Vol. 16, No. 1, pp. 135-137, 2004.
[98] M.-C. M. Lee and M. C. Wu, "MEMS-Actuated Microdisk Resonators With Variable Power Coupling Ratios," *IEEE Photonics Technology Letters*, Vol. 17, No. 5, pp. 1034-1036, May 2005.
[99] K. Djordjev, S. J. Choi and P.D. Dapkus, "Active semiconductor microdisk devices," *IEEE Journal of Lightwave Technology*, Vol. 20, No. 1, pp. 105-113, 2002.
[100] R. Dekker, D. J. Klunder, A. Borreman, M. B. J. Diemeer, K. Wörhoff, A. Driessen, F. C. J. M. van Veggel and J. W. Stouwdam, "Stimulated emission and optical gain in LaF_3 : Nd nanoparticle-doped polymer-based waveguides," *Applied Physics Letters*, Vol. 85, No. 25, pp. 6104-6106, 2004.
[101] G. N. Nielson, D. Seneviratne, F. Lopez-Royo, P. T. Rakich, F. Giacometti, H. L. Tuller and G. Barbastathis, "MEMS based wavelength selective optical switching for integrated photonic circuits," *Lasers and Electro-Optics*, 2004. (CLEO). Vol. 1, 16-21 May 2004.
[102] D. K. Armani, T. J. Kippenberg, S. M. Spillane and K. J. Vahala, "Ultra-high-Q toroid microcavity on a chip," *Nature*, Vol. 421, pp. 925-928, February 2003.
[103] ITU Grid specification, http://www.bayspec.com/pdf/ITU-DWDM.pdf
[104] Isa Kiyat, Atilla Aydinli and Nadir Dagli, "Low-Power Thermooptical Tuning of SOI Resonator Switch," *IEEE Photonics Technology Letters*, Vol. 18, No. 2, pp. 364-366, January 2006.
[105] D. J. W. Klunder, "Photon Physics in Integrated Optics Microresonators," PhD Thesis, University of Twente, ISBN 90-365-1802-4, 2002.
[106] Ladouceur and Love, "Silica-based buried channel waveguides and devices," Springer, ISBN 978-0412579301, 1995.
[107] B. E. Little, J.-P. Laine and S. T. Chu, "Surface-roughness-induced contra-directional coupling in ring and disk resonators," *Optics Letters*, Vol. 22, No. 1, pp. 4-6, January 1997.
[108] K. R. Hiremath, R. Stoffer, M. Hammer, "Modeling of circular integrated optical microresonators by 3-D frequency domain coupled mode theory," *Optics Communications*, Vol. 257, No. 2, pp. 277-279, 2006.
[109] R. Stoffer, K. R. Hiremath, M. Hammer, L. Prkna, J. Ctyroky, "Cylindrical integrated optical microresonators: Modeling by 3-D vectorial coupled mode theory," *Optics Communications* (ISSN 0030-4018), Vol. 256, pp. 46-67, 2005.
[110] AAMP group Homepage, http://www.math.utwente.nl/aamp/
[111] MESA+ Research Institute Homepage, http://www.mesaplus.utwente.nl/
[112] F. Ladouceur and P. Labeye, "A New General Approach to Optical Waveguide Path Design," *Journal of Lightwave Technology*, Vol. 13, No. 3, pp. 481-492, March 1995.
[113] R. Dekker, "All-Optical Processes in Integrated Optical Devices Using Materials with Large Third-Order Nonlinearities and Gain," PhD Thesis, University of Twente, ISBN 90-9021436-4, 2006.
[114] M. M. Spühler, B. J. Offrein, G.-L. Bona, R. Germann, I. Massarek and D. Erni, "A Very Short Planar Silica Spot-Size Converter Using a Nonperiodic

Segmented Waveguide," *Journal of Lightwave Technology*, Vol. 16, No. 9, pp. 1680-1685, September 1998.
[115] B. Luyssaert, P. Vandersteegen, D. Taillaert, P. Dumon, W. Bogaerts, P. Bienstman, D. van Thourhout, V. Wiaux, S. Beckx and R. Baets, "A Compact Photonic Horizontal Spot-Size Converter Realized in Silicon-on-Insulator," *IEEE Photonics Technology Letters*, Vol. 17, No. 1, pp. 73-75, January 2005.
[116] Q. Wang, J. He and S. He, "Y-branch spot-size converter for a buried silica waveguide with large index difference," *Applied Optics*, Vol. 43, No. 16, pp. 3315-3318, June 2004.
[117] G. Jeong, D. Kim, J. Choi, D. Lee, M.-Y. Park, J.-B. Kim, H. J. Lee and H.-Y. Lee, "Low-Loss Compact Arrayed Waveguide Grating with Spot-Size Converter Fabricated by a Shadow-Mask Etching Technique," *ETRI Journal*, Vol. 27, No. 1, pp. 89-94, February 2005.
[118] A. Leinse, "Polymeric microring resonator based electro-optic modulator," PhD Thesis, University of Twente, ISBN 90-365-2168-8, 2005.
[119] J. T. Verdeyen, Laser Electronics, third edition, Prentice Hall, New Jersey 1881, ISBN 013706666X.
[120] Microsoft Visual C++, http://msdn2.microsoft.com/en-us/visualc/default.aspx
[121] Rudolf Bayer, "Binary B-Trees for Virtual Memory," *ACM-SIGFIDET Workshop 1971*, San Diego, California, Session 5B, pp. 219-235.
[122] Donald Knuth, "Fundamental Algorithms," Third Edition. Addison-Wesley, 1997. ISBN 0-201-89683-4. Section 2.3, pp.318–348.
[123] William Pugh, "Skip lists: a probabilistic alternative to balanced trees," *Communications of the ACM*, June 1990, 33(6), pp. 668-676.
[124] OptiSystem Simulation Software, http://www.optiwave.com/2007/products/optisystem/index.htm
[125] ASPIC Simulation Software, http://www.phoenixbv.com/product.php?prodid=50010401&prodname=ASPIC
[126] J. H. Berends, Ph.D. Thesis, "Integrated optical Bragg Reflectors as Narrowband Wavelength Filters", University of Twente, Enschede 1997.
[127] H. J. W. M. Hoekstra, W. C. L. Hopman, J. Krautz, R. Dekker and R. M. De Ridder, "A simple coupled mode model for near band-edge phenomena in grated waveguides," *Optical and Quantum Electronics* – Special issue on optical waveguide modeling, Article in press, 2006.
[128] A. Thelen, "Design of Optical Interference Coatings," McGraw-Hill, ISBN 0070637865, 1989.
[129] Simulayer, http://www.daglain.com
[130] K.Wörhoff, L. T. H. Hilderink, A. Driessen, P. V. Lambeck, "Silicon oxinitride – a versatile material for integrated optics applications," *J. Electrochemical Society*, Vol. 149, No 8, pp. 85-91, 2002.
[131] R.G. Heideman, A. Melloni, M. Hoekman, A. Borreman, A. Leinse and F. Morichetti, "Low loss, high contrast optical waveguides base don CMOS compatible LPCVD processing: technology and experimental results," *Proceedings IEEE/LEOS Symposium Benelux Chapter*, p.71-74, December. 2005.
[132] Murphy's Law, http://en.wikipedia.org/wiki/Murphy's_law
[133] ASML Homepage, http://www.asml.nl
[134] PAS 5500/275 Stepper information, http://www.asml.nl/asmldotcom/show.do?ctx=6677&rid=7787

[135] A. Driessen, D. H. Geuzebroek, D. J. W. Klunder, F. S. Tan, "Analysis of a microring resonator based ultra-compact transceiver for the access network," *In (Ed), Proceedings IEEE / LEOS*, ISBN 90-548727-0, pp. 25-28, Brussel, Belgie.

[136] B. E. Little, and S. T. Chu, "Theory of Polarization Rotation and Conversion in Vertically Coupled Microresonators," IEEE *Photonics Technology Letters*, Vol. 12, No. 4, pp. 401-403, April 2000.

[137] F. Morichetti, A. Melloni, and M. Martinelli, "Effects of Polarization Rotation in Optical Ring-Resonator-Based Devices," *Journal of Lightwave Technology*, Vol. 24, No. 1, pp. 573-585, January 2006.

[138] M.C. Larciprete, E.J. Klein, A.Belardini, D.H. Geuzebroek, A.Driessen and F.Michelotti, "Polarisation conversion in vertically coupled Si_3N_4/SiO_2 microring resonators," in Microresonators as building block for VLSI photonics, M. Bertolotti, A. Driessen, F. Michelotti (Eds.), AIP, NY 2004.

[139] B. E. Little, S. T. Chu, W. Pan, and Y. Kokobun., "Microring resonator arrays for VLSI photonics," IEEE *Photonic Technology Letters*, Vol. 12, No. 3, pp. 323-325, 2000.

[140] M.B. J. "Polymeric thermo-optic space switches for optical communications," *Optical Materials*, Vol. 9, No. 1-4, pp. 329-333, January 1998.

[141] E.J.Klein, "Wavelength selective switching using thermally tunable microring resonators," MSc. Thesis, University of Twente, 2002.

[142] Alice Hong, "Electric field to produce spark in air," http://hypertextbook.com/facts/2000/AliceHong.shtml

[143] Chromium properties and articles http://web.mit.edu/6.777/www/materials/chromium/source1.html

[144] C. G. H. Roeloffzen, F. Horst, B. J. Offrein, R. Germann, G. L. Bona, H. W. M. Salemink and R. M. de Ridder, "Tunable passband flattened 1-from-16 binary-tree structured add-after-drop multiplexer using SiON waveguide technology," *IEEE Photonics Technology Letters*, Vol. 12, No. 9, pp. 1201-1203, September 2000.

[145] S. T. Chu, B. E. Little, W. Pan, T. Kaneko, S. Sato, and Y. Kokobun, "An Eight Channel Add-Drop Filter Using Vertically Coupled Microring Resonators over a Cross Grid," *IEEE Photonic Technology Letters*, Vol. 11. No. 6, pp. 691-693, June 1999.

[146] Y. Kokubun, Y. Hatakeyama, M. Ogata, S. Suzuki and N. Zaizen, "Fabrication Technologies for Vertically Coupled Microring Resonator With Multilevel Crossing Busline and Ultracompact-Ring Radius," *IEEE Journal of Selected Topics in Quantum Electronics*, Vol. 11, No. 1, January/February 2005.

[147] E. J. Klein, D. H. Geuzebroek, H. Kelderman, G. Sengo, N. Baker, and A. Driessen, "Reconfigurable optical add-drop multiplexer using microring resonators," *IEEE Photonics Technology Letters*, Vol. 17, No. 11, pp. 2358-2360, November 2005.

[148] D.H. Geuzebroek, E. J. Klein, H. Kelderman, C. Bornholdt and A. Driessen, "40 Gbis/s Reconfigurable Optical Add-Drop Multiplexer based on Microring Resonators," *Proceedings European Conference on Optical Communications ECOC 2005*, Glasgow, UK, Invited.

[149] D. H. Geuzebroek, "Flexible Optical Network Components based on Densely Integrated Microring Resonators," PhD Thesis, University of Twente, ISBN 90-365-2258-7, 2005.

[150] M. K. Smit and C. van Dam, "Phasar based WDM devices: Principles, design and applications," IEEE *Journal of Selected Topics in Quantum Electronics*, Vol. 2, No. 2, pp. 236-250, 1996.

[151] T. Shibata, M. Okuno , T. Goh, T. Watanabe, M. Yasu, M. Itoh, M. Ishii, Y. Hibino, A. Sugita and A. Himeno, "Silica-BasedWaveguide-Type 16 16 Optical Switch Module Incorporating Driving Circuits," *IEEE Photonics Technology Letters*, Vol. 15, No. 9, pp. 1300-1302, September 2003.

[152] R. A. Soref and B. E. Little, "Proposed N-Wavelength M-Fiber WDM Crossconnect Switch Using Active Microring Resonators," *IEEE Photonics Technology Letters*, Vol. 10, No. 8, pp. 1121-1123, August 1998.

[153] "Preliminary specifications of system components and modules," Broadband Photonics Deliverable 1.2, April 2005.

[154] T. Koonen, P. Urban, E. Pluk, H. de Waardt, G. van den Hoven, "First design of reconfigurable access network, first specifications for components and modules," Broadband Photonics Deliverable 1.3, December 2005.

[155] M. Kawachi, "Silica waveguides on silicon and their application to integrated optics," *Optical and Quantum Electronics*, Vol. 22, pp. 391-416, 1990.

[156] M.Okuno, A. Sugita, K. Jinguji, and M. Kawachi, "Birefringence Control of Silica Waveguides on Si and Its Application to a Polarization-Beam Splitter/Switch," *Journal of Lightwave Technology*, Vol. 12, No. 4, pp. 625-633, April 1994.

[157] H. Takahashi, Y. Hibino, Y. Ohmori, and M. Kawachi, "Polarization-Insensitive Arrayed-Waveguide Wavelength Multiplexer with Birefringence Compensating Film," *IEEE Photonics Technology Letters*, Vol. 5, No. 6, pp. 707-709, June 1993.

[158] H. Bissessur, F. Gaborit, B. Martin and G. Ripoche, "Polarisation-independent phased-array demultiplexer on InP with high fabrication tolerance," *Electronic Letters*, Vol. 31, No. 16, pp 1372-1373, August 1995.

[159] M. Hoffmann, P. Kopka, and E. Voges, "Low-Loss Fiber-Matched Low-Temperature PECVD Waveguides with Small-Core Dimensions for Optical Communication Systems," *IEEE Photonics Technology Letters*, Vol. 9, N0. 9, pp. 1238-1240, September 1997.

[160] K. Worhoff, B. J. Offrein, P. V. Lambeck, G. L. Bona, and A. Driessen, "Birefringence Compensation Applying Double-Core Waveguiding Structures," *IEEE Photonics Technology Letters*, Vol. 11, No. 2, pp. 206-208, February 1999.

[161] H. H. Yaffe, C. H. Henry, R. F. Kazarinov, and M. A. Milbrodt, "Polarization-Independent Silica-on-Silicon Mach-Zehnder Interferometers," *Journal of Lightwave Technology*, Vol. 12**,** No 1, pp. 64-67, January 1994.

[162] M. K. Chin, "Polarization dependence in waveguide-coupled micro-resonators," *Optics Express*, Vol. 11, No. 15, pp. 1724-1730, July 2003.

[163] W. R. Headley, G. T. Reed, S. Howe, A. Liu and M. Paniccia, "Polarization-independent optical racetrack resonators using rib waveguides on silicon-on-insulator," *Applied Physics Letters*, Vol. 85, No. 23, pp. 5523-5525, December 2004.

[164] D. Xu, S. Janz, and P. Cheben, "Design of Polarization-Insensitive Ring Resonators in Silicon-on-Insulator Using MMI Couplers and Cladding Stress Engineering," *IEEE Photonics Technology Letters*, Vol. 18, No. 2, pp. 343-345, January 2006.

[165] T. Barwicz, M. R. Watts, M. A. Popovic, P. T. Rakich, L. Socci, F. X. Kärtner, E. P. Ippen and H. I. Smith, "Polarization-transparent microphotonic devices in the strong confinement limit," *Nature Photonics*, Vol. 1, No. 1, pp. 57-60, January 2007.

[166] Y. Inoue, Y. Ohmori, M. Kawachi, S . Ando, T. Sawada, and H. Takahashi, "Polarization Mode Converter With Polyimide Half Waveplate in Silica-Based Planar Lightwave Circuits," *IEEE Photonics Technology Letters*, Vol. 6, No. 5, pp. 626-628, May 1994.

[167] J. J. G. M. van der Tol, F. Hakimzadeh, J. W. Pedersen, D. Li, and H. van Brug, "A New Short and Low-Loss Passive Polarization Converter on InP," *IEEE Photonics Technology Letters*, Vol. 7, No. 1, pp. 32-34, January 1995.

[168] H. El-Refaei, D. Yevick , and T. Jones , "Slanted-Rib Waveguide InGaAsP–InP Polarization Converters," *Journal of Lightwave Technology*, Vol. 22, No. 5, pp. 1352- 1357, May 2004.

[169] C. van Dam, L. H. Spiekman, F. P. G. M. van Ham, F. H. Groen, J. J. G. M. van der Tol, I. Moerman, W. W. Pascher, M. Hamacher, H. Heidrich, C. M. Weinert, and M. K. Smit, "Novel Compact Polarization Converters Based on Ultra Short Bends," *IEEE Photonics Technology Letters*, Vol. 8, No. 10, pp. 1346-1348, October 1996.

[170] D. J. W. Klunder, C. G. H. Roeloffzen and A. Driessen, "A Novel Polarization-Independent Wavelength-Division-Multiplexing Filter Based on Cylindrical Microresonators," *IEEE Journal of Selected Topics in Quantum Electronics*, Vol. 8, No. 6, pp. 1294-1299, November/December 2002.

[171] T. Koster and P. V. Lambeck, "Passive Polarization Converter in SiON Technology," *Journal of Lightwave Technology*, Vol. 19, No. 6, pp. 876-883, June 2001.

[172] M. C. Zhou, C.-H. Wang and X. Zhao, "Automating Mason's Rule and Its Application to Analysis of Stochastic Petri Nets," *IEEE Transactions on Control Systems Technology*, Vol. 3, No. 2, pp. 238-244, June 1995.

[173] J. van Amerongen, "*Regeltechniek*", Open Universiteit, Heerlen, 1990, ISBN 90 358 0705 7.

Publication List

Patents (pending)

E. J. Klein, D. H. Geuzebroek and A. Driessen, "Device comprising a polarization-independent micro-resonator," Patent filed at the United States Patent Office, December 2006.

G. v/d Hoven, E. Pluk, D. H. Geuzebroek, E. J. Klein, R. Dekker, "Werkwijze voor het bedrijven van een communicatiesysteem en communicatiesysteem geschikt voor het uitvoeren van een dergelijke werkwijze", Patent filed at the Dutch Patent Office, May 2006.

Book Chapter

E. J. Klein, A. Driessen, "Densely integrated optical micro-resonator based components for the access network," in A. Matsko (Eds.), Title currently unknown, to be published in 2008.

Peer reviewed journals

E. J. Klein, D. H. Geuzebroek, H. Kelderman, G. Sengo, N. Baker and A. Driessen, "Reconfigurable optical add-drop multiplexer using microring resonators," IEEE Photonics Technology Letters, Vol. 17, No. 11, pp. 2358-2360, 2005.

D. H. Geuzebroek, E.J. Klein, H. Kelderman, N. Baker and A. Driessen, "Compact Wavelength-Selective Switch for Gigabit Filtering in Access Networks," IEEE Photonics Technology Letters, Vol. 17, No. 2, pp. 336-338, 2005.

A. Driessen, D. H. Geuzebroek, E. J. Klein, R. Dekker, R. Stoffer and C. Bornholdt, "Propagation of short lightpulses in microring resonators: ballistic transport versus interference in the frequency domain," Optics Communications, 2006

Oral contributions

E. J. Klein, G. Sengo, L. T. H. Hilderink, M. Hoekman, R. Pellens, P. W. L. van Dijk and A. Driessen, "Densely integrated photonic devices based on microring resonators for use in access networks," In (Ed.), Proceedings of the 13th European Conference on Integrated Optics (ECIO), Kopenhagen, Denmark, 2007.

E. J. Klein, D. H. Geuzebroek, H. Kelderman, G. Sengo, N. Baker, and A. Driessen "Reconfigurable Optical Add-Drop Multiplexer Using Microring Resonators," In Proceedings of the 12th European Conference on Integrated Optics (ECIO), Grenoble, France, 2005.

E.J. Klein, D. H. Geuzebroek and A. Driessen, "Optical Microring Resonators: One of the key components for the BBP network testbed", Invited, Freeband annual meeting, June 16th 2005.

E. J. Klein, D. H. Geuzebroek, H. Kelderman and A. Driessen, "Wavelength selective switch using thermally tunable resonators," In (Ed.), Proceedings 2004 Symposium LEOS Annual Meeting 2003 (pp. MM1), Tucson, Arizona, U.S.A., ISBN issn:1092-8081.

Conference proceedings

E. J. Klein, G. Sengo, L. T. H. Hilderink, M. Hoekman and A. Driessen, "Reconfigurable λ-Router based on thermally tunable vertically coupled microring resonators in Si_3N_4/SiO_2," poster at the ePIXnet Winterschool 2007, 11-16 March, Pontresina, Switzerland, 2007.

E. J. Klein, D. H. Geuzebroek, H. Kelderman, C. Bornholdt and A. Driessen, "40 Gbit/s Optical Add-Drop Multiplexer in Si_3N_4 based on Microring Resonators," Poster at the Mesa+ Meeting 2005, University of Twente, Enschede, The Netherlands, 29 September 2005.

E. J. Klein, D. H. Geuzebroek, H. Kelderman and A. Driessen, "Integrated Optical adddrop multiplexer using thermally tunable microring resonators," In (Ed.), Proceedings 2004 Symposium LEOS/LEOS Benelux Chapter, University of Ghent, ISBN: 9076546061.

M. Balakrishnan, E. J. Klein, M. Faccini, M. B. J. Diemeer, W. Verboom, A. Driessen, D. N. Reinhoudt, A. Leinse, "Fabrication of an electro-optic polymer microring resonator," In (Ed.), Proceedings of 11th annual symposium of IEEE/LEOS Benelux, pp. 73-76, 2006, ISBN:90-6144-989-8.

R. Dekker, E. J. Klein, J. Niehusmann, M. Först, F. Ondracek, J. Ctyroky, N. Usechak and A. Driessen, "Self Phase Modulation and Broadband Raman Gain in Silicon-on-Insulator Waveguides," poster at the ePIXnet Winterschool 2006, 13-17 March, Pontresina, Switzerland, 2006.

R. Dekker, E. J. Klein, J. Niehusmann, M. Forst, F. Ondracek, J. Ctyroky, N. Usechak and A. Driessen, "Self phase modulation and stimulated raman scattering due to high power femtosecond pulse propagation in silicon-on-insulator waveguides", Poster in Proceedings of the Symposium IEEE LEOS Benelux, Mons, Belgium, 1-2 December 2005, Pp. 197-200, Editors: P. Mégret, M. Wuilpart, S. Bette, N. Staquet, ISBN: 2-9600226-4-5.

R. Dekker, M. B. J. Diemeer, E. J. Klein, L. T. H. Hilderink, K. Wörhoff and A. Driessen, "Photo-Patternable Polymer Waveguides for microring Resonators," Proceedings of the 31st European Conference on Optical Communications (ECOC), Glasgow, Scotland, 25-29 September 2005, Vol. 2, Paper Tu 1.6.7, pp. 187-188, ISBN 0-86341-544-X.

R. Dekker, E. J. Klein, A. Driessen, J. Niehusman, M. Forst, F. Ondracek and J. Ctyroky, "Femtosecond pulse propagation through nanophotonic structures," Poster at the Mesa+ Meeting 2005, University of Twente, Enschede, the Netherlands, 29 September 2005.

R. Dekker, L.T.H.Hilderink, M.B.J. Diemeer, E.J. Klein, K. Wörhoff and A. Driessen, "Rare-earth-doped nanoparticles dispersed in photo-definable polymers for use in microring resonator devices," LEOS Benelux Workshop, Eindhoven, May 20th 2005.

A. Driessen, D. H. Geuzebroek, H. J. W. M. Hoekstra, H. Kelderman, E. J. Klein, D. J. W. Klunder, C. G. H. Roeloffzen, F. S. Tan, E. Krioukov, C. Otto, H. Gersen, N. F. van Hulst and L. Kuipers, "Microresonators as building blocks for VLSI photonics," In F. Michelotti, A. Driessen, M. Bertolotti (Eds.), Proceedings 39th Course of the International School of Quantum Electronics "Microresonators as building blocks for VLSI photonics," pp. 413-414, Melville, New York, USA: American Institute of Physics, 2004.

A. Driessen and E.J. Klein, "Optical microring resonators as promising building blocks for VLSI photonics", Invited talk, 3rd International Symposium on VLSI Photonics, 2006, Opera-Inha University, Inha, South Korea.

A. Driessen and E.J. Klein, "Photonic integration technology of silicon oxynitride based microring devices", Invited talk, WAPITI/PICMOS workshop, 7-12-2006, Halle, Germany.

A. Driessen, D.H. Geuzebroek and E.J. Klein, "Optical network components based on microring resonators," Invited talk, In (Ed.), Proceedings ICTON 2006, Nottingham, 2006, IEEE Catalog Number: 06EX1326, ISBN: 1-4244-0236-0, Library of Congress: 2006921097.

A. Driessen, D.H. Geuzebroek and E.J. Klein, "High index contrast photonics components for optical data communication," Invited talk, OFC 2006, Anaheim (Ca), paper OThE3. 9-3-2006.

A. Driessen, R. Dekker, M. B. J. Diemeer, D. H. Geuzebroek, H. J. W. M. Hoekstra, E. J. Klein, A. Leinse, "Microresonators as promising building blocks for VLSI photonics," Invited paper, Proceedings of SPIE, Conference on Integrated Optics: Theory and Applications, Warsaw, Poland, 31 August – 2 September 2005, Vol. 5956, Pp. 59560Q-1 – 59560Q-14, ISBN number: 0-8194-5963-1, ISSN: 0277-786X, Editors: P.V. Lambeck, C. Gorecki. Organized by SPIE Poland Chapter, SPIE Europe and Warsaw University of Technology, Poland.

D. H. Geuzebroek, R. Dekker, E. J. Klein, C. Bornholdt, J. Niehusmann and A. Driessen, "Behavior of picosecond and femtosecond pulses in SiO_2/Si_3N_4 microring resonator filters," In (Ed.), Proceedings of the Symposium IEEE LEOS Benelux, Mons, Belgium, 1-2 December 2005, Pp. 51-54, Editors: P. Mégret, M. Wuilpart, S. Bette, N. Staquet, ISBN: 2-9600226-4-5.

D. H. Geuzebroek, E. J. Klein, H. Kelderman, C. Bornholdt and A. Driessen, "40 Gbit/s Reconfigurable Add-Drop Multiplexer base don Microring Resonators," In (Ed.), Proceedings of the 31st European Conference on Optical Communications (ECOC), Glasgow, Scotland, 25-29 September 2005, Vol. 4, Invited Paper Tu 3.6.1, pp. 983-986, ISBN 0-86341-544-X.

D. H. Geuzebroek, E. J. Klein, H. Kelderman and A. Driessen, “Wavelength selective switch using thermally tunable microring resonators,” In F. Michelotti, A. Driessen, M. Bertolotti (Eds.), Proceedings 39th Course of the International School of Quantum Electronics “Microresonators as building blocks for VLSI photonics,” pp. 413-414, Melville, New York, USA: American Institute of Physics, 2004.

D. H. Geuzebroek, E.J. Klein, H. Kelderman and A. Driessen, “Compact wavelength selective switch,” In (Ed.) Proceedings of the 30st European Conference on Optical Communications (ECOC), Stockholm, Sweden, 2004, pp. 580-581, ISBN 91-975291-3-3.

D. H. Geuzebroek, E. J. Klein, H. Kelderman and A. Driessen, “Wavelength tuning and switching of a thermo-optic micro ring resonator,” In J. Ctyroky, M. Hubalek, F. Ondrcek (Eds.), In (Ed.) Proceedings of the 11th European Conference on Integrated Optics (ECIO) 2003, pp. 395-398, Prague, Czech Republic: Czech Technical University Prague, ISBN 80-01-02729-5.

D. H. Geuzebroek, E. J. Klein, H. Kelderman, F. S. Tan, D. J. W. Klunder and A. Driessen, “Thermal tunable, Wide FSR switch based on Microring Resonators,” In (Ed.), T. D. Visser, D. Lenstra, H. F. Schouten (Eds.), Proceedings of IEEE/LEOS 2002, pp. 155-158, Amsterdam: IEEE/LEOS Benelux Chapter, c/o Vrije Universiteit van Amsterdam, ISBN 90-807519-1-x.

D. H. Geuzebroek, E. J. Klein, H. Kelderman, F. S. Tan, D. J. W. Klunder and A. Driessen, “Thermal wavelength-selective switch based on micro-ring resonators,” In (Ed.), Proceedings of the 28st European Conference on Optical Communications (ECOC), Copenhagen, Denmark, 2002.

R. G. Heideman, D. H. Geuzebroek, A. Leinse, A. Melloni, F. Morichetti, C. G. H. Roeloffzen, A. Meijerink, L. Zhuang, E. van Etten, E. J. Klein and A. Driessen, “Low loss, high contrast optical waveguides based on CMOS compatible LPCVD processing,” Invited, In (Ed.), Proceedings of the 13th European Conference on Integrated Optics (ECIO), Kopenhagen, Denmark, 2007.

M. C. Larciprete, E. J. Klein, A. Belardini, D. H. Geuzebroek, A. Driessen and F. Michelotti, “Polarization conversion in vertically coupled Si_3N_4/SiO_2 microring resonators,” In (Ed.), F. Michelotti, A. Driessen, M. Bertolotti (Eds.), Proceedings 39th Course of the International School of Quantum Electronics “Microresonators as building blocks for VLSI photonics,” pp. 413-414, Melville, New York, USA: American Institute of Physics, 2004.

R. Meijerink, D. H. Geuzebroek, E. J. Klein, H. Kelderman, R. Dekker, M. B. J. Diemeer and A. Driessen, “Optimization of driving signal fort hermal modulation of a microring resonator,” In R. M. de Ridder, G. Altena, D. H. Geuzebroek, R. Dekker (Eds.), In (Ed.) Proceedings 8th Annual Symposium IEEE/LEOS Benelux Chapter, pp 85-88, 2003, Enschede: IEEE LEOS Benelux, p/a Universiteit Twente, Integrated Optical Microsystems, ISBN 90-365-1990-X.

P. J. Urban, E. G. C. Pluk, E. J. Klein, A. M. J. Koonen, G. D. Khoe and H de Waardt, “Simulation Results of Dynamically Reconfigurable Broadband Photonic Access

Networks (BB Photonics),” International Conference on Access Technologies, Cambridge, 2006.

Dankwoord/Acknowledgements

Zo, dit is het dan. Na vele honderden uren typen, vele tientallen flessen cola (tsja, als je geen koffie drinkt…) en ongeveer 400.000 letters getyped te hebben, zit het erop. Althans…
Waarschijnlijk had ik me een heleboel typewerk kunnen besparen aangezien de kans statistisch gezien vrijwel nul is dat iemand de pagina's hiervoor ook echt doorleest.
Aangezien ik natuurlijk graag wil dat iedereen weet ik gedaan heb, druk ik hier alsnog een korte samenvatting af van al het voorgaande zodat jullie het wel moeten lezen:

Microring resonatoren blah blah blah…

Dat dekt de lading wel voor ongeveer 99% dacht ik zo.
Natuurlijk was dit boekje nooit mogelijk geweest zonder de fijne samenwerking met een groot aantal mensen die ik bij deze wil bedanken.

Allereerst wil ik mijn promotor Alfred Driessen bedanken voor zijn steun en adviezen (Een piramide heeft een punt Edwin…). Dit geldt vooral ook voor de laatste maanden waarin een externe rem af en toe echt nodig was.
Furthermore I would like to thank the members of my committee: Markus Pollnau, Wim van Etten, Roel Baets, René Heideman, Huug de Waardt, Andrea Melloni and Ton Mouthaan who have taken the time to read through a considerable number of pages. In addition I would like to thank Wim van Etten for his additional comments and Andrea Melloni for traveling all the way from Milano to Enschede.

En dan, tsja, het liefst zou ik jullie helemaal niet willen noemen, gewoon om jullie te jennen maar ik kon het echt niet over mijn moordkuil verkrijgen dus: Dekkie en Hop, lieve nimfjes, bedankt! Ik heb met jullie een geweldige tijd gehad, zowel vanwege de discussies op hoog niveau alsook vanwege onze bijzonder creatieve beeldvormende taal momenten (en laten we het daar maar gewoon op houden). Andere mensen waar ik ook liever niet mee geassocieerd wil worden zijn Douwe (ex-meester) Geuzebroek, Arne (kipje) Leinse en CMP-Guru en Meester der verlichting Marcel Hoekman.

Natuurlijk kan in mijn dankwoord ook onmogelijk Anton Hollink onbreken voor alle support (voor wat dan ook) door de jaren heen. Onder het kopje "voor vanalles en nog wat" horen zeker ook Mart Diemeer en Rita ter Weele thuis. Tevens wil ik Lucie Hilderink, Henry Kelderman en de best geklede man in de cleanroom, Gabriel Sengo, bedanken voor de meer dan 200.000 (ja echt) ring resonatoren die ze in totaal in de afgelopen jaren voor mij gefabriceerd hebben. Ook moet ik hier Meindert Dijktra bedanken voor al zijn fabricage advies. Ik wil in dit rijtje zeker ook de ASML-boys Rudy Pellens en Paul van Dijk bedanken voor hun bijzondere inzet bij de fabricage van de Router. Dit geldt tevens voor een paar bijzonder getalenteerde wirebonders bij LioniX, Arjan Hoekman en Robert Wijn. En als we dan toch in de LioniX hoek zitten wil ik ook gelijk even Hans v/d Vlekkert en Albert Borreman bedanken.

I would also like to thank Patryk Urban for performing BER measurements on the OADM.

One of the great things of the NAIS project was that I could travel to some very nice cities in Europe. Even better, however, was the fact that I got to meet a few great people who made my already highly enjoyable journeys even better. Maria Christina, Christan and Francesco, thank you so much for that!

Verder wil ik natuurlijk ook alle andere (ex)IOMS-ers bedanken voor hun hulp of gewoonweg de “good company”: René de Ridder, Henk van Wolferen, Geert Altena, Els Kok, Wouter Engbers, Paul Lambeck, Hugo Hoekstra, Dimitri Geskus and Jonathan Bradley (whatever happens in the F1…), Muralidharan Balakrishnan, Freddy Tan, Henry Uranus, Boudewijn Docter, Kerstin Wörhoff, Gamar Hussein, Cazimir Bostan, Wenbin Hu, Dion Klunder, Sami Musa, Chris Roeloffzen, Lasse Kauppinen, Chaitanya Dongre, Didit Yudistira, Tristan Doornebosch, Feridun Ay, Frank van Soest, Jing Yang, Remco Stoffer en Joris van Lith. Wat betreft de niet IOMS-ers gaat mijn dank ook zeker nog uit naar Mark Smithers, Peter Linders en Eddy Ruiter. (Mocht je jezelf hier niet tussen vinden dan kun je bij mij langskomen voor een biertje).

And, specifically for you Dorleta: I still think you should do a PhD ;-)

Mijn ouders, Jan en Trijnie, wil ik bedanken voor hun onvoorwaardelijke steun voor meer dingen dan ik onder woorden kan brengen en natuurlijk ook Baudyn, gewoon omdat ze mijn zusje is…

Ten slotte wil ik Floor bedanken. Hoewel ik mijn thesis alleen geschreven heb, was het (helaas) toch een gezamelijk onderneming. Gelukkig kon ik bij jou altijd even ontstressen zodat ik het weer even vol kon houden. Dank je wel liefje…

Edwin